



HAL
open science

Generation of intense terahertz sources by ultrashort laser pulses

Pedro González de Alaiza Martínez

► **To cite this version:**

Pedro González de Alaiza Martínez. Generation of intense terahertz sources by ultrashort laser pulses. Optics [physics.optics]. Université Paris Saclay (COMUE), 2016. English. NNT : 2016SACLS350 . tel-01430627

HAL Id: tel-01430627

<https://theses.hal.science/tel-01430627>

Submitted on 10 Jan 2017

HAL is a multi-disciplinary open access archive for the deposit and dissemination of scientific research documents, whether they are published or not. The documents may come from teaching and research institutions in France or abroad, or from public or private research centers.

L'archive ouverte pluridisciplinaire **HAL**, est destinée au dépôt et à la diffusion de documents scientifiques de niveau recherche, publiés ou non, émanant des établissements d'enseignement et de recherche français ou étrangers, des laboratoires publics ou privés.

NNT : 2016SACLS350

THESE DE DOCTORAT
DE
L'UNIVERSITE PARIS-SACLAY
PREPAREE A
L'UNIVERSITE PARIS-SUD

COMMISSARIAT À L'ÉNERGIE ATOMIQUE ET AUX ÉNERGIES ALTERNATIVES

ECOLE DOCTORALE N° 572
École Doctorale Ondes et Matière

Spécialité de doctorat : Physique

Par

M. Pedro GONZÁLEZ DE ALAIZA MARTÍNEZ

Generation of intense terahertz sources
by ultrashort laser pulses

Thèse présentée et soutenue à Orsay, le 21 octobre 2016 :

Composition du Jury :

M. BONNAUD, Guy	Directeur de Recherche CEA	Président
M. TIKHONCHUK, Vladimir	Professeur à l'Université de Bordeaux	Rapporteur
M. JEPSEN, Peter Uhd	Professeur à l'Université Technique du Danemark	Rapporteur
M. WOLF, Jean-Pierre	Professeur à l'Université de Genève	Examineur
M. SKUPIN, Stefan	Chargé de Recherche CNRS	Examineur
M. BERGÉ, Luc	Directeur de Recherche CEA	Directeur de thèse
M ^{me} VÁZQUEZ CENDÓN, María Elena	Professeur à l'Université Saint-Jacques de Compostelle	Invitée

A mis padres
À mes parents

Génération de sources térahertz intenses par des impulsions laser ultrabrèves

Mots-clés: Sources térahertz intenses, Interaction laser-matière, Optique non-linéaire, Oscillations plasma, Photoionisation

Résumé en français:

Le spectre électromagnétique possède une zone étroite, localisée entre les micro-ondes et l'infrarouge, appelée région des ondes térahertz (THz), qui est comprise entre 0.1 et 30 THz. Ces ondes, longtemps inaccessibles car situées à la frontière entre l'électronique et l'optique, connaissent aujourd'hui un intérêt grandissant et possèdent des applications prometteuses dans divers secteurs de la science comme l'imagerie médicale et l'identification des explosifs à distance. Cependant, la production de rayonnement THz intense, d'amplitude proche du GV/m, qui devrait permettre de sonder efficacement des matériaux à distance, reste encore une question en suspens. Cette thèse a précisément pour but d'étudier la génération d'un tel rayonnement THz par couplage de deux impulsions laser ultracourtes —une onde fondamentale et son harmonique deux— capables d'ioniser un gaz (par exemple, l'air ou l'argon). Le plasma ainsi créé joue le rôle de convertisseur nonlinéaire de fréquence, transformant une partie de l'énergie du champ laser dans la bande THz via une gamme riche de mécanismes physiques, notamment l'effet Kerr, la photoionisation et les forces pondéromotrices induites dans le plasma. Grâce à un travail de modélisation analytique et numérique de ces principaux mécanismes, nous avons examiné de manière complète la génération d'impulsions THz pour des intensités laser allant de celles rencontrées en filamentation laser (10^{12} - 10^{14} W cm⁻²) jusqu'aux intensités proches de la limite relativiste (10^{15} - 10^{18} W cm⁻²), une fourchette d'intensités peu étudiée jusqu'à présent dans ce domaine. Il est déjà connu qu'à basses intensités la photoionisation induite par le champ laser domine l'émission térahertz, laquelle dépend

fortement de la configuration des couleurs (ou harmoniques) laser. Nous démontrons ici que, au-delà de la configuration laser « classique » à deux couleurs, coupler plusieurs fréquences laser suivant les harmoniques d'une forme d'onde en dents de scie est optimal pour renforcer la production de rayonnement. Les simulations prévoient une efficacité de conversion d'énergie THz de 2% avec quatre couleurs, valeur record inégalée à ce jour. De plus, en nous aidant d'une expérience faite dans l'air, nous identifions la signature de l'effet Kerr dans le spectre THz émis, qui, plus faible, se révèle complémentaire de la signature plasma. Quand l'intensité de l'impulsion laser est augmentée au-delà de $10^{15} \text{ W cm}^{-2}$, nous démontrons que le rayonnement térahertz émis croît de manière non-monotone, dû au fait qu'il existe une valeur d'intensité maximisant l'énergie THz produite par chaque couche électronique. Finalement, nous avons étudié en géométrie 2D l'effet combiné de la photoionisation et des forces pondéromotrices plasma à des intensités proches de $10^{18} \text{ W cm}^{-2}$, nous permettant d'obtenir des champs THz excédant le GV/m dans l'argon. Ces dernières forces augmentent avec l'intensité laser et ouvrent des perspectives intéressantes pour la génération de champs térahertz très intenses dans le régime relativiste de l'interaction laser-matière.

Generation of intense terahertz sources by ultrashort laser pulses

Keywords: Intense terahertz sources, Laser-matter interaction, Nonlinear optics, Plasma oscillations, Photoionization

Abstract in English:

The electromagnetic spectrum has a narrow frequency band, lying between microwaves and infrared, known as terahertz (THz) waves and extending from 0.1 to 30 THz. These waves, inaccessible until a recent past because they are situated at the boundary between electronics and optics, are raising interest because of their promising applications in several areas such as medical imaging and remote identification of explosives. However, producing intense THz radiation with amplitudes belonging to the GV/m range should allow us to probe efficiently remote materials, which still remains an open issue. The goal of this thesis is precisely to study the generation of such intense THz radiation by coupling two ultrashort laser pulses —the fundamental and its second harmonic— able to ionize a gas target (for example, air or argon). The plasma created by photoionization then acts as a nonlinear frequency converter, transforming part of the laser energy into the THz band via a wide range of physical mechanisms including the Kerr effect, the photoionization and ponderomotive forces induced inside the plasma. By means of an analytical and numerical modelling of these key mechanisms, we have comprehensively examined the generation of THz pulses at laser intensities ranging from characteristic intensities met in laser filamentation (10^{12} - 10^{14} W cm⁻²) to near-relativistic intensities (10^{15} - 10^{18} W cm⁻²), this latter intensity range having been little investigated so far in this domain. It is already known that at low intensities laser-induced photionization dominates in terahertz generation, which strongly depends on the configuration of the laser colours (or harmonics). We demonstrate here that, beyond the “classical” two-colour laser

setup, coupling several laser frequencies following the harmonics of a sawtooth waveform is optimal to enhance THz production. Simulations predict a laser-to-THz energy conversion efficiency of 2% with four colours, a record value unequalled so far. Moreover, with an experiment realized in air, we identify the Kerr signature in the emitted THz spectrum, which, even weaker, looks complementary to the plasma signature. When the intensity of the laser pulse is increased beyond $10^{15} \text{ W cm}^{-2}$, we prove that the growth of the emitted terahertz radiation is nonmonotonic, due to the fact that there exists an optimal intensity value that maximizes the THz energy produced by each electronic shell of the irradiated atom. Finally, we have studied in 2D geometry the combined effect of photoionization and ponderomotive forces at intensities close to $10^{18} \text{ W cm}^{-2}$, allowing us to obtain THz fields exceeding the GV/m threshold in argon. These latter forces increase with the laser intensity and thus open interesting perspectives for the generation of very intense terahertz fields in the relativistic regime of laser-matter interaction.

Generación de fuentes de radiación Terahertz intensas mediante pulsos láser ultrabreves

Palabras clave: Fuentes Terahertz intensas, Interacción láser-materia, Óptica no lineal, Oscilaciones plasma, Fotoionización

Resumen en español:

El espectro electromagnético posee una zona estrecha, localizada entre las microondas y la radiación infrarroja, llamada región de las ondas Terahertz (THz), que está comprendida entre 0.1 et 30 THz. Estas ondas, durante mucho tiempo inaccesibles debido a que se encuentran situadas en la frontera entre la electrónica y la óptica, están despertando un interés creciente por la gran cantidad de aplicaciones prometedoras que poseen en diversos sectores científicos, como la imagen médica y la identificación de explosivos a distancia. No obstante, la producción de radiación THz intensa, de amplitud cercana al GV/m, la cual debería permitir sondear materiales energéticos a distancia, sigue siendo una cuestión abierta. Esta tesis tiene precisamente como objetivo el estudio de la generación de dicha radiación THz intensa acoplando dos pulsos láser —una onda fundamental y su segundo armónico— capaces de ionizar un gas (por ejemplo, aire o argón). El plasma creado de este modo desempeña el papel de convertidor no lineal de frecuencia, transformando una parte de la energía del láser en la banda THz mediante una rica gama de mecanismos físicos, entre los que destacan el efecto Kerr, la fotoionización y las fuerzas ponderomotrices inducidas dentro del plasma. Gracias a un trabajo de modelización tanto numérico como analítico de estos mecanismos clave, hemos examinado de forma integral la generación de pulsos THz a intensidades láser yendo desde las encontradas en la filamentación láser (10^{12} - 10^{14} W cm⁻²) hasta las cercanas al límite relativista (10^{15} - 10^{18} W cm⁻²), habiendo sido este último rango de intensidades poco estudiado en este campo hasta el presente. Ya es sabido que a bajas intensidades la fotoionización inducida por el láser domina la emisión

Terahertz, la cual depende enormemente de la configuración de los colores (o armónicos) del láser. Demostramos aquí que, más allá de la “clásica” configuración del láser en dos colores, acoplar varias frecuencias láser siguiendo los armónicos de una forma de onda en diente de sierra es óptimo para incrementar la producción THz. Las simulaciones predicen una eficacia de conversión de energía THz de 2% empleando cuatro colores, un valor récord inigualado hasta hoy. Además, ayudándonos de un experimento realizado en aire, identificamos la firma del efecto Kerr en el espectro THz emitido, la cual, pese a ser más débil, resulta complementaria a la firma del plasma. Cuando se aumenta la intensidad del láser más allá de $10^{15} \text{ W cm}^{-2}$, demostramos que la radiación Terahertz emitida crece de manera no monotónica, debido a que existe un valor de intensidad que maximiza la energía THz producida por cada capa electrónica. Finalmente, hemos estudiado en geometría 2D el efecto conjunto de la fotoionización y de las fuerzas ponderomotrices a intensidades próximas a $10^{18} \text{ W cm}^{-2}$, lo que nos permite obtener campos THz cuyas amplitudes exceden el GV/m en argón. Estas últimas fuerzas aumentan con la intensidad láser y, por tanto, ofrecen perspectivas interesantes para la generación de campos Terahertz muy intensos en un régimen de interacción láser-materia relativista.

Remerciements

L'aboutissement de ma thèse, réalisée au sein de la Direction des Applications Militaires d'Île de France du Commissariat à l'Énergie Atomique et aux Énergies Alternatives (CEA, DAM, DIF), est le résultat de trois ans de travail assidu et collaboratif. Ces recherches ont été cofinancées par le CEA et l'École Doctorale Ondes et Matière (EDOM) que je remercie pour leur soutien.

Ce travail m'a permis de rencontrer de très nombreuses personnes auxquelles je veux ici exprimer ma gratitude.

Tout d'abord, je tiens à exprimer ici un vif et sincère remerciement à mon directeur de thèse, Monsieur Luc Bergé, pour m'avoir encadré pendant ces trois ans. Je suis reconnaissant de m'avoir encouragé à faire un beau travail de recherche, riche en résultats, à travers ses conseils, ses contributions, ses orientations pendant ma thèse et pour mon futur postdoc, ses réflexions et ses critiques constructives. Il a toujours été prêt à m'aider, même très chargé de travail. Merci beaucoup pour tout, Luc !

Par ailleurs, je remercie tous les membres de mon jury d'avoir accepté de venir siéger à mon jury de soutenance. Notamment les rapporteurs, Messieurs Vladimir Tikhonchuk et Peter Uhd Jepsen pour leurs avis éclairés, aussi que les autres membres du jury, Messieurs Guy Bonnaud, Jean-Pierre Wolf, Stefan Skupin et Madame María Elena Vázquez Cendón, pour leur bienveillance à l'égard de mon travail.

Je souhaite aussi adresser ma reconnaissance à tous les membres de l'équipe de travail « *Photonic Sources Group* », un groupe très dynamique dont les travaux conduisant régulièrement à des publications de haut niveau. Spécialement, un très grand merci à Xavier Davoine, Laurent Gremillet et Arnaud Debayle pour ces trois ans de fructueuse collaboration pendant lesquelles j'ai beaucoup appris d'eux ! Je voudrais également transmettre mes remerciements aux collaborateurs externes avec lesquels j'ai publié et/ou partagé d'intéressantes discussions scientifiques: Ihar Babushkin, Stefan Skupin, Illia Thielle, Olga Kosareva, Christian Köhler (merci pour tes explications au début de ma thèse !), A. P. Shkurinov, S. L. Chin, J. V. Moloney, J.-C. Saut et A. C. Newell.

Je veux aussi exprimer ma gratitude à tous mes collègues du Service pour m'avoir si bien accueilli pendant tout le déroulement de ma thèse: Franck, Florian, Jean-Étienne (merci beaucoup pour tes remarques sur mon manuscrit !), Serge, Sylvie, Brigitte, Michel,

Antoine, Patrick, Didier, Alain... La vie quotidienne dans le laboratoire n'aurait pas été la même sans la compagnie vivifiante des jeunes chercheurs, stagiaires et thésards, ayant séjourné au CEA pendant mes recherches de doctorat: Jérémie, Christian, Mathieu, Charles, Sébastien, Julien F., Julien M., Simon, Bertrand, Alisée, Jérémy, Witold, Vivien, Giacomo, Thibault, Adélie, Antoine, Maxime, Pierre-Louis, Victor, Guillaume... J'espère n'avoir oublié personne et encore merci à tous, les amis !

Enfin, je remercie ma famille et Carmen, qui sont en Espagne, pour tout son soutien pour faire cette thèse. ¡Muchas gracias a todos! Aussi merci à mes amis qui sont à Vitoria (Espagne) et à tous les amis que j'ai connus à Paris pendant ces trois ans (Alberto, Ingrid, Riccardo, Nicolas, Maura, Marco, Adriano, Cécile...). Je veux aussi adresser mes remerciements à María Luisa Garzón Martín, professeur à mon école d'ingénieurs, pour m'avoir aidé et encouragé à suivre le chemin de la recherche.

Synthèse en français

Le spectre électromagnétique possède une zone étroite, localisée entre les micro-ondes et l'infrarouge, appelée région des ondes térahertz (THz ou rayons T) et qui est traditionnellement comprise entre 0.1 et 30 THz (cette limite supérieure est de nos jours étendue jusqu'à 100 THz). Le rayonnement THz est non-ionisant et il est capable de pénétrer quelques millimètres de matériaux non conducteurs tels que textiles, papier, carton, plastique, céramique, bois ou tissus biologiques. Il peut également traverser le brouillard et les nuages, mais il est absorbé sur de courtes distances de l'ordre du mètre à cause de la présence de vapeur d'eau. Du point de vue de la spectroscopie moléculaire, cette bande de fréquences fournit de nombreuses informations sur la structure des molécules et leurs mouvements associés. En effet, chaque molécule a une signature unique dans cette bande, qui peut être exploitée pour l'identification de groupes chimiques fonctionnels spécifiques.

Ces ondes furent longtemps inaccessibles par la technologie courante, car elles sont situées à la frontière entre les domaines de l'électronique et de l'optique. Longtemps réservée à l'observation astrophysique, elles connaissent aujourd'hui un intérêt grandissant et possèdent des applications prometteuses dans divers secteurs de la science comme l'imagerie médicale et l'identification des explosifs à distance. Néanmoins, la production de rayonnement THz intense, d'amplitude proche du GV/m et à bande spectrale large ajustable au-delà de 30 THz, qui devrait permettre de sonder efficacement de nombreux matériaux à distance dans l'infrarouge lointain, reste encore une question en suspens. Diverses technologies pour la génération du rayonnement THz existent aujourd'hui comme les lasers à cascade quantique ou la rectification optique dans des cristaux non linéaires. Cependant, ces techniques sont basées sur des émetteurs solides et elles sont donc limitées par leur seuil d'endommagement et l'étroitesse de leur spectre THz émis.

Dans ce contexte, une méthode alternative apparut il y a moins de deux décennies, offrant le potentiel de fournir des champs THz intenses à large bande. Cette méthode consiste à coupler plusieurs impulsions laser ultracourtes —typiquement deux impulsions, une onde fondamentale et son harmonique deux—, lesquelles, focalisées, sont capables d'ioniser un gaz (par exemple, l'air ou l'argon). Le plasma ainsi créé joue le rôle de convertisseur nonlinéaire de fréquence, transformant une partie de l'énergie du champ laser dans la bande THz via une gamme riche de mécanismes physiques, notamment l'effet

Kerr, la photoionisation et les forces pondéromotrices induites dans le plasma. Comme le plasma est un état de la matière qui peut supporter des puissances très élevées sans subir d'endommagement, cette technique peut donc fournir des champs THz importants et à large bande spectrale avec des efficacités de conversion en énergie laser-THz les plus grandes ($\gg 10^{-4}$) parmi toutes les technologies explorées.

Cette thèse a précisément pour but d'étudier cette technique afin de mieux comprendre les principaux mécanismes responsables de la conversion d'énergie laser dans la bande spectrale THz et, en outre, d'explorer de nouveaux régimes d'interaction laser-matière propices à l'émission THz. En effet, nous avons examiné de manière complète la génération d'impulsions THz pour des intensités optiques allant de celles rencontrées en filamentation laser (10^{12} - 10^{14} W cm⁻²) jusqu'aux intensités proches de la limite relativiste pour le mouvement des électrons (10^{15} - 10^{18} W cm⁻²), un domaine d'intensités laser peu étudié jusqu'à présent dans ce contexte. Notre objectif était de proposer les meilleures configurations d'une onde de pompe laser et d'un gaz d'interaction pour maximiser l'énergie du champ THz émis, et d'en contrôler les caractéristiques (amplitude et largeur spectrale). La plupart de notre étude a notamment consisté en un travail de modélisation analytique et de simulation numérique haute-performance, dont une partie a été confrontée à de nouvelles mesures expérimentales. Nous avons commencé par étudier le régime d'interaction à basse intensité laser, où les gaz sont faiblement ionisés ($Z^* < 1$). En nous aidant d'une expérience d'interaction laser-air, nous identifions grâce à des simulations numériques la signature de l'effet Kerr dans le spectre THz émis, qui, plus faible et à fréquences plus élevées, se révèle complémentaire de la signature plasma. En effet, au front de propagation du filament laser, la polarisation nonlinéaire des électrons liés crée une émission THz sur l'axe par le mécanisme dit de mélange à quatre ondes. L'émission THz provenant des photocourants induits ensuite par le plasma formé domine la contribution de l'autofocalisation Kerr et se propage dans un cône présentant un petit angle d'émission ($< 10^\circ$). Nous démontrons l'existence d'une diminution abrupte de la fréquence centrale du spectre THz des hautes fréquences associées à l'effet Kerr aux basses fréquences proches de la fréquence plasma, accompagnée d'une croissance de plus de deux ordres de grandeur dans l'intensité spectrale quand la photoionisation a lieu.

Il est déjà connu qu'aux intensités élevées la photoionisation induite par le champ laser constitue le mécanisme principal de l'émission térahertz. Cependant, celle-ci dépend fortement de la configuration des couleurs (ou harmoniques) laser, comme expliqué par le modèle appelé « Local Current » (LC). En effet, ce modèle est construit sur l'hypothèse que localement, dans un volume plasma infinitésimal, le champ rayonné est proportionnel à la dérivée du courant des électrons libres. Sachant que l'ionisation apparaît au voisinage des extrema du champ laser (ces instants sont appelés « relativement événements

d'ionisation »), la densité électronique croît de manière échelonnée, avec un saut de densité à chaque évènement d'ionisation. Le courant dépend de cette densité électronique et d'une vitesse électronique fluide, laquelle est proportionnelle à l'intégrale du champ laser. Selon la configuration laser, ce courant développe une composante à variation lente, qui est responsable de l'émission THz par photoionisation et qui dépend de la somme de tous les évènements d'ionisation produits au cours de l'impulsion optique. Le modèle LC explique donc le rayonnement THz comme une interférence de ces évènements d'ionisation.

Nous nous sommes posé la question de savoir quelle est la configuration laser, au-delà de la configuration « classique » à deux couleurs, optimisant la valeur vitesse aux évènements d'ionisation de façon à maximiser la génération de rayonnement THz. Comme la vitesse fluide est liée à l'intégrale du champ électrique, la seule façon de placer ses extrema aux évènements d'ionisation est de casser la continuité du champ laser. Nous démontrons ici qu'un tel profil laser optimal est la forme d'onde en dents de scie. Suivre les harmoniques de cette forme d'onde nous donne le couplage optimal de plusieurs fréquences laser. Nous avons vérifié ce résultat avec des simulations 3D dans l'argon. Elles prévoient une efficacité de conversion d'énergie THz de 2% avec quatre couleurs laser, une valeur record inégalée à ce jour. Quand l'intensité de l'impulsion laser est augmentée au-delà de 10^{15} W cm⁻², le gaz est ionisé plusieurs fois ($Z^* > 1$). Nous démontrons analytiquement et à l'aide de simulations numériques que le rayonnement THz émis croît de manière non-monotone. Nous lions ce phénomène aux seuils d'ionisation de chaque couche électronique d'un atome donné (hydrogène, helium ou argon). En effet, quand l'intensité laser est augmentée, nous avons, d'un côté, des évènements d'ionisation plus intenses, mais d'un autre côté, l'ionisation du gaz est réalisée avec très peu de cycles laser, donc moins d'évènements d'ionisation. Il existe donc une valeur d'intensité maximisant l'énergie THz produite par chaque couche électronique et pour laquelle ces deux effets opposés se compensent. Finalement, nous avons étudié, en géométrie 2D pour un volume de plasma fini, comment le rayonnement THz est généré à partir de l'effet combiné de la photoionisation et des forces pondéromotrices plasma (longitudinales et transversales) à des intensités proches de 10^{18} W cm⁻². Nous avons aussi examiné les composantes du champ THz susceptibles d'être transmises hors de ce volume plasma. Aussi grâce à une étude analytique, nous démontrons que la photoionisation est encore le mécanisme dominant à ces intensités laser élevées proches de la limite relativiste et elle nous permet d'obtenir des champs THz excédant le GV/m se propageant sur l'axe dans l'argon. Les forces pondéromotrices augmentent avec l'intensité laser dans le plasma. Hors du plasma, nous décrivons, par la première fois, une forte émission THz hors axe due aux forces pondéromotrices transverses, laquelle dépend des gradients de densité aux interfaces plasma-vide. Ces résultats ouvrent des perspectives intéressantes pour la génération de champs térahertz très intenses dans

le régime relativiste de l'interaction laser-matière.

General physical constants

S.I. accounts for International System of units.

Symbol	Description	Value (S.I.)
c	speed of light in vacuum	$2.99792458 \times 10^8 \text{ m s}^{-1}$
μ_0	vacuum permeability	$1.256637061435917 \times 10^{-6} \text{ V s A}^{-1} \text{ m}^{-1}$
ε_0	vacuum permittivity	$8.854187817620391 \times 10^{-12} \text{ F m}^{-1}$
h	Planck constant	$6.62606957 \times 10^{-34} \text{ J s}$
$\hbar = h/(2\pi)$	reduced Planck constant	$1.05457173 \times 10^{-34} \text{ J s}$
$K_C = (4\pi\varepsilon_0)^{-1}$	Coulomb constant	$8.987551787368176 \times 10^9 \text{ N m}^2 \text{ C}^{-2}$
e	elementary charge	$1.602176565 \times 10^{-19} \text{ C}$
m_e	electron mass	$9.10938291 \times 10^{-31} \text{ kg}$
N_A	Avogadro number	$6.02214129 \times 10^{23} \text{ mol}^{-1}$
R_0	ideal gas constant	$8.3144621 \text{ J K}^{-1} \text{ mol}^{-1}$
k_B	Boltzmann constant	$1.3806488 \times 10^{-23} \text{ J K}^{-1}$

The values of c , μ_0 and ε_0 are related by:

$$\varepsilon_0\mu_0 = \frac{1}{c^2}. \quad (0.0.1)$$

Mathematical identities

Vector calculus identities

Let ϕ and ψ be scalar functions; \mathbf{u} and \mathbf{v} are vectors. We recall here the definition of the tensor product $\mathbf{u} \otimes \mathbf{v}$, whose (i, j) -th component is given by $(\mathbf{u} \otimes \mathbf{v})_{i,j} = u_i v_j$.

First-order differentiation identities

$$\nabla \cdot (\phi \mathbf{u}) = \mathbf{u} \cdot \nabla \phi + \phi (\nabla \cdot \mathbf{u}). \quad (0.0.2)$$

$$\nabla \times (\phi \mathbf{u}) = \phi (\nabla \times \mathbf{u}) + (\nabla \phi) \times \mathbf{u}. \quad (0.0.3)$$

$$\nabla \cdot (\mathbf{u} \times \mathbf{v}) = \mathbf{v} \cdot (\nabla \times \mathbf{u}) - \mathbf{u} \cdot (\nabla \times \mathbf{v}). \quad (0.0.4)$$

$$\nabla \cdot (\mathbf{u} \otimes \mathbf{v}) = (\nabla \cdot \mathbf{v}) \mathbf{u} + (\nabla \mathbf{u}) \mathbf{v}. \quad (0.0.5)$$

$$\nabla \cdot (\mathbf{u} \otimes \mathbf{v}) = (\nabla \cdot \mathbf{v}) \mathbf{u} + (\mathbf{v} \cdot \nabla) \mathbf{u}. \quad (0.0.6)$$

Second-order differentiation identities

$$\nabla \times (\nabla \phi) = \mathbf{0}. \quad (0.0.7)$$

$$\nabla \cdot (\nabla \times \mathbf{u}) = 0. \quad (0.0.8)$$

$$\nabla \times (\nabla \times \mathbf{u}) = \nabla (\nabla \cdot \mathbf{u}) - \nabla^2 \mathbf{u}. \quad (0.0.9)$$

Fourier transform

The Fourier transform and the inverse Fourier transform used in this dissertation are defined as

$$\hat{f}(\omega) = \mathcal{F}[f(t)] = \frac{1}{\sqrt{2\pi}} \int_{-\infty}^{+\infty} f(t)e^{-i\omega t} dt, \quad (0.0.10)$$

$$f(t) = \mathcal{F}^{-1}[\hat{f}(\omega)] = \frac{1}{\sqrt{2\pi}} \int_{-\infty}^{+\infty} \hat{f}(\omega)e^{i\omega t} d\omega. \quad (0.0.11)$$

Convolution product

The convolution product of two functions f and g is defined as follows:

$$f * g = (f * g)(t) = \frac{1}{\sqrt{2\pi}} \int_{-\infty}^{+\infty} f(\tau)g(t - \tau)d\tau = \frac{1}{\sqrt{2\pi}} \int_{-\infty}^{+\infty} f(t - \tau)g(\tau)d\tau. \quad (0.0.12)$$

The convolution theorem states that

$$\mathcal{F}[f * g] = \mathcal{F}[f]\mathcal{F}[g], \quad (0.0.13)$$

$$\mathcal{F}[fg] = \mathcal{F}[f] * \mathcal{F}[g]. \quad (0.0.14)$$

Contents

Résumé en français	iii
Abstract in English	v
Resumen en español	vii
Remerciements	ix
Synthèse en français	xi
General physical constants	xv
Mathematical identities	xvii
1 Introduction	1
1.1 The terahertz radiation	1
1.1.1 Applications of terahertz radiation	2
1.1.2 Technologies for generation and detection of terahertz waves	6
1.1.3 Laser-based terahertz sources	8
1.2 Motivation of this PhD work	11
2 Terahertz waves driven by laser pulses	15
2.1 Laser-plasma interaction	16
2.1.1 Maxwell equations	16
2.1.2 Vlasov equation	22
2.1.3 Moments for electrons	24
2.1.4 Cold-plasma fluid equations	24
2.1.5 Forward propagating electric fields	26
2.2 Ionization of gases	32
2.2.1 Ionization parameters	35
2.2.2 Single ionization	36
2.2.3 Multiple ionization	41

2.3	From optical self-focusing to UHI plasmas	51
2.3.1	Laser filamentation	51
2.3.2	Plasma waves	53
2.4	Laser-based terahertz emitters	57
2.4.1	The Four-wave mixing mechanism: Kerr effect	57
2.4.2	The local current model and the photocurrent mechanism	59
2.4.3	Electron-impact ionization	68
2.4.4	Longitudinal plasma wakefield	69
3	Numerical modelling	73
3.1	Propagation and PIC codes	79
3.1.1	The UPPE code	79
3.1.2	The CALDER code	80
3.2	A new Maxwell-Fluid code: MAXFLU	83
3.2.1	Numerical strategy	86
3.3	Comparing MAXFLU with UPPE and CALDER	95
3.3.1	MAXFLU versus UPPE	95
3.3.2	MAXFLU versus CALDER: relativistic plasmas at 10^{18} - 10^{19} W cm ⁻²	98
3.4	Simplified ½D semi-analytical Maxwell-Fluid model	107
4	Terahertz generation at moderate intensities	115
4.1	Experimental study of the terahertz emission by laser-plasma filaments: action of bound electrons versus free electrons	126
4.2	Boosting terahertz generation using a sawtooth-wave shape	137
5	Terahertz generation in high-intensity regimes	149
5.1	1D configuration: non-monotonic growth of the terahertz energy through multiple ionization	156
5.2	Multidimensional configuration: competition between photoionization and wakefield effects	166
	Conclusions and perspectives	179
	Appendices	183
A	Atomic units	183
B	Gaussian and squared-cosine slowly-varying envelopes	184
C	Moments of Vlasov equation for electrons	186
D	An algorithm to calculate the matrix of ionization probabilities	190
E	ADK-based degree of ionization for single-colour lasers	192

F	Anti-dispersive correction conserving the monotonicity	195
	List of communications	201
	Bibliography	205

1 Introduction

1.1 The terahertz radiation

The terahertz radiation, usually abbreviated as THz or even T-rays, traditionally refers to the electromagnetic radiation lying in the frequency band from 0.1 THz to 30 THz. Nowadays, with the emergence of ultra-broadband terahertz-wave generation and related detection techniques, the upper limit of this range is usually extended to 100 THz. In terms of wavelength, the THz band goes from $3\ \mu\text{m}$ to 3 mm. With regard to energy, the corresponding photon energies are between 0.4 and 400 meV. Concerning the temperature, the extended frequency range of this radiation can lie in between 5 and 5000 K. As shown in Fig. 1.1.1, the so-called “THz gap” corresponds in the electromagnetic spectrum to the boundary between the microwaves and the infrared waves. If it is seen as the upper limit of microwaves, it is sometimes called *submillimetre waves*. Seen as the lower limit of infrared waves, it is sometimes referred as *far infrared*.

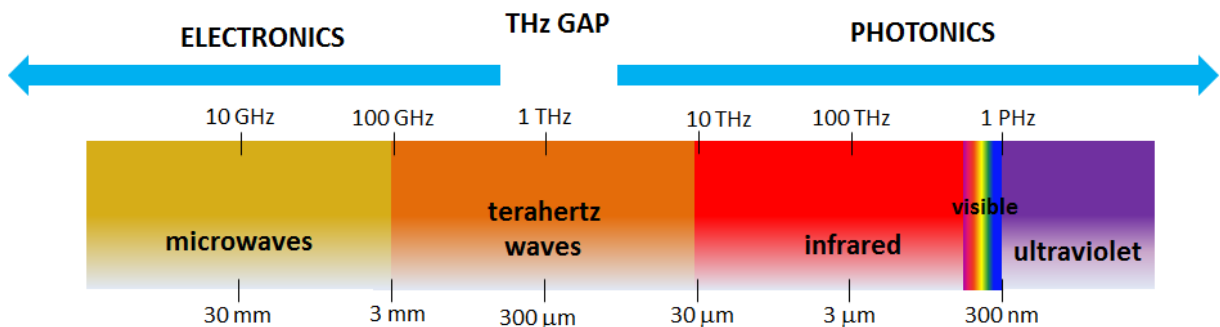


Figure 1.1.1: Electromagnetic spectrum as a function of the wavelength (lower axis) and frequency (upper axis) in the electromagnetic spectrum.

The terahertz radiation is non-ionizing and can penetrate a few millimetres of non-conducting materials such as clothes, paper, cardboard, plastic, ceramics, wood and body tissues. Regarding the latter, it does not jeopardize biological tissues. It can also pass through fog and clouds, but is absorbed by water vapour over short distances $< 10\ \text{m}$. Metals and water are opaque for these waves. Highly polarized materials as well as samples

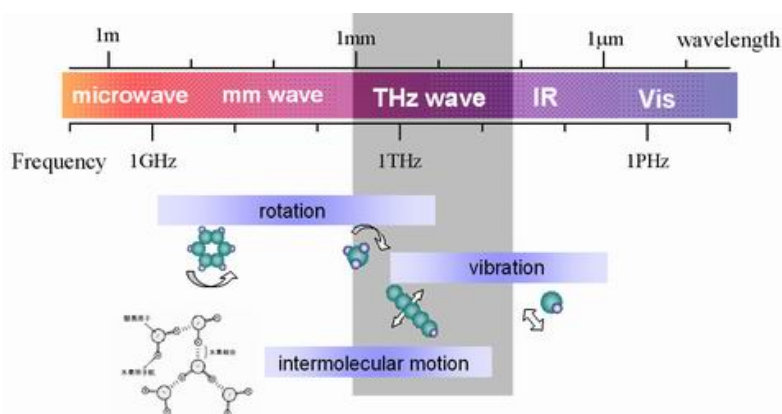


Figure 1.1.2: Terahertz spectrum and its impact on molecular dynamics. Source: www.riken.jp.

with high absorption coefficients in the THz range can attenuate dramatically the THz signals in spectroscopy experiments.

From the viewpoint of molecular spectroscopy, the THz band provides a lot of information about molecular structures and related motions, such as the fundamental rotational modes of molecules and intermolecular vibrations (see Fig. 1.1.2). Each molecule has unique fingerprints in this frequency band, a property which can be exploited to identify some chemical functional groups in complex molecules. Even more, high-power THz sources could be utilized to engineer transient states of matter [83].

From the technological point of view, the terahertz radiation lies at the boundary between the electronics and optics technological domains and it remains one of the least explored spectral regions. The frequency band lying approximately from 0.3 to 30 THz is difficult to access by conventional technologies. Indeed, the frequencies generated by transistors and lasers, typical semiconductor devices, do not overlap within this band and only advanced semiconductor technology can barely convert an electrical power into electromagnetic radiation belonging to that range [150]. This is the reason why this band of the electromagnetic spectrum is usually referred as the *terahertz gap*.

1.1.1 Applications of terahertz radiation

For a long time, the interest in THz radiation has remained confined to astrophysical submillimetre observation of cold bodies at temperatures of a few Kelvins, e.g., the cold dust of the interstellar medium in the Milky Way (10-20 K) and starburst galaxies.

With the advent of THz time-domain spectroscopy (THz-TDS), terahertz radiation is nowadays fully attractive thanks to its many applications in a large number of scientific domains. For example, we shall highlight the following ones:

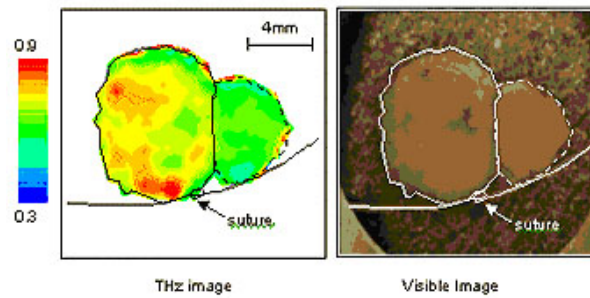


Figure 1.1.3: THz imaging for epithelial cancer diagnosis. Source: <http://www.teraview.com>.

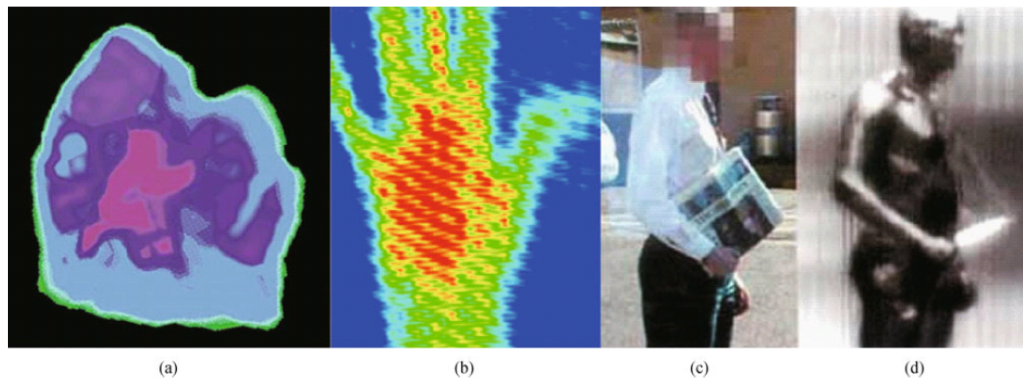


Figure 1.1.4: (a) Internal structure of human tooth mapped out by THz imaging. (b) THz image of a human hand. (c) Optical image of a person carrying a concealed weapon. (d) THz image of the same person. Source: Liu and Zhang [112].

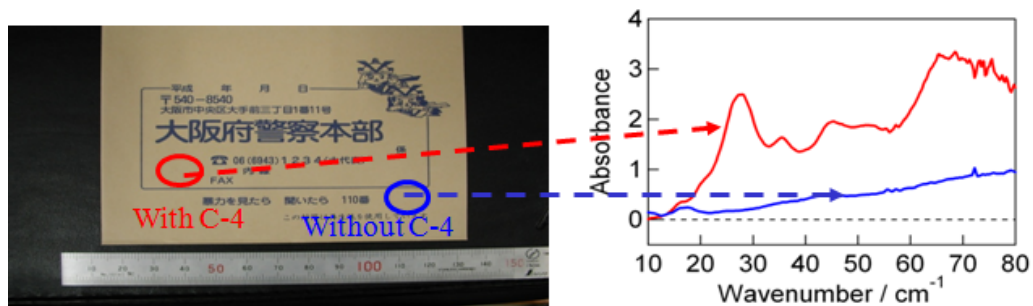


Figure 1.1.5: THz absorption of an envelope containing C-4 inside and its position dependence. (Left) Circles indicate the areas of the envelope where THz pulses were transmitted: (red) C-4 fragment inside and (blue) envelope only. (Right) THz absorption spectra obtained from the transmission at the two selected areas. Source: Yamamoto *et al.* [183].

- Medical THz imaging [Fig. 1.1.3 and Fig. 1.1.4(a,b)]. Unlike X-rays, THz radiation is not ionizing and it can pass through several millimetres of tissue of low water

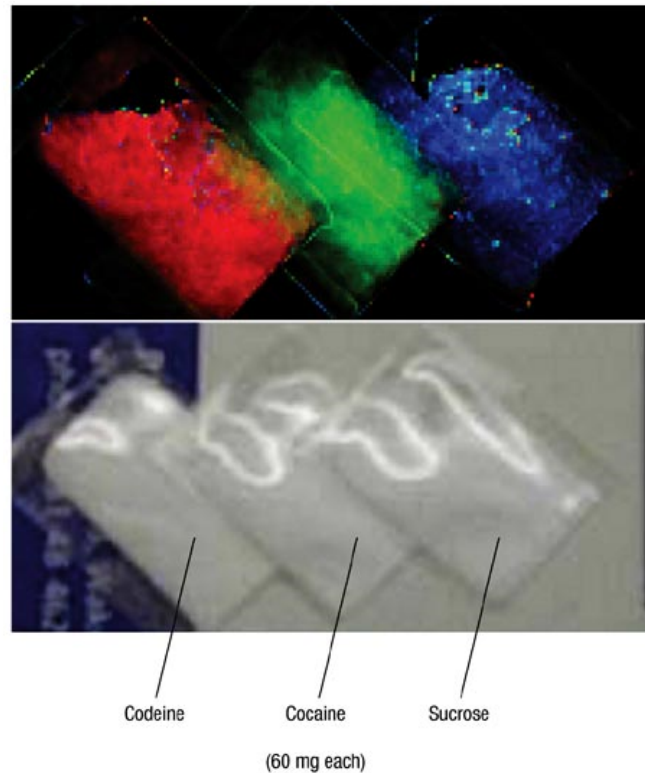


Figure 1.1.6: Terahertz detection of narcotics. THz image (upper) and photograph (lower) of specimens under inspection. Three kinds of powder (codeine, cocaine and sucrose) are hidden in an envelope and can be distinguished using THz-TDS spectroscopy by their own THz signatures. Source: Tonouchi [162].

content (e.g., fatty tissue) and be reflected back, without causing damage to DNA. Due to its ability to recognize spectral fingerprints, THz imaging provides good contrast between different types of soft tissue, and offers a non-invasive sensitive means for detecting the degree of water content as well as other markers for, e.g., epithelial cancer and other diseases [187]. Figure 1.1.3 presents the advantages of THz imaging on epithelial cancer diagnosis. The standard methodology for its diagnosis is the excision biopsy to remove tissues from the body and examination under a microscope. Terahertz imaging offers the ability to produce 3D images at high resolution through thick tissues using molecular markers, such as water, to provide spectral and absorption information in order to differentiate between cancerous and non-cancerous tissues, non-invasively and using non-ionising radiation. This greatly improves conventional biopsy and associated surgery by identifying more precisely the areas to be excised, thereby facilitating earlier and more accurate diagnosis.

- Homeland security [Fig. 1.1.4(c,d), Fig. 1.1.5, Fig. 1.1.6 and Fig. 1.1.12]. Since THz rays can penetrate fabrics, papers and plastics, they can be applied to security

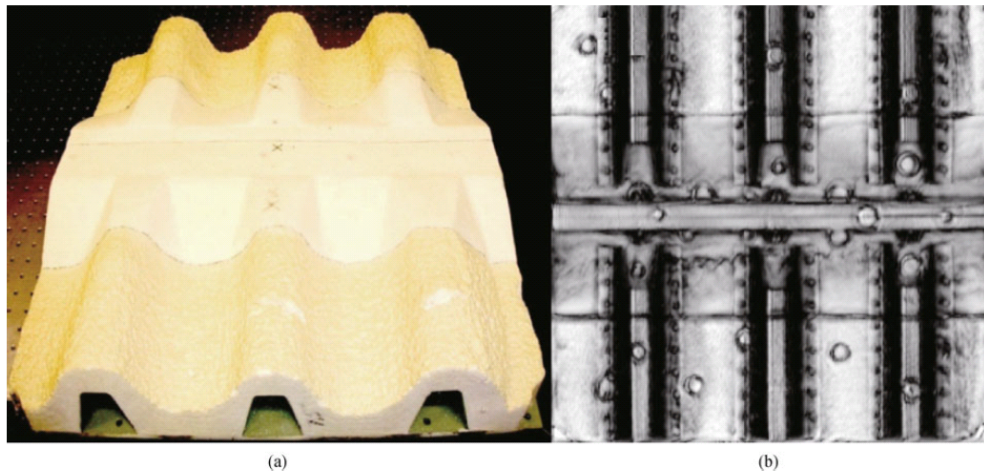


Figure 1.1.7: (a) Optical image of a 600 mm \times 600 mm panel of foam insulation on a metal substrate. There exist some hidden defects underneath the surface. (b) THz image of the same panel. Black circles are the embedded defects. Source: Liu and Zhang [112].

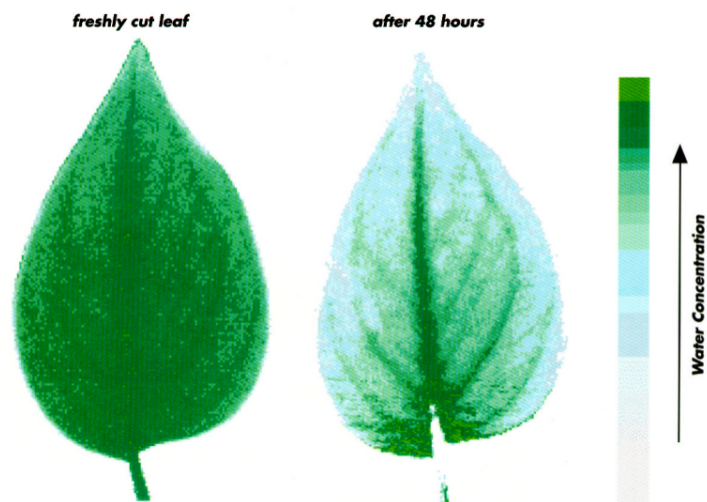


Figure 1.1.8: (Left) THz image of a fresh leaf. Attenuation of THz radiation through the leaf is largely due to water within the leaf. (Right) THz image of the same leaf after 48 h later. Water has clearly evaporated from the leaf, except from its stems. The colour scale indicates the relative water concentration within the leaf; darker green corresponds to higher water concentration. Source: Hu and Nuss [75].

screening to remote imaging and identification [111] of concealed weapons, explosives or drugs on a person or in a package, for instance.

- Non-destructive evaluation [Fig. 1.1.7]. THz-TDS and THz tomography are suit-

able for imaging samples which are opaque in the visible and near-infrared regions of the electromagnetic spectrum. It can be used, for instance, in manufacturing, quality control, and process monitoring to inspect packaged goods, since plastic and cardboard are transparent to THz radiation. It can also be employed to see murals hidden beneath coats of plaster or paint in centuries-old buildings (heritage applications), without harming the artwork.

- Information and communication technology. Ishigaki *et al.* set a record for wireless data transmission by using THz rays [78], which could be used in high-altitude telecommunications, above altitudes where water vapour causes signal absorption, such as aircraft-to-satellite or satellite-to-satellite communications.
- Global environmental monitoring of greenhouse gases and pollutants [166], and non-invasive and continuous measuring and monitoring of the water content in leaves and plants [62] (see Fig. 1.1.8).

The current challenge for open-air broadband THz spectroscopy technology, such as homeland security and environmental monitoring, is to deal with high ambient moisture absorption, which acts at distances below ~ 10 m [151]. Therefore, there is nowadays an increasing and yet unmet demand on intense THz sources (\sim GV/m) to overcome this absorption over longer distances. Nevertheless, producing the intense and broadband THz pulses appropriate for these applications is still nowadays a challenging technological task.

1.1.2 Technologies for generation and detection of terahertz waves

Besides conventional devices (e.g., photoconductive antennas, photoconductive switches—see Fig. 1.1.9(b)—, resonant tunnelling diodes, Schottky barrier diodes), which emit weak and narrow THz emissions, there exist two main techniques based on solid gain media to produce sub-picosecond THz sources in the microjoule range:

- Terahertz Quantum Cascade Laser (QCL) [175]. These devices can deliver mW-level power from continuous-wave coherent radiation throughout a narrow terahertz range below < 10 THz.
- Optical rectification in second-order nonlinear crystals, such as ZnTe and LiNbO₃ [see Fig. 1.1.9(a)]. Pumped by multi-mJ single colour pulses, this technique requiring phase matching can generate THz pulses up to 10 μ J energy, but the resulting bandwidth is limited to a few THz [185]. Recently, large-sized organic crystals were used to deliver THz pulses with GV/m electric field strength, and a conversion efficiency of about 1% was demonstrated [167].

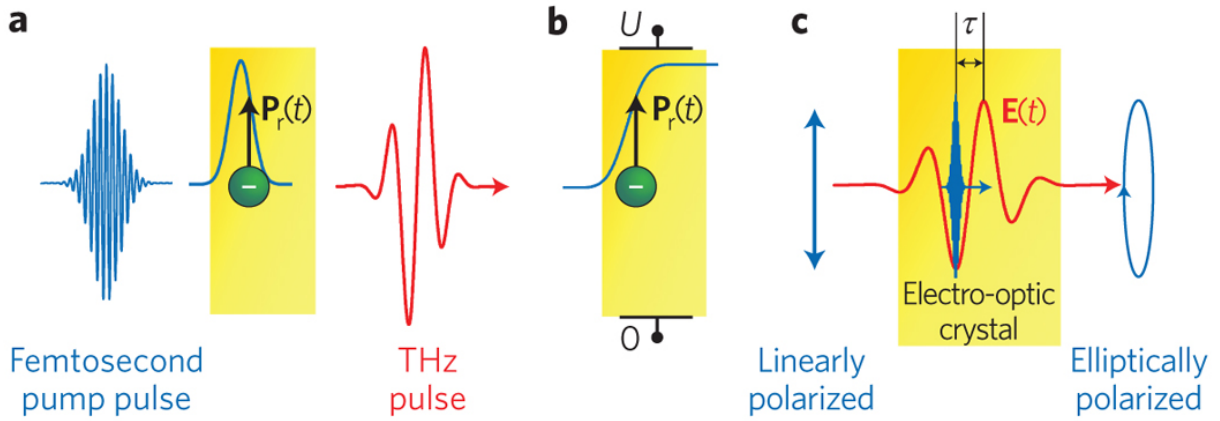


Figure 1.1.9: (a) THz generation by optical rectification in asymmetric crystals. An intense femtosecond pump pulse inside a non-inversion-symmetric transparent crystal induces a charge displacement with a rectified component $\mathbf{P}_r(t)$ that roughly follows the intensity envelope of the pulse (blue curve in yellow crystal). $\mathbf{P}_r(t)$ acts as a source of a THz electromagnetic transient (red curve). (b) Photoconductive switch. Pump-induced mobile charge carriers are accelerated by an external voltage U , leading to a current burst and emission of THz radiation. Pump and THz pulses are not shown. (c) Electro-optic sampling. The THz electric field $\mathbf{E}(t)$ (red) is detected by a time-delayed, co-propagating laser pulse (blue) that acquires an elliptical polarization. The ellipticity is proportional to \mathbf{E} , thereby providing access to \mathbf{E} as a function of the delay τ . Source: Kampfrath *et al.* [83].

T-rays can be detected similarly to how they are generated, for instance by means of photoconductive and electro-optic methods [192]. A photoconductive antenna was first used to detect THz rays [6]. Electro-optic sampling, depicted in Fig. 1.1.9(c), is a widely met THz detection method. In such setup, the field-induced birefringence of the sensor crystal, due to an applied electric field (THz wave), modulates the polarization ellipticity of an optical probe beam that passes through the crystal. This ellipticity modulation (i.e., change in polarization) of the latter beam can then be analysed to provide information on both the amplitude and the phase of the applied electric field.

Alternatively (see Section 1.1.3), a gas such as air can be used to detect THz pulses through optical rectification [41]. This technique is known as THz Air-Biased-Coherent-Detection (THz-ABCD). Mixing the THz pulse with the fundamental harmonic gives rise to second-harmonic generation, whose intensity is proportional to the square of the intensity of the fundamental laser pump and to the intensity of the THz pulse, supplying an efficient method of THz detection [see Fig. 1.1.10(e)]. However, just measuring the intensity of the second harmonic supplies only data on incoherent beams, because the information about the phase is lost. This problem is overcome by introducing a second-

order oscillator controlled by an AC or DC external bias [85]. When measuring the intensity of the THz-induced second-order harmonic mixed with that bias-induced second-order harmonic (known), the coherent cross term provides the information about the phase of the former and thus of the complete THz signal (i.e., the THz field).

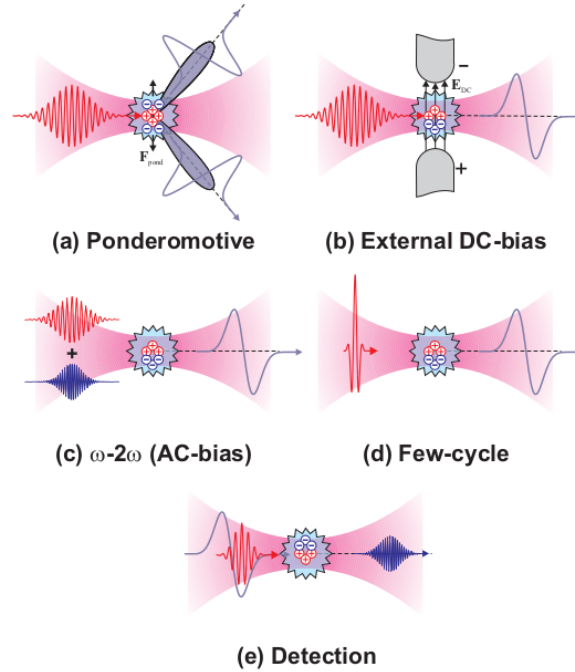


Figure 1.1.10: Overview of different plasma-based THz generation techniques. (a) Conical THz emission by ponderomotive forces. (b) THz emission when an external DC bias is applied to the plasma region [113, 114]. (c) THz generation from two laser colours (fundamental and second harmonic) [37, 89, 90]. (d) THz generation by few-cycle single-colour laser [95]. (e) THz detection by second-harmonic generation (THz-ABCD) [41, 85]. Source: Thomson *et al.* [140].

1.1.3 Laser-based terahertz sources

In this thesis, we study an alternative technique of producing intense, coherent, broadband and highly-directional THz waves, which has been discovered and exploited for over two decades, namely, the laser-driven terahertz sources [8, 36, 37, 44, 89, 90, 181]. Basically, these THz waves result from the coupling of an ultrashort infrared laser colour (usually with wavelength between 800 nm and 2000 nm, and duration of tens of femtoseconds) with its second harmonic (see Fig. 1.1.11). The overall laser beam is then focused into a gas, e.g., air or noble gases such as argon or helium. If the laser pulse is intense enough to exceed the ionization threshold of the gas, a plasma is created. The medium composed by

the neutral atoms and the plasma acts as a nonlinear frequency converter which produces “low-frequency” harmonics belonging to the THz band through a rich variety of physical mechanisms [e.g., Fig. 1.1.10(a-d)].

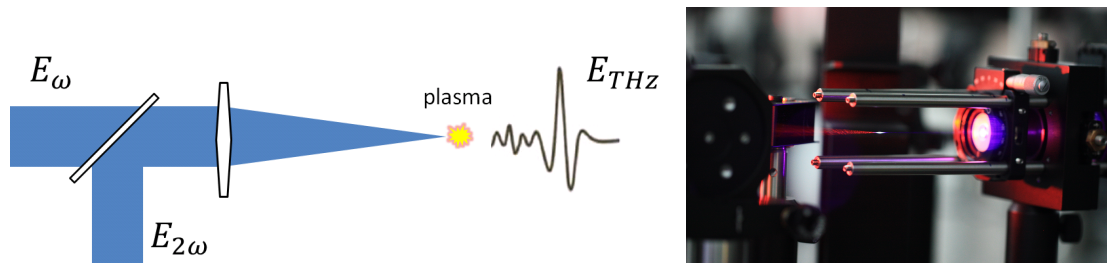


Figure 1.1.11: (Left) Schematic representation of THz generation by a two-colour laser. (Right) Picture a plasma created in air in the detection zone of the THz-ABCD method. Source: <http://www.iiserpune.ac.in/~pankaj/resources.html>.

Because it is mainly based on plasma nonlinearities, this technique presents several advantages over the conventional THz emitters recalled above:

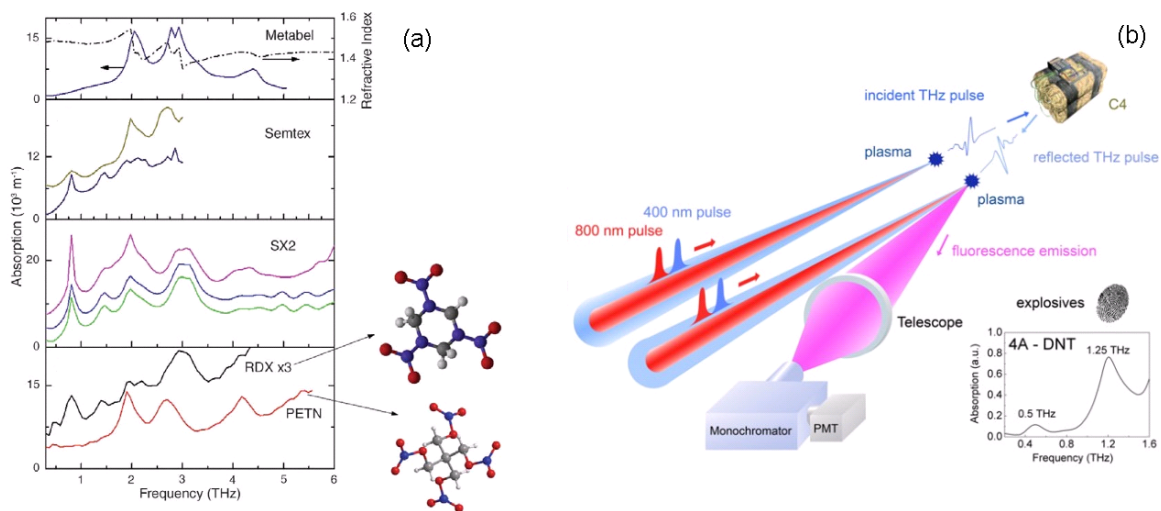


Figure 1.1.12: (a) Absorption THz spectra of conventional explosives. Different spectra are shown depending on the sample, here Semtex and SX2. A measurement of the refractive index of Metabel is also plotted. (b) The schematic configuration proposed in Ref. [26] of the broadband remote THz wave sensing using the technique of “radiation-enhanced emission of fluorescence” (REEF) with two-colour laser pulses to detect explosives, in this case C4. Source: <http://erc-assoc.org>.

- Conventional THz emitters are based on solid materials, where the THz emission results from elementary atomic transitions, which produce a narrow THz spectrum.

In laser-driven sources, instead, nonlinear processes induced by ultrashort high-intensity laser pulses lead to broad THz spectra from 1 to 100 THz (see Fig. 1.1.13).

- Since plasmas are not subject to material damage and have high breakdown thresholds, THz fields with strong amplitudes can be produced. Typically, laser-driven THz sources are expected to deliver amplitudes of \sim GV/m and mean powers of 100 W, whereas conventional methods do not usually go beyond \sim 0.1 GV/m and mean powers of \sim mW. This implies a real advantage because high-power THz pulses propagate more successfully over longer distances, as they can better overcome absorption by water vapour molecules.
- Laser filamentation allows the generation of THz pulses remotely. The absorption of THz frequencies by water molecules in the atmosphere can indeed be circumvented by controlling the distance where the plasma is created. In this way, target materials at distances of tens of metres can be analyzed using THz spectroscopy [42, 170, 172].
- The energy contained by the THz pulse scales with the fundamental laser wavelength λ_0 as $\sim \lambda_0^4$, at least in the range 800 nm to 2000 nm, and it may also augment at increasing laser durations [15, 35]. Since near- and mid-infrared laser devices delivering few optical cycles are already available [73], this opens the door to enrich THz pulse generation and achieve higher THz energy by optimizing the optical propagation aspects and related conversion efficiency.
- The “modus operandi” of laser-driven THz-TDS spectroscopy is relatively simple. As schematically shown by Fig. 1.1.12(b), the spectra of two time-recordings of THz signals, obtained with and without the characterized material, are calculated in amplitude and phase by simple Fourier transform. The ratio between the two spectra leads to the refraction index, the absorption coefficient and the depth of the irradiated material with a low noise level. As said above, these spectra restore also unique fingerprints of intermolecular vibrations, intramolecular torsions and the vibration modes of crystalline structures (phonons).

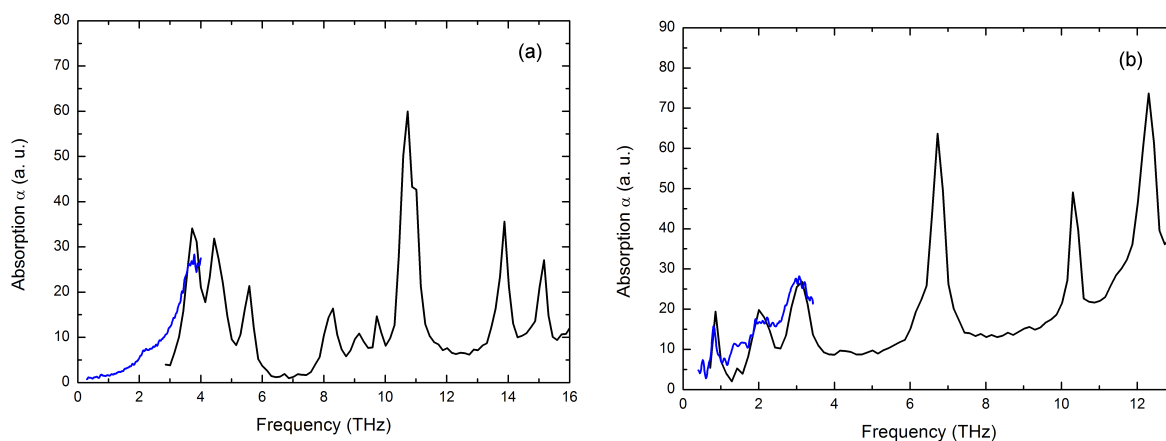


Figure 1.1.13: Experimental THz absorption spectra of (a) TNT and (b) RDX explosive samples, obtained from THz-TDS spectroscopy using laser-driven sources (black curves) and conventional photoconductive antennas (blue curves). A much better identification of the molecule is obtained with the former THz setup. Source: DTU Lyngby / ISL.

1.2 Motivation of this PhD work

This PhD work has been achieved at the Commissariat à l'Énergie Atomique et aux Énergies Alternatives (CEA), in the centre Direction des Applications Militaires Île de France (DAM DIF). Our research team has collaborated with various groups and researchers such as Institut für Quantenoptik (University of Leibniz, Germany), Centre Lasers Intenses et Applications (CELIA, Université de Bordeaux, France), Facultad de Óptica y Optometría (Complutense University of Madrid, Spain), Institute for Scientific Computing (Technical University of Dresden, Germany), Max-Born-Institut für Nichtlineare Optik und Kurzzeitspektroskopie (Germany), Faculty of Physics (M. V. Lomonosov Moscow State University, Russia), and Centre d'Optique, Photonique et Laser (University of Laval, Canada).

My work is essentially theoretical and numerical. All the numerical simulations have been carried out on the supercomputers CURIE and AIRAIN belonging to the “Très Grand Centre de Calcul” (TGCC) infrastructure of CEA, an infrastructure for scientific high-performance computing and Big Data, which is able to host petascale supercomputers. We have been awarded the access to CURIE supercomputer by the European project PRACE¹ (CAPITOL² Project) and through national projects GENCI@CEA³.

The objective of the present thesis is to analyze theoretically and numerically the physical mechanisms underlying the laser-driven terahertz sources and their dependence on

¹Partnership foR Advanced Computing in Europe.

²Computing Accelerated Particles, Intense Terahertz and Optical radiation by Lasers.

³Grand Équipement National de Calcul Intensif.

laser and gas parameters, in order to propose the best configurations allowing to produce the strongest and broadest terahertz pulses with the best laser-to-terahertz energy conversion efficiency when possible. We have specially devoted our work on the generation of intense THz radiation at high laser intensities by addressing multiple ionization and multi-dimensional plasma effects, a domain which had been little studied so far. The perspective for the CEA is that such intense THz pulse generation could improve in a near future homeland security technologies such as the remote detection of energetic materials (explosives), as illustrated for instance by Fig. 1.1.13.

This dissertation is divided into four main sections. Section 2 introduces the physical concepts exploited throughout our study. We start by introducing the general physical models describing the laser pulse propagation through the target medium (in filamentation and focusing regimes), the nonlinear response of gas targets (nonlinear optics and ionization), and the dynamics of the created plasma (triggering plasma oscillations that appear in both the longitudinal and transverse directions). We end this section by exposing the known mechanisms yielding terahertz radiation, which mainly consist in Kerr optical rectification, photocurrents and longitudinal plasma waves.

Section 3 presents the three numerical codes used during this thesis and named UPPE (spectral code), CALDER (Particle-In-Cell code), and MAXFLU. It is mostly committed to the last code, a new Finite-Volume code that solves relativistic cold-plasma Maxwell-Fluid equations and allows us to study both nonlinear optics and plasma dynamics, discussed here in the scope of THz pulse generation. Finally, we comment on our simplified Maxwell-Fluid model, which is a semi-analytical solution of the complete Maxwell-Fluid model that unifies the photocurrent mechanisms with longitudinal plasma current oscillations at high intensities ($\sim 10^{17}$ W cm $^{-2}$).

Section 4 is dedicated to typical laser filamentation intensities ($< 10^{14}$ W cm $^{-2}$). First, we have investigated experimentally the signatures of the THz spectrum of bound and free electrons in two-colour air filaments. These experimental results obtained at the International Laser Center of M. V. Lomonosov Moscow State University (Russia) are interpreted theoretically by means of Maxwell-Fluid and Unidirectional Pulse Propagation Equation (UPPE) models. Second, we have explored the possibility of coupling more than two laser colours to boost the laser-to-THz energy conversion efficiency. Harmonics of a specific laser waveform, shaped on a sawtooth profile, appear quite promising for this goal.

Section 5 is devoted to the THz generation at high laser intensities (10^{15} - 10^{18} W cm $^{-2}$). First, we study the nonmonotonic growth of the THz radiation due to the photoionization of different electronic shells. This nonmonotonic growth is explained by the fact that, for each electron extracted from an atom, there exists a maximum THz field resulting from

the best compromise between high laser intensity and a minimum number of optical cycles contributing to photoionization. Then we examine how the photocurrent mechanism competes with plasma wakefield effects in a two-dimensional geometry. Our Particle-In-Cell (PIC) simulations performed for this purpose demonstrate that, besides photoionization, we have to account for transverse ponderomotive forces in order to explain THz generation at high laser intensities, up to the relativistic limit.

Section 5.2 concludes this work.

2 Terahertz waves driven by laser pulses

Contents

1.1	The terahertz radiation	1
1.1.1	Applications of terahertz radiation	2
1.1.2	Technologies for generation and detection of terahertz waves	6
1.1.3	Laser-based terahertz sources	8
1.2	Motivation of this PhD work	11

This section is devoted to the physical models used in this thesis in order to understand the terahertz generation by laser sources. Section 2.1 treats the different models of laser-plasma interaction, while Section 2.2 is more dedicated to ionization. All the basic physics concerned with nonlinear optical and plasma phenomena is discussed in Section 2.3. Finally, the mechanisms responsible for terahertz emissions are explained in Section 2.4.

2.1 Laser-plasma interaction

When an intense femtosecond laser pulse propagates through a gas, this gas becomes ionized and produces an electron plasma. The resulting plasma acts as a nonlinear frequency converter, capable of emitting higher harmonics of the laser central frequency as well as much lower frequencies belonging to the terahertz band. The models presented here describe the underlying physical mechanisms converting a small part of the laser energy into a residual spectral source corresponding to terahertz radiation.

Plasmas are considered as cold (the electron temperature is assumed close to some tens of eV) and weakly collisional. Moreover, for laser intensities up to 10^{19} W cm⁻² and over time scales fixed by the laser pulse duration (usually 10 – 100 fs), ion motions are discarded in THz pulse generation, and we only focus on the electron motion.

In this context, the plasma can be appropriately described by the kinetic approach given by the Vlasov equation (Section 2.1.2), which is coupled to the Maxwell equations (Section 2.1.1) governing the electromagnetic fields. From the numerical point of view, Particle-In-Cell codes solve this system of equations (Section 3.1.2). Additionally, for non-relativistic intensities ($< 10^{18}$ W cm⁻²), a fluid description of the plasma (Section 2.1.4) couples the macroscopic average of the electron velocity governed by the Vlasov equation to Maxwell equations, and thereby provides an equivalent approach to study the physics intrinsic to laser-driven terahertz sources. Although approximative, this fluid approach is computationally faster and its numerical results satisfactorily agree with those of Particle-In-Cell codes (Section 3.3.2). Particle-In-Cell and Maxwell-Fluid computations can both be limited by the propagated distances that can be covered in reasonable time by the current computers. However, because they embed a rich plasma physics, they are suitable for understanding how the plasma medium contributes to terahertz emission over short distances of the order of, e.g., hundreds of micrometres. So they may not be appropriate for simulating laser-driven terahertz radiation cumulating over long distances.

Alternatively, to describe laser-plasma interactions in the context of extreme nonlinear optics, the unidirectional pulse propagation equation (UPPE; see Section 2.1.5.3) may be sufficient to study the action of nonlinear optical effects (spatial diffraction, temporal dispersion, Kerr response and photoionization with related losses) over metre-long propagation ranges. This model comes directly from Maxwell equations and it integrates a first-order approximation of the cold-plasma fluid equations for the free electron density.

2.1.1 Maxwell equations

The Gauss law [Eq. (2.1.1)], the law for absence of magnetic monopoles [Eq. (2.1.2)], the Faraday's law [Eq. (2.1.3)] and the Ampère's law [Eq. (2.1.4)] constitute the Maxwell

equations:

$$\nabla \cdot \mathbf{D} = \rho_f, \quad (2.1.1)$$

$$\nabla \cdot \mathbf{B} = 0, \quad (2.1.2)$$

$$\partial_t \mathbf{B} + \nabla \times \mathbf{E} = \mathbf{0}, \quad (2.1.3)$$

$$-\partial_t \mathbf{D} + \nabla \times \mathbf{H} = \mathbf{J}_f + \mathbf{J}_{\text{loss}}, \quad (2.1.4)$$

where $\rho_f = \rho - \rho_b$ is the free charge density, ρ is the total charge density, ρ_b is the density for bound charges, \mathbf{J}_f is the free current density, \mathbf{E} is the electric field, \mathbf{B} is the magnetic field, \mathbf{D} is the electric displacement field and \mathbf{H} is the magnetic field strength [1]. To assure the energy conservation, we heuristically add to Ampère's law (2.1.4) an artificial current density, the ionization loss current density \mathbf{J}_{loss} , to account for the energy lost by the laser pulse during the photoionization process (see Section 2.2.3.3 for details). In order to close this system of equations, two constitutive equations of the medium are added, which relate \mathbf{E} and \mathbf{D} [Eq. (2.1.5)], together with \mathbf{B} and \mathbf{H} [Eq. (2.1.6)]:

$$\mathbf{D} = \varepsilon_0 \mathbf{E} + \mathbf{P}, \quad (2.1.5)$$

$$\mathbf{B} = \mu_0 \mathbf{H} + \mathbf{M}, \quad (2.1.6)$$

where $\nabla \cdot \mathbf{P} = -\rho_b$ is the electric polarization, $\mathbf{M} = \mu_0 \chi_m \mathbf{H}$ is the magnetic polarization, and χ_m is the magnetic susceptibility. The S.I. units for all these fields are summarized in Table 2.1.

In the following, the medium is assumed to be nonmagnetic, i.e., $\mathbf{M} = \mathbf{0}$. The electric polarization is separated into the linear electric polarization (\mathbf{P}_L) and the nonlinear electric polarization (\mathbf{P}_{NL}):

$$\mathbf{P} = \mathbf{P}_L + \mathbf{P}_{\text{NL}}. \quad (2.1.7)$$

2.1.1.1 Linear polarization

The linear electric polarization is modelled as

$$\mathbf{P}_L(t) = \varepsilon_0 \chi^{(1)}(t) * \mathbf{E}(t), \quad (2.1.8)$$

Symbol	Name	S.I. units
\mathbf{E}	electric field	V/m
\mathbf{D}	electric displacement field	C/m ²
\mathbf{P}	electric polarization	C/m ²
\mathbf{B}	magnetic field	T
\mathbf{H}	magnetic field strength	A/m
\mathbf{M}	magnetic polarization	T
ρ	charge density	C/m ³
ρ_b	bound charge density	C/m ³
ρ_f	free charge density	C/m ³
\mathbf{J}_f	free current density	A/m ²

Table 2.1: S.I. units of electromagnetic fields, charge densities and current density governed by Maxwell equations.

where $*$ stands for the convolution product in time and $\chi^{(1)}(t) = \mathcal{F}^{-1}[\hat{\chi}^{(1)}(\omega)]$ is the first-order electric susceptibility given by

$$\hat{\chi}^{(1)}(\omega) = \hat{n}(\omega)^2 - 1 \quad (2.1.9)$$

in the Fourier domain. By abuse of language, the angular frequency ω (also known as pulsation) will be called “frequency” henceforth.

In Eq. (2.1.9), $\hat{n}(\omega)$ is the frequency-dependent linear refractive index of the gas medium at the local pressure p_{gas} :

$$\hat{n}(\omega)^2 - 1 = \frac{p_{\text{gas}}}{1 \text{ bar}} \left(\hat{n}_{1\text{bar}}(\omega)^2 - 1 \right), \quad (2.1.10)$$

where $\hat{n}_{1\text{bar}}$ accounts for the refractive index at 1-bar pressure. In the most simplified situation, a constant refractive index $n_0 = \hat{n}(\omega_0)$ is considered [and thus $n_{0,1\text{bar}} = \hat{n}_{1\text{bar}}(\omega_0)$]. For ultrashort laser pulses the linear refractive index depends on the frequency. $\hat{n} = \hat{n}(\omega)$ determines the chromatic dispersion of the material, as evaluated, for instance, in the articles by Dalgarno and Kingston [43], Leonard [103], Mansfield [119], Börzsönyi *et al.* [21], and Bideau-Mehu *et al.* [16]. Here different linear dispersion relations depending on even powers of the optical frequency (e.g., ω^2 , ω^4 , etc.) are proposed for approaching $\hat{n}(\omega)$ of different gases (argon, xenon, neon, helium, etc.). To pass to the time domain, a differential equation on $n(\omega)$ can be used through the Sellmeier equation [145]. For example, Leonard [103], Mansfield [119], Börzsönyi *et al.* [21], and Bideau-Mehu *et al.*

[16] propose linear refractive indices in the general form

$$\hat{n}_{1\text{bar}}(\omega) - 1 = \sum_i \frac{f_{i,1\text{bar}}}{\omega_i^2 - \omega^2}, \quad (2.1.11)$$

where $f_{i,1\text{bar}}$ is the absorption oscillator strength for the transition at a resonant frequency ω_i , measured at a pressure of 1 bar. In most of practical situations, we assume pulse propagation within a frequency window far from such material resonances.

Since $|\hat{n}(\omega)|$ is expected to remain close to unity, it is reasonable to approximate the first-order electric susceptibility, formally defined by $\hat{\chi}_{1\text{bar}}^{(1)}(\omega) = \hat{n}_{1\text{bar}}(\omega)^2 - 1$, as

$$\hat{\chi}_{1\text{bar}}^{(1)}(\omega) \approx 2[\hat{n}_{1\text{bar}}(\omega) - 1], \quad (2.1.12)$$

because $[\hat{n}_{1\text{bar}}(\omega)^2 - 1] - 2[\hat{n}_{1\text{bar}}(\omega) - 1] = [\hat{n}_{1\text{bar}}(\omega) - 1]^2 \ll \hat{\chi}_{1\text{bar}}^{(1)}(\omega)$. By combining Eqs. (2.1.10), (2.1.11) and (2.1.12), a model for the first-order electric susceptibility can be obtained, which fits Sellmeier's equation [145]:

$$\hat{\chi}^{(1)}(\omega) = \sum_i \frac{2f_i}{\omega_i^2 - \omega^2}, \quad (2.1.13)$$

$$f_i = \frac{p_{\text{gas}}}{1 \text{ bar}} f_{i,1\text{bar}}. \quad (2.1.14)$$

Since the linear polarization is defined as $\mathbf{P}_L(t) = \varepsilon_0 \mathcal{F}^{-1}[\hat{\chi}^{(1)}(\omega)\hat{\mathbf{E}}(\omega)]$ according to Eq. (2.1.8), the Sellmeier-like model of Eq. (2.1.13) gives the following differential equation for the linear polarization in time:

$$\mathbf{P}_L(t) = \sum_i \mathbf{P}_{L,i}(t), \quad (2.1.15)$$

$$(\partial_t^2 + \omega_i^2) \mathbf{P}_{L,i}(t) = 2\varepsilon_0 f_i \mathbf{E}(t), \quad (2.1.16)$$

whose exact solution, for the initial condition $\mathbf{P}_{L,i}(0) = \mathbf{0}$, expresses as

$$\mathbf{P}_{L,i}(t) = 2\varepsilon_0 f_i \int_0^t \cos^2(\omega_i(\tau - t)) \mathbf{E}(\tau) d\tau. \quad (2.1.17)$$

Note that instead of using the first-order electric susceptibility, alternatively, the relative permittivity $\hat{\varepsilon}_r$ and the permittivity $\hat{\varepsilon}$ of the medium can be used. They are linked through the relationships:

$$\hat{\varepsilon}_r(\omega) = 1 + \hat{\chi}^{(1)}(\omega) = \hat{n}(\omega)^2, \quad (2.1.18)$$

$$\hat{\epsilon}(\omega) = \epsilon_0 \hat{\epsilon}_r(\omega). \quad (2.1.19)$$

2.1.1.2 Nonlinear polarization

Besides \mathbf{P}_L , the polarization vector contains nonlinear contributions that become active at high laser intensities. For an isotropic medium, the nonlinear polarization can be expressed as a power series in the electric field through high-order electric susceptibilities [1, 23]. Even-order electric susceptibilities vanish for a medium whose molecules are centrosymmetric (i.e., they stay invariant under a point reflection), which applies to the gases which are considered here. Only third-order electric susceptibility will be treated in this work, which characterizes the Kerr effect. It is expressed as a frequency-dependent four-rank tensor and is responsible for third-harmonic generation and four-wave mixing:

$$\hat{\mathbf{P}}_{\text{NL}} = \epsilon_0 \hat{\chi}^{(3)}(\omega) : \hat{\mathbf{E}} \hat{\mathbf{E}} \hat{\mathbf{E}}, \quad (2.1.20)$$

where $:$ stands for tensor product [1].

Third-order electric polarization [Eq. (2.1.20)] has an instantaneous response only—Raman scattering by anisotropic molecules is not taken into account [14, 153]—and its i th vectorial component ($i = x, y, z$) is given by

$$\hat{P}_{\text{NL},i}(\omega) = \epsilon_0 \sum_{j=x,y,z} \sum_{k=x,y,z} \sum_{l=x,y,z} \hat{\chi}_{i,j,k,l}^{(3)}(\omega) \hat{E}_j(\omega) \hat{E}_k(\omega) \hat{E}_l(\omega). \quad (2.1.21)$$

The tensor $\hat{\chi}^{(3)}$ is considered as isotropic and the nonlinear dispersion will be neglected; in other words, its diagonal components satisfy $\hat{\chi}_{x,x,x,x}^{(3)}(\omega) = \hat{\chi}_{y,y,y,y}^{(3)}(\omega) = \hat{\chi}_{z,z,z,z}^{(3)}(\omega) = \hat{\chi}^{(3)}(\omega_0) = \chi^{(3)}$ while the remaining ones are zero. Therefore, the nonlinear electric polarization will here reduce to

$$\mathbf{P}_{\text{NL}} = \epsilon_0 \chi^{(3)} \begin{pmatrix} E_x^3 \\ E_y^3 \\ E_z^3 \end{pmatrix}. \quad (2.1.22)$$

The third-order electric susceptibility $\chi^{(3)}$ is often expressed as a function of the nonlinear refractive index of the medium, n_2 :

$$\chi^{(3)} = \frac{4}{3} c \epsilon_0 n_{0,1\text{bar}}^2 n_2, \quad (2.1.23)$$

where the nonlinear refractive index at a certain pressure p_{gas} is given by

$$n_2 = \frac{p_{\text{gas}}}{1 \text{ bar}} n_{2,1\text{bar}}. \quad (2.1.24)$$

Here $n_{2,1\text{bar}}$ denotes the nonlinear refractive index at 1-bar pressure.

Remark 1. As $\chi^{(3)}$ depends on the nonlinear response of the neutrals to an external electric field, the nonlinear polarization could be better modelled if it were corrected at every position and instant by the ratio between the density of neutral atoms still existing at those coordinates and the initial density of neutrals. However, in the intensity domain where the Kerr response acts efficiently on terahertz generation, the density of neutrals is not significantly impacted by the density of freed electrons. Therefore, $\chi^{(3)}$ will always be viewed as constant in what follows.

In connexion with \mathbf{P}_{NL} , the optical refractive index of the medium is defined at central frequency ω_0 as [23]:

$$\bar{n} = n_0 + n_2 I_0, \quad (2.1.25)$$

where I_0 is the averaged intensity of the laser pulse $E(t)$ over one period $T_0 = 2\pi\omega_0^{-1}$:

$$I_0 = n_0 \varepsilon_0 c \langle E(t)^2 \rangle = n_0 \varepsilon_0 c \frac{1}{T_0} \int_0^{T_0} E(t)^2 dt. \quad (2.1.26)$$

In Eq. (2.1.25), the nonlinearities are assumed small: $n_2 I_0 \ll n_0$. Equation (2.1.23) can be retrieved from Eq. (2.1.25). Let

$$E(t) = a_0 \cos(\omega_0 t) \quad (2.1.27)$$

be a scalar single-colour laser plane wave. The scalar polarization, according to Eqs. (2.1.7), (2.1.8) and (2.1.22), reads as

$$P(t) = \varepsilon_0 \chi^{(1)} E(t) + \varepsilon_0 \chi^{(3)} E(t)^3 = \varepsilon_0 \chi^{(1)} E(t) + \frac{3}{4} \varepsilon_0 \chi^{(3)} a_0^2 E(t) + \frac{1}{4} \varepsilon_0 \chi^{(3)} a_0^3 \cos(3\omega_0 t), \quad (2.1.28)$$

which, in the Fourier domain, yields for $\omega = \omega_0$:

$$\hat{P}(\omega_0) = \varepsilon_0 \left(\chi^{(1)} + \frac{3}{4} \chi^{(3)} a_0^2 \right) \hat{E}(\omega_0) = \varepsilon_0 \chi_{\text{eff}} \hat{E}(\omega_0), \quad (2.1.29)$$

where χ_{eff} denotes the *effective susceptibility* at frequency ω_0 . Taking into account that $a_0^2 = 2\langle E(t)^2 \rangle$, this effective susceptibility should be given by the optical refractive index of Eq. (2.1.25) in accordance with Eq. (2.1.9):

$$\chi_{\text{eff}} = \bar{n}^2 - 1 \approx n_0^2 - 1 + 2n_0 n_2 I_0 = \underbrace{n_0^2 - 1}_{\chi^{(1)}} + \underbrace{\varepsilon_0 c n_0^2 n_2 a_0^2}_{\frac{3}{4} \chi^{(3)}}, \quad (2.1.30)$$

where the simplification $n_2 I_0 \ll n_0$ is applied. By comparing Eq. (2.1.30) with Eq. (2.1.29), one recovers the electric susceptibilities of Eqs. (2.1.9) and (2.1.23).

The previous results also hold for a N -colour laser pulse in the form

$$E(t) = \sum_{k=0}^N a_k \mathcal{E}_k(t) \cos(\omega_k t + \phi_k), \quad (2.1.31)$$

where a_k , $k\omega_0$ and ϕ_k are the amplitude, the frequency and the phase of the k th colour (harmonic), respectively. In this situation, the cycle-average intensity is

$$I_0 = n_0 \varepsilon_0 c \langle E(t)^2 \rangle = \frac{1}{2} n_0 \varepsilon_0 c \sum_{k=1}^N a_k^2, \quad (2.1.32)$$

and thus the cycle-average amplitude is defined by $a_0 = \sqrt{\sum_{k=1}^N a_k^2}$.

2.1.2 Vlasov equation

A plasma can be seen as a dynamical system of N charged particles ($N \gg 1$) of several species (free electrons and different types of ions), which move under the influence of both external fields and fields generated by the particles themselves. Such system will be described in the following by the Hamiltonian mechanics, a formalism based on the concept of energy and specially convenient when the particles have complex and chaotic trajectories. At every instant t , the state of each particle i , to which a mass m_i and a charge q_i are associated, is characterized by two vectors: its position $\mathbf{r}_i(t)$ and its linear momentum $\mathbf{p}_i(t)$. In a three-dimensional geometry, this state represents a point in the phase space of six dimensions: $\mathbf{r}_i(t) = (x_i(t), y_i(t), z_i(t))$ and $\mathbf{p}_i(t) = (p_{x,i}(t), p_{y,i}(t), p_{z,i}(t))$. The Hamiltonian density $\mathcal{H} = \mathcal{H}(t, \mathbf{r}, \mathbf{p})$ is a scalar function on this phase space, describing the motion of each particle through Hamilton's equations:

$$\frac{d\mathbf{r}_i}{dt} = \frac{\partial \mathcal{H}}{\partial \mathbf{p}_i} = \mathbf{v}_i, \quad (2.1.33)$$

$$\frac{d\mathbf{p}_i}{dt} = -\frac{\partial \mathcal{H}}{\partial \mathbf{r}_i} = \mathbf{F}_i = q_i (\mathbf{E}_i + \mathbf{v}_i \times \mathbf{B}_i), \quad (2.1.34)$$

where $\mathbf{v}_i = \mathbf{p}_i(m_i \gamma_i)^{-1}$ is the velocity, $\gamma_i = (1 - v_i^2/c^2)^{-1/2}$ is the Lorentz factor, $\mathbf{F}_i = \mathbf{F}(t, \mathbf{r}_i) = q_i (\mathbf{E}_i + \mathbf{v}_i \times \mathbf{B}_i)$ is the Lorentz force, $\mathbf{E}_i = \mathbf{E}(t, \mathbf{r}_i)$ and $\mathbf{B}_i = \mathbf{B}(t, \mathbf{r}_i)$ are the electric and magnetic fields acting on the particle, respectively.

The microscopic state of the plasma is known when Eqs. (2.1.33) and (2.1.34) are solved for all the N particles. In three dimensions this implies solving $12N$ degrees of freedom in the dynamical system, which is far to be accessible for current computers. Nevertheless, the evolution of macroscopic variables can be described thanks to statistical physics. To

species σ a smooth distribution function $f_\sigma(t, \mathbf{r}, \mathbf{p})$ is associated, which must verify:

$$\lim_{|\mathbf{p}| \rightarrow \infty} |\mathbf{p}|^\alpha f_\sigma(t, \mathbf{r}, \mathbf{p}) = 0, \quad \forall \alpha \in \mathbb{R}^+. \quad (2.1.35)$$

This distribution function represents a probability density function. Therefore, the averaged number density of species σ is calculated as

$$\langle N_\sigma(t, \mathbf{r}) \rangle = \iiint_{\mathbb{R}^3} f_\sigma(t, \mathbf{r}, \mathbf{p}) d\mathbf{p}. \quad (2.1.36)$$

Analogously, the mean value of a certain field Φ_σ acting on the phase space for species σ (for example, velocity or linear momentum) is given by

$$\langle \Phi_\sigma(t, \mathbf{r}) \rangle = \frac{\iiint_{\mathbb{R}^3} \Phi_\sigma(t, \mathbf{r}, \mathbf{p}) f_\sigma(t, \mathbf{r}, \mathbf{p}) d\mathbf{p}}{\iiint_{\mathbb{R}^3} f_\sigma(t, \mathbf{r}, \mathbf{p}) d\mathbf{p}} = \frac{\iiint_{\mathbb{R}^3} \Phi_\sigma(t, \mathbf{r}, \mathbf{p}) f_\sigma(t, \mathbf{r}, \mathbf{p}) d\mathbf{p}}{\langle N_\sigma(t, \mathbf{r}) \rangle}, \quad (2.1.37)$$

and thus the mean value of $\Phi_\sigma N_\sigma$ verifies

$$\langle \Phi_\sigma(t, \mathbf{r}) N_\sigma(t, \mathbf{r}) \rangle = \iiint_{\mathbb{R}^3} \Phi_\sigma(t, \mathbf{r}, \mathbf{p}) f_\sigma(t, \mathbf{r}, \mathbf{p}) d\mathbf{p} = \langle \Phi_\sigma(t, \mathbf{r}) \rangle \langle N_\sigma(t, \mathbf{r}) \rangle. \quad (2.1.38)$$

The Vlasov equation modelizes the time derivative of this distribution function:

$$\frac{d}{dt} f_\sigma(t, \mathbf{r}, \mathbf{p}) = \mathcal{S}_\sigma(t, \mathbf{r}, \mathbf{p}), \quad (2.1.39)$$

where the source term $\mathcal{S}_\sigma(t, \mathbf{r}, \mathbf{p})$ is discussed in Section 2.1.3. Taking Eqs. (2.1.33) and (2.1.34) into account, the time derivative of f_σ is:

$$\begin{aligned} \frac{d}{dt} f_\sigma(t, \mathbf{r}, \mathbf{p}) &= \frac{\partial}{\partial t} f_\sigma(t, \mathbf{r}, \mathbf{p}) + \frac{d\mathbf{r}}{dt} \cdot \frac{\partial}{\partial \mathbf{r}} f_\sigma(t, \mathbf{r}, \mathbf{p}) + \frac{d\mathbf{p}}{dt} \cdot \frac{\partial}{\partial \mathbf{p}} f_\sigma(t, \mathbf{r}, \mathbf{p}) = \\ &= \frac{\partial}{\partial t} f_\sigma(t, \mathbf{r}, \mathbf{p}) + \mathbf{v} \cdot \frac{\partial}{\partial \mathbf{r}} f_\sigma(t, \mathbf{r}, \mathbf{p}) + q_\sigma (\mathbf{E} + \mathbf{v} \times \mathbf{B}) \cdot \frac{\partial}{\partial \mathbf{p}} f_\sigma(t, \mathbf{r}, \mathbf{p}), \end{aligned} \quad (2.1.40)$$

where q_σ is the charge associated to the species σ . By substituting Eq. (2.1.40) into Eq. (2.1.39), the general expression of Vlasov equation for species σ is obtained:

$$\frac{\partial}{\partial t} f_\sigma(t, \mathbf{r}, \mathbf{p}) + \mathbf{v} \cdot \frac{\partial}{\partial \mathbf{r}} f_\sigma(t, \mathbf{r}, \mathbf{p}) + q_\sigma (\mathbf{E} + \mathbf{v} \times \mathbf{B}) \cdot \frac{\partial}{\partial \mathbf{p}} f_\sigma(t, \mathbf{r}, \mathbf{p}) = \mathcal{S}_\sigma(t, \mathbf{r}, \mathbf{p}). \quad (2.1.41)$$

2.1.3 Moments for electrons

Discarding ion motions, Vlasov equation (2.1.41) only treating electrons with the distribution function $f = f(t, \mathbf{r}, \mathbf{p})$ then expresses as

$$\frac{\partial}{\partial t} f(t, \mathbf{r}, \mathbf{p}) + \frac{\mathbf{p}}{m_e \gamma(\mathbf{p})} \cdot \frac{\partial}{\partial \mathbf{r}} f(t, \mathbf{r}, \mathbf{p}) - e \left(\mathbf{E} + \frac{\mathbf{p}}{m_e \gamma(\mathbf{p})} \times \mathbf{B} \right) \cdot \frac{\partial}{\partial \mathbf{p}} f(t, \mathbf{r}, \mathbf{p}) = S(\mathbf{E}, \mathbf{p}) \delta(\mathbf{p}), \quad (2.1.42)$$

where $\mathbf{p} = m_e \gamma(\mathbf{p}) \mathbf{v}$, δ is the Dirac distribution and $S(\mathbf{E}, \mathbf{p})$ is a source term that represents laser-induced ionization. This source term is modelled with a Dirac distribution because electrons are assumed to be ionized with zero initial momentum.

The equations for the averaged macroscopic fields can next be obtained by calculating the d -degree moments of Eq. (2.1.42), which are extracted by computing the integral over \mathbf{p} of Eq. (2.1.42) multiplied by \mathbf{p}^d . Only the zeroth-order moment (conservation of the averaged electron density) and the first-order moment (conservation of the averaged electron linear momentum) will be established. After some manipulations shown in Section C, these moments read as

$$\partial_t \langle N_e \rangle + \nabla \cdot \langle N_e \mathbf{v} \rangle = S(\mathbf{E}, \mathbf{p} = \mathbf{0}), \quad (2.1.43)$$

$$\partial_t \langle N_e \mathbf{p} \rangle + \nabla \cdot \bar{\bar{\Psi}} + \nabla \cdot [\langle N_e \rangle \langle \mathbf{v} \rangle \otimes \langle \mathbf{p} \rangle] = -e \langle N_e \rangle (\mathbf{E} + \langle \mathbf{v} \rangle \times \mathbf{B}), \quad (2.1.44)$$

respectively, where $\bar{\bar{\Psi}}$ is the kinetic pressure tensor [Eq. (C.21)]. Equation (2.1.43) is the continuity equation for the electron density. Equation (2.1.44) is the fundamental fluid equation for the charged particles (electrons).

2.1.4 Cold-plasma fluid equations

The symbol $\langle \rangle$ denoted the phase-space-averaged macroscopic variables in Section 2.1.3. These variables will be considered hereinafter as *fluid* variables and consequently renamed as $N_e \equiv \langle N_e \rangle$, $\mathbf{p} \equiv \langle \mathbf{p} \rangle$ and $\mathbf{v} \equiv \langle \mathbf{v} \rangle$, linked together through the relationships:

$$\mathbf{p} = m_e \gamma \mathbf{v}, \quad (2.1.45)$$

$$\gamma = \frac{1}{\sqrt{1 - \frac{v^2}{c^2}}}. \quad (2.1.46)$$

The conservation of the averaged electron density, Eq. (2.1.43), is directly rewritten into its *fluid version*:

$$\partial_t N_e + \nabla \cdot (N_e \mathbf{v}) = \partial_t \sum_s \sum_j \frac{q_{j,s}}{e} N_{j,s}, \quad (2.1.47)$$

where the source term, which accounts for ionization, is expressed as the time derivative of the charge density of all ions species indexed by s (see Section 2.2.3). Here, $N_{j,s}$ is the density of j -th ion for the s -th species and $q_{j,s}$ denotes its corresponding charge. As we neglect ion velocities under the assumption $v_{\text{ion}} \ll v_e$, the fluid electron current simply expresses as

$$\mathbf{J} = -eN_e \mathbf{v}. \quad (2.1.48)$$

It is then more interesting to express Eq. (2.1.47) in terms of \mathbf{J} :

$$\partial_t N_e - \frac{1}{e} \nabla \cdot \mathbf{J} = \partial_t \sum_s \sum_j \frac{q_{j,s}}{e} N_{j,s}. \quad (2.1.49)$$

Equation (2.1.49) is equivalent to the well-known continuity equation

$$\partial_t \rho_f + \nabla \cdot \mathbf{J}_f = 0, \quad (2.1.50)$$

where $\rho_f = -eN_e + \sum_s \sum_j q_{j,s} N_{j,s}$ is the free charge density, as the total free current density follows from the motion of electrons, i.e., $\mathbf{J}_f = \mathbf{J}$. This continuity equation can also be obtained from Maxwell equations, by taking the divergence of Eq. (2.1.4) and neglecting $\nabla \cdot \mathbf{J}_{\text{loss}}$.

The assumption of a *cold* plasma implies that we omit pressure effects, i.e., $\nabla \cdot \bar{\Psi} = \mathbf{0}$ in Eq. (2.1.44). This can be justified by viewing the plasma as an ideal polytropic gas, verifying $\Psi V^n = \text{cst}$ and $T_e V^{n-1} = \text{cst}$, where Ψ , T_e and V account for the electron pressure, temperature and volume, respectively, and n is the polytropic index. The gradient of pressure is thus

$$\nabla \Psi = \frac{n}{n-1} \frac{\Psi}{T_e} \nabla T_e, \quad (2.1.51)$$

which implies that neglecting thermal effects is equivalent to neglect this pressure gradient.

For completeness, a collisional term can be heuristically introduced into Eq. (2.1.44) *by hand*, proportional to $N_e \mathbf{p}$ and characterized by a collision rate ν_c . This exponential damping of the electron linear momentum accounts for the average of different elastic and inelastic collisions (electron-neutral, electron-ion, and electron-electron) [130, 154]. In underdense and weakly ionized plasmas (like in filamentation regime), electron-electron collisions are not significant. In single or highly ionized plasmas, instead, electron-electron

collision rate is about ten times higher than the rate of inelastic collisions (i.e., collisional ionization). In spite of this fact, we will analyse separately the collisional ionization in Sections 2.2.3.2 and 2.4.3 as a potential THz emitter. With this collisional rate, the resulting fluid equation thus becomes:

$$\partial_t (N_e \mathbf{p}) + \nabla \cdot (N_e \mathbf{v} \otimes \mathbf{p}) = -eN_e (\mathbf{E} + \mathbf{v} \times \mathbf{B}) - \nu_c N_e \mathbf{p}. \quad (2.1.52)$$

The value of ν_c can be adjusted to describe the collisions in the current density over long times. Equation (2.1.52) was already proposed by Sprangle *et al.* in Ref. [154] for a nonrelativistic plasma. Alternatively, it may be useful to express it in terms of the electron current density \mathbf{J} :

$$\partial_t (\gamma \mathbf{J}) + \nabla \cdot (\mathbf{v} \otimes \gamma \mathbf{J}) = \frac{e^2}{m_e} N_e \mathbf{E} - \frac{e}{m_e} \mathbf{J} \times \mathbf{B} - \nu_c \gamma \mathbf{J}. \quad (2.1.53)$$

2.1.5 Forward propagating electric fields

Maxwell equations [Eqs. (2.1.1), (2.1.3) and (2.1.4)], together with Eqs. (2.1.5) and (2.1.6), can be combined to lead to the following equation for the electric field:

$$\nabla^2 \mathbf{E} - \frac{1}{c^2} \partial_t^2 (\varepsilon_r * \mathbf{E}) - \nabla (\nabla \cdot \mathbf{E}) = \mu_0 [\partial_t \mathbf{J}_f + \partial_t \mathbf{J}_{\text{loss}} + \partial_t^2 \mathbf{P}_{\text{NL}}], \quad (2.1.54)$$

where

$$\nabla \cdot \mathbf{E} = \frac{1}{\varepsilon} * (\rho_f - \nabla \cdot \mathbf{P}_{\text{NL}}). \quad (2.1.55)$$

Briefly speaking, Eqs. (2.1.5) and (2.1.6) are inserted into the Ampère's equation [Eq. (2.1.4)], assuming $\mathbf{M} = \mathbf{0}$ and by applying Eq. (0.0.1):

$$\nabla \times \mathbf{B} = \mu_0 \mathbf{J}_f + \mu_0 \mathbf{J}_{\text{loss}} + \frac{1}{c^2} \partial_t \mathbf{E} + \mu_0 \partial_t \mathbf{P}.$$

Next, by differentiating in time and using Eq. (2.1.3), we find:

$$-\nabla \times (\nabla \times \mathbf{E}) = \mu_0 \partial_t \mathbf{J}_f + \mu_0 \partial_t \mathbf{J}_{\text{loss}} + \frac{1}{c^2} \partial_t^2 \mathbf{E} + \mu_0 \partial_t^2 \mathbf{P}.$$

Applying the identity (0.0.9) and Eqs. (2.1.7) and (2.1.8), we obtain

$$\nabla^2 \mathbf{E} = \mu_0 \partial_t \mathbf{J}_f + \mu_0 \partial_t \mathbf{J}_{\text{loss}} + \frac{1}{c^2} \partial_t^2 \mathbf{E} + \frac{1}{c^2} \partial_t^2 (\chi^{(1)} * \mathbf{E}) + \mu_0 \partial_t^2 \mathbf{P}_{\text{NL}} + \nabla (\nabla \cdot \mathbf{E}),$$

which yields Eq. (2.1.54) after employing Eq. (2.1.18).

By combining Eqs. (2.1.1), (2.1.5), (2.1.7) and (2.1.8), we furthermore get

$$\nabla \cdot \mathbf{E} = \frac{1}{\varepsilon_0} \left(\rho_f - \varepsilon_0 \nabla \cdot (\chi^{(1)} * \mathbf{E}) - \nabla \cdot \mathbf{P}_{\text{NL}} \right),$$

from which Eq. (2.1.55) follows after using Eqs. (2.1.18) and (2.1.19).

2.1.5.1 The non-relativistic limit of the forward propagation equations

The free current density \mathbf{J}_f in Eq. (2.1.54) in the nonrelativistic regime is given by Eq. (2.1.53) with $\gamma \approx 1$. It is even more simplified when assuming $v \ll c$ and neglecting the convective term $\nabla \cdot (\mathbf{v} \otimes \mathbf{J})$, because it is of second order in \mathbf{v} , and the Lorentz force $em_e^{-1} \mathbf{J} \times \mathbf{B}$, because it scales as $\approx |N_e \mathbf{E} \times \mathbf{v}/c| \ll |N_e \mathbf{E}|$:

$$\partial_t \mathbf{J} = \frac{e^2}{m_e} N_e \mathbf{E} - \nu_c \mathbf{J}. \quad (2.1.56)$$

Assuming a neutral plasma (i.e., $\rho_f = 0$), the electron density is calculated from the ion densities (see Section 2.2.3 for details), so that:

$$N_e = \sum_s \sum_j \frac{q_{j,s}}{e} N_{j,s}, \quad (2.1.57)$$

Because $\rho_f = 0$, Eq. (2.1.55) turns into $\nabla \cdot \mathbf{E} = -\varepsilon^{-1} * \nabla \cdot \mathbf{P}_{\text{NL}}$. The nonlinear polarization is supposed to be very small compared with the linear one ($|\mathbf{P}_{\text{NL}}| \ll |\mathbf{P}_{\text{L}}|$). Thus it is reasonable to neglect the term $\nabla (\nabla \cdot \mathbf{E})$ in Eq. (2.1.54) and assume $\nabla \cdot \mathbf{E} = 0$ henceforth. The following wave equation for the electric field then readily follows:

$$\nabla^2 \mathbf{E} - \frac{1}{c^2} \partial_t^2 (\varepsilon_r * \mathbf{E}) = \mu_0 \left[\partial_t \mathbf{J} + \partial_t \mathbf{J}_{\text{loss}} + \partial_t^2 \mathbf{P}_{\text{NL}} \right]. \quad (2.1.58)$$

Equation (2.1.58) is now rewritten in Fourier domain:

$$\nabla^2 \hat{\mathbf{E}} + \frac{1}{c^2} \omega^2 \hat{\varepsilon}_r \hat{\mathbf{E}} = \mu_0 \left[i\omega \hat{\mathbf{J}} + i\omega \hat{\mathbf{J}}_{\text{loss}} - \omega^2 \widehat{\mathbf{P}}_{\text{NL}} \right]. \quad (2.1.59)$$

From now on, the propagation axis is z and the laser pulse is assumed to be linearly polarized over the x axis:

$$\mathbf{E}(x, y, z) = E(x, y, z) \hat{\mathbf{x}}. \quad (2.1.60)$$

With $\mathbf{J} = J \hat{\mathbf{x}}$ and $\mathbf{P}_{\text{NL}} = P_{\text{NL}} \hat{\mathbf{x}}$, Eq. (2.1.59) turns to the scalar equation

$$\left(\partial_z^2 + \nabla_{\perp}^2 + \frac{1}{c^2} \omega^2 \hat{\varepsilon}_r \right) \hat{E} = \mu_0 \left[i\omega \hat{J} + i\omega \hat{J}_{\text{loss}} - \omega^2 \widehat{P}_{\text{NL}} \right], \quad (2.1.61)$$

where $\nabla_{\perp}^2 = \partial_x^2 + \partial_y^2$. As the wavenumber is defined as

$$k(\omega) = \frac{\omega}{c} \sqrt{\widehat{\epsilon}_r(\omega)}, \quad (2.1.62)$$

Eq. (2.1.61) can be rewritten as the extended Helmholtz equation:

$$(\partial_z^2 + \nabla_{\perp}^2 + k^2) \hat{E} = \mu_0 [i\omega \hat{J} + i\omega \hat{J}_{\text{loss}} - \omega^2 \widehat{P}_{\text{NL}}]. \quad (2.1.63)$$

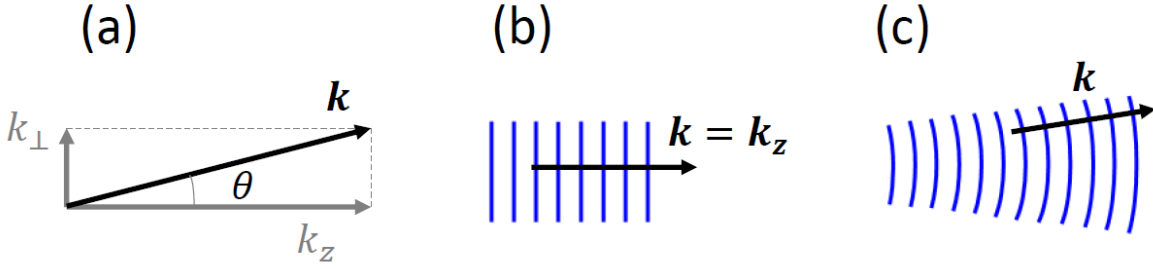


Figure 2.1.1: (a) Components of the wavevector \mathbf{k} , k_z and k_{\perp} , with the diffraction angle $\theta = \arcsin(k_{\perp}/k)$. (b) No diffracting pulse (plane wave): $\theta = 0$ at every position. (c) Diffracting pulse: $|\theta| \geq 0$ varies with the position.

The wavevector \mathbf{k} is defined as the vector parallel to the propagation direction of the laser field and whose modulus is the wavenumber given by Eq. (2.1.62). The transverse component of this vector is $k_{\perp} = \sqrt{k_x^2 + k_y^2}$ while the longitudinal one is k_z , verifying $k^2 = k_{\perp}^2 + k_z^2$ [see Fig. 2.1.1(a)]. For the laser pulse propagating along z , the diffraction angle with respect to that axis is $\sin \theta = k_{\perp}/k$ [see Fig. 2.1.1(b,c)].

The scalar approach of Eq. (2.1.63) holds under the hypothesis that $k_{\perp} \ll k_z$, which means that the propagation is mostly paraxial, i.e., it only supports small diffraction angles $\theta \ll 1$. From Eq. (2.1.63) several approaches modelling the forward propagation of the laser pulse can be done [14, 24, 61, 76, 93, 94]. Two well-known equations can be derived from Eq. (2.1.63), namely, the Forward Maxwell Equation (Section 2.1.5.2) and the Unidirectional Pulse Propagation Equation (Section 2.1.5.3).

2.1.5.2 The Forward Maxwell Equation (FME)

For technical convenience, the following propagation operators are introduced:

$$\hat{D}_{\pm}(\omega) = \partial_z \mp ik(\omega), \quad (2.1.64)$$

where \hat{D}_+ is the forward propagation operator associated to the propagation of linear modes $\sim \exp(ikz)$, and \hat{D}_- the backward propagation operator associated to the coun-

terpropagating linear modes $\sim \exp(-ikz)$. Since $\hat{D}_+\hat{D}_- = \partial_z^2 + k^2$, Eq. (2.1.63) can be rewritten as

$$\hat{D}_+\hat{D}_-\hat{E} = -\nabla_{\perp}^2\hat{E} + \mu_0 \left[i\omega\hat{J} + i\omega\hat{J}_{\text{loss}} - \omega^2\widehat{P}_{\text{NL}} \right]. \quad (2.1.65)$$

Accordingly, the laser field is decomposed on the basis of the two linear modes, i.e.,

$$\hat{E} = \hat{E}_+e^{ikz} + \hat{E}_-e^{-ikz}, \quad (2.1.66)$$

where \hat{E}_+ refers to the forward propagating optical field and \hat{E}_- to its backward propagating part. Under the hypothesis $k_{\perp} \ll k_z$ and small nonlinearities, the backscattered part \hat{E}_- can be separated from the forward field, viewed as the dominant pulse component [58]. Therefore, the laser field is approximated by a forward propagating pulse:

$$\hat{E} = \hat{E}_+e^{ikz}. \quad (2.1.67)$$

We apply the operator \hat{D}_- onto Eq. (2.1.67):

$$\hat{D}_-\hat{E} = (\partial_z + ik) \left(\hat{E}_+e^{ikz} \right) \approx e^{ikz} \left(\partial_z\hat{E}_+ + 2ik\hat{E}_+ \right). \quad (2.1.68)$$

Thanks to the paraxiality assumption, $|\partial_z\hat{E}_+| \ll |ik\hat{E}_+|$, which states that $\hat{E}_+(\omega)$ does not vary significantly on propagation distances of order of $2\pi c\omega^{-1}$, the above equation is simplified to

$$\hat{D}_-\hat{E} = e^{ikz} \left(\cancel{\partial_z\hat{E}_+} + 2ik\hat{E}_+ \right) \approx 2ik\hat{E}_+e^{ikz} = 2ik\hat{E}. \quad (2.1.69)$$

Applying next the operator \hat{D}_+ to Eq. (2.1.69), one has

$$\hat{D}_+\hat{D}_-\hat{E} = \hat{D}_+ \left(2ik\hat{E} \right) = (\partial_z - ik) \left(2ik\hat{E} \right) = 2ik \left(\partial_z\hat{E} - ik\hat{E} \right). \quad (2.1.70)$$

Substituting Eq. (2.1.70) into Eq. (2.1.65) yields the Forward Maxwell Equation (FME):

$$\partial_z\hat{E} = ik\hat{E} + \frac{i}{2k}\nabla_{\perp}^2\hat{E} + \frac{\mu_0}{2k} \left[\omega\hat{J} + \omega\hat{J}_{\text{loss}} + i\omega^2\widehat{P}_{\text{NL}} \right], \quad (2.1.71)$$

which was first proposed by Husakou and Herrmann in Ref. [76].

Anterior models as, e.g., that proposed by Brabec and Krausz [24], have often dealt with improved envelope equations where the wavenumber given by Eq. (2.1.62) is expanded through Taylor series around a central frequency ω_0 [1]:

$$k(\omega) = k_0 + k_1(\omega - \omega_0) + \hat{\mathcal{D}}, \quad (2.1.72)$$

where $k_0 = k(\omega_0) = \omega_0 n_0/c$, $n_0 = \hat{n}(\omega_0)$, $k_1 = \partial_{\omega}k(\omega)|_{\omega=\omega_0}$ is the inverse of the *group*

velocity of the pulse, and $\hat{\mathcal{D}}$ accounts for high-order dispersion:

$$\hat{\mathcal{D}} = \sum_{m=2}^{\infty} \frac{k_m}{m!} (\omega - \omega_0)^m, \quad (2.1.73)$$

with $k_m = \partial_{\omega}^m k(\omega)|_{\omega=\omega_0}$. k_2 is called the *group velocity dispersion* (GVD) and k_3 the *third-order dispersion* (TOD). Such extended envelope equations, however, assume that most of the propagation physics is carried out around ω_0 only. They are usually expressed in the co-moving reference frame that travels at the group velocity k_1^{-1} [24]. The resulting ‘‘Nonlinear Envelope Equation’’ (NEE) has consisted in an important progress in modelling ultrashort pulse propagation compared with the standard Nonlinear Schrödinger Equation (NSE) [1], as it accounts, e.g., for self-steepening effects through operators in the form $T = 1 + i\omega_0^{-1}\partial_t$ that correct the slowly-varying envelope approximation. This phenomenon, modelled by the term $T\widehat{P}_{\text{NL}} \sim T|\hat{E}|^2\hat{E}$, induces a steepening of the trailing edge of the pulse, which manifests into an important blueshifting of the spectrum.

2.1.5.3 The Unidirectional Pulse Propagation Equation (UPPE)

Similarly to Eq. (2.1.64), instead of excluding the diffraction term from the elementary linear modes, one can account for it through the propagation operators

$$\hat{D}_{\pm}^{\perp}(\omega) = \partial_z \mp ik_z(\omega) = \partial_z \mp i\sqrt{k(\omega)^2 - k_{\perp}(\omega)^2}, \quad (2.1.74)$$

where $k_{\perp}^2 = k_x^2 + k_y^2$, \hat{D}_{+}^{\perp} is the forward propagation operator associated to linear modes $\sim \exp(ik_z z)$ and \hat{D}_{-}^{\perp} the backward propagation operator associated to linear modes $\sim \exp(-ik_z z)$. The key idea here is to express Eq. (2.1.65) in the transverse Fourier variables k_x and k_y occurring through $\nabla_{\perp} \rightarrow -ik_{\perp}$. By doing so, the composition of these two operators gives

$$\hat{D}_{+}^{\perp}\hat{D}_{-}^{\perp} = (\partial_z - ik_z)(\partial_z + ik_z) = \partial_z^2 + k_z^2 = \partial_z^2 + k^2 - k_{\perp}^2 = \partial_z^2 + \nabla_{\perp}^2 + k^2. \quad (2.1.75)$$

Equations (2.1.63) and (2.1.75) are combined into

$$\hat{D}_{+}^{\perp}\hat{D}_{-}^{\perp}\hat{E} = \mu_0 \left[i\omega\hat{J} + i\omega\hat{J}_{\text{loss}} - \omega^2\widehat{P}_{\text{NL}} \right]. \quad (2.1.76)$$

The laser pulse is again decomposed into forward (\hat{E}_{+}) and backward (\hat{E}_{-}) field components as

$$\hat{E} = \hat{E}_{+}e^{ik_z z} + \hat{E}_{-}e^{-ik_z z}. \quad (2.1.77)$$

Neglecting the backscattered field, the laser field simplifies into

$$\hat{E} = \hat{E}_+ e^{ik_z z}. \quad (2.1.78)$$

By applying the paraxiality assumption to Eq. (2.1.78), it is then easy to verify that

$$\hat{D}_-^\perp \hat{E} = (\partial_z + ik_z) (\hat{E}_+ e^{ik_z z}) = e^{ik_z z} (\partial_z \hat{E}_+ + 2ik_z \hat{E}_+) \approx 2ik_z \hat{E}_+ e^{ik_z z} = 2ik_z \hat{E}, \quad (2.1.79)$$

$$\hat{D}_+^\perp \hat{D}_-^\perp \hat{E} = (\partial_z - ik_z) (2ik_z \hat{E}) = 2ik_z (\partial_z \hat{E} - ik_z \hat{E}). \quad (2.1.80)$$

Substituting Eq. (2.1.80) into Eq. (2.1.76) gives the Unidirectional Pulse Propagation Equation (UPPE):

$$\partial_z \hat{E} = i\sqrt{k^2 - k_\perp^2} \hat{E} + \frac{\mu_0}{2\sqrt{k^2 - k_\perp^2}} [\omega \hat{J} + \omega \hat{J}_{\text{loss}} + i\omega^2 \hat{P}_{\text{NL}}], \quad (2.1.81)$$

which was proposed by Kolesik, Moloney and Mlejnek in Refs. [93] and [94]. Both Eqs. (2.1.71) and (2.1.81) provide quite similar results when the condition $k_\perp \ll k_z \approx k$ applies. The major difference with the FME model is that Eq. (2.1.81) allows to describe direct-current (DC) field components in the limit $\omega \rightarrow 0$, i.e., strongly diffracting waves, whereas Eq. (2.1.71) is strictly limited to weakly dispersive and diffractive waves. This can be seen from the term accounting for linear dispersion and diffraction $i[k - k_\perp^2/(2k)]\hat{E}$ in Eq. (2.1.71), which diverges in the limit $k \rightarrow 0$, unlike the term $i\sqrt{k^2 - k_\perp^2}\hat{E}$ in Eq. (2.1.81). The former proceeds from the latter in the limit $k^2 \gg k_\perp^2$.

The UPPE equation gives a complete description of the electromagnetic spectrum, including low frequencies and high-order harmonics. The terahertz field in time domain is recovered by applying a filter at a cut-off frequency ν_{co} and then calculating the inverse Fourier transform:

$$E^{\nu_{\text{co}}} = \mathcal{F}^{-1} [\Pi(\omega) \hat{E}(\omega)], \quad (2.1.82)$$

where $\Pi(\omega)$ represents the filter. We use the simplest filter, which is the rectangular function:

$$\Pi(\omega) = \begin{cases} 1, & \text{if } |\omega| \leq 2\pi\nu_{\text{co}} \\ 0, & \text{otherwise.} \end{cases} \quad (2.1.83)$$

2.2 Ionization of gases

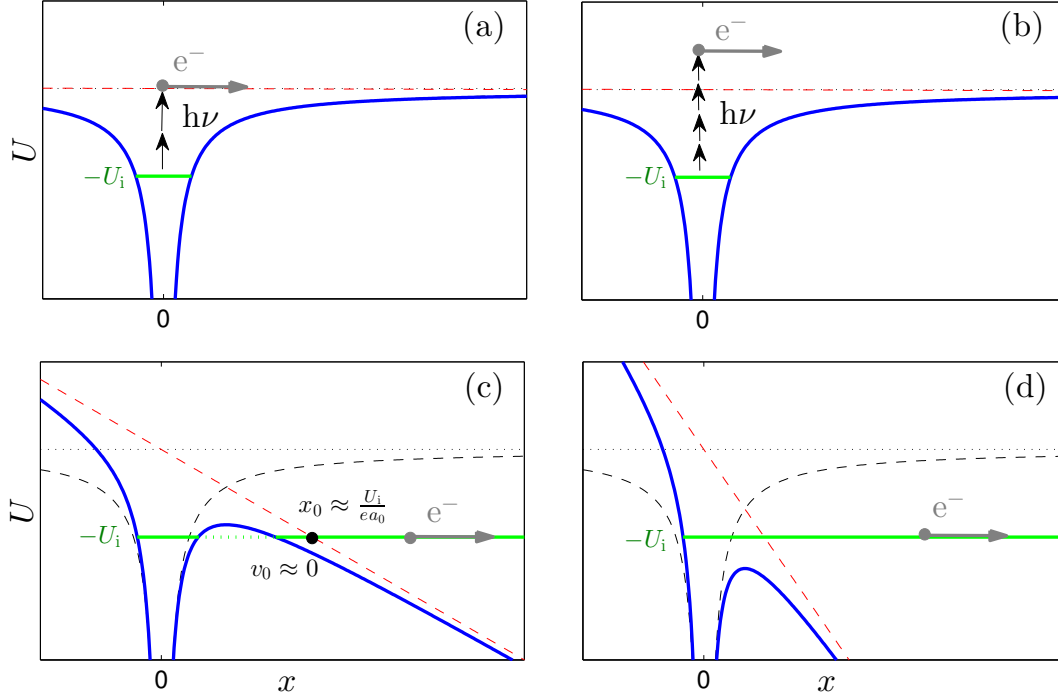


Figure 2.2.1: Schematic representation of photoionization regimes. The Coulomb energy potential of Eq. (2.2.1) is the blue solid curve, the sum of the potentials due to the electrostatic attraction of the core (black dashed curve) and the external electric field (red dashed curve). The energy level ($-U_i < 0$) of the bound electron is represented by the green solid line. The black dotted line stands for the zero energy level. (a) Multiphoton ionization: the electron absorbs a minimum number of photons to get freed. (b) Above threshold ionization: the electron gains from absorbed photons more energy than necessary to be ionized. (c) Tunnelling ionization: the Coulomb potential is bent by the strong external electric field and the resulting barrier is narrow enough for the electron to tunnel it through. The black dot refers to the position of electron birth. (d) Over-barrier ionization: the Coulomb potential is heavily deformed, such that the energy of the bound electron exceeds the height of the barrier and the electrons can thus escape.

The atomic Coulomb potential acts as an energy barrier that binds the *bound* electrons to atoms, because the electrons are in an energy level (negative) below this potential. This barrier is created by the electrostatic attraction of the atom nucleus and the external electric field, of amplitude a_0 , undergone by an irradiated atom. By reducing the geometry

to one dimension for the sake of simplicity, this potential reads:

$$U(x) = - \underbrace{\frac{Ze^2}{4\pi\epsilon_0|x|}}_{\text{core}} - \underbrace{ea_0x}_{\text{external field}}, \quad (2.2.1)$$

where Ze is the charge of the core and x is the distance of the electron from the nucleus.

When the atoms are subject to strong enough electric fields, bound electrons can be ionized due to different processes. The most important mechanism is the *optical-field-induced ionization*, simply known as *photoionization*, which encompasses the multi-photon ionization and the tunnel ionization (see Fig. 2.2.1). For *low* intensities (below 10^{13} W cm⁻²), the electric field is not intense enough to deform the Coulomb potential. In this situation, electrons can absorb photons until they overcome the energy barrier, becoming *free electrons*. This photoionization regime is known as *multi-photon ionization* (MPI), as shown in Fig. 2.2.1(a). A special case of this regime is the *above threshold ionization*, when electrons absorb more than the minimum number of photons needed to get free [Fig. 2.2.1(b)]. On the other hand, strong electric fields with intensities above 10^{13} W cm⁻² deform the Coulomb potential to such a point that electrons can be ionized by passing through the Coulomb potential barrier by tunnel effect [Fig. 2.2.1(c)]. The distance from the nucleus where the electrons are *born* to the outer side of the potential barrier, with zero initial velocity $v_0 \approx 0$ [38, 61], is $x_0 \approx U_i/(ea_0)$ [61, 169]. An extreme case is the *over-barrier ionization*, when the potential barrier disappears [Fig. 2.2.1(d)].

Keldysh [87] was a pioneer in the theory of photoionization. For an electric field of strength a_0 , he defined the so-called adiabaticity parameter:

$$\gamma_K = \frac{\omega_0 \sqrt{2m_e U_i}}{ea_0} = \omega_0 t_t, \quad (2.2.2)$$

where U_i is the energy necessary to extract one electron from a given atom, known as *ionization energy*. This parameter compares the laser frequency ω_0 with the electron tunnelling time, defined by

$$t_t = \frac{\sqrt{2m_e U_i}}{ea_0}. \quad (2.2.3)$$

Here, ea_0 is the value of the electric force acting on the electron and $m_e v_t = \sqrt{2m_e U_i}$ is the electron linear momentum associated to the tunnelling velocity v_t . The latter is estimated by supposing that the kinetic energy of the electron that tunnels through is equal to the ionization energy: $m_e v_t^2/2 = U_i$. When $\gamma_K \ll 1$ the atom is ionized in the MPI regime; when $\gamma_K \gg 1$, instead, ionization occurs by tunnel effect.

The early photoionization models (see Section 2.2.2) assumed hydrogen-like atoms supporting only a single-electron ionization. However, because this thesis is also devoted to

high intensity levels $> 10^{15} \text{ W cm}^{-2}$, a more realistic multiple ionization scheme will be considered (see Section 2.2.3).

Since electrons are ionized from the outermost to the innermost atomic shells, leading to a sequential production of ion charge states, photoionization is usually referred as a *sequential* process. Apart from it, there is a wide variety of *non-sequential* ionization mechanisms, where atoms lose several electrons simultaneously via inelastic collisional processes [5, 11, 39, 59, 98, 105, 169, 180]. One example is the non-sequential double ionization (NSDI), which is explained in two steps by Corkum thanks to his electron rescattering model [39]. In a first step, the outmost electron of an atom is released near the peak of the oscillating laser field, by passing over or tunnelling the effective barrier created by the Coulomb attraction of the ion core and the instantaneous laser electric field. In a second step, as shown in Fig. 2.2.2, the laser field accelerates the freed electron away from the ion and, then, the electron, if it has not enough kinetic energy, is driven back when the field reverses its sign. This returning first electron can collisionally ionize a second electron by kicking it out provided that the former has enough energy to liberate the latter. The maximum and most probable kinetic energy that the first electron can have is 3.17 times the laser ponderomotive energy, $U_p = e^2 a_0^2 / (4m_e \omega_0^2)$.

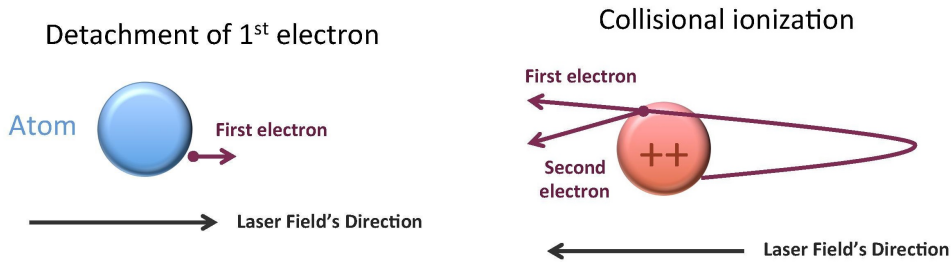


Figure 2.2.2: Schematic representation of the two steps of the electron rescattering model. Source: Wikipedia.

When electrons are freed, they can contribute to enhance even more the plasma density by collisional processes. These non-sequential mechanisms can be modelled using experimental data for *electron-impact ionization* (EII) cross-sections [137]. The measured electron-impact cross-sections, directly dependent on the electron kinetic energy, provide the probabilities of ionizing one or several electrons through electron-neutral and electron-ion processes. The EII model is closely related to the avalanche ionization model [115, 88, 182], also known as cascade ionization or Drude model. Because it may contribute to terahertz radiation, the effect of the electron-impact ionization will be analyzed in Sections 2.2.3.2 and 2.4.3.

We will not consider electron recombination that acts over long times in gases. For

example, Tzortzakis *et al.* measured an electron recombination time of the order of the nanosecond in air [165].

2.2.1 Ionization parameters

Before proceeding further with the concepts of photoionization, some useful quantities are introduced:

Notation	Description
Z_s	atomic number
$U_{i,j,s}$	ionization energy to create j -th ion
$Z_{\text{eff},j,s}$	effective charge to create j -th ion
$n_{j,s}^*$	effective principal quantum number of j -th ion
$l_{j,s}^*$	effective angular quantum number of j -th ion
$l_{j,s}$	angular quantum number of j -th ion
$m_{j,s}$	magnetic quantum number of j -th ion

In laser-driven plasmas, the gas target is formed, in general, from a mixture of several atomic and/or molecular species. The s -th species of such mixtures is first defined by its *atomic number*, Z_s , which is the total number of electrons that can be extracted from that species (1 for hydrogen, 2 for helium, 18 for argon and so on). Hence, there will be $Z_s + 1$ possible ions corresponding to such species, indexed by their charge j . The neutral state is thus denoted with $j = 0$ and the fully ionized state with $j = Z_s$.

The energy necessary to ionize the $(j - 1)$ -th ion into the j -th ion is known as *ionization energy* or *binding energy*, $U_{i,j,s}$. There are Z_s ionization energies associated to the s -th species, one for each electron ranging from $U_{i,1,s}$ to $U_{i,Z_s,s}$. All values will be taken from the NIST¹ Atomic Spectra Database [124] recalled in Table 2.2.

The ionization properties of each ion ($0 \leq j \leq Z_s$) are determined by its valence electrons, which are in turn characterized by several quantum numbers used in the ionization theory: $n_{j,s}^*$ (effective principal quantum number), $l_{j,s}$ (angular quantum number), $l_{j,s}^*$ (effective angular quantum number), and $m_{j,s}$ (magnetic quantum number).

The effective principal quantum number $n_{j,s}^*$ is defined by

$$n_{j,s}^* = \frac{Z_{\text{eff},j+1,s}}{\sqrt{2U_{i,j+1,s}/U_{\text{au}}}}, \quad (2.2.4)$$

where $U_{\text{au}} \simeq 27.21$ eV is the atomic unit of energy and $Z_{\text{eff},j,s}$ refers to the effective charge of the created j -th ion. For atomic gases such as hydrogen, helium or argon, $Z_{\text{eff},j,s} = j$

¹National Institute of Standards and Technology (U.S.).

j	H	He	Ne	Ar	O ₂	N ₂
1	13.60	24.59	21.56	15.76	12.07	15.58
2	-	54.42	40.96	27.63	-	-
3	-	-	63.42	40.74	-	-
4	-	-	97.19	59.58	-	-
5	-	-	126.25	74.84	-	-
6	-	-	157.93	91.29	-	-
7	-	-	207.27	124.41	-	-
8	-	-	239.10	143.46	-	-
9	-	-	1195.81	422.60	-	-
10	-	-	1362.20	479.76	-	-

Table 2.2: First binding energies, in eV, of some gases.

is widely used. For molecules, instead, the effective charge is sometimes calculated semi-empirically. Talebpour *et al.* proposed in [158] the values of $Z_{\text{eff},1,\text{O}_2} = 0.53$ for dioxygen molecule (O₂) and $Z_{\text{eff},1,\text{N}_2} = 0.9$ for dinitrogen molecule (N₂), in order to describe the apparent reduction in the ionization level observed from ion signals.

The angular quantum number $l_{j,s}$ is given by the orbital which the valence electron belongs to (0 for s-orbital, 1 for p-orbital, etc.). In contrast, the effective angular quantum number is defined by

$$l_{j,s}^* = n_{j,s}^* - 1. \quad (2.2.5)$$

The magnetic quantum number, $m_{j,s}$, can take any integer value in the interval from $-l_{j,s}$ to $l_{j,s}$. In practice, the value $m_{j,s} = 0$ mostly applies, because the ionization rate associated to $m_{j,s} = 0$ has a larger probability than the one associated to any values $|m_{j,s}| > 0$.

2.2.2 Single ionization

For the sake of clarity and in accordance with the chronological development, the ionization models will be first presented in this section for hydrogenoid atoms (i.e., they cannot lose more than one electron). They will be next extended to the more realistic context of multiple ionization in Section 2.2.3.

The ionization energy of an hydrogen-like atom will be denoted simply as U_i and its quantum numbers as n^* , l^* , l and m . The laser pulse is viewed as the monochromatic plane wave defined by Eq. (2.1.27):

$$E(t) = a_0 \cos(\omega_0 t). \quad (2.2.6)$$

If initially the density of neutral hydrogenoid atoms is N_a , then the electron density is governed by the following differential equation:

$$\partial_t N_e(t) = W(t) [N_a - N_e(t)], \quad (2.2.7)$$

where $W(t)$ is the ionization rate. With initial condition $N_e(t \rightarrow -\infty) = 0$, the solution of Eq. (2.2.7) is thus

$$N_e(t) = N_a \left[1 - \exp \left(- \int_{-\infty}^t W(\tau) d\tau \right) \right]. \quad (2.2.8)$$

If T_{gas} is the temperature of the gas and p_{gas} its pressure (total or partial if the target is formed of a mixture of gases), the initial density of neutrals is calculated assuming an ideal gas as

$$N_a = \frac{N_A p_{\text{gas}}}{R_0 T_{\text{gas}}}. \quad (2.2.9)$$

2.2.2.1 The PPT ionization rate

The PPT ionization rate refers to Perelomov, Popov and Terent'ev, who constructed a theory of ionization for hydrogen-like atoms by single-colour laser fields [131, 132, 133]. This theory encompasses both MPI and tunnel regimes, based mostly on the earlier theory by Keldysh [87]. Assuming that the values of the external electric field of Eq. (2.2.6) are largely smaller than the atomic ones [$\omega_0 \ll U_i/\hbar$ and $a_0 \ll \sqrt{2U_i^3 m_e}/(\hbar e)^2$], these authors reduced the problem to the solving of the one-dimensional motion of an electron under short-range forces [the Coulomb potential of Eq. (2.2.1) is replaced by a Dirac-delta-like potential], resulting in the Schrödinger equation

$$\left[i\hbar\partial_t + \frac{\hbar^2}{2m_e}\partial_x^2 \right] \Psi(x, t) = \left[-eE(t)x - \sqrt{\frac{2U_i\hbar^2}{m_e}}\delta(x) \right] \Psi(x, t), \quad (2.2.10)$$

where $\Psi(x, t)$ is the electron wave function and $\delta(x)$ is the Dirac delta function. As initial condition, the solution to Eq. (2.2.10) with $E(t) = 0$ is applied, which is the wave function associated to the electron in the bound state of energy U_i . The ionization rate is determined by the associated probability current at infinity, $x \rightarrow \pm\infty$, averaged over one laser period $2\pi/\omega_0$:

$$W = \frac{\omega_0}{2\pi} \int_0^{2\pi\omega_0^{-1}} \left[\lim_{x \rightarrow -\infty} j(x, t) + \lim_{x \rightarrow +\infty} j(x, t) \right] dt = \frac{\omega_0}{\pi} \int_0^{2\pi\omega_0^{-1}} \lim_{x \rightarrow +\infty} j(x, t) dt, \quad (2.2.11)$$

$$j(x, t) = \frac{\hbar i}{2m_e} (\Psi(x, t) \partial_x \Psi^*(x, t) - \Psi^*(x, t) \partial_x \Psi(x, t)), \quad (2.2.12)$$

where Ψ^* stands for the complex conjugate of Ψ .

This theory was later extended in the tunnel regime to complex atoms of atomic number Z by Ammosov, Delone and Krařnov (ADK) [2, 3, 77, 99, 125]. The resulting ionization rate reads

$$W_{\text{PPT}}(a_0, \omega_0) = \frac{4\sqrt{2}}{\pi} \nu_{\text{au}} C A(a_0, \omega_0) H_{\text{PPT}}(a_0, \omega_0), \quad (2.2.13)$$

where the coefficient C takes into account the nature of the electronic shell:

$$C(n^*, l^*, l, m) = \frac{2^{2n^*} (2l+1)(l+|m|)!}{2^{|m|} |m|! (l-|m|)! n^* \Gamma(n^* + l^* + 1) \Gamma(n^* - l^*)}, \quad (2.2.14)$$

Γ is the Euler's Gamma function, $A(a_0, \omega_0)$ is the transcendental function associated to the MPI regime:

$$A(a_0, \omega_0) = \frac{1}{1 + \gamma_{\text{K}}^2} \times \sum_{k=0}^{\infty} \left(\Phi_m \left(\sqrt{\frac{2\gamma_{\text{K}}(\kappa - \nu + k)}{\sqrt{1 + \gamma_{\text{K}}^2}}} \right) \exp \left[(\kappa - \nu + k) \left(\frac{2\gamma_{\text{K}}}{\sqrt{1 + \gamma_{\text{K}}^2}} - 2 \operatorname{arcsinh} \gamma_{\text{K}} \right) \right] \right), \quad (2.2.15)$$

$$\nu = \frac{U_i}{\hbar\omega_0} \left(1 + \frac{1}{2\gamma_{\text{K}}^2} \right), \quad (2.2.16)$$

$\kappa = \langle \nu + 1 \rangle$ is the number of absorbed photons ($\langle z \rangle$ represents the integer part of z),

$$\Phi_m(z) = \frac{e^{-z^2}}{|m|!} \int_0^z (z^2 - \zeta^2)^{|m|} e^{\zeta^2} d\zeta, \quad (2.2.17)$$

and the function $H_{\text{PPT}}(a_0, \omega_0)$ describes the tunnelling ionization as

$$H_{\text{PPT}}(a_0, \omega_0) = \frac{U_i}{U_{\text{au}}} \left(\frac{2(2U_i U_{\text{au}}^{-1})^{3/2}}{a_0 E_{\text{au}}^{-1} \sqrt{1 + \gamma_{\text{K}}^2}} \right)^{2n^* - \frac{3}{2} - |m|} \times \exp \left[-2\nu \left(\operatorname{arcsinh} \gamma_{\text{K}} - \frac{\gamma_{\text{K}} \sqrt{1 + \gamma_{\text{K}}^2}}{1 + 2\gamma_{\text{K}}^2} \right) \right]. \quad (2.2.18)$$

By taking the limit of Eq. (2.2.13) when $\gamma_{\text{K}} \rightarrow +\infty$, the MPI rate, proportional to the κ th power of the laser intensity, is obtained (for $m = 0$)

$$W_{\text{MPI}}(a_0) = \sigma_{\text{MPI}} a_0^{2\kappa}, \quad (2.2.19)$$

with

$$\sigma_{\text{MPI}} = \frac{8\sqrt{2}}{\pi} 2^{-3\kappa} \frac{\nu_{\text{au}}^{3\kappa} \hbar^{\kappa-1/2}}{E_{\text{au}}^{2\kappa}} C \left(\frac{U_i^{3/2-\kappa}}{\omega_0^{1/2+2\kappa}} \right) \exp(2\kappa - \nu) \Phi_0(\sqrt{2\kappa - \nu}). \quad (2.2.20)$$

2.2.2.2 The ADK tunnelling rate

The limit of Eq. (2.2.13) when $\gamma_K \rightarrow 0$ represents ionization in the tunnel regime. It converges when $m = 0$ and $|m| = 1$ towards:

$$W_{\text{ADK}}(a_0) = \sqrt{\frac{6}{\pi}} \nu_{\text{au}} C H_{\text{ADK}}(a_0), \quad (2.2.21)$$

where

$$H_{\text{ADK}}(a_0) = \frac{U_i}{U_{\text{au}}} \left(\frac{2(2U_i U_{\text{au}}^{-1})^{3/2}}{a_0 E_{\text{au}}^{-1}} \right)^{2n^* - \frac{3}{2} - |m|} \exp\left(\frac{2(2U_i U_{\text{au}}^{-1})^{3/2}}{3a_0 E_{\text{au}}^{-1}} \right). \quad (2.2.22)$$

This formulation originally applied to a constant field strength. In the context of ultrashort propagation, however, the variations in the ionization levels along each field cycle need to be described. Therefore, to account for the rapid oscillations of the electric field, a quasi-static approximation of Eq. (2.2.21) responding quasi-instantaneously to the rapid pulse oscillations in time, $W_{\text{ADK-inst}}(t)$, must be employed. This uses the absolute value of the electric field, $|E(t)| = a_0 |\cos(\omega_0 t)|$. The relationship between $W_{\text{ADK}}(a_0)$ and $W_{\text{ADK-inst}}(t)$ follows from averaging the resulting ADK rate over one optical cycle:

$$W_{\text{ADK}}(a_0) = \frac{\omega_0}{2\pi} \int_0^{2\pi/\omega_0} W_{\text{ADK-inst}}(\tau) d\tau, \quad (2.2.23)$$

which gives

$$W_{\text{ADK-inst}}(t) = \sqrt{\frac{6}{\pi}} \nu_{\text{au}} C H_{\text{ADK-inst}}(t), \quad (2.2.24)$$

$$H_{\text{ADK-inst}}(t) = \frac{U_i}{U_{\text{au}}} \left(\frac{2(2U_i U_{\text{au}}^{-1})^{3/2}}{|E(t)| E_{\text{au}}^{-1}} \right)^{2n^* - 1 - |m|} \exp\left(\frac{2(2U_i U_{\text{au}}^{-1})^{3/2}}{3|E(t)| E_{\text{au}}^{-1}} \right). \quad (2.2.25)$$

After some manipulations, the prevalence of the configuration $m = 0$ over the cases $|m| \geq 1$ announced above can be proven:

$$\frac{W_{\text{ADK}}(t)|_{|m|=1}}{W_{\text{ADK}}(t)|_{|m|=0}} = \frac{l(l+1)}{2} \left(\frac{2(2U_i U_{\text{au}}^{-1})^{3/2}}{|E(t)| E_{\text{au}}^{-1}} \right)^{-1} \ll 1, \quad (2.2.26)$$

because the inequality $|E(t)| \ll 2(2U_i U_{\text{au}}^{-1})^{3/2} E_{\text{au}}$ applies, which delimits the effective range of atom ionization. For this reason, henceforth, only the case $m = 0$ will be used and, consequently, after some manipulations, Eq. (2.2.24) reduces to

$$W_{\text{ADK-inst}}(|E(t)|) = \nu_{\text{au}} \frac{2^{\frac{8}{5}(n^*-1)}}{n^* \Gamma(2n^*)} (2l+1) \frac{\left[4(2U_i U_{\text{au}}^{-1})^{\frac{5}{2}}\right]^{\frac{6n^*-1}{5}}}{(|E(t)| E_{\text{au}}^{-1})^{2n^*-1}} \times \exp\left[-\frac{2}{3} \frac{(2U_i U_{\text{au}}^{-1})^{\frac{3}{2}}}{|E(t)| E_{\text{au}}^{-1}}\right]. \quad (2.2.27)$$

So far, original ionization theories were established for single-colour laser fields [Eq. (2.1.27)]. Further, Eq. (2.2.27) will be assumed to remain valid when $|E(t)|$ is an arbitrary laser pulse containing N -colours [Eq. (2.1.31)].

2.2.2.3 The QST ionization rate

For hydrogen-like atom ($n^* = 1$ and $l = 0$), Eq. (2.2.27) recovers the Quasi-Static Tunnelling (QST) ionization rate, which was originally derived by Landau and Lifschitz [97] and later exploited by Corkum *et al.* for high-order harmonic generation [38]:

$$W_{\text{QST}}(|E(t)|) = \nu_{\text{au}} \frac{4(2U_i U_{\text{au}}^{-1})^{\frac{5}{2}}}{|E(t)| E_{\text{au}}^{-1}} \exp\left[-\frac{2}{3} \frac{(2U_i U_{\text{au}}^{-1})^{\frac{3}{2}}}{|E(t)| E_{\text{au}}^{-1}}\right]. \quad (2.2.28)$$

Differences between the QST and the instantaneous ADK ionization rates have been discussed in Ref. [66]. Figure 2.2.3 compares the rates (2.2.28) and (2.2.27) for helium and argon. They increase with the electric field amplitude until a peak value E_{peak} , before they decay to zero. For hydrogen, helium and argon, the maximum fields reach the physical amplitudes of 342.5, 832.8 and 427.3 GV/m for QST and 342.5, 1707.3 and 497.9 GV/m for ADK, respectively. The ionization rates are expected to be valid for electric fields lower than E_{peak} , as ionization probability is expected to grow at increasing field values. Also, the growth of ionized atoms to the detriment of the population of neutral atoms is well described at high enough field levels before E_{peak} is reached.

Ionization efficiency is mainly determined by the slope of the curve $W(|E(t)|)$ in the interval $[0, E_{\text{peak}}]$. This slope nonlinearly depends on the position of the peak, which is function of n^* and U_i [see Eqs. (2.2.29) and (2.2.30)]. The higher $W(E_{\text{peak}})$ and the lower E_{peak} , the higher ionization. The peaks are found by differentiating Eqs. (2.2.28) and (2.2.27):

$$E_{\text{peak}}^{\text{QST}} = \frac{2}{3} \left(2 \frac{U_i}{U_{\text{au}}}\right)^{\frac{3}{2}} E_{\text{au}}, \quad (2.2.29)$$

$$E_{\text{peak}}^{\text{ADK}} = \frac{1}{2n^* - 1} E_{\text{peak}}^{\text{QST}}. \quad (2.2.30)$$

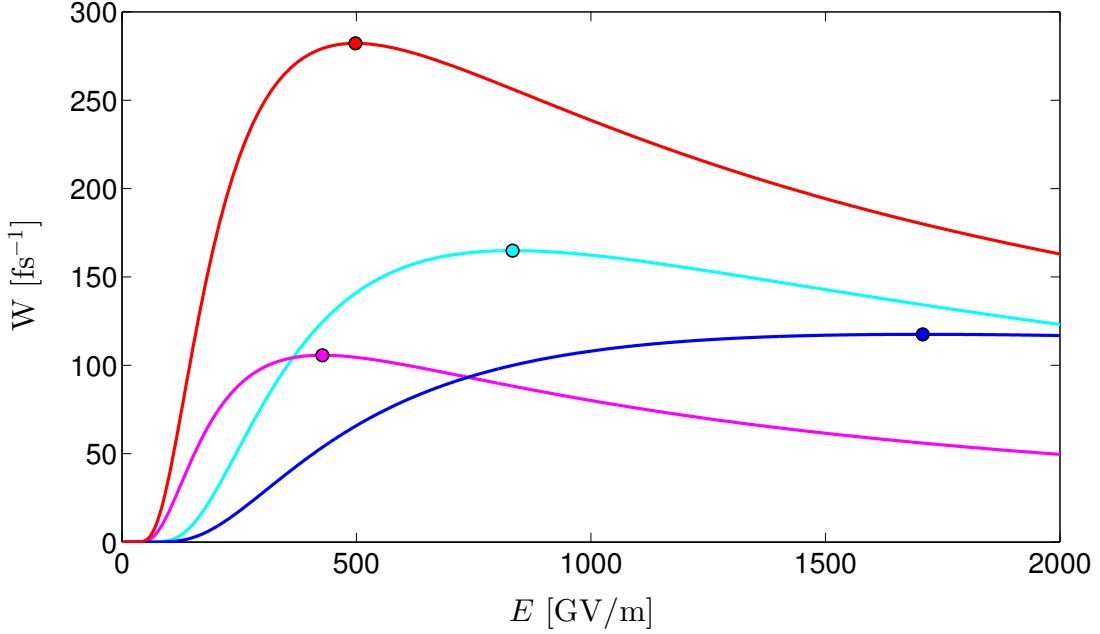


Figure 2.2.3: Comparison between QST and ADK ionization rates for helium and argon (single-electron ionization): red curve (argon and ADK), magenta curve (argon and QST), blue curve (helium and ADK), and cyan curve (helium and QST). The peak values are indicated by circles.

Figure 2.2.3 evinces that the QST model, widely used because of its simplicity, overestimates —for helium— or underestimates —for argon— the tunnelling ionization rates [66].

2.2.3 Multiple ionization

At high enough laser intensities, atoms as well as molecules are expected to be ionized multiple times. For a given gas, if Z is the atomic number, there will be $Z + 1$ possible ion densities, from $N_0(t)$ (neutrals) to $N_Z(t)$ (fully-ionized ions). Each ion $N_j(t)$, for $0 \leq j \leq Z$, is expected to be ionized following a rate (PPT or ADK) involving the ionization energy ($U_{i,j}$) and the associated quantum numbers (n_j^* , l_j^* , l_j and m_j), for a given electron shell j . Ion densities vary according to the following system of rate

equations:

$$\begin{cases} \partial_t N_0(t) = -W_1(t)N_0(t), \\ \partial_t N_j(t) = -W_{j+1}(t)N_j(t) + W_j(t)N_{j-1}(t), & j = 1, \dots, Z-1, \\ \partial_t N_Z(t) = W_Z(t)N_{Z-1}(t), \end{cases} \quad (2.2.31)$$

which can be written into the matrix form:

$$\partial_t \begin{pmatrix} N_0 \\ N_1 \\ N_2 \\ \vdots \\ N_{Z-1} \\ N_Z \end{pmatrix} = A(t) \begin{pmatrix} N_0 \\ N_1 \\ N_2 \\ \vdots \\ N_{Z-1} \\ N_Z \end{pmatrix}, \quad (2.2.32)$$

$$A(t) = \begin{pmatrix} -W_1 & 0 & 0 & \dots & 0 & 0 \\ W_1 & -W_2 & 0 & \dots & 0 & 0 \\ 0 & W_2 & -W_3 & \dots & 0 & 0 \\ \vdots & \vdots & \vdots & \ddots & \vdots & \vdots \\ 0 & 0 & 0 & \dots & -W_Z & 0 \\ 0 & 0 & 0 & \dots & W_Z & 0 \end{pmatrix}. \quad (2.2.33)$$

The initial conditions for Eq. (2.2.31) or Eq. (2.2.32) are

$$\begin{cases} N_0(t \rightarrow -\infty) = N_a, \\ N_j(t \rightarrow -\infty) = 0, & j = 1, \dots, Z. \end{cases} \quad (2.2.34)$$

From Eq. (2.2.31) or Eq. (2.2.32) and the initial conditions (2.2.34), matter conservation holds:

$$\sum_{j=0}^Z N_j(t) = N_a. \quad (2.2.35)$$

The solution to Eq. (2.2.32) between two instants t_n and $t_{n+1} = t_n + \Delta t$, assuming that the ionization rate keeps its value at t_n over the whole time interval, then expresses as

$$\begin{pmatrix} N_0(t_{n+1}) \\ \vdots \\ N_Z(t_{n+1}) \end{pmatrix} = P(t_n, \Delta t) \begin{pmatrix} N_0(t_n) \\ \vdots \\ N_Z(t_n) \end{pmatrix}, \quad (2.2.36)$$

where the matrix $P(t_n, \Delta t)$ reads

$$P(t_n, \Delta t) = V(t_n) \exp[D(t_n)\Delta t]V(t_n)^{-1}. \quad (2.2.37)$$

Here, $D(t_n)$ denotes the diagonal matrix of $A(t_n)$ (i.e., its eigenvalues) and $V(t_n)$ is a matrix containing by columns the eigenvectors of $A(t_n)$. Moreover:

$$\exp[D(t_n)\Delta t] = \begin{pmatrix} \exp[-W_1(t_n)\Delta t] & 0 & \dots & 0 & 0 \\ 0 & \exp[-W_2(t_n)\Delta t] & \dots & 0 & 0 \\ \vdots & \vdots & \ddots & \vdots & \vdots \\ 0 & 0 & \dots & \exp[-W_Z(t_n)\Delta t] & 0 \\ 0 & 0 & \dots & 0 & 1 \end{pmatrix}. \quad (2.2.38)$$

Note that, since the system given by Eq. (2.2.32) conserves the matter at every instant [Eq. (2.2.35)], the sum of the elements in each column of $P(t_n, \Delta t)$, given by Eq. (2.2.37), takes the value 1.

The matrix elements $P(t_n, \Delta t)$ [Eq. (2.2.37)] are the probabilities of ionizing each ion over the time interval $[t_n, t_{n+1}]$. Nuter *et al.* calculated all these probabilities in Ref. [126]. Nevertheless, those analytic formulae are numerically weak, as several subcases must be distinguished to avoid some divisions by zero. Moreover, the calculation of analogous formulae when the electron-impact ionization rates are added in Eq. (2.2.33) (see Section 2.2.3.2) almost becomes an unaffordable task. Therefore, in practice, all the codes used in this dissertation will employ a new numerical algorithm that calculates the eigenvectors $V(t_n)$ in order to obtain, with no subcases, the matrix of ionization probabilities, $P(t_n, \Delta t)$, thanks to Eq. (2.2.37). For the interested reader, the original algorithm which we developed is presented in Appendix D.

2.2.3.1 ADK-based degree of ionization for single-colour laser pulses

An important factor impacting laser-driven sources is the ionization degree, defined as the ratio between the final electron density and the initial density of neutrals:

$$Z^* = \frac{N_e(t \rightarrow +\infty)}{N_a}, \quad (2.2.39)$$

for a laser pulse with intensity I_0 and FWHM duration τ_p . In general, the ionization degree has to be computed numerically. However, for single-colour pulses in the form

$$E(t) = \sqrt{\frac{2I_0}{\varepsilon_0 c}} \exp \left[-2 \ln 2 \left(\frac{t}{\tau_p} \right)^2 \right] \cos(\omega_0 t), \quad (2.2.40)$$

it is possible to calculate analytically the degree of ionization based on the ADK ionization rate of Eq. (2.2.27) [46]. The analytical ionization degree is cumbersome. Therefore, its derivation, which was led during the present thesis, has been postponed to a proof given in Appendices, Section E. Its expression reads as

$$Z^*(I_0, \tau_p) = Z - \sum_{j=0}^{Z-1} \exp \left[-\Phi_j \frac{\tau_p}{t_{\text{ref}}} \left(\frac{\bar{I}_{0,j}}{I_{\text{ref}}} \right)^{1-n_j^*} \exp \left(-\Psi_j \sqrt{\frac{I_{\text{ref}}}{\bar{I}_{0,j}}} \right) \right], \quad (2.2.41)$$

where

$$\Phi_j = (2l_j + 1) \frac{(j+1)^{6n_j^*-4} (n_j^*)^{3-6n_j^*}}{\Gamma(2n_j^*)}, \quad (2.2.42)$$

$$\Psi_j = \frac{1}{6} \left(\frac{j+1}{n_j^*} \right)^3, \quad (2.2.43)$$

$$t_{\text{ref}} = \frac{\sqrt{\pi}}{12} t_{\text{au}} \simeq 3.57 \times 10^{-3} \text{ fs}, \quad (2.2.44)$$

$$I_{\text{ref}} = 8c\varepsilon_0 E_{\text{au}}^2 \simeq 5.62 \times 10^{17} \text{ W cm}^{-2}, \quad (2.2.45)$$

$$\bar{I}_{0,j} = \begin{cases} I_0, & \text{if } n_j^* \leq 1, \\ \min \left\{ I_0, \frac{(j+1)^6}{144 (n_j^{*8} - 2n_j^{*7} + n_j^{*6})} I_{\text{ref}} \right\}, & \text{otherwise.} \end{cases} \quad (2.2.46)$$

Alternatively, employing hand-waving arguments, the intensities I_j for which each electronic shell is fully ionized (i.e., the ionization degree is an integer j , $1 \leq j \leq Z$) are those for which the j -th ADK ionization rate is equal to the laser frequency ω_0 divided by the number of cycles, i.e., $c\tau_p\lambda_0^{-1}$, where λ_0/c is the fundamental period of the laser field:

$$W_{\text{ADK-inst}}(I_j) = \frac{\omega_0}{\tau_p c \lambda_0^{-1}} = \frac{2\pi}{\tau_p}. \quad (2.2.47)$$

Figure 2.2.4 shows the ionization degree of hydrogen, helium and argon as a function of the intensity and for two laser durations, calculated with Eqs. (2.2.41) and (2.2.47). The ionization degree is weakly dependent on the pulse duration τ_p . From this figure one

concludes that Eq. (2.2.47) is a good approximation of Eq. (2.2.41).

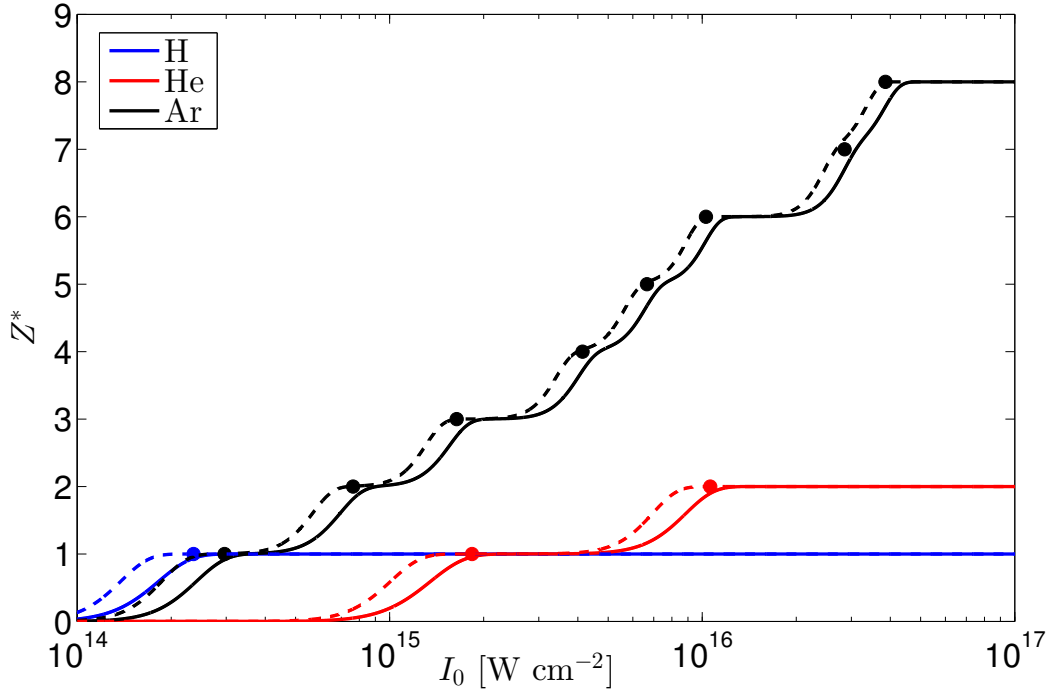
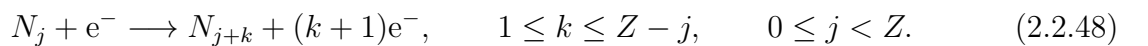


Figure 2.2.4: Analytical degree of ionization [Eq. (2.2.41)] of hydrogen (blue curve), helium (red curve) and argon (black curve), as a function of the single-colour laser intensity and FWHM durations of 10 cycles ($\tau_p \simeq 33.4$ fs, solid curves) and 40 cycles ($\tau_p \simeq 133.4$ fs, dashed curves). Dots are calculated according to Eq. (2.2.47).

2.2.3.2 Electron-Impact ionization

In this thesis the model proposed by Rae and Burnett in Ref. [137] for the electron-impact ionization (EII) has also been implemented in some of our codes. An electron e^- that collides with an ion can ionize the latter one or several times. For the the j -th ion there are $Z - j$ possible reactions:



Accordingly, we define by $R_{j+k}^j(t)$ the partial electron-impact ionization rate to ionize the j -th ion into the $(j+k)$ -th ion. To satisfy the matter conservation law (2.2.35) at every instant, Rae and Burnett add these partial ionization rates to the matrix given by

Ionization reaction	Experimental measurements
$\text{H} + \text{e}^- \longrightarrow \text{H}^+ + 2\text{e}^-$	[147]
$\text{He} + \text{e}^- \longrightarrow \text{He}^+ + 2\text{e}^-$	[122][138][144][155]
$\text{He} + \text{e}^- \longrightarrow \text{He}^{2+} + 3\text{e}^-$	[138][144][155]
$\text{He}^+ + \text{e}^- \longrightarrow \text{He}^{2+} + 2\text{e}^-$	[52][129]
$\text{Ne} + \text{e}^- \longrightarrow \text{Ne}^+ + 2\text{e}^-$	[138][144][155]
$\text{Ne} + \text{e}^- \longrightarrow \text{Ne}^{2+} + 3\text{e}^-$	[138][144][155]
$\text{Ne} + \text{e}^- \longrightarrow \text{Ne}^{3+} + 4\text{e}^-$	[138][144][155]
$\text{Ne}^+ + \text{e}^- \longrightarrow \text{Ne}^{2+} + 2\text{e}^-$	[51][53][101][118]
$\text{Ne}^+ + \text{e}^- \longrightarrow \text{Ne}^{3+} + 3\text{e}^-$	[101][190]
$\text{Ne}^+ + \text{e}^- \longrightarrow \text{Ne}^{4+} + 4\text{e}^-$	[101]
$\text{Ne}^{2+} + \text{e}^- \longrightarrow \text{Ne}^{3+} + 2\text{e}^-$	[10][120]
$\text{Ne}^{3+} + \text{e}^- \longrightarrow \text{Ne}^{4+} + 2\text{e}^-$	[70]
$\text{Ne}^{4+} + \text{e}^- \longrightarrow \text{Ne}^{5+} + 2\text{e}^-$	[10][54]
$\text{Ne}^{5+} + \text{e}^- \longrightarrow \text{Ne}^{6+} + 2\text{e}^-$	[10][54]
$\text{Ne}^{5+} + \text{e}^- \longrightarrow \text{Ne}^{7+} + 3\text{e}^-$	[54]
$\text{Ne}^{6+} + \text{e}^- \longrightarrow \text{Ne}^{7+} + 2\text{e}^-$	[10][54]
$\text{Ne}^{6+} + \text{e}^- \longrightarrow \text{Ne}^{8+} + 3\text{e}^-$	[54]
$\text{Ne}^{7+} + \text{e}^- \longrightarrow \text{Ne}^{8+} + 2\text{e}^-$	[48][54]
$\text{Ne}^{8+} + \text{e}^- \longrightarrow \text{Ne}^{9+} + 2\text{e}^-$	[54]

Table 2.3: Compilation of references proposing electron-impact ionization cross-sections for hydrogen, helium and neon, and their corresponding channels.

Eq. (2.2.33) as follows

$$A(t) = \begin{pmatrix} -\left(W_1 + \sum_{k=1}^Z R_k^0\right) & 0 & \dots & 0 & 0 \\ W_1 + R_1^0 & -\left(W_2 + \sum_{k=2}^Z R_k^1\right) & \dots & 0 & 0 \\ \vdots & \vdots & \ddots & \vdots & \vdots \\ R_{Z-1}^0 & R_{Z-1}^1 & \dots & -\left(W_Z + R_{Z-1}^Z\right) & 0 \\ R_Z^0 & R_Z^1 & \dots & W_Z + R_{Z-1}^Z & 0 \end{pmatrix}. \quad (2.2.49)$$

Each partial electron-impact ionization rate is modelled via partial cross-sections $\sigma_{j+k}^j = \sigma_{j+k}^j(U_K)$, which depend on the kinetic energy of the freed electrons, U_K :

$$R_{j+k}^j(t) = \sigma_{j+k}^j(U_K) N_e(t) |\mathbf{v}(t)|. \quad (2.2.50)$$

Ionization reaction	Experimental measurements
$\text{Ar} + e^- \longrightarrow \text{Ar}^+ + 2e^-$	[138][155][157]
$\text{Ar} + e^- \longrightarrow \text{Ar}^{2+} + 3e^-$	[138][155][157]
$\text{Ar} + e^- \longrightarrow \text{Ar}^{3+} + 4e^-$	[138][155][157]
$\text{Ar} + e^- \longrightarrow \text{Ar}^{4+} + 5e^-$	[138][157]
$\text{Ar}^+ + e^- \longrightarrow \text{Ar}^{2+} + 2e^-$	[12][118][176]
$\text{Ar}^+ + e^- \longrightarrow \text{Ar}^{3+} + 3e^-$	[12][123]
$\text{Ar}^+ + e^- \longrightarrow \text{Ar}^{4+} + 4e^-$	[12]
$\text{Ar}^+ + e^- \longrightarrow \text{Ar}^{5+} + 5e^-$	[12]
$\text{Ar}^{2+} + e^- \longrightarrow \text{Ar}^{3+} + 2e^-$	[120]
$\text{Ar}^{2+} + e^- \longrightarrow \text{Ar}^{4+} + 3e^-$	[161]
$\text{Ar}^{3+} + e^- \longrightarrow \text{Ar}^{4+} + 2e^-$	[70]
$\text{Ar}^{3+} + e^- \longrightarrow \text{Ar}^{5+} + 3e^-$	[161]
$\text{Ar}^{4+} + e^- \longrightarrow \text{Ar}^{5+} + 2e^-$	[40][191]
$\text{Ar}^{4+} + e^- \longrightarrow \text{Ar}^{6+} + 3e^-$	[123][135]
$\text{Ar}^{5+} + e^- \longrightarrow \text{Ar}^{6+} + 2e^-$	[191]
$\text{Ar}^{5+} + e^- \longrightarrow \text{Ar}^{7+} + 3e^-$	[161][191]
$\text{Ar}^{6+} + e^- \longrightarrow \text{Ar}^{7+} + 2e^-$	[191]
$\text{Ar}^{6+} + e^- \longrightarrow \text{Ar}^{8+} + 3e^-$	[161][191]
$\text{Ar}^{7+} + e^- \longrightarrow \text{Ar}^{8+} + 2e^-$	[136]

Table 2.4: Compilation of references proposing electron-impact ionization cross-sections for argon, and their corresponding channels.

The total cross-section for the j -th ion, σ^j , is the sum of the partial ones:

$$\sigma^j(U_K) = \sum_{k=1}^{Z-j} \sigma_{j+k}^j(U_K). \quad (2.2.51)$$

The model by Rae and Burnett [Eq. (2.2.49)] is the matter-conservation generalization of the classical avalanche ionization model [115, 84, 88, 182]. Indeed, for hydrogen, Eq. (2.2.49), combined with Eq. (2.1.49) where $\nabla \cdot \mathbf{J} = 0$, leads to the following equation for the electron density:

$$\partial_t N_e = (W_1 + \sigma_1^1 N_e |\mathbf{v}|)(N_a - N_e). \quad (2.2.52)$$

If Eq. (2.2.52) is expanded and the hypothesis $N_e \ll N_a$ is applied to the EII part (i.e., low degree of ionization), the following equation is obtained:

$$\partial_t N_e = W_1(N_a - N_e) + \sigma_1^1 N_e |\mathbf{v}|(N_a - N_e) = W_1(N_a - N_e) + \sigma_1^1 N_a |\mathbf{v}| N_e, \quad (2.2.53)$$

which recovers the classical avalanche ionization model:

$$\partial_t N_e = W_1(N_a - N_e) + \bar{\sigma} \frac{I}{U_i} N_e, \quad (2.2.54)$$

where $\bar{\sigma}$ is the avalanche cross-section.

These collisional ionization cross-sections are here estimated from experimental measurements. Tawara and Kato compiled many experimental measurements of cross-sections available at their moment for a wide collection of gases in [159]. Tables 2.3 and 2.4 summarize all the references used in this work (for hydrogen, helium, neon and argon) in order to analyse the action of the electron-impact ionization on terahertz generation. These experimental data have been fitted by least-squares following the formula proposed by Kim and Rudd in [91]:

$$\sigma(x) = \frac{\alpha}{\beta + x} \left[\ln x + \gamma \left(\frac{x-1}{x} - \frac{\ln x}{1+x} \right) \right], \quad (2.2.55)$$

where the abscissa x accounts for the kinetic energy of electrons (U_K) and α , β and γ are fitting constants that need to be determined by the method of nonlinear least-squares. Figure 2.2.5 presents the fitted partial cross-sections of helium, with the corresponding experimental references, proving that Eq. (2.2.55) is quite appropriate. Note that the partial cross-sections follow the hierarchy: $\sigma_{j+1}^j > \sigma_{j+2}^{j+1}$ and $\sigma_{j+k}^j > \sigma_{j+k+1}^j$.

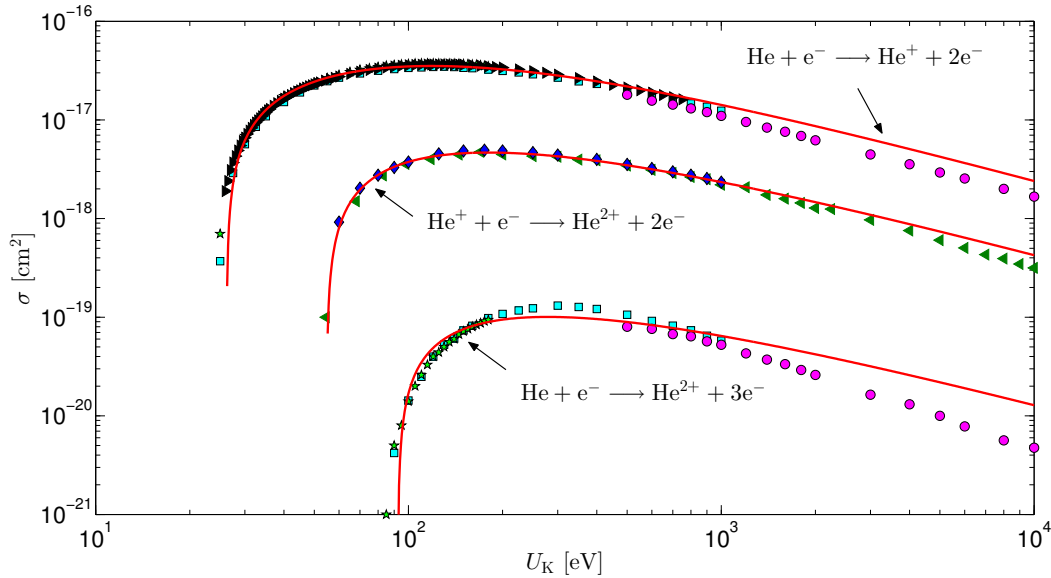


Figure 2.2.5: Fitted partial cross-sections using Eq. (2.2.55) for helium (red solid curves). Experimental data: blue rhombus [52], black right triangles [122], dark-green left triangles [129], cyan squares [138], magenta dots [144], green stars [155].

The model by Rae and Burnett [Eq. (2.2.49)], together with Eq. (2.2.55), reproduces quite well experimental measurements of the ion densities reported in the current bibliography: Walker *et al.* for helium [169], Larochelle *et al.* for neon [98], and Augst *et al.* for argon [5]. For instance, Fig. 2.2.6 compares the experimental measurements of helium ions reported by Walker *et al.* for an ADK ionization rate with and without electron-impact ionization. With Eq. (2.2.49), the density of He^{2+} is better modelled over a higher range of intensities than with Eq. (2.2.33) alone. The differences between the measurements and this EII model are visible at low and moderate intensities $< 10^{15} \text{ W cm}^{-2}$, where secondary non-sequential ionization mechanisms, discarded here, also contribute to the density of He^{2+} . From the present comparisons, we anticipate that the model (2.2.49) should be enough to study the effect of electron-impact ionization on terahertz generation (see Section 2.4.3).

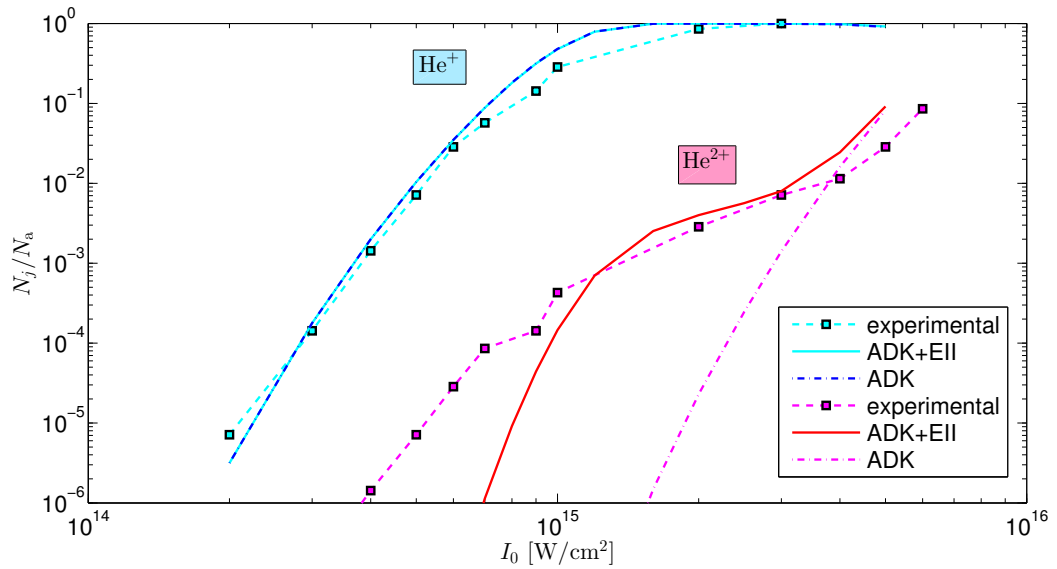


Figure 2.2.6: Comparison of the densities He^+ (cyan curves) and He^{2+} (magenta curves): experimental measurements by Walker *et al.* [169] (dashed curves with solid squares), calculated with ADK ionization rate (dashed dotted curves), and calculated with ADK plus EII (solid curves).

2.2.3.3 Ionization loss current

The ionization loss current density, \mathbf{J}_{loss} , is added heuristically to Ampère's law [Eq. (2.1.4)] in order to account for the laser energy consumed during ionization. Rae and Burnett proposed in Ref. [137] the following expression \mathbf{J}_{loss} , obtained by just matching the Ohmic power dissipation ($\mathbf{J}_{\text{loss}} \cdot \mathbf{E}$) to the energy employed to ionize the electrons

for all ions:

$$\mathbf{J}_{\text{loss}}(t) = \frac{\mathbf{E}(t)}{E(t)^2} \sum_s \sum_{j=0}^{Z_s-1} U_{i,j+1,s} N_{j,s}(t) W_{j+1,s}(t), \quad (2.2.56)$$

which follows the same direction and sense as the electric field. This model for ionization energy losses depends on the instantaneous value of the electric field and thus, strictly speaking, it is only valid for tunnelling ionization.

Going back to Fig. 2.2.1(c), for single-electron ionization, Geissler *et al.* in Ref. [61] derived similar losses by introducing the overall polarization vector for free electrons, expressed with the classical trajectory of the freed electron, $x(t)$, as $P = -eN_e x$. The time derivative of P is the free electron current density J such as

$$\partial_t J = \partial_t^2 P = -e \partial_t (x \partial_t N_e) - e \partial_t N_e \partial_t x - e N_e \partial_t^2 x. \quad (2.2.57)$$

In Eq. (2.2.57), $\partial_t^2 x$ is given by the Newton's equation of motion $m_e \partial_t^2 x(t) = -eE(t)$. By substituting the terms in x and $\partial_t x$ of Eq. (2.2.57) by the electron birth position and velocity, $x_0 = U_i/(eE(t))$ and $v_0 = 0$, respectively, one recovers Eq. (2.1.56):

$$\partial_t \left(J + \frac{U_i}{E(t)} \partial_t N_e \right) = \frac{e^2}{m_e} N_e E(t). \quad (2.2.58)$$

For single ionization $\partial_t N_e(t) \approx W(t) N_0(t)$, the loss current obtained in Eq. (2.2.58) and defined by

$$\mathbf{J}_{\text{loss}} \cdot \mathbf{E} = U_i \partial_t N_e, \quad (2.2.59)$$

is then equivalent to Eq. (2.2.56).

2.3 From optical self-focusing to UHI² plasmas

2.3.1 Laser filamentation

The Forward Maxwell Equation (2.1.71) describes a competition between two opposite effects when the laser pulse propagates through a nonlinear medium. On the one hand, the term $i(2k)^{-1}\nabla_{\perp}^2\hat{E}$ accounts for linear diffraction and broadens the laser beam spatially in the transverse plane. On the other hand, the Kerr term $i\mu_0(2k)^{-1}\omega^2\widehat{P}_{\text{NL}} \sim \varepsilon_0\widehat{\chi^{(3)}}E^3$ leads to a local increase of the optical refractive index ($n_0 + n_2I$), causing a transverse compression of the beam.

For simplicity, when linear dispersion and photocurrents are discarded, setting $k(\omega_0) = k_0$ and considering only the complex slowly-varying envelope of the electric field³ (\mathcal{E}), Eq. (2.1.71) easily reduces to the nonlinear Schrödinger equation [14]:

$$i\partial_z\mathcal{E} + \frac{1}{2k_0}\nabla_{\perp}^2\mathcal{E} + \frac{\omega_0}{c}n_2|\mathcal{E}|^2\mathcal{E} = 0, \quad (2.3.1)$$

which can be easily normalized to unity through simple field and spatial rescalings⁴ as

$$i\partial_z\mathcal{E} + \nabla_{\perp}^2\mathcal{E} + |\mathcal{E}|^2\mathcal{E} = 0. \quad (2.3.2)$$

In Eq. (2.3.2) there are two physical quantities that are conserved upon propagation, namely the power P and the Hamiltonian H , defined as

$$P = \iint_{\mathbb{R}^2} |\mathcal{E}|^2 dx dy, \quad (2.3.3)$$

$$H = \iint_{\mathbb{R}^2} \left(|\nabla_{\perp}\mathcal{E}|^2 - \frac{1}{2}|\mathcal{E}|^4 \right) dx dy. \quad (2.3.4)$$

Let $\langle r_{\perp}^2 \rangle$ be the transverse mean squared radius of the pulse

$$\langle r_{\perp}^2 \rangle = \frac{1}{P} \iint_{\mathbb{R}^2} (x^2 + y^2) |\mathcal{E}|^2 dx dy. \quad (2.3.5)$$

From Eq. (2.1.71) the following *virial* equality can be obtained for $\langle r_{\perp}^2 \rangle$ after multiplying Eq. (2.3.2) by $\langle r_{\perp}^2 \rangle \mathcal{E}^*$ and then by $\langle r_{\perp}^2 \rangle \nabla_{\perp}^2 \mathcal{E}^*$, yielding after classical (but not

²Ultra-High Intensity.

³The complex slowly-varying envelope of the electric field is defined as $\mathcal{E} = \sqrt{2n_0c\varepsilon_0}(E + i\mathcal{H}[E])$, where \mathcal{H} denotes the Hilbert transform.

⁴These rescalings are: $x \rightarrow w_0x$ (w_0 is the initial beamwidth), $y \rightarrow w_0y$, $z \rightarrow 2\omega_0n_0w_0^2c^{-1}z$, and $\mathcal{E} \rightarrow c\omega_0^{-1}w_0^{-1}(2n_2n_0)^{-1/2}\mathcal{E}$.

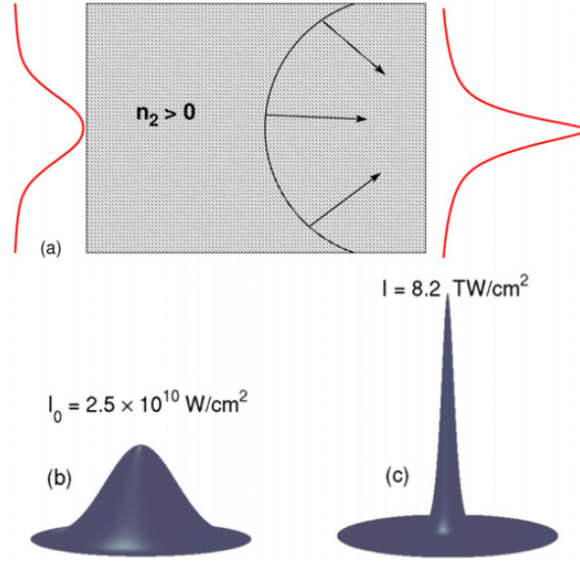


Figure 2.3.1: (a) Principle of wave self-focusing. Insets (b) and (c) detail some intensity profiles of the solution to Eq. (2.3.1) applied to silica ($n_2 = 3.2 \times 10^{-16} \text{ cm}^2 \text{ W}^{-1}$). The initial condition is the Gaussian pulse $\mathcal{E}(z = 0, r_\perp, t) = \mathcal{E}_0 \exp(-r_\perp^2/w_0^2 - t^2/t_p^2)$, where $w_0 = 130 \mu\text{m}$, $P/P_{\text{cr}} = 3$, $t_p = 85 \text{ fs}$. Source: Bergé *et al.* [14].

straightforward) calculations [14, 64, 168]:

$$\partial_z^2 \langle r_\perp^2 \rangle = 8 \frac{H}{P}. \quad (2.3.6)$$

The previous expression can be integrated twice over z to give

$$\langle r_\perp^2 \rangle = 8 \frac{H}{P_{\text{in}}} z^2 + [\partial_z \langle r_\perp^2 \rangle]_{z=0} z + [\langle r_\perp^2 \rangle]_{z=0}. \quad (2.3.7)$$

Equation (2.3.7) demonstrates that if $H < 0$ then the pulse blows up at a finite distance by self-compressing in the diffraction plane [96]. In other words, Kerr compression overcomes the transverse linear diffraction and the laser beam self-focuses at a finite distance $z_{\text{cr}} < +\infty$: $\langle r_\perp^2 \rangle \rightarrow 0$ and $\iint_{\mathbb{R}^2} |\nabla_\perp \mathcal{E}|^2 dx dy \rightarrow +\infty$ (see Fig. 2.3.1). Using the constancy of H and the Sobolev inequality $\iint_{\mathbb{R}^2} |\mathcal{E}|^4 dx dy < 2(P_{\text{in}}/P_{\text{cr}}) \iint_{\mathbb{R}^2} |\nabla_\perp \mathcal{E}|^2 dx dy$, a necessary condition for collapse is that P_{in} exceeds a critical value [33]. Expressed in physical units, this critical power for self-focusing reads as

$$P_{\text{cr}} = \frac{3.72 \lambda_0^2}{8\pi n_0 n_2}. \quad (2.3.8)$$

Therefore, when the laser input power is larger than the critical power, the laser beam

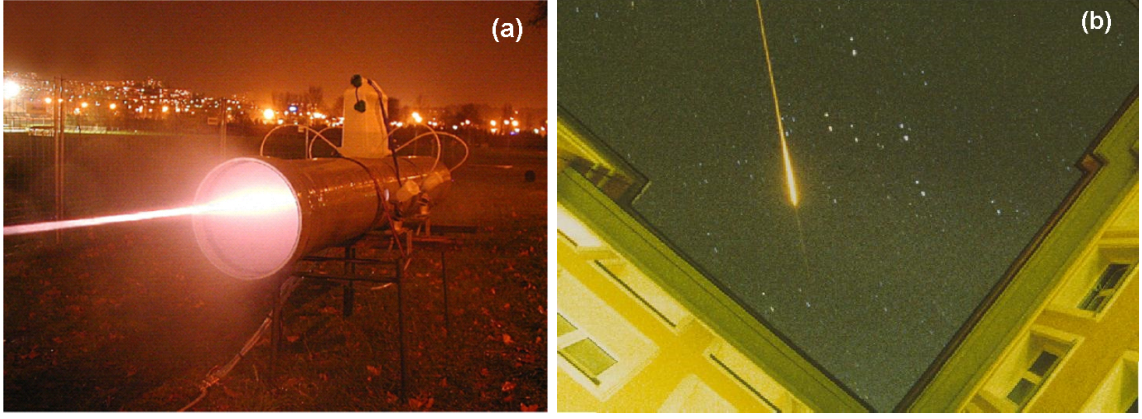


Figure 2.3.2: (a) Remote detection of biological aerosols. The tube in the centre of the picture is an open cloud chamber generating a bioaerosol simulant. The laser beam arrives from the left and spans a filamentary beam extending over 10 m. Source: Bergé *et al.* [14]. (b) Photograph of a self-guided filament induced in air by a high-power, infrared (800 nm) laser pulse. Source: www.teramobile.org.

can self-focus. This process leads to the singular increase of the beam intensity. This intensity diverges near the so-called “collapse point” or “nonlinear focus”, until plasma generation comes into play through photoionization, where $\partial_t J \propto N_e \mathcal{E}$ and $\partial_t N_e = \sigma_K I^K$ in the MPI regime [Eq. (2.2.19)]. The latter mechanism stops the self-focusing process. So a laser pulse can propagate over long distances through one or several *filaments* along successive cycles of Kerr-focusing and plasma defocusing. For example, Fig. 2.3.2 show two pictures of laser filaments clamped at moderate intensities (10^{13} - 10^{14} W cm⁻²).

2.3.2 Plasma waves

Whereas laser filamentation involves moderate intensities, other nonlinear mechanisms can occur at higher intensities and supply potential THz emitters. These are plasma waves. A plasma channel of volume V that is created due to laser interaction is neutral and verifies:

$$\iiint_V N_e(t, x, y, z) dx dy dz = \iiint_V \sum_s \sum_j N_{j,s}(t, x, y, z) dx dy dz. \quad (2.3.9)$$

The propagation of the driver pulse is strongly influenced by this plasma channel as schematically illustrated in Fig. 2.3.3 [44, 152, 153, 154]. In a nonrelativistic situation, for a highly ionized plasma ($Z^* \geq 1$) where the fluid approach holds, the current density is

described by Eq. (2.1.53), rewritten as

$$(\partial_t + \nu_c)(\gamma \mathbf{J}) = \varepsilon_0 \omega_p^2 \mathbf{E} + \mathbf{\Pi}, \quad (2.3.10)$$

where ω_p denotes the characteristic plasma frequency

$$\omega_p = \sqrt{\frac{e^2 N_e}{m_e \varepsilon_0}}. \quad (2.3.11)$$

The laser pulse propagates through the plasma only if $\omega > \omega_p$, since the refractive index of a plasma is

$$\hat{n}_p(\omega) = \sqrt{1 - \frac{\omega_p^2}{\omega^2}}. \quad (2.3.12)$$

Equation (2.3.12) is derived from Eqs. (2.1.56) and (2.1.58) by neglecting transverse diffraction ($\partial_x = \partial_y = 0$), collisions ($\nu_c = 0$), medium dispersion ($\varepsilon_r = 1$ and $\mathbf{P}_{\text{NL}} = \mathbf{0}$) and losses ($\mathbf{J}_{\text{loss}} = \mathbf{0}$):

$$c^2 \partial_z^2 E - \partial_t^2 E = \omega_p^2 E. \quad (2.3.13)$$

If the linear mode $E = a_0 \cos(kz - \omega t)$ is substituted into Eq. (2.3.13), the following dispersion relation is obtained:

$$-c^2 k^2 + \omega^2 = \omega_p^2, \quad (2.3.14)$$

which leads to Eq. (2.3.12) knowing that $k = \hat{n}_p(\omega)\omega/c$ [Eq. (2.1.62)]. The critical density $N_{e,c}$ is defined as the density for which the plasma frequency given by Eq. (2.3.11) equals ω_0 . In this manuscript the plasma will always be underdense ($N_e < N_{e,c}$) and thus transparent for the laser field.

In Eq. (2.3.10), the source $\mathbf{\Pi}$ encompasses the convective terms and the Lorentz force:

$$\mathbf{\Pi} = \frac{(\nabla \cdot \mathbf{J})}{eN_e} \gamma \mathbf{J} + (\mathbf{J} \cdot \nabla) \left(\frac{\gamma \mathbf{J}}{eN_e} \right) - \underbrace{\frac{e}{m_e} \mathbf{J} \times \mathbf{B}}_{\text{Lorentz force}}, \quad (2.3.15)$$

The source $\mathbf{\Pi}$ can be decomposed [9, 44] into the ponderomotive force—its longitudinal component proceeds from the Lorentz force and is proportional to the gradient of the intensity envelope, whereas its transverse components come from the quadratic terms in \mathbf{J} —and the radiation pressure force—related to the collision rate ν_c —, as exploited in Section 2.4.4 for a one-dimensional geometry.

The laser pulse is assumed to be linearly polarized in the transverse xy plane and it propagates along the z axis. After easy manipulations, Eq. (2.3.10) can be decomposed into longitudinal [$\mathbf{J}_{\parallel} = (0, 0, J_z)$] and transverse [$\mathbf{J}_{\perp} = (J_x, J_y, 0)$] components as follows:

$$(\partial_t + \nu_c)(\gamma \mathbf{J}_{\parallel}) = \varepsilon_0 \omega_p^2 \mathbf{E}_{\parallel} + \mathbf{\Pi}_{\parallel}, \quad (2.3.16)$$

$$(\partial_t + \nu_c)(\gamma \mathbf{J}_{\perp}) = \varepsilon_0 \omega_p^2 \mathbf{E}_{\perp} + \mathbf{\Pi}_{\perp}, \quad (2.3.17)$$

where the driving forces are given by

$$\mathbf{\Pi}_{\parallel} = \frac{(\nabla \cdot \mathbf{J})}{eN_e} \gamma \mathbf{J}_{\parallel} + (\mathbf{J} \cdot \nabla) \left(\frac{\gamma \mathbf{J}_{\parallel}}{eN_e} \right) - \frac{e}{m_e} \mathbf{J}_{\perp} \times \mathbf{B}_{\perp}, \quad (2.3.18)$$

$$\mathbf{\Pi}_{\perp} = \frac{(\nabla \cdot \mathbf{J})}{eN_e} \gamma \mathbf{J}_{\perp} + (\mathbf{J} \cdot \nabla) \left(\frac{\gamma \mathbf{J}_{\perp}}{eN_e} \right) - \frac{e}{m_e} (\mathbf{J}_{\perp} \times \mathbf{B}_{\parallel} + \mathbf{J}_{\parallel} \times \mathbf{B}_{\perp}). \quad (2.3.19)$$

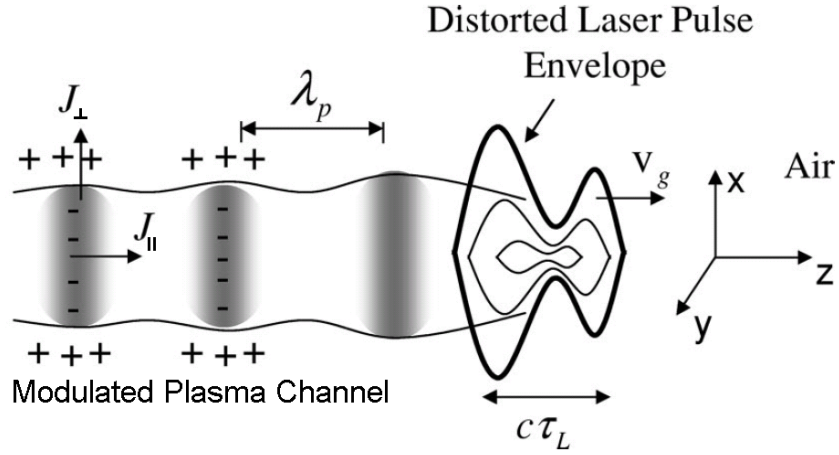


Figure 2.3.3: Schematic diagram of the plasma channel created by the propagation of the laser pulse. The ponderomotive forces associated with the laser pulse envelope drive the transverse and axial currents, \mathbf{J}_{\perp} and \mathbf{J}_{\parallel} , respectively. Source: Sprangle *et al.* [154].

Following Sprangle *et al.* [152, 154], electrons are ionized during the first cycles of the laser pulse, i.e., the head of the laser pulse where transverse fields dominate. The laser field drags the electrons from their equilibrium position through the longitudinal Lorentz force induced by the transverse fields $\mathbf{\Pi}_{\parallel} \sim -em_e^{-1} \mathbf{J}_{\perp} \times \mathbf{B}_{\perp}$ in the beam head. This displacement of charges induces a longitudinal electrostatic field, \mathbf{E}_{\parallel} , to which electrons are subject because they are attracted by ions. Ionized electrons under this longitudinal field end up by oscillating around their corresponding ions, at the frequency $\sim \omega_p / \sqrt{\gamma}$ according to Eq. (2.3.16), creating plasma waves in the wake of the laser pulse (“plasma wakefield”). This plasma frequency—more precisely $\nu_p = \omega_p (2\pi)^{-1}$ —takes typical values between 2.8 and 9.0 THz for densities between 10^{17} and 10^{18} cm^{-3} . Thus it lies in

the THz bandwidth. These longitudinal plasma waves, which are almost sinusoidal at nonrelativistic intensities [Fig. 2.3.4(a)] and whose amplitude grows with the intensity, become nonlinear at relativistic intensities, enhancing high-order harmonics of ω_p ($2\omega_p$, $3\omega_p$, etc.) in the spectrum of the wakefield. In intensity regimes above 10^{18} W cm $^{-2}$, the electron density develops sharp peaks above the equilibrium density [Fig. 2.3.4(b)], which is a consequence of the accumulation of electrons whose velocity becomes close to the phase velocity of the laser pulse ($\approx c$).

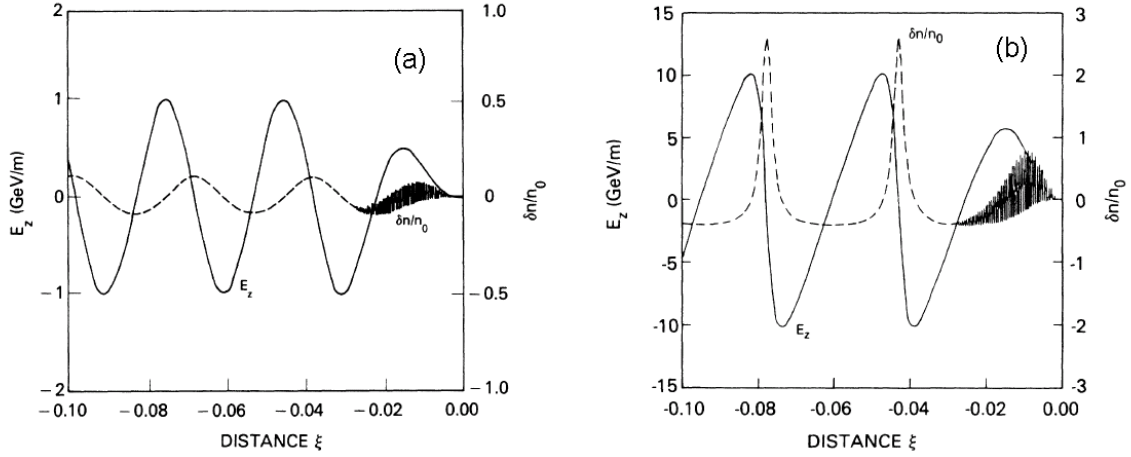


Figure 2.3.4: Longitudinal electric field E_z (solid curve) and electron density variation $\delta n/n_0 = N_e/(Z^*N_a) - 1$ (dashed curve) as a function of the laser-comoving distance $\xi = (z - ct)/\lambda_0$ at a vector potential of (a) $A_L = 0.5 m_e c/e$ and (b) $A_L = 2 m_e c/e$. Source: Sprangle *et al.* [152].

Equation (2.3.17) indicates that transverse plasma waves, perpendicular to the polarization direction of the laser pulse, can also be created from $\mathbf{\Pi}_\perp$. This will be discussed in Section 5.2.

2.4 Laser-based terahertz emitters

In this section, the main mechanisms yielding terahertz radiation in laser-driven sources are presented, supported by two simplified models. The idea is to show how an ultrashort infrared laser pulse (λ_0 of order of $1 \mu\text{m}$) radiates components in the terahertz spectrum (from 0.1 to 100 THz) due to the nonlinearities of the medium, namely, the Kerr effect, the photoionization and the plasma waves associated to ponderomotive and radiative forces. As the THz spectrum concerns frequencies whose typical values are at least two orders of magnitude lower than the laser frequency ω_0 , the limit $\omega/\omega_0 \rightarrow 0$ is considered here as representative of the *terahertz* domain.

2.4.1 The Four-wave mixing mechanism: Kerr effect

Optical rectification via the four-wave mixing mechanism was the first explanation given by Cook and Hochstrasser in [37] to explain terahertz generation measured in experiments, using two-colour laser pulses in gases.

With two colours, the third-order nonlinear polarization given by Eq. (2.1.22) develops direct-current (DC) components in the electric field by addition and subtraction of frequencies, the latter down-conversion process contributing to the THz (i.e., low-frequency) spectrum. The existence of such signature is made possible by using femtosecond pulses having broad bandwidths. Let us consider the following two-colour laser plane wave:

$$E(t) = a_0 \left[\sqrt{1-r} \cos(\omega_0 t) + \sqrt{r} \cos(2\omega_0 t + \phi) \right], \quad (2.4.1)$$

where r and ϕ are the intensity ratio and relative phase between the second harmonic and the fundamental, respectively. After trigonometric manipulations, the electric field [Eq. (2.4.1)] substituted into Eq. (2.1.22) yields the following nonlinear polarization with a component coming from *frequency mixing*:

$$P_{\text{NL}}(t) = \frac{3}{4} \varepsilon_0 \chi^{(3)} a_0^3 \sqrt{r} (1-r) \cos \phi + \dots, \quad (2.4.2)$$

where \dots refers to the fundamental and high-order harmonics: ω_0 , $2\omega_0$, $3\omega_0$ and so on. This DC component reflects the possibility to generate low-frequency radiation using Kerr sources. It is maximal at $\phi = 0$ and zero with $\phi = \pi/2$. From the viewpoint of the intensity ratio, it is maximal at $r = 1/3$ and zero with one colour ($r = 0$ and $r = 1$).

From Helmholtz equation [Eq. (2.1.58)], we can anticipate that the radiated field $\tilde{E}(t)$

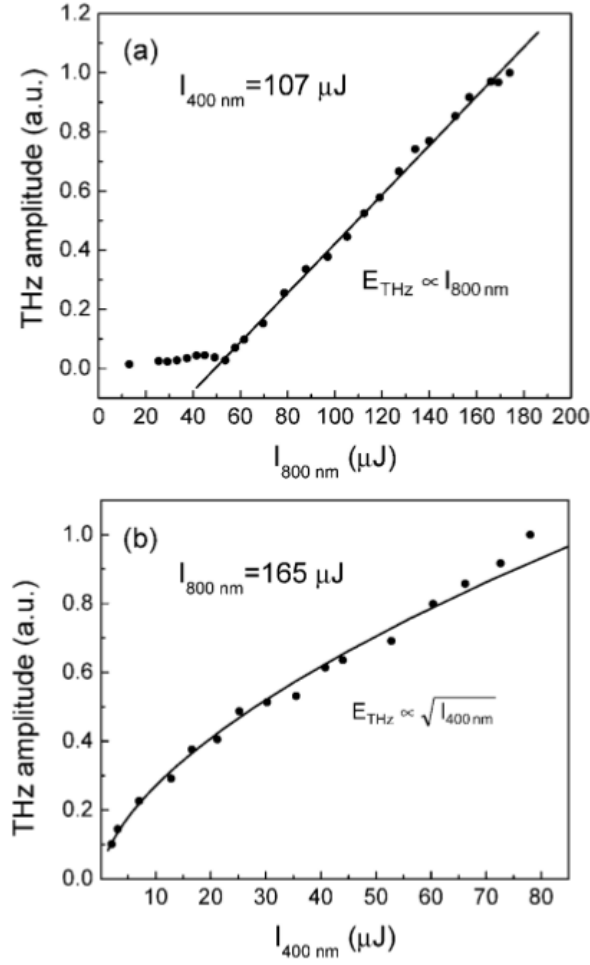


Figure 2.4.1: Experimental verification of the dependence of THz amplitude generated by a 800+400-nm laser beam on (a) the intensity of the fundamental harmonic and (b) the square root of the second harmonic intensity. The solid curves are linear fit and square-root fit, respectively. Once the plasma is created, the THz wave signal follows Eq. (2.4.4). Source: Xie *et al.* [181].

is *locally* proportional to $\partial_t^2 P_{\text{NL}}(t)$, i.e.,

$$\hat{E}(\omega) \propto -\omega^2 \hat{P}_{\text{NL}}(\omega). \quad (2.4.3)$$

Therefore, the DC component of Eq. (2.4.2) is translated into a *parabolic* signature of the Kerr effect on the THz spectrum:

$$\hat{E}(\omega) \propto \omega^2 \frac{3}{4} \varepsilon_0 \chi^{(3)} a_0^3 \sqrt{r} (1-r) \cos \phi \propto \omega^2 \chi^{(3)} I_{\omega_0} \sqrt{I_{2\omega_0}} \cos \phi, \quad (2.4.4)$$

where $I_{\omega_0} \propto a_0^2 (1-r)$ is the mean intensity of the fundamental pulse and $I_{2\omega_0} \propto a_0^2 r$ is the mean intensity of the second harmonic. This formula was first validated experimentally

by Cook and Hochstrasser, and later by Xie *et al.* [181] as recalled by Fig. 2.4.1.

Recent experiments conducted by Andreeva *et al.* in air [4] showed that this Kerr signature is actually present in the THz spectrum at filament intensities in air, which contributes to broaden the pump and second harmonic spectra along propagation through self-phase modulation and constructively interfere with the plasma-driven THz radiation (see Section 4.1). Nevertheless, this signature, which is related to bound electrons and is beyond the plasma frequency, is small compared with the signature of the photocurrents and plasma effects, the response of free electrons. It is thus a secondary mechanism, expected to emit on-axis mostly at low intensities prior to gas ionization.

2.4.2 The local current model and the photocurrent mechanism

Few years after Cook and Hochstrasser, Kim *et al.* understood in Refs. [89, 90] that the so-called *photocurrent mechanism*, i.e., the effect of the free-electron current, is the dominant mechanism for two-colour laser pulses ionizing a gas. This was explicitly shown by Li *et al.* in Ref. [108], who recorded the THz yield as a function of the two-colour phase difference.

The *local current* (LC) model, proposed by Babushkin *et al.* [8] and later improved by González de Alaiza Martínez *et al.* [67], is a zero-dimensional (0D) model that explains how terahertz radiation is produced from photocurrents, i.e., the electron currents induced by photoionization. This simple model explains why two-colour laser pulses produce impressive terahertz fields, while single-colour ones cannot reach similar conversion efficiencies, as experimentally observed by Kim and his collaborators.

The 0D model is constructed on the *local current limit* hypothesis, which claims that locally, in an infinitesimal volume of plasma, the radiated electric field, \tilde{E} , is proportional to the time derivative of the electron current, J :

$$\tilde{E}(t) = g\partial_t J(t), \quad (2.4.5)$$

where g is a geometrical factor [8]. Equation (2.4.5) was proposed as a mere hypothesis, sustained anyway from the Jefimenko's equations (see Jefimenko [80], and Dushek and Kuzmin [55]), where the electric field radiated by accelerated charges depends, amongst other variables, on the time derivative of the current and the geometry between the point where the field is measured and the point where the charge is placed. From these equations the geometrical factor was early evaluated as

$$g = -\frac{1}{4\pi\epsilon_0 c^2} \frac{\Delta V}{d}, \quad (2.4.6)$$

where ΔV is the volume of the plasma spot and d is the distance at which the radiated field is measured. Since the ratio $\Delta V/d$ is actually unknown due to the 0D geometry assumption, the LC model is not able to estimate *quantitatively* the accurate amplitude of the terahertz field.

Originally, the model was developed for weakly ionized gases in tunneling regime ($\sim 10^{13}$ W cm $^{-2}$) using the QST ionization rate [Eq. (2.2.28)] for hydrogen-like gases. Nevertheless, because the photoionization mechanism may also play a crucial role even at relativistic intensities for which multiple ionization events take place, an improved formulation is necessary (see Sections 3.4, 5.1 and 5.2). For the sake of simplicity, only the LC model for a hydrogen-like atom ionized through the QST rate will be presented here in detail. The extension to a complex atom ionized at high intensities is straightforward as the superposition principle holds for each atomic shell.

To evaluate the electron current, the first step is to calculate the QST ionization rate for a given laser field $E(t)$, which, by hypothesis, does not have DC components [i.e., $\int_{-\infty}^{+\infty} E(t) dt = 0$]. As shown in Fig. 2.4.2, ionization occurs at the neighbourhood of the extrema of the electric field, which hereinafter will be referred as *ionization events* and labelled as $\{t_n\}$. Near each of these ionization events, the absolute value of the electric field is approximated through a second-degree Taylor series:

$$|E(t)| \approx |E(t_n)| - \frac{1}{2} |\ddot{E}(t_n)| (t - t_n)^2, \quad (2.4.7)$$

where $\ddot{E}(t) = \partial_t^2 E(t)$.

The QST ionization rate, according to Eq. (2.2.28), is expressed as

$$W[E(t)] = \frac{\alpha}{|E(t)|} \exp\left(-\frac{\beta}{|E(t)|}\right), \quad (2.4.8)$$

where $\alpha = 4(2U_i U_{\text{au}}^{-1})^{5/2} \nu_{\text{au}} E_{\text{au}}$ and $\beta = 2E_{\text{au}}(2U_i U_{\text{au}}^{-1})^{3/2}/3$, U_i being the ionization potential of an hydrogen-like atom. Assuming $|E(t)| \ll \beta$, which holds as long as atoms are not fully ionized, the ionization rate (see grey curves in Fig. 2.4.2) can be approximated via a Gaussian profile in the vicinity of each instant $t = t_n$ as

$$W_n(t) \approx W(|E(t_n)|) \exp\left[-\left(\frac{t - t_n}{\tau_n}\right)^2\right], \quad (2.4.9)$$

where τ_n is the characteristic duration of the n th ionization event given by

$$\tau_n = \sqrt{\frac{2|E(t_n)|^2}{\beta|\ddot{E}(t_n)|}}. \quad (2.4.10)$$

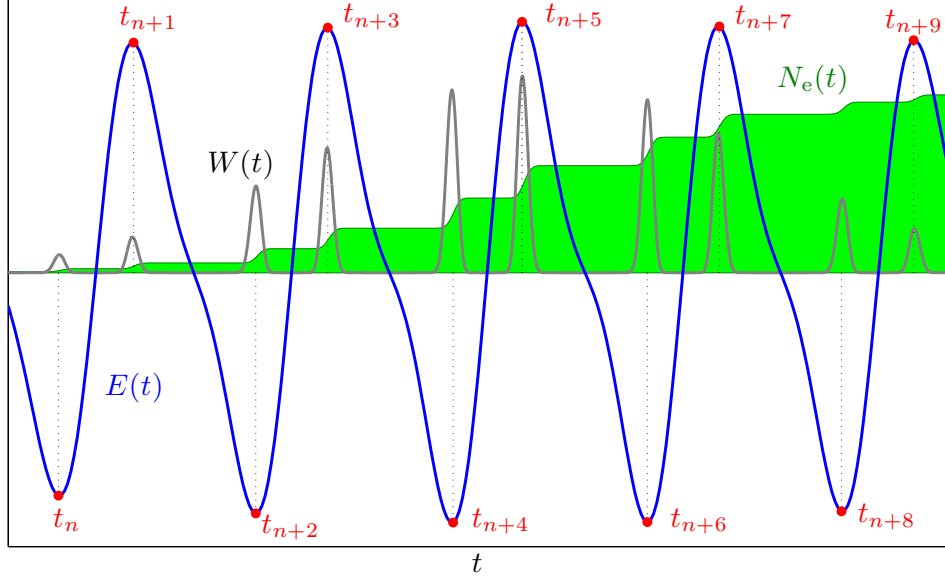


Figure 2.4.2: LC model: electric field [$E(t)$, blue curve], ionization rate [$W(t)$, grey curve] and electron density [$N_e(t)$, green curve with filled area beneath].

Equation (2.4.9) is obtained from the Taylor expansion of Eq. (2.4.8) using Eq. (2.4.7) [8]. By virtue of the superposition principle, the ionization rate is finally

$$W(t) \approx \sum_n W_n(t) = \sum_n W(|E(t_n)|) \exp \left[- \left(\frac{t - t_n}{\tau_n} \right)^2 \right]. \quad (2.4.11)$$

The second step is to calculate the electron density given by Eq. (2.2.8) and whose integral is easily approximated with Eq. (2.4.11):

$$\int_{-\infty}^t W(\tau) d\tau = \sum_n \left[\sqrt{\pi} \tau_n W(|E(t_n)|) H_n(t - t_n) \right]. \quad (2.4.12)$$

Here $H_n(t)$ is the step-like function

$$H_n(t - t_n) = \frac{1}{2} \left[1 + \operatorname{erf} \left(\frac{t - t_n}{\tau_n} \right) \right], \quad (2.4.13)$$

which tends to the Heaviside step function $\Theta(t)$ when $\tau_n \rightarrow 0$:

$$\lim_{\tau_n \rightarrow 0} H_n(t - t_n) = \Theta(t) = \begin{cases} 1, & \text{if } t \geq 0, \\ 0, & \text{otherwise.} \end{cases} \quad (2.4.14)$$

By treating the functions $H_n(t)$ as Heaviside step functions to approximate the expo-

nential of Eq. (2.4.12) in Eq. (2.2.8), a recurrence reasoning gives the following step-like growth of the electron density (see filled green curve in Fig. 2.4.2):

$$N_e(t) \approx \sum_n \delta N_e^n H_n(t - t_n), \quad (2.4.15)$$

where δN_e^n are the *density steps* at ionization events given by [67]:

$$\delta N_e^n = N_a \epsilon_n \left[1 - \exp \left(-\sqrt{\pi} \tau_n W(|E(t_n)|) \right) \right], \quad (2.4.16)$$

$$\epsilon_n = \begin{cases} 1, & \text{if } n = 1, \\ \exp \left[-\sqrt{\pi} \sum_{j=1}^{n-1} W(|E(t_j)|) \tau_j \right], & \text{otherwise.} \end{cases} \quad (2.4.17)$$

Finally, the current is calculated from the scalar version of Eq. (2.1.56). After plugging Eq. (2.4.15) into Eq. (2.1.56), the following two components of the electron current are obtained:

$$J(t) \approx J_A(t) + J_B(t), \quad (2.4.18)$$

$$J_A(t) = -e v_f(t) N_e(t), \quad (2.4.19)$$

$$J_B(t) = -e \sum_n v_f(t_n) \delta N_e^n \exp \left(-\frac{t - t_n}{\tau_n} \right) H_n(t - t_n). \quad (2.4.20)$$

Here $v_f(t)$ is the velocity of the free electrons ionized at $t \rightarrow -\infty$:

$$v_f(t) = -\frac{e}{m_e} \exp(-\nu_c t) \int_{-\infty}^t E(\tau) \exp(\nu_c \tau) d\tau, \quad (2.4.21)$$

where the initial condition $v_f(t \rightarrow -\infty) = 0$ holds. These free electrons oscillate around their equilibrium position, $r_f(t \rightarrow -\infty) = 0$. Their position is given by the integral of Eq. (2.4.21), when discarding the effect of the pulse envelopes⁵:

$$r_f(t) = \int_{-\infty}^t v_f(\tau) d\tau \sim \frac{e}{m_e} \sum_k \frac{E_k(t)}{\omega_k^2}, \quad (2.4.22)$$

where $E(t) = \sum_k E_k(t)$ is the Fourier series of the electric field, $\omega_k = k\omega_0$ being the frequency of the k -th harmonic, $E_k(t)$.

⁵Note that the assumption of $\int_{-\infty}^{+\infty} E(t) dt = 0$ implies that also $\int_{-\infty}^{+\infty} v_f(t) dt = \int_{-\infty}^{+\infty} r_f(t) dt = 0$, which means that the phase space of the free electrons, $(r_f, v_f(r_f))$, must be closed spirals that reflect their

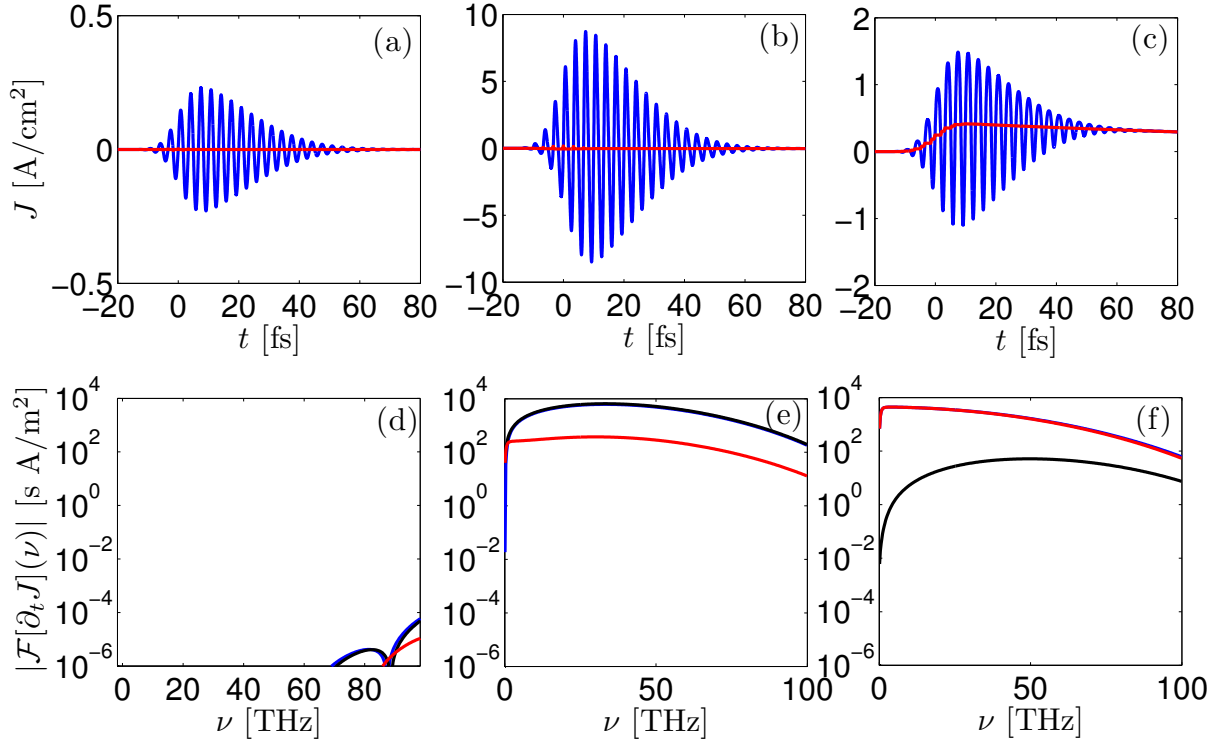


Figure 2.4.3: Comparison of $J(t)$ [Eq. (2.4.18), blue curves], $J_B(t)$ [Eq. (2.4.20), red curves] and $J_A(t)$ [Eq. (2.4.19), black curves, only shown in spectra], calculated in argon with $1/\nu_c = 200$ fs and a $1\text{-}\mu\text{m}$ Gaussian laser pulse. (a) Single-colour laser field of 35 fs-FWHM and $5 \times 10^{13} \text{ W cm}^{-2}$. (d) Corresponding spectra. Note that there are almost no components in the THz band. (b) Two-colour laser pulse of 35 fs-FWHM (both harmonics), $5 \times 10^{13} \text{ W cm}^{-2}$ (10% of intensity in the second harmonic) and 0 phaseshift. (e) Corresponding spectra. (c) Two-colour laser pulse of 35 fs-FWHM (both harmonics), $5 \times 10^{13} \text{ W cm}^{-2}$ (10% of the intensity in the second harmonic) and $\pi/2$ phaseshift. (f) Corresponding spectra.

The current $J_A(t)$ is the *fast* component of $J(t)$ and mostly covers the high-harmonic generation due to plasma effects (see Brunel [25]). However, this current component can also have an impact on the terahertz band of the spectrum. The current $J_B(t)$, instead, is the *slow* component of $J(t)$ and its influence reduces to the terahertz band of the spectrum. Figure 2.4.3 plots in time $J(t)$, $J_A(t)$ and $J_B(t)$ and their corresponding time derivatives in Fourier space for three different situations, anticipating that the impact on the THz band of $J_A(t)$ and $J_B(t)$ strongly depends on the laser configuration. Figures 2.4.3(a,d) display evidence that single-colour laser fields are likely to yield almost no THz radiation by either $J_A(t)$ or $J_B(t)$. For two-colour pulses, the phaseshift between the fundamental and the second harmonic determines how strongly $J_A(t)$ and $J_B(t)$ build the THz band of conservative oscillatory motion around the equilibrium position $r_f(t \rightarrow -\infty) = 0$ and $v_f(t \rightarrow -\infty) = 0$.

the spectrum: $J_A(t)$ seems to dominate over $J_B(t)$ when the two colours are in phase [see Fig. 2.4.3(b,e)], whereas THz generation due to $J_B(t)$ clearly overshadows $J_A(t)$ when the phaseshift is equal to $\pi/2$ [see Fig. 2.4.3(c,f)].

To understand how terahertz radiation is produced from both $J_A(t)$ and $J_B(t)$, the Fourier transforms of their time derivatives are analyzed. These are approximated in the low-frequency domain as [67]

$$\mathcal{F}[\partial_t J_A](\omega) \approx -\frac{e}{\sqrt{2\pi}} i\omega \sum_n \delta N_e^n r_f(t_n), \quad (2.4.23)$$

$$\mathcal{F}[\partial_t J_B](\omega) \approx \frac{e}{\sqrt{2\pi}} \frac{\omega}{(i\nu_c + \omega)} \sum_n \delta N_e^n v_f(t_n) \exp(it_n\omega). \quad (2.4.24)$$

On the one hand, the amplitude of the THz field due to $J_A(t)$ is proportional to the sum over all ionization events of the products $\delta N_e^n r_f(t_n)$, i.e., the density steps multiplied by the positions of the free electrons. On the other hand, through $J_B(t)$ each ionization event contributes in the limit $\omega \rightarrow 0$ with a cosine-like wave $\sim \delta N_e^n v_f(t_n) \cos(t_n\omega)$ because $\lim_{\omega \rightarrow 0} \exp(it_n\omega) \sim \cos(t_n\omega) \sim 1$. Therefore, the interference is governed by the density steps, δN_e^n , being always non-negative and closely related to the laser intensity and duration, and the phase space of the free electrons, $(r_f(t_n), v_f(t_n))$. This phase space contains all the information on the shape of the laser electric field and determines if these interferences are constructive or destructive, conforming to whether the positions and velocities at ionization events are sign-definite or not.

To explain the previous statement we again make use of the two-colour plane wave (2.4.1). Ignoring the collisions for simplicity, this electric field gives the following phase space according to Eqs. (2.4.21) and (2.4.22):

$$v_f(t) = -\frac{e}{m_e} a_0 \left[\frac{\sqrt{1-r}}{\omega_0} \sin(\omega_0 t) + \frac{\sqrt{r}}{2\omega_0} \sin(2\omega_0 t + \phi) \right], \quad (2.4.25)$$

$$r_f(t) = \frac{e}{m_e} a_0 \left[\frac{\sqrt{1-r}}{\omega_0^2} \cos(\omega_0 t) + \frac{\sqrt{r}}{4\omega_0^2} \cos(2\omega_0 t + \phi) \right]. \quad (2.4.26)$$

For the particular case of a 1- μm laser pulse with $5 \times 10^{13} \text{ W cm}^{-2}$ intensity, the phase spaces given by Eqs. (2.4.25) and (2.4.26) are represented in Fig. 2.4.4 for four different laser configurations: (a) $r = 0$ (single-colour laser pulse), (b) $r = 0.1$ and $\phi = 0$, (c) $r = 0.1$ and $\phi = \pi/4$, and (d) $r = 0.1$ and $\phi = \pi/2$. In Fig. 2.4.4 the dots correspond to the maxima (black) and minima (red) of the laser electric field. The strongest extrema are signalled by squared. Since in the limit $r \rightarrow 0$ the ionization events of Eq. (2.4.1) are

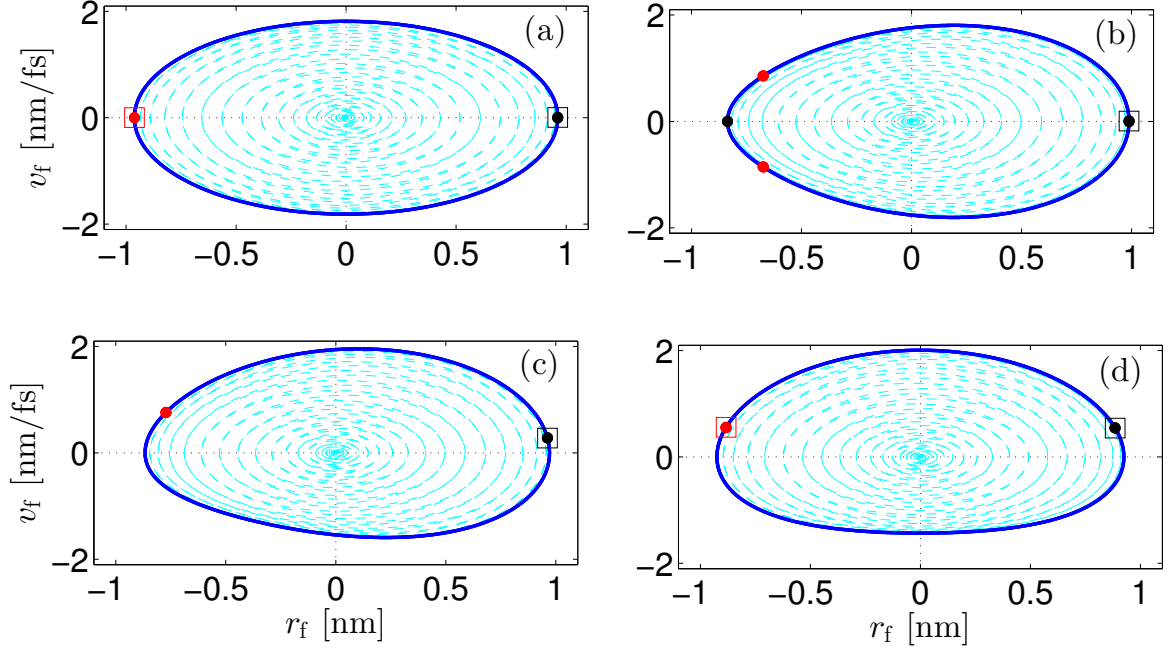


Figure 2.4.4: Phase spaces given by Eqs. (2.4.25) and (2.4.26) for a 1- μm laser pulse with $5 \times 10^{13} \text{ W cm}^{-2}$ intensity [Eq. (2.4.1)]. (a) $r = 0$ (single-colour laser pulse). (b) $r = 0.1$ and $\phi = 0$. (c) $r = 0.1$ and $\phi = \pi/4$. (d) $r = 0.1$ and $\phi = \pi/2$. The points of the phase space corresponding to the maxima (black dots) and minima (red dots) of the electric field are also depicted. The strongest extrema are signalled by squares. The phase spaces for a 35-fs-FWHM Gaussian envelope are plotted by cyan dashed curves.

given by:

$$\omega_0 t_n \approx n\pi - 2(-1)^n \sqrt{\frac{r}{1-r}} \sin \phi, \quad (2.4.27)$$

one finds that $v_f(t_n) \sim \sin \phi$ and $r_f(t_n) \sim \cos \phi$ [7, 8]. These phase spaces thus allow us to discuss qualitatively how the ionization events interfere between each other:

- Figure 2.4.4(a). This phase space justifies why single-colour laser pulse *a priori* do not yield THz radiation, as already seen in Fig. 2.4.3(d). On the one hand, there is no interference due to $J_B(t)$ because $v_f(t_n) = 0$. On the other hand, as the phase space is completely symmetrical, the interference due to $J_A(t)$ is destructive and the contribution of the maxima and minima cancel exactly one another.
- Figure 2.4.4(b). This phase space, symmetric with respect to the r_f -axis, explains why, with a two-colour in-phase laser field, THz generation is dominated by $J_A(t)$, as shown in Fig. 2.4.3(e). On the one hand, the maxima of $J_B(t)$ do not contribute

to the THz [$v_f(t_n) = 0$] and its minima cancel exactly each other. On the other hand, from $J_A(t)$, the contribution of the laser extrema on the r_f -axis do not cancel out, resulting in a net THz yield.

- Figure 2.4.4(c). This asymmetric phase space is close to (d), evidencing that the contribution to the THz band from $J_B(t)$ is the most relevant one.
- Figure 2.4.4(d). This phase space, symmetric with respect to the v_f -axis, shows that $J_B(t)$ prevails over $J_A(t)$, as seen in Fig. 2.4.3(f). On the one hand, $v_f(t_n) \sim \sin \phi$ is sign-definite and therefore the interference due to $J_B(t)$ is constructive. On the other hand, with respect to $J_A(t)$, the contributions from r_f exactly cancel out and thus no net THz yield is expected from $J_A(t)$.

The conclusion based on the above plane wave approximation is that, in order to produce a net THz pulse, an *asymmetric* arrangement of the extrema of the laser pulse in the phase space is necessary, making that current contributions do not cancel each other or are sign-definite.

Of course, the pulse envelope affects the phase space, as shown in Fig. 2.4.4 (see cyan dashed curves). First, the values of the extrema and thus the corresponding density steps are modified. In addition, the location of the extrema in the phase space and the phase space itself are perturbed. Hence, the nature of the previous *ideal* interference patterns can be altered substantially. For example, a completely symmetric situation becomes also asymmetric in terms of δN_e^n and produces a net THz pulse. This is the case of single-colour laser fields, which do yield THz radiation at high intensities with short pulse duration, coming from the envelope contribution in $J_A(t)$.

The phase space reveals only *qualitatively* if a laser configuration better promotes terahertz generation from $J_A(t)$ and/or $J_B(t)$. To compare *quantitatively* two laser configurations, it is necessary to estimate the value of g introduced in Eq. (2.4.5). The most reasonable assumption, without accounting for propagation effects, is that the radiated field has the same energy than the laser pulse, namely

$$g = -\sqrt{\frac{\int_{-\infty}^{+\infty} |E(t)|^2 dt}{\int_{-\infty}^{+\infty} |\partial_t J(t)|^2 dt}}, \quad (2.4.28)$$

where the sign $-$ follows from Eq. (2.4.6). Neglecting collisions, the derivative of the current is $\partial_t J(t) = e^2 m_e^{-1} N_e(t) E(t)$ according to the scalar version of Eq. (2.1.56). The laser pulse is assumed centred at $t = 0$ and completely symmetric. Following Eq. (2.4.15), the electron density can be approximated via a Heaviside step function centred at $t = 0$: $N_e \approx Z^* N_a \Theta(t)$, where $Z^* = N_e(t \rightarrow +\infty)/N_a$ is the degree of ionization. Under these

approximations, the prefactor g of Eq. (2.4.28) is expressed as

$$g \approx - \sqrt{\frac{\int_{-\infty}^{+\infty} |E(t)|^2 dt}{\left(\frac{e^2}{m_e} Z^* N_a\right)^2 \int_0^{+\infty} |E(t)|^2 dt}} = - \frac{m_e \sqrt{2}}{e^2 Z^* N_a} \sim \frac{1}{Z^* N_a}. \quad (2.4.29)$$

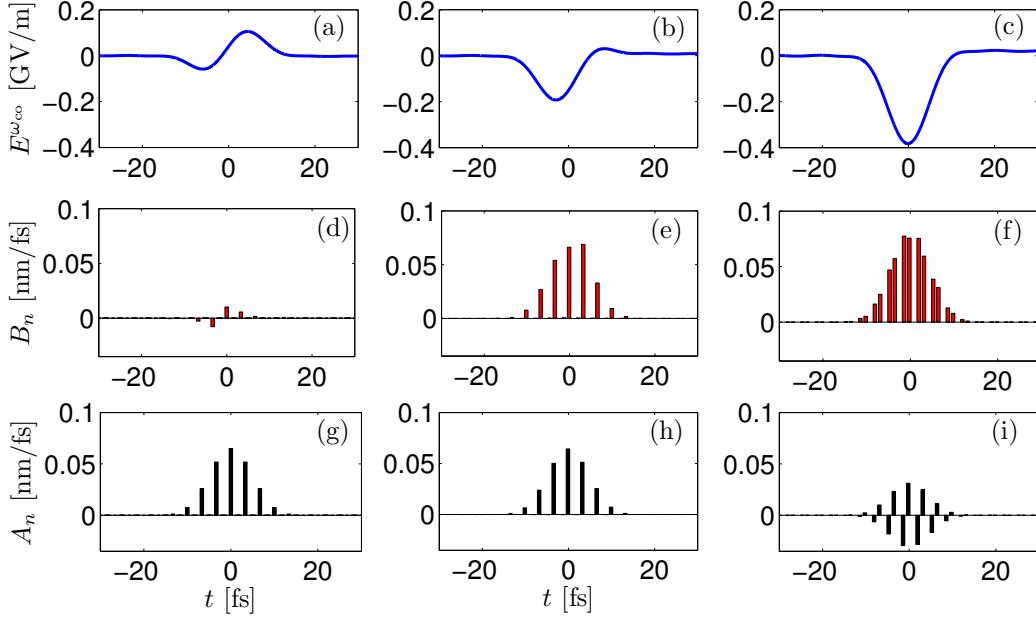


Figure 2.4.5: Terahertz field given by Eqs. (2.4.5) and (2.4.28) filtered at $\nu_{co} = 90$ THz calculated in argon ($N_a = 2.7 \times 10^{21} \text{ cm}^{-3}$, $\nu_c^{-1} = 200$ fs) and with a two-colour 1- μm 35-fs-FWHM laser pulse with $5 \times 10^{13} \text{ W cm}^{-2}$ of intensity (second harmonic: 10% of the intensity, same FWHM duration). The prefactor g has been estimated with Eq. (2.4.28). (a) $\phi = 0$. (b) $\phi = \pi/4$. (c) $\phi = \pi/2$. Contributions of the ionization events to $J_B(t)$, B_n . (d) $\phi = 0$. (e) $\phi = \pi/4$. (f) $\phi = \pi/2$. Contributions of the ionization events to $J_A(t)$, A_n . (g) $\phi = 0$. (h) $\phi = \pi/4$. (i) $\phi = \pi/2$.

Equation (2.4.29) indicates that the THz yield is inversely proportional to the degree of ionization, as confirmed in Section 3.4. Taking this fact into account, the contributions to the THz domain from $J_A(t)$ and $J_B(t)$ can be compared on equal terms via the following contributions of ionization events, homogeneous to a velocity:

$$A_n = C \frac{\delta N_e^n}{Z^* N_a} \omega_{co} r_f(t_n), \quad (2.4.30)$$

$$B_n = \frac{\delta N_e^n}{Z^* N_a} v_f(t_n), \quad (2.4.31)$$

where $C \approx 0.4362$ comes from the inverse Fourier transform of Eq. (2.4.23).

Figure 2.4.5(a,b,c) plot THz generation (filtered at $\nu_{\text{co}} = 90$ THz) predicted by the LC model for the configurations corresponding to Fig. 2.4.4(b,c,d) and a 35-fs-FWHM laser pulse. They confirm numerically that the case of $\phi = \pi/2$, the most favorable for $J_{\text{B}}(t)$ and with the greatest number of ionization events acting constructively to build the THz signal, yields the most intense and energetic THz pulse. The contributions B_n and A_n , displayed in Fig. 2.4.5(d,e,f) and Fig. 2.4.5(g,h,i), respectively, agree with the qualitative predictions of Fig. 2.4.4(b,c,d).

2.4.3 Electron-impact ionization

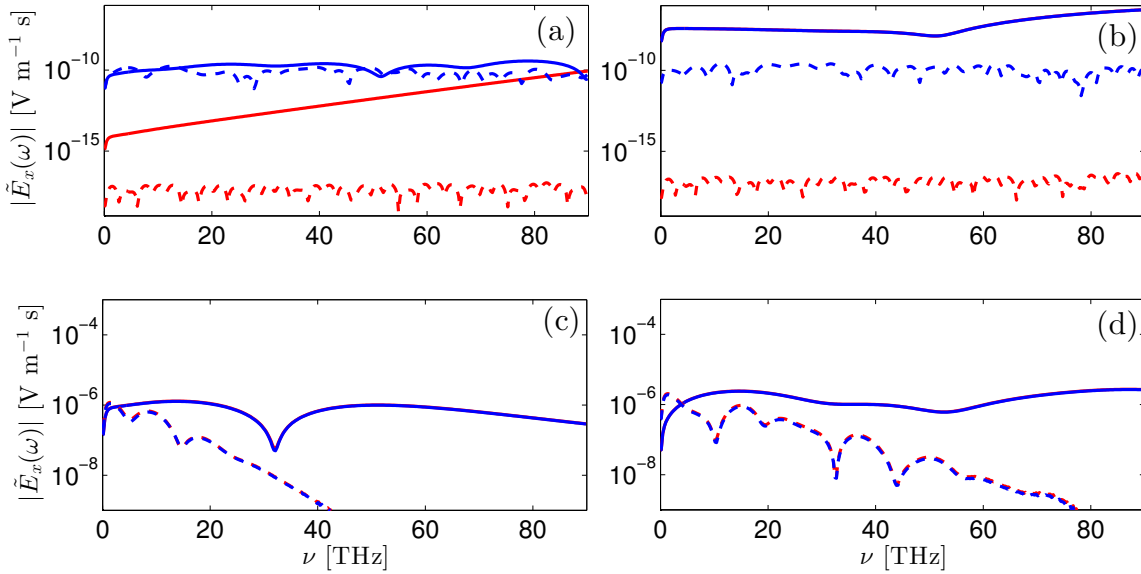


Figure 2.4.6: Comparison of the terahertz yield calculated from LC model [Eqs. (2.4.5) and (2.4.28)] in argon (at 1-bar pressure) without (red) and with (blue) collisional ionization. The collision rate is set to $\nu_{\text{c}}^{-1} = 190$ fs. Single-colour 1- μm laser pulse (50 fs in solid curves, 300 fs in dashed curves) at (a) $5 \times 10^{14} \text{ W cm}^{-2}$ and (c) $5 \times 10^{15} \text{ W cm}^{-2}$. Two-colour laser pulse (phaseshift: 0; second harmonic: 10% intensity and half duration; 50 fs in solid curves; 300 fs in dashed curves): (b) $5 \times 10^{14} \text{ W cm}^{-2}$ and (d) $5 \times 10^{15} \text{ W cm}^{-2}$. Both curves are superimposed.

Since the LC model predicts that photocurrents through tunnel ionization have a direct impact on the THz yield, electron-impact ionization [Section 2.2.3.2] may also contribute to the total THz yield, as it takes part of the ionization process. However, the non-sequential ionization rates such as EII are, at least, two or three orders of magnitude

smaller than the sequential tunnelling ionization rates (ADK, for example) and, therefore, their signatures on the THz spectrum should be very limited. This is numerically confirmed by comparing Eq. (2.2.33) with Eq. (2.2.49).

Figure 2.4.6(a,c) compare, for argon at 1-bar pressure ($N_a = 2.7 \times 10^{19} \text{ cm}^{-3}$), the terahertz yield obtained with one-colour pulses when using only ADK ionization rate and ADK plus EII ionization rates (see Table 2.4), calculated from the LC model [Eqs. (2.4.5) and (2.4.28)]. Two different FWHM durations are used, 50 fs and 300 fs (with two-colour pulses, the second harmonic has half duration); the latter produces less THz signal because the asymmetries in the pulse envelope are less important over long pulse durations. At low intensities, in both cases with ADK plus EII, at least five orders of magnitude stronger THz amplitudes are obtained, because with single-colour laser pulse at low intensities the photocurrent mechanism is not active. However, with 50-fs pulse duration, when photocurrents start to contribute, no significant difference exists between ADK and ADK plus EII. The difference of more than five orders of magnitude at low intensities is, however, not interesting, because the produced THz signal is too weak for applications. With a two-colour pulse, as depicted in Fig. 2.4.6(b,d), the photocurrent mechanism engaging photoionization is always dominant and no difference can be seen between ADK and ADK plus EII.

Thus, the present results signify that the role of impact ionization in laser-driven THz generation can be neglected in practice.

2.4.4 Longitudinal plasma wakefield

Last but not least, an efficient laser-to-THz converter can be a plasma wave. Assuming that the laser spot size is large compared to the plasma channel produced in laser-matter interaction, Sprangle *et al.* claimed in Ref. [154] that Eq. (2.3.16), evaluated on laser field, gives a good approximation of the amplitude of longitudinal electric fields induced inside the plasma. They constructed a nonrelativistic ($\gamma \approx 1$) model propagating over z -axis, discarding transverse ponderomotive sources. Assuming that the laser pulse is polarized along the x -axis, the electric and magnetic fields can be reduced in a simplified geometry to $\mathbf{E} = (E_x, 0, E_z)$ and $\mathbf{B} = (0, B_y, 0)$, and consequently $\mathbf{J} = (J_x, 0, J_z)$. Under these hypothesis, ignoring the Kerr term and for an optical refractive index equal to unity ($n_0 = 1$), Ampère's law [Eq. (2.1.4)] gives the following equation for E_z :

$$\partial_t E_z = -\frac{J_z}{\varepsilon_0}, \quad (2.4.32)$$

which, by multiplying by $(\partial_t + \nu_c)$ and substituting into Eq. (2.3.16), yields the longitudinal wave equation

$$\left(\partial_t^2 + \nu_c \partial_t + \omega_p^2\right) E_z = \Pi_z. \quad (2.4.33)$$

It is reasonable to approximate the driving source term on the laser field, $\mathbf{\Pi} \approx \Pi_L$, where Π_L comes from Eqs. (2.3.18) and (2.3.19) when $\mathbf{E} \approx \mathbf{E}_L = (E_L, 0, 0)$ and $\mathbf{B} \approx \mathbf{B}_L = (0, E_L/c, 0)$. This laser electric field is here a single-colour forward-propagating wave

$$E_L(t, z) = a_0 \mathcal{E}(k_0 z - \omega_0 t) \cos(k_0 z - \omega_0 t), \quad (2.4.34)$$

where a_0 is the laser amplitude, $k_0 = n_0 \omega_0 / c$, and $0 \leq \mathcal{E} \leq 1$ is the slowly-varying envelope. Therefore, according to Eqs. (2.3.18) and (2.3.19), the driving forces reduce to:

$$\Pi_{L,z} = -\frac{e}{m_e c} J_L E_L, \quad (2.4.35)$$

$$\Pi_{L,x} = \frac{(\nabla \cdot \mathbf{J})}{e N_e} J_L. \quad (2.4.36)$$

In the rear of the laser pulse, where the ionization process is ended, the divergence of the current can be approximated as $(\nabla \cdot \mathbf{J})/e \approx \partial_t N_e$ and thus Eq. (2.4.36) reads as:

$$\Pi_{L,x} = \frac{\partial_t N_e}{N_e} J_L. \quad (2.4.37)$$

The laser current J_L is readily calculated from Eq. (2.3.17):

$$(\partial_t + \nu_c) J_L = \varepsilon_0 \omega_p^2 E_L + \Pi_{L,x}, \quad (2.4.38)$$

whose solution is

$$J_L = \frac{\varepsilon_0 \omega_p^2 a_0 \mathcal{E}}{\omega_0^2 + (\nu_c + \partial_t N_e / N_e)^2} [(\nu_c + \partial_t N_e / N_e) \cos(k_0 z - \omega_0 t) + \omega_0 \sin(k_0 z - \omega_0 t)]. \quad (2.4.39)$$

Equation (2.4.39) is simplified by assuming $(\nu_c + \partial_t N_e / N_e)^2 \ll \omega_0^2$ in the denominator. Taking into account that $\omega_0 \sin(k_0 z - \omega_0 t) = -c \partial_z \cos(k_0 z - \omega_0 t)$, Eq. (2.4.39) reduces to:

$$J_L = \frac{\varepsilon_0 \omega_p^2}{\omega_0^2} \left[\nu_c + \frac{\partial_t N_e}{N_e} - c \partial_z \right] E_L. \quad (2.4.40)$$

By substituting Eq. (2.4.40) into Eq. (2.4.41) and $\partial_t N_e / N_e = \partial_t(\omega_p^2) / \omega_p^2$, the longitudinal driving term is thus

$$\Pi_{L,z} \approx -\frac{e \omega_p^2}{2 \omega_0^2 m_e c} \left[\frac{2 \nu_c}{c} + \frac{2}{c \omega_p^2} \partial_t(\omega_p^2) - \partial_z \right] I_L, \quad (2.4.41)$$

where $I_L = \varepsilon_0 c E_L(t)^2$ is the instantaneous laser intensity. The dominant terms in $\Pi_{L,z}$ are the radiation pressure created by the laser pulse ($\sim \nu_c I_L$) and the ponderomotive force ($\sim \partial_z I_L$) [154]. In Fig. 2.4.7 an example of the longitudinal electric field computed from Eqs. (2.4.33) and (2.4.41) and extracted from [44] is shown. The plasma wave pulse is rather short, containing few oscillations before damping out within the time scale of ν_c^{-1} .

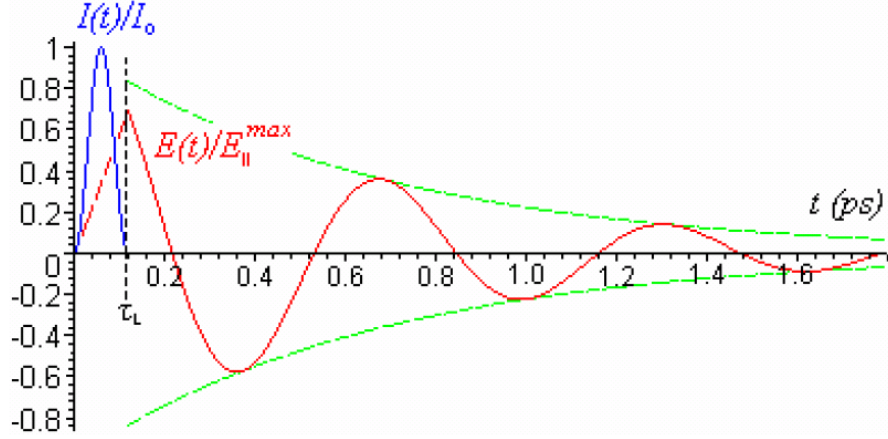


Figure 2.4.7: Temporal profile of the longitudinal electric field [Eqs. (2.4.33) and (2.4.41), with $\nu_c^{-1} = 1.3$ ps and $\omega_p^{-1} = 10$ ps] in the plasma channel (red curve), created in the wake of a square-sine laser pulse pulse intensity $I_L(t) = I_0 \sin^2(\pi t/\tau_L)$, with $I_0 = 24$ TW cm $^{-2}$ and $\tau_L = 120$ fs (blue curve). Source: D’Amico *et al.* [44].

Neglecting the time variations of ω_p^2 in Eq. (2.4.41) and since $\partial_z = -c^{-1}\partial_t$ according to Eq. (2.4.34), the spectrum of the longitudinal electric field reads as

$$\hat{E}_z(\omega) = \frac{e\omega_p^2(2\nu_c\omega - i\omega)}{2\omega_0^2 m_e c^2 (\omega^2 - i\nu_c\omega - \omega_p^2)} \hat{I}_L(\omega), \quad (2.4.42)$$

which confirms that it is peaked at the plasma frequency, belonging to the terahertz domain. The amplitude of the longitudinal field grows linearly with the pump intensity.

The longitudinal current density in this scenario is the responsible for a transition-Cherenkov conical terahertz radiation emitted by the plasma [9, 35, 44, 117, 128, 130]. According to Eqs. (2.4.32) and (2.4.42), its spectrum expresses as

$$\hat{J}_z(\omega) = -\frac{e\varepsilon_0\omega_p^2\omega(2\nu_c i + \omega)}{2\omega_0^2 m_e c^2 (\omega^2 - i\nu_c\omega - \omega_p^2)} \hat{I}_L(\omega), \quad (2.4.43)$$

which also exhibits a pronounced maximum around the plasma frequency.

3 Numerical modelling

Contents

2.1	Laser-plasma interaction	16
2.1.1	Maxwell equations	16
2.1.2	Vlasov equation	22
2.1.3	Moments for electrons	24
2.1.4	Cold-plasma fluid equations	24
2.1.5	Forward propagating electric fields	26
2.2	Ionization of gases	32
2.2.1	Ionization parameters	35
2.2.2	Single ionization	36
2.2.3	Multiple ionization	41
2.3	From optical self-focusing to UHI plasmas	51
2.3.1	Laser filamentation	51
2.3.2	Plasma waves	53
2.4	Laser-based terahertz emitters	57
2.4.1	The Four-wave mixing mechanism: Kerr effect	57
2.4.2	The local current model and the photocurrent mechanism	59
2.4.3	Electron-impact ionization	68
2.4.4	Longitudinal plasma wakefield	69

In Section 2, three physical models have been presented to study laser-driven terahertz generation:

1. The Maxwell-Vlasov model, which couples Maxwell equations [Section 2.1.1] to Vlasov equation [Section 2.1.2].
2. The Maxwell-Fluid model, which combines Maxwell equations [Section 2.1.1] with the cold-plasma fluid equations [Section 2.1.4]. This model is the average in the phase space of the Maxwell-Vlasov model over the electron velocities.
3. The forward propagation equations such as FME [Section 2.1.5.2] and UPPE [Section 2.1.5.3]. These consist in some simplifications of the wave equation obtained

from the Maxwell-Fluid model to describe only the forward propagation of the laser electric field through a nonrelativistic plasma.

The complete analytical solution of any of these models, which might reveal how the terahertz radiation depends on all the physical laser and material parameters, is, unfortunately, not achievable. Solely a simplified analytical solution has been obtained recently and in the framework of this thesis, as we shall explain in Section 3.4. In spite of the applied simplifications, such solution can appear in good agreement with the results of comprehensive numerical simulations and, therefore, it will help to understand how the main emitters of terahertz fields behave. It must be emphasized here that, in the course of this thesis, experimental measurements of THz spectra were not available except in Section 4.1. Therefore, numerical modelling appears to us as a fundamental tool to clear up the physics underlying laser-driven terahertz emissions.

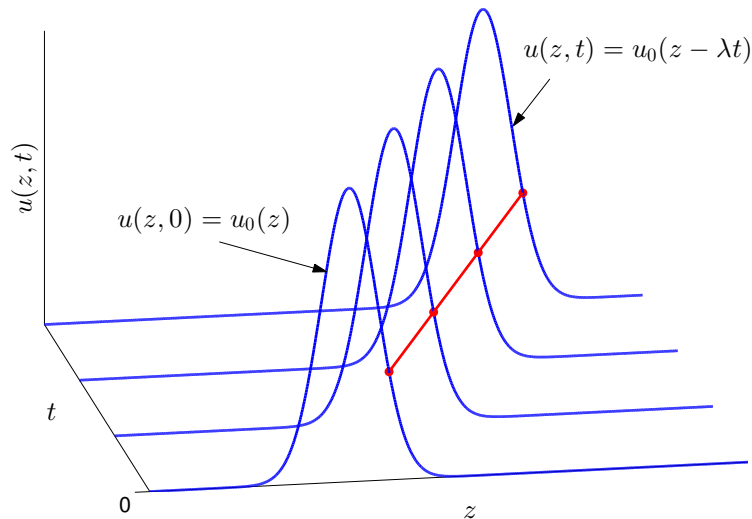


Figure 3.0.1: Linear advection of a Gaussian pulse (blue curves), for $\lambda > 0$, at different instants. One characteristic is plotted (red curve), along which the field is conserved.

In this section three different numerical codes are described, each of which involves different ingredients treated within different strategies:

- CALDER, which solves the Maxwell-Vlasov equations by the Particle-In-Cell technique [Section 3.1.2].
- MAXFLU, a new code developed during this thesis that solves the Maxwell-Fluid equations thanks to finite volumes [Section 3.2].

- UPPE, which solves the UPPE equation through spectral algorithm [Section 3.1.1].

These codes have to integrate numerically the equations presented in Section 2, which are *hyperbolic equations* and model fields that propagate in space and time at finite velocity. In this section we shall focus mostly on MAXFLU, because the other two codes are already known in the literature. Before dwelling on technical details, we introduce basic concepts about hyperbolic equations, from both the physical and numerical viewpoints.

The simplest example of hyperbolic equations is the one-dimensional *scalar linear advection equation*, formally given by the following initial value problem:

$$\begin{cases} \partial_t u(z, t) + \lambda \partial_z u(z, t) = 0, \\ u(z, t = 0) = u_0(z), \end{cases} \quad (3.0.1)$$

where λ refers to the constant velocity at which the field $u(z, t)$ propagates and $u_0(z)$ is the initial condition [104, 163]. In particular, when $u(z, t)$ represents an electromagnetic (EM) wave, λ is its phase velocity. The solution to this problem is straightforward and expresses as $u(z, t) = u_0(z - \lambda t)$. This means, as depicted in Fig. 3.0.1 for $\lambda > 0$, that the solution is conserved along the *characteristics lines* given by $z(t) = z(0) + \lambda t$, along which the equality $u(z(t)) = u(z(0)) = u_0(z(0))$ holds. This is the reason why u is usually called *conserved quantity* in this context.

More generally, we can consider a one-dimensional hyperbolic system with source term:

$$\partial_t \mathbf{U}(z, t) + \partial_z \mathbf{F}(\mathbf{U}(z, t)) = \mathbf{S}(z, t, \mathbf{U}(z, t)), \quad (3.0.2)$$

where \mathbf{U} is the conserved vector, \mathbf{F} is called physical flux and \mathbf{S} is the source term. The Jacobian matrix of the flux, $A = \partial_{\mathbf{U}} \mathbf{F}$, defines the characteristic curves and thus contains the information about the phase velocities for EM fields. By definition, the system is *strictly* hyperbolic if this matrix is diagonalizable and its eigenvalues are real and distinct from each other. This definition is equivalent to state that at every position and instant the characteristic curves are unambiguously defined. Here the vector \mathbf{U} evolves along the characteristics due to the presence of the source term. When the propagation velocities depend on z , t and/or \mathbf{U} , the hyperbolic system is said *nonlinear* and the characteristics may overlap causing a singularity, i.e., a shock wave.

Explicit versions of finite difference methods, which discretize differential operators in time and space, are very interesting for solving numerically hyperbolic systems because they are easy to implement for parallel computing: as the waves travel at finite velocity, to calculate the solution at a given point, only the values at its neighbourhood are necessary. The spatial and time dimensions are discretized with the steps Δz and Δt , respectively, i.e., the mesh $\{z_i\} \times \{t_n\}$ is defined, where $z_{i+1} = z_i + \Delta z$ and $t_{n+1} = t_n + \Delta t$. Therefore,

as shown in Fig. 3.0.2, the conserved vector $\mathbf{U}(z, t_n)$ takes the constant discrete value of \mathbf{U}_i^n on the cell $[z_i - \Delta z/2, z_i + \Delta z/2]$, where $z_{i\pm 1/2} = z_i \pm \Delta z/2$ locate the interfaces. The finite difference method is convergent if its discretized solution tends to the solution of the system when both $\Delta z \rightarrow 0$ and $\Delta t \rightarrow 0$. The *speed* at which the numerical method converges towards the physical solution, $\mathbf{U}_i^n \xrightarrow{\Delta z, \Delta t \rightarrow 0} \mathbf{U}(z, t_n)$, is determined by its order of accuracy in space and time. For instance, the method is n -order accurate in space if the error between the discrete and physical solution is divided by 2^n when the spatial step Δz is divided by 2 (idem for time). One resolution level is accepted if the norm of the difference between the solution obtained with that grid and the solution obtained with a finest grid (usually half steps) is below a small tolerance value. In practice, the three codes mentioned above use second-order accurate methods because they are a good compromise between the convergence speed and the computational cost.

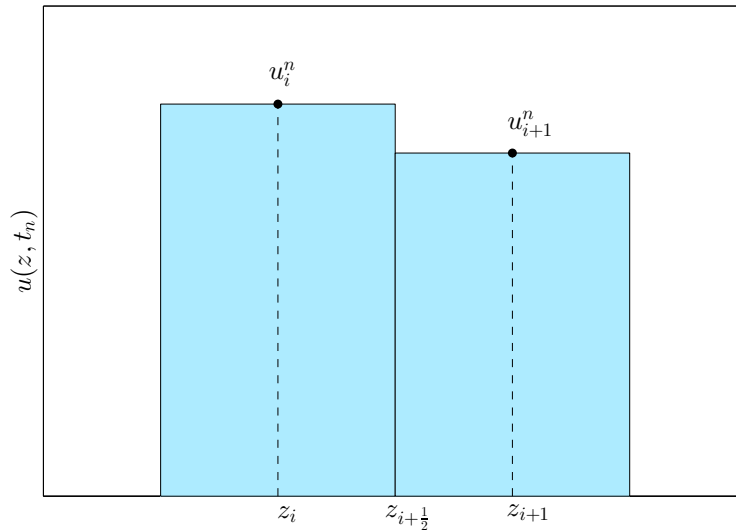


Figure 3.0.2: Finite volume discretization at t_n . The interfaces $\{z_{i\pm 1/2}\}$ delimit the cells. On each cell $[z_{i-1/2}, z_{i+1/2}]$, centred at $z = z_i$ and of length Δz , the solution is assumed constant and equal to u_i^n .

Discretizing successfully a whole system like Eq. (3.0.1) is difficult and challenging, because many physical phenomena are mutually competing. In general, finite difference schemes discretizing both advection and evolution operators fail when working with non-linear systems. The best and most robust way of overcoming this problem is to apply the *splitting* approach (Strang [156]), also known as fractional-step method. Two examples of splitting schemes support the UPPE and CALDER codes. The former, which is an evolution equation along the z -axis (i.e., the solution advances in z), separates the source term into the linear part and the nonlinear part. The latter solves on the one hand Maxwell

equations and on the other hand Vlasov equation.

The Maxwell-Fluid model fits the structure of the nonlinear hyperbolic system given by Eq. (3.0.2). As explained in Section 3.2, MAXFLU code benefits from the splitting approach to solve such system, dividing the latter into an *advection stage* [Eq. (3.0.3)] and an *evolution stage* [Eq. (3.0.4)]:

$$\partial_t \mathbf{U}(z, t) + \partial_z \mathbf{F}(\mathbf{U}(z, t)) = \mathbf{0}, \quad (3.0.3)$$

$$\partial_t \mathbf{U}(z, t) = \mathbf{S}(z, t, \mathbf{U}(z, t)). \quad (3.0.4)$$

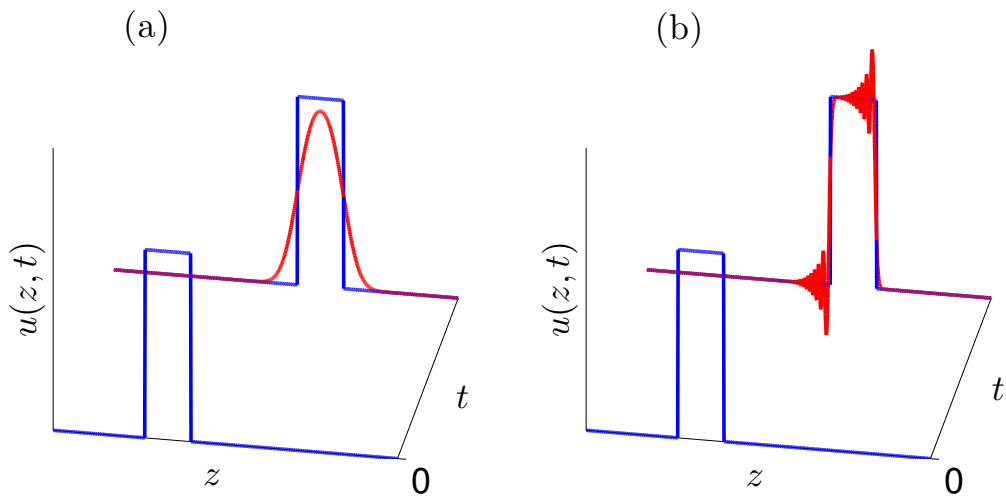


Figure 3.0.3: Illustration of (a) numerical diffusion and (b) numerical dispersion for the linear advection equation given by Eq. (3.0.1), with $\lambda > 0$, for a rectangular function as initial condition (blue curve at $t = 0$). The exact solution (blue curve) is compared with the numerical solution (red curves), calculated with (first-order) FORCE scheme [a, Eq. (3.2.30)] and (second-order) Lax-Wendroff scheme [b, Eq. (3.2.31)]. The integration uses a small time step, $\lambda \Delta t = \Delta z / 10$, to render both numerical effects more visible.

Classical Runge-Kutta methods can be employed for solving the evolution stage with no stability restriction on Δt . The numerical challenge for the Maxwell-Fluid model lies in its advective part, whose cold-plasma fluid equations are strongly nonlinear [Eqs. (2.1.49) and (2.1.53)]. The advection will be discretised through finite volume methods, which are a subfamily of finite difference methods especially adapted to deal with nonlinear hyperbolic systems (see LeVeque [104] and Toro [163]). As with Particle-In-Cell codes, the so-called Courant-Friedrichs-Lewy (CFL) stability condition must be also satisfied, which

reduces the practical computational domain of the Maxwell-Fluid code to small interaction volumes. The main problem of finite volumes and finite difference schemes when applied to nonlinear systems is that two opposite intrinsic numerical problems can strongly affect the numerical solution to a point that is not acceptable, namely, the numerical diffusion and the numerical dispersion. As depicted in Fig. 3.0.3, the former increases unphysically the diffusion dynamics and forces the maxima and minima of the fields to reduce at every iteration (fields *spread out*). The latter causes unphysical oscillations (Gibbs phenomenon) mostly in the neighbourhood of sharp field gradients such as the electron density profile when it is computed, e.g., by MAXFLU.

Numerical diffusion is inherent to monotonic schemes ($\|\mathbf{U}_i^n\| \leq \|\mathbf{U}_{i+1}^n\| \Leftrightarrow \|\mathbf{U}_i^{n+1}\| \leq \|\mathbf{U}_{i+1}^{n+1}\|$) and the Godunov theorem states that these schemes must at most be first-order accurate. This, however, becomes a huge dilemma for the numerical strategy of the MAXFLU code. Indeed, if first-order monotonic schemes are used, the amplitude of the laser electric field will unphysically decrease. Moreover, if second-order nonmonotonic (thus dispersive) schemes are used, unphysical oscillations can appear in the electron density, which will perturb the spectra in the best case and create instability in the worst case. Actually, overcoming this problem is still an open issue for nonlinear hyperbolic systems. In this thesis, the flux-corrected transport (FCT) algorithm has been chosen for MAXFLU. This technique, initially proposed by Boris and Book [18] (see the work by Zalesak [189]), controls the appearance of oscillations by weighting locally and nonlinearly a first-order diffusive scheme with a high-order dispersive scheme. The weighting factor is called *flux limiter*. The critical point of this approach is, obviously, the calculation of this flux limiter, i.e., which oscillations are *accepted* or *rejected* when pondering the two schemes. In this thesis, we have obtained a simple flux limiter (see Section F), which prevents any unphysical (i.e., numerical) oscillation of the plasma without affecting the physical harmonics that are generated (including, of course, terahertz radiation).

3.1 Propagation and PIC codes

These two codes, known as UPPE (for “Unidirectional Pulse Propagation Equation”) and CALDER (in tribute to the famous American sculptor Alexander Calder [1898-1976]), already exist and have often been described in the literature [7, 102]. Only a short sketch of their structure will be recalled below.

3.1.1 The UPPE code

The UPPE 3D code is a fully parallel spectral code that resolves in three dimensions the UPPE equation (2.1.81). It has been successfully validated against several experiences, in particular for reproducing THz spectra emitted from low-pressure argon cells (see Fig. 3.1.1).

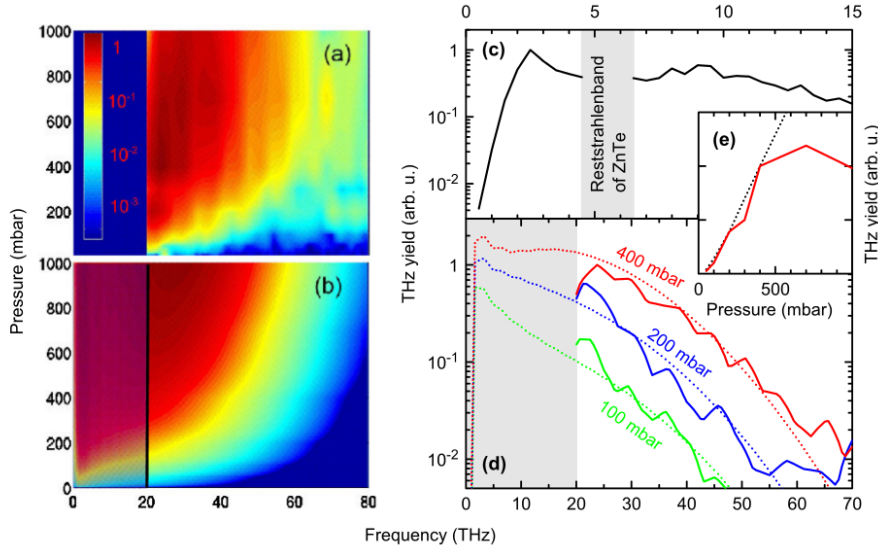


Figure 3.1.1: (a) Measured THz spectra and (b) simulation results for argon pressures between 1 and 1000 mbar. In (d), experimental (solid lines) and theoretical (dashed lines) spectra are compared for various pressures. In (e), the overall THz yield versus pressure is shown (simulation: dashed line, experiment: solid line). (c) Low-frequency spectrum for 1000 mbar measured by electro-optic sampling in ZnTe. Shading signifies frequency ranges where no experimental data were available. Source: Babushkin *et al.* [7].

Numerically, the UPPE equation, which describes the electric field propagation along the z -axis, is split thanks to a *split-step Fourier* algorithm [1]. The code solves separately the linear source terms (e.g., transverse diffraction and temporal dispersion) from the nonlinear ones (among which the Kerr effect and photoionization). Equation (2.1.81) is

split into two equations, which indeed account for opposite physical effects:

$$\begin{cases} \partial_z \hat{E} = i\sqrt{k^2 - k_\perp^2} \hat{E}, & (3.1.1a) \\ \partial_z \hat{E} = \frac{\mu_0}{2\sqrt{k^2 - k_\perp^2}} \left[\omega \hat{J} + i\omega^2 \widehat{P_{\text{KERR}}} + \omega \hat{J}_{\text{loss}} \right] = \hat{\mathcal{L}}(\hat{E}). & (3.1.1b) \end{cases}$$

The integration domain is discretized over a regular grid in x , y and t by means of steps Δx , Δy and Δt , respectively. The propagation step Δz self-adapts¹ along the propagation direction z by evaluating the growth of the nonlinear phase of the pulse. The code uses a fully spectral scheme with absorbing boundary conditions in (x, y, t) . Parallelization is done by spatial domain decomposition using MPI (Message Passing Interface protocole), for which the real laser field is discretized in stripes along dimension y . The UPPE code is written in Fortran 90 and uses the library FFTW3.

The two evolution equations (3.1.1) over z are solved alternatively at each longitudinal step. In other words, the value $\hat{E}(z + \Delta z)$ is calculated from $\hat{E}(z)$ in two stages. First, Eq. (3.1.1a), the linear part, is solved exactly in Fourier space:

$$\hat{E}^{\text{linear}}(z + \Delta z) = \exp(i\Delta z \sqrt{k^2 - k_\perp^2}) \hat{E}(z). \quad (3.1.2)$$

Second, Eq. (3.1.1b), the nonlinear part, is integrated as

$$\hat{E}(z + \Delta z) = \hat{E}^{\text{linear}}(z + \Delta z) + \int_z^{z+\Delta z} \hat{\mathcal{L}}(\hat{E}(\zeta)) d\zeta. \quad (3.1.3)$$

The integral of Eq. (3.1.3) is solved via classical Runge-Kutta methods, e.g.,

$$\int_z^{z+\Delta z} \hat{\mathcal{L}}(\zeta) d\zeta \approx \hat{\mathcal{L}}(\hat{E}^{\text{linear}}(z + \Delta z)) \Delta z. \quad (3.1.4)$$

3.1.2 The CALDER code

CALDER is a multi-dimensional (1D, 2D and 3D) fully-parallel Particle-In-Cell code, written in Fortran 90 and devoted to study laser-plasma interactions in many physical contexts (see Lefebvre *et al.* [102]).

A kinetic description given by Vlasov equation applied to seven dimensions (t , x , y , z , p_x , p_y , p_z) entails a very large computational load, which is required for the strongly nonequilibrium physics of intense laser-matter interaction. In order to lighten the computational cost when solving Vlasov equation, the distribution function is approximated

¹This is the great advantage of the UPPE code: Δz can be significantly larger than the step of Particle-In-Cell and Maxwell-Fluid codes, e.g., at moderate intensities or in the absence of sharp gradients, which allows it to describe pulse propagation over long distances in reasonable computing time.

as the sum of a collection of *macroparticles* p , each of which is endowed with a position (\mathbf{r}_p) and a linear momentum (\mathbf{p}_p).

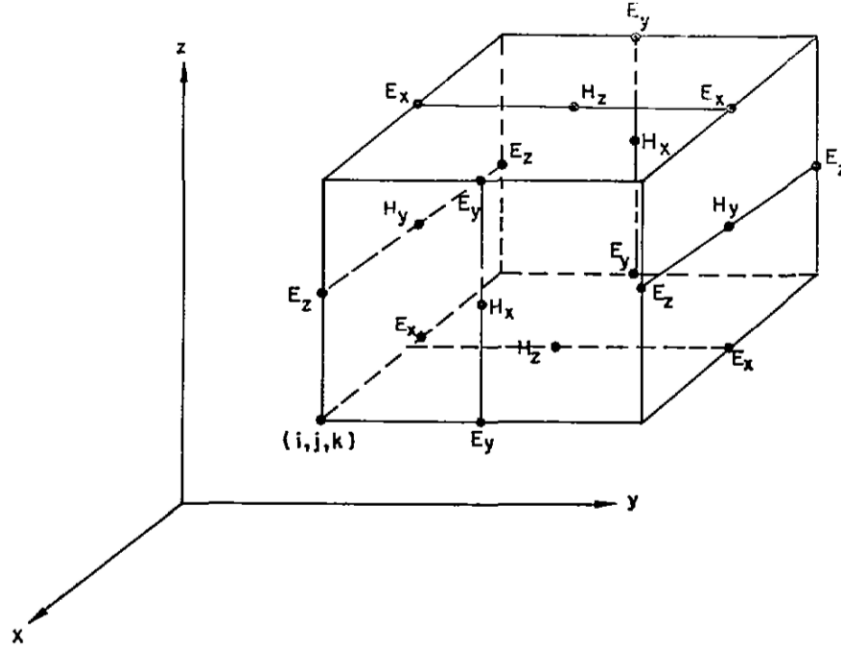


Figure 3.1.2: Positions of various field components. The electric field components (E_x , E_y , E_z) are in the middle of the edges and the magnetic field strength components (H_x , H_y , H_z) are in the centre of the faces. Source: Yee [184].

Maxwell equations are discretized on a regular, fixed, staggered Cartesian mesh (Δx , Δy , Δz and Δt) according to the well-known Yee scheme [184]. As shown in Fig. 3.1.2, this second-order accurate method locates the magnetic field components in the centre of the faces of a cell and the electric field components and related current densities lie in the middle of the edges of cells. Magnetic fields and current densities are delayed by $\Delta t/2$ with respect to the electric fields. Magnetic fields and electric fields are calculated alternatively; for example, the discretizations for B_x and E_x are:

$$B_x|_{i,j+1/2,k+1/2}^{n+1/2} = B_x|_{i,j+1/2,k+1/2}^{n-1/2} + \frac{\Delta t}{\Delta z} [E_y|_{i,j+1/2,k+1}^n - E_y|_{i,j+1/2,k}^n] - \frac{\Delta t}{\Delta y} [E_z|_{i,j+1,k+1/2}^n - E_z|_{i,j,k+1/2}^n], \quad (3.1.5)$$

$$E_x|_{i+1/2,j,k}^{n+1} = E_x|_{i+1/2,j,k}^n + \frac{c^2 \Delta t}{\Delta y} [B_z|_{i+1/2,j+1/2,k}^{n+1/2} - B_z|_{i+1/2,j-1/2,k}^{n+1/2}] - \frac{c^2 \Delta t}{\Delta z} [B_y|_{i+1/2,j,k+1/2}^{n+1/2} - B_y|_{i+1/2,j,k-1/2}^{n+1/2}] + \frac{\Delta t}{\varepsilon_0} J_x|_{i+1/2,j,k}^{n+1/2}. \quad (3.1.6)$$

Both the Maxwell Solver and the Particle Mover advance in time in explicit ways. The code is parallelized using MPI with a domain decomposition technique, according to which the simulation volume is partitioned among the calculation cores. The CALDER code possesses Monte Carlo modules describing strong-field-induced elastic collisions, inelastic collisions and tunnel multiple ionization. Its main numerical steps are (see Fig. 3.1.3):

1. **Maxwell Solver:** electromagnetic fields are computed at nodes of the Yee mesh.
2. Interpolate the electromagnetic fields at the positions of the macroparticles.
3. **Particle Mover:** advance macroparticle trajectories by solving relativistic equations of motion.
4. Communicate the macroparticles across sub-domain boundaries (parallel simulations).
5. Deposit the charge and the current densities of macroparticles on the Yee mesh. The current densities given by the movement of the macroparticles are interpolated into the Maxwell grid thanks to the Esirkepov method [57]. This method calculates the current density \mathbf{J}^n on the Yee grid from the particle positions $\mathbf{x}^{n-1/2}$ and $\mathbf{x}^{n+1/2}$ in such a way that the Gauss law [Eq. (2.1.1)] is verified exactly at discrete level.
6. Compute and use output diagnostics. Return to step 1, the Maxwell Solver.

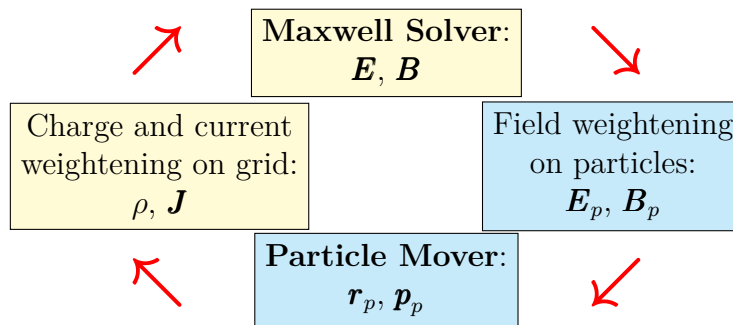


Figure 3.1.3: Sketch of one iteration loop of Particle-In-Cell codes (e.g., CALDER).

Particle-In-Cell codes suffer from a restrictive stability condition imposed by the Yee scheme and reading as $c\Delta t \leq \sqrt{\Delta x^2 + \Delta y^2 + \Delta z^2}$. This stability condition makes these codes be computationally expensive. Nowadays treating plasmas over scales from hundreds of micrometres to several millimetres can, however, be achieved by such codes by means of massively-parallel computers.

3.2 A new Maxwell-Fluid code: MAXFLU

The Maxwell-Fluid model is a nonlinear hyperbolic system that couples Maxwell equations [Eqs. (2.1.3), (2.1.4) and (2.1.6)] with the cold-plasma fluid equations [Eqs. (2.1.49) and (2.1.53)]:

$$\begin{cases} \partial_t \mathbf{B} + \nabla \times \mathbf{E} = \mathbf{0}, & (3.2.1a) \\ -\partial_t (\varepsilon_0^{-1} \mathbf{D}) + c^2 \nabla \times \mathbf{B} = \frac{\mathbf{J}}{\varepsilon_0} + \frac{\mathbf{J}_{\text{loss}}}{\varepsilon_0}, & (3.2.1b) \\ \partial_t N_e - \frac{1}{e} \nabla \cdot \mathbf{J} = \partial_t \sum_s \sum_j \frac{q_{j,s}}{e} N_{j,s}, & (3.2.1c) \\ \partial_t (\gamma \mathbf{J}) + \nabla \cdot (\mathbf{v} \otimes \gamma \mathbf{J}) = \frac{e^2}{m_e} N_e \mathbf{E} - \frac{e}{m_e} \mathbf{J} \times \mathbf{B} - \nu_c \gamma \mathbf{J}, & (3.2.1d) \end{cases}$$

where the electric displacement field is given by Eqs. (2.1.5), (2.1.7) and (2.1.8):

$$\varepsilon_0^{-1} \mathbf{D} = \mathbf{E} + \varepsilon_0^{-1} \mathbf{P}_L + \varepsilon_0^{-1} \mathbf{P}_{\text{KERR}} = \mathbf{E} + \chi^{(1)} * \mathbf{E} + \varepsilon_0^{-1} \mathbf{P}_{\text{KERR}}, \quad (3.2.2)$$

and the current density and Lorentz factor are:

$$\mathbf{J} = -e N_e \mathbf{v}, \quad (3.2.3)$$

$$\gamma = \frac{1}{\sqrt{1 - \frac{v^2}{c^2}}}. \quad (3.2.4)$$

The linear momentum of electrons is defined by

$$\mathbf{p} = m_e \gamma \mathbf{v}. \quad (3.2.5)$$

This system is well-defined since there is the same number of unknowns (\mathbf{B} , \mathbf{D} , N_e and \mathbf{J}) as equations.

There is little bibliography concerning Maxwell-Fluid codes. Usually the geometry and/or the plasma nonlinearities are simplified due to the numerical difficulty of solving directly the system (3.2.1). For instance, Berenziani *et al.* in Ref. [13] (and similarly Wu *et al.* [177], and Tushentsov *et al.* [164]) performed Maxwell-Fluid simulations in pre-formed overdense plasmas without ionization sources. They ignored all the kinetic effects and, therefore, the electron density never vanishes ($N_e \neq 0$). Following their derivation, after easy manipulations, Eq. (3.2.1d) is transformed through Eqs. (3.2.3) and (3.2.5) when $\nu_c = 0$ into $\mathbf{p}[\partial_t N_e + \nabla \cdot (N_e \mathbf{v})] = -N_e[\partial_t \mathbf{p} + (\mathbf{v} \cdot \nabla) \mathbf{p} + e \mathbf{E} + e \mathbf{v} \times \mathbf{B}]$. Assuming furthermore no ionization, the left-hand side of this equation is zero thanks to

Eq. (3.2.1c) and its expression simplifies into $\partial_t \mathbf{p} + (\mathbf{v} \cdot \nabla) \mathbf{p} = -e\mathbf{E} - e\mathbf{v} \times \mathbf{B}$. However, instead of employing this equation, the authors used the cold unmagnetized electron fluid equation for the linear momentum, $\partial_t \mathbf{p} + m_e c^2 \nabla \gamma = -e\mathbf{E}$ in the framework of relativistic hydrodynamics. Besides, Shadwick *et al.*, instead, in Ref. [146] did solve the previous equation for the linear momentum derived from the system (3.2.1) by the *method of lines* [142]. By expressing this equation in the laser comoving reference frame² they could solve it directly for a non-ionizable preformed plasma ($N_e \neq 0$).

In this section, we shall focus on the one-dimensional version of the MAXFLU code, a fully-parallelized finite-volume-based code developed during the course of this thesis and solving the complete Maxwell-Fluid system (3.2.1). We derive the one-dimensional (1D) version of such system to describe the propagation of secondary and laser fields over the z -axis. We assume that the laser field is linearly polarized along the x -axis. This implies to ignore the transverse gradients (e.g., diffraction) and to adapt the field geometry: $\partial_x = \partial_y = 0$, $\mathbf{D} = (D_x, 0, D_z)$, $\mathbf{B} = (0, B_y, 0)$ and $\mathbf{J} = (J_x, 0, J_z)$. The system (3.2.1) then expresses as

$$\left\{ \begin{array}{l} \partial_t B_y + \partial_z E_x = 0, \\ \partial_t (\varepsilon_0^{-1} D_x) + \partial_z (c^2 B_y) = -\frac{1}{\varepsilon_0} J_x - \frac{1}{\varepsilon_0} J_{\text{loss},x}, \\ \partial_t (\varepsilon_0^{-1} D_z) = -\frac{1}{\varepsilon_0} J_z - \frac{1}{\varepsilon_0} J_{\text{loss},z}, \\ \partial_t N_e + \partial_z \left(-\frac{1}{e} J_z \right) = \partial_t \sum_s \sum_j \frac{q_{j,s}}{e} N_{j,s}, \\ \partial_t (\gamma J_x) + \partial_z (\gamma v_z J_x) = \frac{e^2}{m_e} N_e E_x + \frac{e}{m_e} J_z B_y - \nu_c \gamma J_x, \\ \partial_t (\gamma J_z) + \partial_z (\gamma v_z J_z) = \frac{e^2}{m_e} N_e E_z - \frac{e}{m_e} J_x B_y - \nu_c \gamma J_z. \end{array} \right. \quad \begin{array}{l} (3.2.6a) \\ (3.2.6b) \\ (3.2.6c) \\ (3.2.6d) \\ (3.2.6e) \\ (3.2.6f) \end{array}$$

In the electric displacement field given by Eq. (3.2.2), nonlinear dispersion is not taken into account and therefore \mathbf{P}_{KERR} is given by Eq. (2.1.22):

$$\varepsilon_0^{-1} D_x = E_x + \varepsilon_0^{-1} P_{L,x} + \chi^{(3)} E_x^3, \quad (3.2.7)$$

$$\varepsilon_0^{-1} D_z = E_z + \varepsilon_0^{-1} P_{L,z} + \chi^{(3)} E_z^3. \quad (3.2.8)$$

In the most realistic case, the electric linear polarization $P_{L,x/z}$ should be calculated by using an ordinary differential equation that models the medium response, such as

²They solved the one-dimensional version of these equations along z in the frame: $t, \zeta = ct - z$.

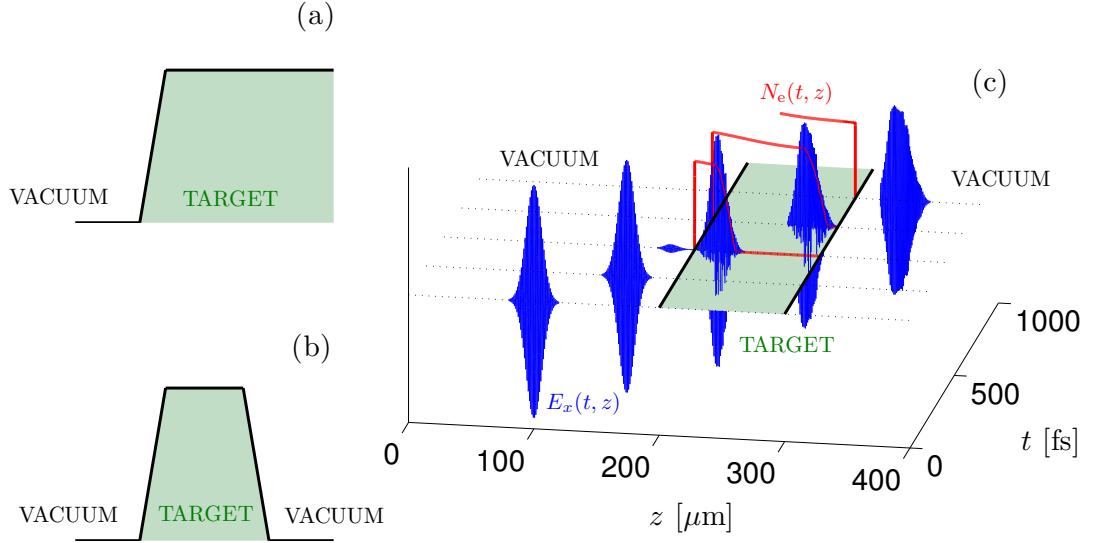


Figure 3.2.1: Example of MAXFLU 1D geometry. (a) Semi-infinite target. (b) Finite target. It is possible to add a gradient at each vacuum-plasma interface. (c) Example of evolving electric field (E_x , blue curves) and electron density (N_e , red curves). The target is positioned between $z = 200$ and $z = 300$ μm (light green area). Initially, at $t = 0$, the laser field is centred at $z = 100$ μm . The laser field and the electron density, both in arbitrary units, are depicted at $t = 200, 400, 600$ and 800 fs. Note that MAXFLU 1D can also simulate the backward field that propagates from the interface at $z = 200$ μm .

the Sellmeier model [Eqs. (2.1.15) and (2.1.16)]. However, in most situations, a constant refractive index is just considered [i.e., $n(\omega) = n_0$], taking into account that the propagated distances simulated by MAXFLU 1D here are usually not long enough to be sensitive to linear dispersion:

$$\varepsilon_0^{-1} D_x = n_0^2 E_x + \chi^{(3)} E_x^3, \quad (3.2.9)$$

$$\varepsilon_0^{-1} D_z = n_0^2 E_z + \chi^{(3)} E_z^3. \quad (3.2.10)$$

Figure 3.2.1 shows the geometrical slab treated by the MAXFLU 1D code. A vacuum region lies at the left of the target ($n_0 = 1$ and $\chi^{(3)} = 0$). At $t = 0$ all the fields are set to zero except the laser field, which is initialized in the left vacuum region and propagates forward. The density of neutrals is also initialized inside the gas (target). The target can be finite (i.e., with vacuum beyond its right boundary) [Fig. 3.2.1(b)] or semi-infinite [Fig. 3.2.1(a)]. The linear and nonlinear indices n_0 and n_2 are considered constant. They

are set to 1 and 0 in vacuum, respectively, and they satisfy $n_0 \geq 1$ and $n_2 \geq 0$ inside the target. When there is a plasma ($N_e > 0$), the full Maxwell-Fluid system applies. Without plasma ($N_e = 0$), like in vacuum, the plasma quantities are zero ($D_z = N_e = J_x = J_z = 0$) and the Maxwell-Fluid system reduces to an advection of the laser pulse:

$$\partial_t B_y + \partial_z E_x = 0, \quad (3.2.11)$$

$$\partial_t (n_0^2 E_x + \chi^{(3)} E_x^3) + c^2 \partial_z B_y = 0. \quad (3.2.12)$$

The critical aspect of this geometry lies at the interface between vacuum and plasma, where $N_e \rightarrow 0$ and thus the fluid part of the model is not well defined [13]. The MAXFLU code overcomes this problem by imposing a small density threshold ϵ_N allowing one to distinguish *vacuum* from *plasma*. Below that value the velocity is set to zero ($v_x = v_z = 0$). This simple technique assures a stable transition at vacuum-plasma interfaces.

3.2.1 Numerical strategy

The 1D Maxwell-Fluid system [Eq. (3.2.6)] fits the general structure of a nonlinear hyperbolic system represented by Eq. (3.0.2) with the following conserved field vector (\mathbf{U}), physical flux (\mathbf{F}) and source term (\mathbf{S}):

$$\mathbf{U} = \begin{pmatrix} B_y \\ \epsilon_0^{-1} D_x \\ \epsilon_0^{-1} D_z \\ N_e \\ \gamma J_x \\ \gamma J_z \end{pmatrix}, \quad (3.2.13)$$

$$\mathbf{F}(\mathbf{U}) = \begin{pmatrix} E_x \\ c^2 B_y \\ 0 \\ -e^{-1} J_z \\ \gamma v_z J_x \\ \gamma v_z J_z \end{pmatrix}, \quad (3.2.14)$$

$$\mathbf{S}(\mathbf{U}) = \begin{pmatrix} 0 \\ -\varepsilon_0^{-1} J_x - \varepsilon_0^{-1} J_{\text{loss},x} \\ -\varepsilon_0^{-1} J_z - \varepsilon_0^{-1} J_{\text{loss},z} \\ \partial_t \sum_s \sum_j \frac{q_{j,s}}{e} N_{j,s} \\ \frac{e^2}{m} N_e E_x + \frac{e}{m_e} J_z B_y - \nu_c \gamma J_x \\ \frac{e^2}{m} N_e E_z - \frac{e}{m_e} J_x B_y - \nu_c \gamma J_z \end{pmatrix}. \quad (3.2.15)$$

The *field variables* of the Maxwell-Fluid system are the components of \mathbf{U} defined by Eq. (3.2.13). The physical unknowns E_x , E_z , J_x and J_z , which intervene in the flux and the source, are calculated from these field variables. For the sake of clarity, the components of \mathbf{U} are underlined below in a box. The electric field, if a constant linear refractive index n_0 is used in Eqs. (3.2.9) and (3.2.10), is calculated as

$$E_{x/z}(\mathbf{U}) = \begin{cases} \frac{\boxed{\varepsilon_0^{-1} D_{x/z}}}{n_0^2}, & \text{if } \chi^{(3)} = 0, \\ \sqrt[3]{\frac{2}{3} n_0^2 \bar{E}_{x/z}(\mathbf{U}) - \frac{1}{\sqrt[3]{18} \chi^{(3)} \bar{E}_{x/z}(\mathbf{U})}}, & \text{otherwise,} \end{cases} \quad (3.2.16)$$

$$\bar{E}_{x/z}(\mathbf{U}) = \left(-9\chi^{(3)2} \boxed{\varepsilon_0^{-1} D_{x/z}} + \sqrt{12\chi^{(3)3} n_0^6 + 81\chi^{(3)4} \left(\boxed{\varepsilon_0^{-1} D_{x/z}} \right)^2} \right)^{-\frac{1}{3}}, \quad (3.2.17)$$

where Eq. (3.2.16) comes from the analytical solution of the cubic equation $\boxed{\varepsilon_0^{-1} D_{x/z}} = n_0^2 E_{x/z}(\mathbf{U}) + \chi^{(3)} E_{x/z}(\mathbf{U})^3$ given by Eqs. (3.2.7) and (3.2.8). Here the subscript x/z refers to both x and z components. The linear dispersion of Eqs. (3.2.7) and (3.2.8) is treated by introducing into the second and third equations of the Maxwell-Fluid system [Eq. (3.2.6)] a linear polarization current density $J_{L,x/z} = \partial_t P_{L,x/z}$. By doing so, dispersion is handled as a source term calculated by solving, for instance, the differential equations given by Eqs. (2.1.15) and (2.1.16):

$$\begin{cases} \partial_t (\varepsilon_0^{-1} D_x) + \partial_z (c^2 B_y) = -\frac{1}{\varepsilon_0} (J_x + J_{L,x} + J_{\text{loss},x}), \\ \partial_t (\varepsilon_0^{-1} D_z) = -\frac{1}{\varepsilon_0} (J_z + J_{L,z} + J_{\text{loss},z}), \end{cases} \quad (3.2.18)$$

where $\varepsilon_0^{-1} D_{x/z} = E_{x/z} + \chi^{(3)} E_{x/z}^3$ and Eqs. (3.2.16) and (3.2.17) can be applied with $n_0 = 1$. For this reason, as a numerical strategy, the electric displacement field is determined by

Eqs. (3.2.9) and (3.2.10).

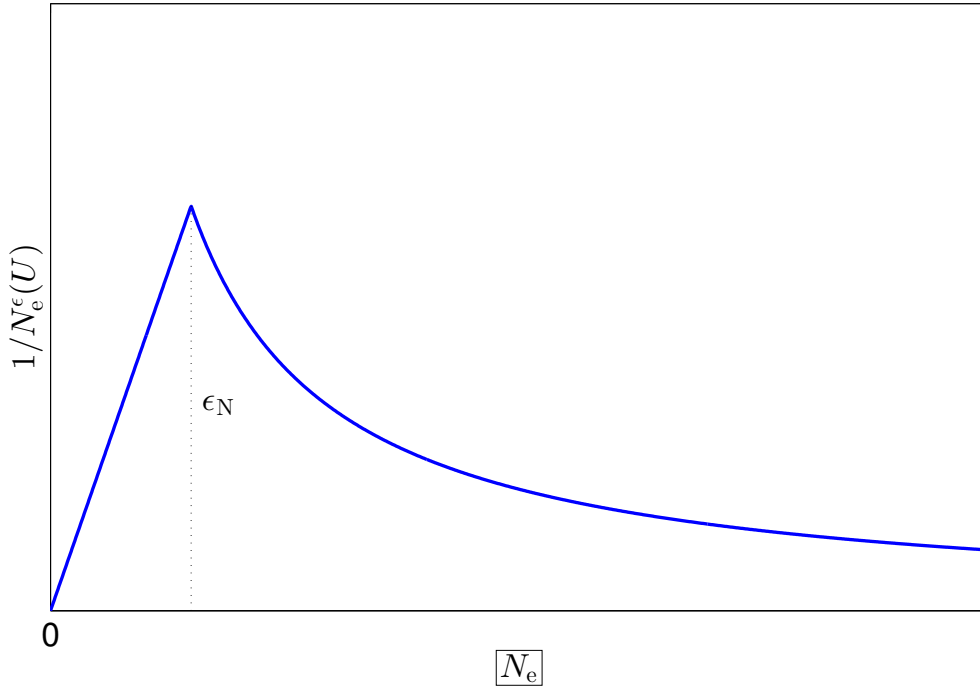


Figure 3.2.2: Inverse of the *corrected* electron density, $1/N_e^\epsilon(\mathbf{U})$ [Eq. (3.2.22)], as a function of $\overline{N_e}$. This quantity is linear from $\overline{N_e} = 0$ to $\overline{N_e} = \epsilon_N = 10^{-16}N_{e,c}$.

Plasma quantities are given by:

$$J_{x/z}(\mathbf{U}) = \frac{\overline{\gamma J_{x/z}}}{\overline{\gamma(\mathbf{U})}}, \quad (3.2.19)$$

$$\overline{\gamma(\mathbf{U})} = \sqrt{1 + \frac{(\overline{\gamma J_x})^2 + (\overline{\gamma J_z})^2}{e^2 c^2 (\overline{N_e^\epsilon(\mathbf{U})})^2}}, \quad (3.2.20)$$

$$v_{x/z}(\mathbf{U}) = -\frac{J_{x/z}(\mathbf{U})}{e \overline{N_e^\epsilon(\mathbf{U})}}, \quad (3.2.21)$$

$$\overline{N_e^\epsilon(\mathbf{U})} = \begin{cases} \overline{N_e}, & \text{if } N_e \geq \epsilon_N, \\ \frac{\epsilon_N^2}{\overline{N_e}}, & \text{otherwise.} \end{cases} \quad (3.2.22)$$

$\overline{N_e^\epsilon(\mathbf{U})}$ accounts for a *corrected* electron density that discriminates between the value of the electron plasma density between *vacuum* ($\overline{N_e} < \epsilon_N$) and *plasma* ($\overline{N_e} \geq \epsilon_N$).

As shown in Fig. 3.2.2, its inverse has been modelled linearly from the value ϵ_N^{-1} when $\boxed{N_e} = \epsilon_N$ to the value 0 when $\boxed{N_e} = 0$. This choice gives a smooth transition at the interface. The value of the tolerance ϵ_N can be taken close to the machine precision. With double precision, the choice $\epsilon_N = 10^{-16} N_{e,c}$ worked well for all simulations, even at relativistic intensities $\approx 10^{19} \text{ W cm}^{-2}$.

For the numerical resolution of the Maxwell-Fluid model, the fields $\mathbf{U}(z, t)$ are discretized as \mathbf{U}_i^n on z (index: i ; step: Δz) and t (index: n ; step: Δt) as in Fig. 3.0.2. The resolution of Eq. (3.0.2), together with Eqs. (3.2.13), (3.2.14) and (3.2.15), is tackled by splitting this equation into Eqs. (3.0.3) and (3.0.4). This technique is very robust because each physical part of the problem is treated separately from the others.

The evolutive part [Eq. (3.0.4) with Eqs. (3.2.13) and (3.2.15)] acts on the fields D_x , D_z , N_e , γJ_x and γJ_z :

$$\left\{ \begin{array}{l} \partial_t D_x = -J_x - J_{\text{loss},x}, \\ \partial_t D_z = -J_z - J_{\text{loss},z}, \\ \partial_t N_e = \partial_t \underbrace{\sum_s \sum_j \frac{q_{j,s}}{e} N_{j,s}}_{\text{ionization}}, \\ \partial_t (\gamma J_x) = \underbrace{\frac{e^2}{m_e} N_e E_x}_{\text{electric force}} + \underbrace{\frac{e}{m_e} J_z B_y}_{\text{Lorentz force}} - \underbrace{\nu_c \gamma J_x}_{\text{collision term}}, \\ \partial_t (\gamma J_z) = \underbrace{\frac{e^2}{m_e} N_e E_z}_{\text{electric force}} - \underbrace{\frac{e}{m_e} J_x B_y}_{\text{Lorentz force}} - \underbrace{\nu_c \gamma J_z}_{\text{collision term}}. \end{array} \right. \quad \begin{array}{l} (3.2.23a) \\ (3.2.23b) \\ (3.2.23c) \\ (3.2.23d) \\ (3.2.23e) \end{array}$$

Equations (3.2.23a) and (3.2.23b) refer to the field induced by the plasma ($\partial_t E_{x/z} \sim -J_{x/z}$) and the Kerr nonlinearity [$\partial_t E_{x/z} \sim -J_{x/z}^{\text{KERR}} = -\partial_t (\chi^{(3)} E_{x/z}^3)$]. Equation (3.2.23c) accounts for ionization, calculated with Eq. (2.2.32). In Eqs. (3.2.23d) and (3.2.23e) there are three important players:

1. The electric force driven by $\partial_t J_{x/z} \sim \gamma^{-1} N_e E_{x/z} \sim \gamma^{-1} \omega_p^2 E_{x/z}$. The transverse component of this force is responsible for inducing the transverse current J_x in the beam head. Moreover, in the rear part of the laser pulse, this force accounts for the contributions oscillating at the plasma frequency ($\omega_p/\sqrt{\gamma}$) on both components of the radiated electric field.
2. The Lorentz force $\partial_t J_{x/z} \sim \gamma^{-1} J_{z/x} B_y$. Its longitudinal component is the laser-induced ponderomotive force that excites longitudinal fields in the beam head.
3. The collision term $\partial_t J_{x/z} \sim \nu_c J_{x/z}$, which damps the field components over long

times, after the laser pulse has interacted with the medium.

Classical Runge-Kutta methods are suitable to solve numerically Eq. (3.2.23) (expressed in the form of Eq. (3.0.4)). MAXFLU 1D uses the classical explicit two-step second-order Runge-Kutta scheme to progress over Δt except for the densities of electrons and ions (i.e., to calculate \mathbf{U}_i^{n+1} from \mathbf{U}_i^n):

$$\begin{cases} \mathbf{U}_i^{n+\frac{1}{2}} = \mathbf{U}_i^n + \frac{\Delta t}{2} \mathbf{S}_i^n, \\ \mathbf{U}_i^{n+1} = \mathbf{U}_i^n + \Delta t \mathbf{S}_i^{n+\frac{1}{2}}, \end{cases} \quad (3.2.24)$$

where $\mathbf{S}_i^n = \mathbf{S}(\mathbf{U}_i^n)$ and $\mathbf{S}_i^{n+\frac{1}{2}} = \mathbf{S}(\mathbf{U}_i^{n+\frac{1}{2}})$. The densities of ions and electrons are integrated with the scheme Eq. (3.2.24) by exploiting the matrix of ionization probabilities given by Eq. (2.2.37) as follows:

$$\begin{cases} \begin{pmatrix} N_{0,s} \\ \vdots \\ N_{Z,s} \end{pmatrix}_i^{n+\frac{1}{2}} = P_s \left(t_n, \frac{\Delta t}{2} \right) \begin{pmatrix} N_{0,s} \\ \vdots \\ N_{Z,s} \end{pmatrix}_i^n, \\ N_{e|i}^{n+\frac{1}{2}} = N_{e|i}^n + \sum_s \sum_j \frac{q_{j,s}}{e} \left(N_{j,s|i}^{n+\frac{1}{2}} - N_{j,s|i}^n \right), \\ \begin{pmatrix} N_{0,s} \\ \vdots \\ N_{Z,s} \end{pmatrix}_i^{n+1} = P_s \left(t_{n+\frac{1}{2}}, \Delta t \right) \begin{pmatrix} N_{0,s} \\ \vdots \\ N_{Z,s} \end{pmatrix}_i^{n+\frac{1}{2}}, \\ N_{e|i}^{n+1} = N_{e|i}^{n+\frac{1}{2}} + \sum_s \sum_j \frac{q_{j,s}}{e} \left(N_{j,s|i}^{n+1} - N_{j,s|i}^{n+\frac{1}{2}} \right), \end{cases} \quad (3.2.25)$$

where the matrices of ionization probabilities $P_s(t_n, \Delta t/2)$ and $P_s(t_{n+\frac{1}{2}}, \Delta t)$ are calculated with the modules of the electric field $\sqrt{(E_x|i^n)^2 + (E_z|i^n)^2}$ and $\sqrt{(E_x|i^{n+\frac{1}{2}})^2 + (E_z|i^{n+\frac{1}{2}})^2}$, respectively. There is no stability restriction for Δt in the evolutive stage.

In the advective part [Eq. (3.0.3) with Eqs. (3.2.13) and (3.2.14)] the kernel acting on the Maxwell fields (B_y and D_x) is actually decoupled from the system treating the Fluid fields (N_e , γJ_x and γJ_z):

$$\begin{cases} \partial_t B_y + \partial_z E_x = 0, \\ \partial_t (\varepsilon_0^{-1} D_x) + \partial_z (c^2 B_y) = 0, \end{cases} \quad (3.2.26)$$

$$\begin{cases} \partial_t N_e + \partial_z (v_z N_e) = 0, \\ \partial_t (\gamma J_x) + \partial_z (v_z \gamma J_x) = 0, \\ \partial_t (\gamma J_z) + \partial_z (v_z \gamma J_z) = 0. \end{cases} \quad (3.2.27)$$

It is interesting to discuss the phase velocities at which the above different fields propagate:

1. Equation (3.2.26) reveals that the phase velocities of transverse electromagnetic fields (B_y and $\varepsilon_0^{-1}D_x$) are:

$$v_{\text{phase}}^{\text{MAX}} = \pm \frac{c}{\sqrt{n_0^2 + \chi^{(3)} E_x^2}} \approx \pm \frac{c}{\bar{n}}, \quad (3.2.28)$$

where \bar{n} is the effective (nonlinear) optical refractive index [Eq. (2.1.25)]. These fields travel at c in vacuum and at a smaller velocity inside the medium due to its refractive index. Indeed, \bar{n} depends on the laser pulse profile: it is maximum at the peak intensity and minimum at its leading and trailing edges. Hence, inside the medium, the laser peaks will travel at a speed lower than that of its leading and trailing edges, which ultimately causes the formation of an optical shock at trailing edges [49, 60]. This phenomenon is known as *pulse self-steepening*.

2. The fact that the longitudinal field $\varepsilon_0^{-1}D_z$ does not intervene in the advection stage reveals that it is electrostatic and thus it will not propagate outside the target.
3. Equation (3.2.27) shows that the phase velocities of the three fluid fields (N_e , γJ_x and γJ_z) are all equal to

$$v_{\text{phase}}^{\text{FLU}} = v_z. \quad (3.2.29)$$

This evidences that the fluid part of the system is actually *weakly hyperbolic* [104]. Fortunately, the potential numerical artifacts which may appear due to this lack of hyperbolicity are successfully overcome thanks to the numerical algorithm which we have designed for the fluid part (see Section F).

The MAXFLU 1D code numerically solves advections defined by Eqs. (3.2.26) and (3.2.27) thanks to explicit centred three-point finite volumes schemes, because they are not expensive to compute and are easily parallelizable. Two major schemes have been chosen. The first scheme is FORCE (First-ORder CEntred scheme), given by Eq. (3.2.30) below, which is the less diffusive first-order-accurate centred three-point finite-volume scheme (proposed by Toro; see chapter 7 of [163]). The second scheme is the Richtmyer

two-step Lax-Wendroff method, given by Eq. (3.2.31) below, the only³ three-point second-order-accurate finite-volume scheme (see Lax and Wendroff [100], and Richtmyer [139]). Both are two-step schemes, solving first the part of the waves travelling from right to left (backward) and then the part of the waves propagating from left to right (forward).

$$\begin{cases} \mathbf{U}_i^{n+\frac{1}{2}} = \frac{\mathbf{U}_{i+1}^n + \mathbf{U}_i^n}{2} - \frac{\Delta t}{2\Delta z} (\mathbf{F}_{i+1}^n - \mathbf{F}_i^n), \\ \mathbf{U}_i^{n+1} = \frac{\mathbf{U}_i^{n+\frac{1}{2}} + \mathbf{U}_{i-1}^{n+\frac{1}{2}}}{2} - \frac{\Delta t}{2\Delta z} (\mathbf{F}_i^{n+\frac{1}{2}} - \mathbf{F}_{i-1}^{n+\frac{1}{2}}). \end{cases} \quad (3.2.30a)$$

$$\begin{cases} \mathbf{U}_i^{n+\frac{1}{2}} = \frac{\mathbf{U}_{i+1}^n + \mathbf{U}_i^n}{2} - \frac{\Delta t}{2\Delta z} (\mathbf{F}_{i+1}^n - \mathbf{F}_i^n), \\ \mathbf{U}_i^{n+1} = \mathbf{U}_i^n - \frac{\Delta t}{\Delta z} (\mathbf{F}_i^{n+\frac{1}{2}} - \mathbf{F}_{i-1}^{n+\frac{1}{2}}), \end{cases} \quad (3.2.30b)$$

$$\begin{cases} \mathbf{U}_i^{n+\frac{1}{2}} = \frac{\mathbf{U}_{i+1}^n + \mathbf{U}_i^n}{2} - \frac{\Delta t}{2\Delta z} (\mathbf{F}_{i+1}^n - \mathbf{F}_i^n), \\ \mathbf{U}_i^{n+1} = \mathbf{U}_i^n - \frac{\Delta t}{\Delta z} (\mathbf{F}_i^{n+\frac{1}{2}} - \mathbf{F}_{i-1}^{n+\frac{1}{2}}), \end{cases} \quad (3.2.31a)$$

$$\begin{cases} \mathbf{U}_i^{n+\frac{1}{2}} = \frac{\mathbf{U}_{i+1}^n + \mathbf{U}_i^n}{2} - \frac{\Delta t}{2\Delta z} (\mathbf{F}_{i+1}^n - \mathbf{F}_i^n), \\ \mathbf{U}_i^{n+1} = \mathbf{U}_i^n - \frac{\Delta t}{\Delta z} (\mathbf{F}_i^{n+\frac{1}{2}} - \mathbf{F}_{i-1}^{n+\frac{1}{2}}), \end{cases} \quad (3.2.31b)$$

where $\mathbf{F}_i^n = \mathbf{F}(\mathbf{U}_i^n)$ and $\mathbf{F}_i^{n+\frac{1}{2}} = \mathbf{F}(\mathbf{U}_i^{n+\frac{1}{2}})$. Since both schemes utilize the first step, they are easy to adapt for hybrid schemes. The CFL stability condition for these two schemes is $v_{\text{phase}}\Delta t \leq \Delta z$, where v_{phase} represents the largest phase velocity in absolute value. MAXFLU 1D works with a constant time step, $\Delta t = c^{-1}\Delta z$, in order to have a regular grid in both space and time. This time step always assures stability because $|v_{\text{phase}}^{\text{MAX}}| \leq c$ and $|v_{\text{phase}}^{\text{FLU}}| \leq c$, according to Eqs. (3.2.28) and (3.2.29). In Section F we justify why the Maxwell advection is solved by Lax-Wendroff scheme, whereas the Fluid advection needs to be solved by a hybrid scheme based on FORCE and Lax-Wendroff.

The evolution [Eq. (3.2.23)] and advection [Eqs. (3.2.26) and (3.2.27)] stages can be numerically combined in different fractional-step schemes converging towards the solution of the whole system (3.2.6). Let $\mathcal{A}^{\Delta t}$ represent the discrete advection operator over the time step Δt . Calculating \mathbf{U}^{n+1} from \mathbf{U}^n by either Eq. (3.2.30) or Eq. (3.2.31) is formally denoted as $\mathbf{U}^{n+1} = \mathcal{A}^{\Delta t}\mathbf{U}^n$ (the spatial index i is omitted because all the points of the grid are solved). Analogously, the discrete evolution operator $\mathcal{S}^{\Delta t}$ is defined, which represents formally Eq. (3.2.24) as $\mathbf{U}^{n+1} = \mathcal{S}^{\Delta t}\mathbf{U}^n$. The first-order accurate splitting combinations are the advection-evolution and the evolution-advection fractional-step schemes: respectively $\mathbf{U}^{n+1} = \mathcal{S}^{\Delta t}\mathcal{A}^{\Delta t}\mathbf{U}^n$ and $\mathbf{U}^{n+1} = \mathcal{A}^{\Delta t}\mathcal{S}^{\Delta t}\mathbf{U}^n$. The advection-evolution splitting first advects the solution over Δt and next makes those advected values evolve over Δt . The evolution-advection splitting, instead, first integrates the solution over Δt and next advects those new values over Δt . For linear hyperbolic systems the splitting of the advection and the source is exact [65, 104, 163]. For nonlinear systems, instead, there exists a splitting error that vanishes when $\Delta t \rightarrow 0$. To converge faster, it is more interesting to use a second-order accurate splitting scheme: either the advection-evolution-

³Strictly speaking, this is true for linear systems. For nonlinear systems there exist alternatives of this scheme such as the MacCormack's scheme [116].

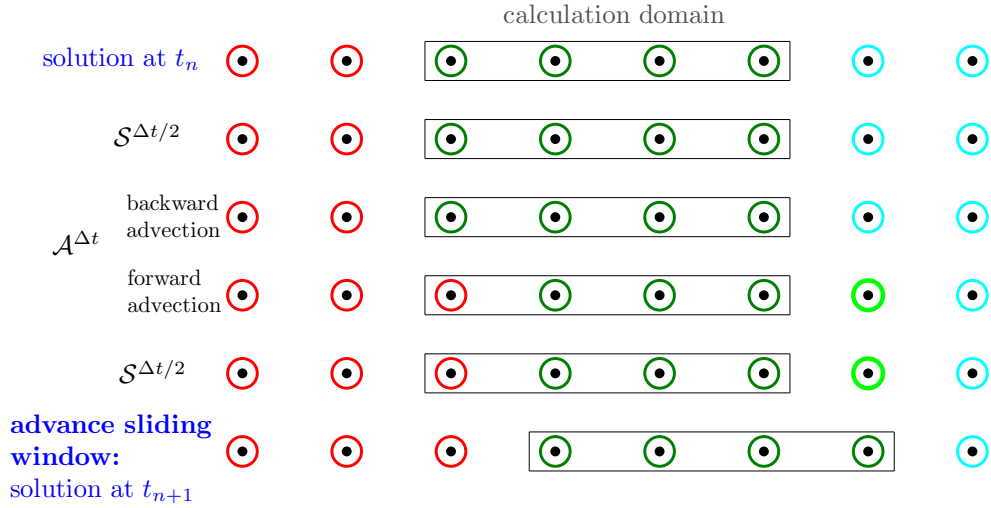


Figure 3.2.3: Illustration of a whole iteration of MAXFLU 1D, which uses the splitting $\mathbf{U}^{n+1} = \mathcal{S}^{\Delta t/2} \mathcal{A}^{\Delta t} \mathcal{S}^{\Delta t/2} \mathbf{U}^n$. The computation domain is represented with a box. The longitudinal positions (black dots) are signalled by a coloured circle: unknown values (red), known values (green) and laser-unperturbed values, i.e., the initial condition (cyan). During the first evolution stage ($\mathcal{S}^{\Delta t/2}$), the values belonging to the computational domain can be calculated and the unperturbed values at the right side do not change. Idem for the backward advection of $\mathcal{A}^{\Delta t}$. In the forward advection, the first value of the computational domain cannot be calculated and the value on its right-hand side is affected and must be stored (indicated with light green). Idem for the second evolution stage ($\mathcal{S}^{\Delta t/2}$). When the computational domain is advanced one longitudinal step forward, the initial situation is restored: all the values inside are known and the values on its left are unperturbed. Thus, apart from the initial condition, no extra boundary conditions are used by MAXFLU 1D.

advection splitting, $\mathbf{U}^{n+1} = \mathcal{A}^{\Delta t/2} \mathcal{S}^{\Delta t} \mathcal{A}^{\Delta t/2} \mathbf{U}^n$, or the evolution-advection-evolution splitting, $\mathbf{U}^{n+1} = \mathcal{S}^{\Delta t/2} \mathcal{A}^{\Delta t} \mathcal{S}^{\Delta t/2} \mathbf{U}^n$. The MAXFLU 1D code uses the latter because it presents two advantages. First, it allows us to solve exactly the propagation of the laser field in vacuum [Eqs. (3.2.30) and (3.2.31) are exact with $n_0 = 1$ and $\chi^{(3)} = 0$, when $\Delta t = c^{-1} \Delta z$]. Second, it reduces the amount of communications between processors when parallelizing the code, since only the advective stage requires such communications.

For computational reasons, the calculation domain of MAXFLU 1D is a sliding window that moves forward at the speed of light (see Fig. 3.2.3). With the fixed time step $\Delta t = c^{-1} \Delta z$, the window is advanced by one spatial step forwards at each time step.

Since the right side of the domain is not yet perturbed by the laser field, the fields are known and given by the initial condition (all the fields are zero except for the densities of neutrals). These values at the right boundary are the only boundary condition used by MAXFLU 1D

3.3 Comparing MAXFLU with UPPE and CALDER

3.3.1 MAXFLU versus UPPE

In this section, we shall discuss the suitability of MAXFLU 1D to deal with nonlinear optical effects on pulse propagation. To do this, we start reproducing with MAXFLU 1D the carrier wave shocks studied by Flesch *et al.* in Ref. [60].

Here, pulse self-steepening is studied for a dispersionless medium. In this context, the shock wave originates from the different phase velocities between the pulse components in the peak and the leading and trailing edges [49], according to Eq. (3.2.26). Figure 3.3.1 shows an optical shock formation at the trailing edge for $n_2 > 0$ as the peak travels slower. The agreement between Ref. [60] and MAXFLU 1D is very good in the spectra. After propagating over $20.2 \mu\text{m}$, the ratio between the third harmonic and the fundamental one is ≈ 0.11 with MAXFLU 1D and ≈ 0.12 in Ref. [60], whereas the fifth harmonics are in identical ratio ≈ 0.04 .

Next, we have examined shock formation in a dispersive medium. In Fig. 3.3.2 the pulse at two different positions is plotted in time, while the corresponding spectra are shown in Fig. 3.3.3. After propagating over $27 \mu\text{m}$, Fig. 3.3.3 reveals that a strong third order harmonic appears due to the Kerr effect, which is in good agreement between MAXFLU and Ref. [60] (relative ratio is ≈ 0.16). Higher harmonics are suppressed by the small GVD which prevents the carrier wave from breaking early. After the pulse has propagated upon $525 \mu\text{m}$, the situation differs: the development of an envelope shock is clearly visible and it is accompanied by a strong spectral broadening and modulations. On the trailing edge the third harmonic pulse starts to separate from the fundamental due to the difference in the group velocities of the fundamental and third harmonic. The agreement between MAXFLU 1D and Ref. [60] is very good, despite MAXFLU 1D utilizes Sellmeier's dispersion relation. Comparing specific values in the spectrum after propagating over $525 \mu\text{m}$, the normalized spectral amplitudes, with respect to the amplitude of the fundamental harmonic after propagating over $27 \mu\text{m}$, at $0.9\omega_0$, ω_0 and $3\omega_0$ are ≈ 0.59 , ≈ 0.22 and ≈ 0.034 with MAXFLU 1D and ≈ 0.56 , ≈ 0.21 and ≈ 0.038 in Ref. [60], respectively.

For completeness, we have compared directly MAXFLU 1D with UPPE 1D spectra in the THz band for argon target, as shown in Fig. 3.3.4. The agreement between the two codes is very good after propagating over 1 mm, because the differences due to the dispersion, only computed by UPPE 1D, appear over longer distances ($> 1 \text{ cm}$).

Figure 3.3.5 shows an example of results obtained in a filamentation regime promoting THz generation in air, calculated by the UPPE 3D code. The filamentation process manifests by the balance between Kerr self-focusing and plasma defocusing, leading

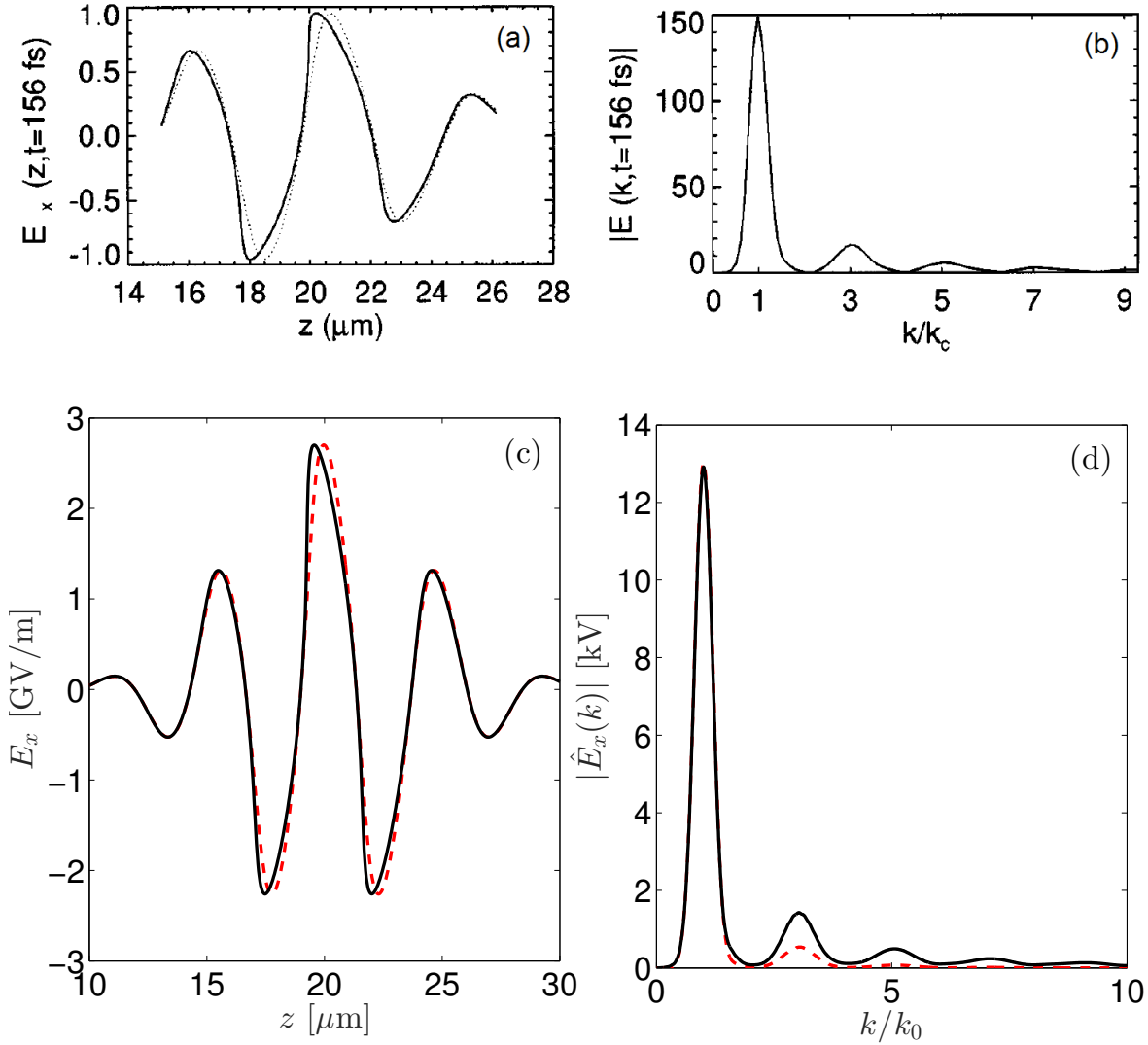


Figure 3.3.1: Kerr-induced wave shock in a dispersionless medium. One-colour laser pulse of wavelength $4.71 \mu\text{m}$ and FWHM-duration of 21.21 fs . For computational convenience, a strong third-order susceptibility $\chi^{(3)} = 0.022a_0^{-2}$ is considered. (a) Normalized electric field calculated by Ref. [60] after propagating over $6.8 \mu\text{m}$ (dotted curve, translated to the position of the solid curve) and $20.2 \mu\text{m}$ (solid curve). (b) Spectrum of the solid curve of (a) in terms of wavenumber k/k_0 . (c) Electric field calculated by MAXFLU 1D after propagating $6.8 \mu\text{m}$ (dashed red curve, translated to the position of the solid curve) and $20.2 \mu\text{m}$ (solid black curve). A laser intensity of $10^{12} \text{ W cm}^{-2}$ is chosen; the nonlinear refractive index is thus $n_2 = 8.25 \times 10^{-15} \text{ cm}^2/\text{W}$. (d) Spectra of (c) in terms of k/k_0 . Source: Flesch *et al.* [60].

to the “intensity clamping” phenomenon. The beam intensity, initially chosen around 25 TW cm^{-2} , increases during propagation due to the beamwidth narrowing caused by

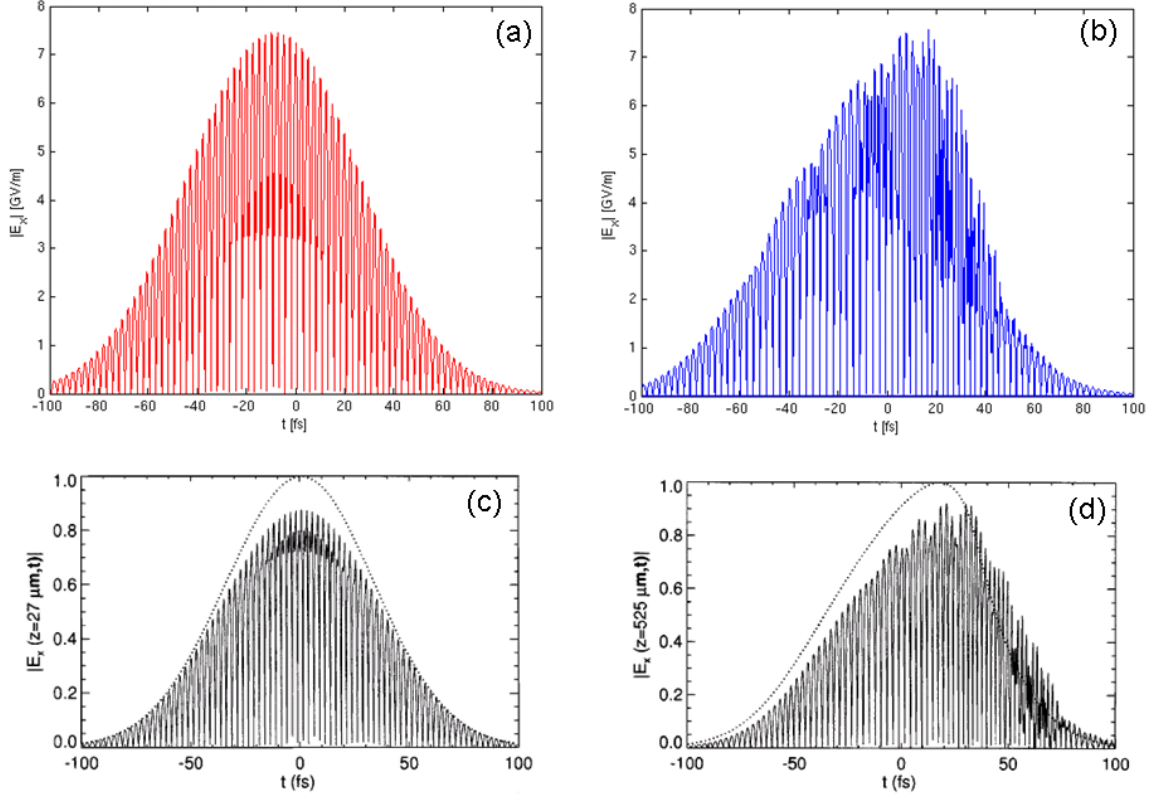


Figure 3.3.2: Kerr-induced optical shock in a dispersive medium. One-colour laser pulse of wavelength $1.5 \mu\text{m}$ and FWHM-duration of 56.6 fs . A strong third-order susceptibility $\chi^{(3)} = 0.01a_0^{-2}$ is considered. The linear refractive index of the medium is $n_0 = 1.1$ and the group velocity dispersion is $\text{GVD} = 25 \text{ fs}^2/\text{cm}$. MAXFLU 1D uses the Sellmeier dispersion model [Eqs. (2.1.15) and (2.1.16)]. (a) Electric field calculated by MAXFLU 1D over $27 \mu\text{m}$. (c) Normalized counterpart calculated in Ref. [60]. The dotted line refers to the solution to “classical” envelope equation. (b) Electric field calculated by MAXFLU 1D at $z = 525 \mu\text{m}$. (d) Normalized field calculated in Ref. [60]. Source: Flesch *et al.* [60].

the Kerr effect, until becoming high enough to trigger photoionization and creating free electrons. The balance between the two processes clamps the beam intensity around $80\text{--}100 \text{ TW cm}^{-2}$. We have compared, in time and Fourier domains, the THz fields obtained by UPPE 3D, filtered at 80 THz , with the results of MAXFLU 1D (overall intensity of 100 TW cm^{-2}) at three different positions, namely, $z = 1 \text{ cm}$, $z = 5 \text{ cm}$, and $z = 15 \text{ cm}$. For short distances — $z = 1 \text{ cm}$ and $z = 5 \text{ cm}$ — the results of both codes are quite resembling, even if MAXFLU 1D overestimates THz field amplitudes because the absence of transverse diffraction ($\partial_x = \partial_y = 0$) in 1D geometry makes the fields be confined along one dimension only. Because of this, the MAXFLU 1D code yields at $z = 15 \text{ cm}$ highly

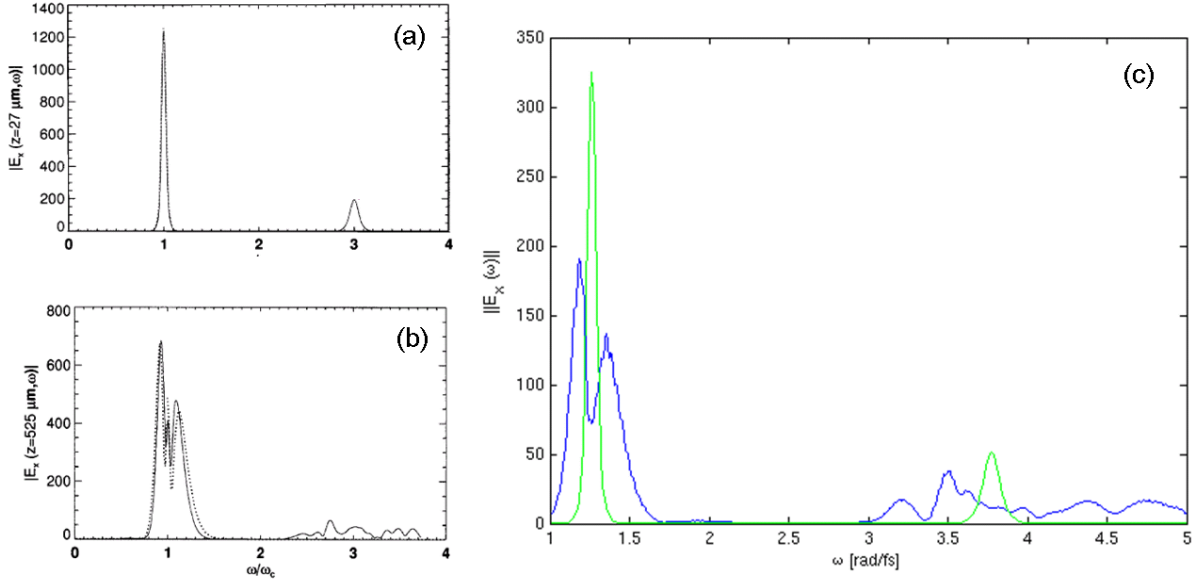


Figure 3.3.3: (a) Spectra of Fig. 3.3.2(c). (b) Spectra of Fig. 3.3.2(d). (c) Spectra of Fig. 3.3.2(a) (green curve) and Fig. 3.3.2(b) (blue curve).

diverging THz fields and produce results which cannot hold the comparison with full 3D numerical modelling as provided by UPPE 3D.

3.3.2 MAXFLU versus CALDER: relativistic plasmas at 10^{18} - 10^{19} W cm $^{-2}$

The Maxwell-Fluid approach is the *phase-space average* of the Maxwell-Vlasov model in the sense that it mainly holds whenever the phase space is monokinetic and applies to a single distribution function. In this section, we discuss the limits of this model at relativistic intensities. The results of MAXFLU 1D are compared with those of CALDER 1D, at different intensities and with different laser-gas configurations. The objective of this section is to prove that the Maxwell-Fluid model is able to capture the physics underlying laser-driven terahertz sources up to relativistic intensities, with the advantage that fluid codes are computationally faster than Particle-In-Cell codes.

In the classical scenario, plasma generation is initiated from the very first cycles of the laser pulse. These first ionized electrons are longitudinally displaced to the right from their equilibrium position (the position of their corresponding ions, assumed fixed) by the Lorentz force $\sim J_x B_y$ [Eq. (3.2.6f)], which corresponds to the longitudinal ponderomotive force. This ponderomotive force first pushes forward the electrons, which start to copropagate with the laser pulse. By feedback of this plasma motion, a positive longitudinal electric field is induced, which attracts the electrons back to the ions (i.e., to the

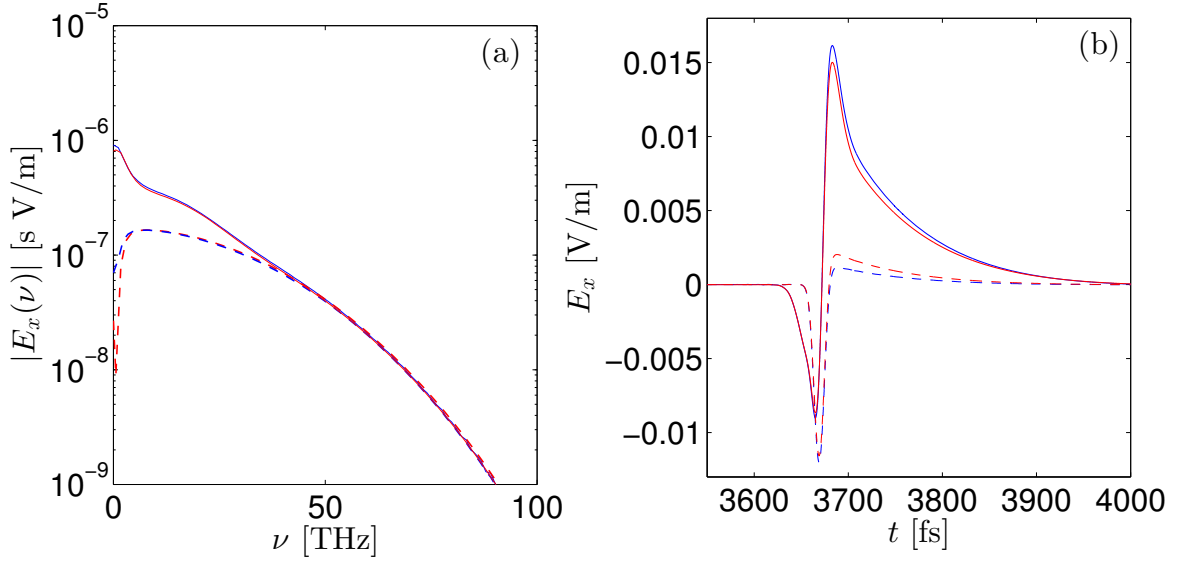


Figure 3.3.4: Comparison between MAXFLU 1D and UPPE 1D. A $1\text{-}\mu\text{m}$ 50-fs-FWHM one-colour laser pulse of 50 TW cm^{-2} is employed. The target is 1-bar argon, which is singly ionized according to QST ionization rate [Eq. (2.2.28)]. The nonlinear refractive index is $n_2 = 10^{-19}\text{ cm}^2/\text{W}$. UPPE 1D considers the dispersion model by Leonard [103], whereas MAXFLU 1D discards dispersion. (a) Terahertz spectra after propagating upon 1 mm, computed by MAXFLU 1D (blue curves) and UPPE 1D (red curves). Solid curves are calculated by taking into account Kerr and plasma effects; dashed curves do not consider the Kerr effect. (b) Corresponding radiated electric fields filtered at 90 THz.

left). This causes a longitudinal oscillation of the ionized electrons around the ions at the plasma frequency $\omega_p/\sqrt{\gamma}$ [152]. This plasma oscillation is associated to the generation of an oscillatory electrostatic longitudinal electric field in the wake of the laser beam, which leads to the creation of the wakefield. This scenario, depicted in the left-hand side of Fig. 3.3.6, can be well described up to *relativistic intensities* by the Maxwell-Fluid model because the phase space remains essentially monokinetic in helium or argon.

The intensity threshold from which relativistic effects start to play a significant role is usually considered at $\varepsilon_0\omega_0^2m_e^2c^3e^{-2}/2$ ($\sim 1.4 \times 10^{18}\text{ W cm}^{-2}$ for a wavelength of $1\text{ }\mu\text{m}$). At those intensities, if the cycles inside the pulse still ionize the gas, those electrons, born when the longitudinal electrostatic field is already created from the very first freed electrons, will acquire high velocities. The regions where the longitudinal electric field is negative correspond to accelerating regions for the electrons. At the back of this first accelerating region, the electrons whose velocity is above the group velocity of the laser pulse will be enough accelerated to co-propagate with the wakefield structure (which

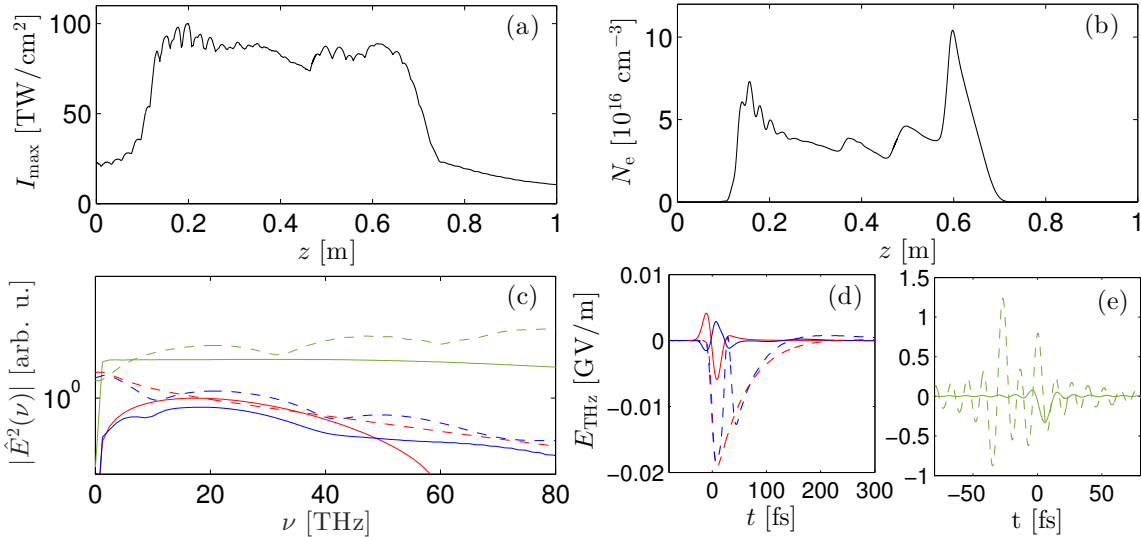


Figure 3.3.5: Laser filamentation in air. We employ a two-colour laser pulse with fundamental at 800 nm (second harmonic has its central wavelength at 400 nm) for an initial intensity of 25 TW cm^{-2} (10% in the second harmonic). The FWHM duration is 40 fs (20 fs for the second harmonic). The initial beamwidth is equal to $400 \mu\text{m}$. The cut-off frequency closing the THz window over which the THz field is evaluated by inverse Fourier transform is $\nu_{\text{co}} = 80 \text{ THz}$. (a) Maximum intensity and (b) maximum electron density forming an extended plasma channel computed over one metre-long distance. (c) THz spectra calculated by UPPE 3D (solid curves) and MAXFLU 1D (dashed curves) at different distances: $z = 1 \text{ cm}$ (red), $z = 5 \text{ cm}$ (blue), and $z = 15 \text{ cm}$ (green). Temporal profiles of THz field at (d) $z = 1 \text{ cm}$ and $z = 5 \text{ cm}$, and (e) $z = 15 \text{ cm}$.

travels at the laser group velocity) and stay in the accelerating region. These electrons are then *trapped* by the plasma wave and are accelerated to relativistic velocities, as plotted in the right side of Fig. 3.3.6, instead of acquiring an oscillatory motion. This phenomenon is referred as ionization-induced electron injection [50, 56]. This acceleration consumes energy from the longitudinal electric field, whose strength, therefore, decreases after the first cycle. This means that the first ionized electrons, which do not have enough initial velocity to get injected, will oscillate at a higher frequency than the relativistic one ($\omega_p/\sqrt{\gamma}$), closer to classical frequencies (ω_p). Due to electron injection, the space phase also broadens into two kinetic families of electrons and the Maxwell-Fluid model may no longer be valid after the first cycle of the longitudinal field in this context.

The comparison between both codes is done with the geometry represented in Fig. 3.3.7. A $100\text{-}\mu\text{m}$ -long linear gradient in the density of neutral argon is placed at the right of the vacuum-plasma interface in order to minimize the boundary effects on electrons. The

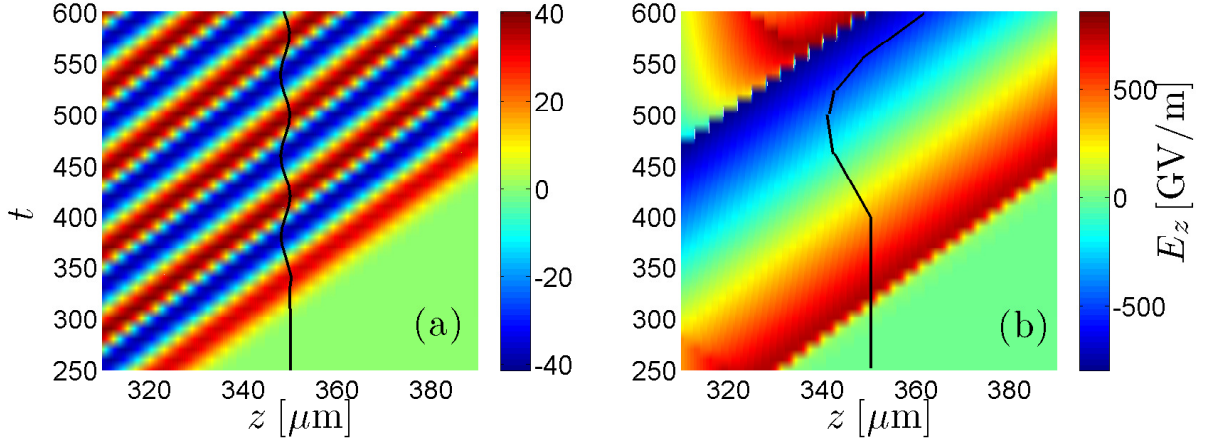


Figure 3.3.6: (a) Example of *fluid electrons* trajectory (black curve) for a one-colour 1- μm 35-fs-FWHM laser pulse with $1.4 \times 10^{18} \text{ W cm}^{-2}$, calculated with MAXFLU 1D (geometry: semi-infinite argon target starting from $z = 300 \mu\text{m}$, the peak of the laser envelope being at $z = 200 \mu\text{m}$ at $t = 0$). Electrons oscillate longitudinally, seeing an alternating longitudinal electric field (colour map). (b) Example of the trajectory followed by trapped electrons (the intensity is $2.2 \times 10^{19} \text{ W cm}^{-2}$). At high intensities, the electrons born in the second semi-cycle of the longitudinal electric field are strongly accelerated to the right. With the adequate initial velocity, they are accelerated in such a way that they always see a negative electric field and are accelerated close to the speed of light, by being trapped by the plasma wave.

density of neutrals at the plateau is $N_a = 2.4 \times 10^{17} \text{ cm}^{-3}$ (0.009-bar pressure). The peak of the laser envelope (one or two colours) is initially located at $39.8 \mu\text{m}$ at the left of the interface. The results of the two codes, MAXFLU 1D and CALDER 1D, are compared in time at $300 \mu\text{m}$ at the right of the interface, and in space after propagating during 1061 fs, i.e., after the laser envelope peak has propagated over $\sim 318 \mu\text{m}$. Comparisons are carried out with one-colour laser pulses (wavelength of $1 \mu\text{m}$ and FWHM of 35 fs) at two intensities: $1.4 \times 10^{18} \text{ W cm}^{-2}$ (the relativistic threshold) and $2.2 \times 10^{19} \text{ W cm}^{-2}$ (sixteen times the relativistic intensity threshold).

Two different gas targets are considered: helium and argon. As shown in Fig. 3.3.8 for 35-fs single-colour laser pulses, helium is completely ionized far before relativistic intensities ($\sim 10^{16} \text{ W cm}^{-2}$) and no ionization-induced electron injection is expected. Argon, instead, has a different behaviour. Its first eight electronic shells are ionized before the relativistic intensities: the Ar^{8+} ion has a very stable electronic configuration till the relativistic range 10^{17} - $10^{18} \text{ W cm}^{-2}$. Close to $10^{19} \text{ W cm}^{-2}$, argon can be ionized further and the additional ionized electrons will be injected at relativistic velocities. In this high-intensity regime, strong differences between the results of MAXFLU 1D and

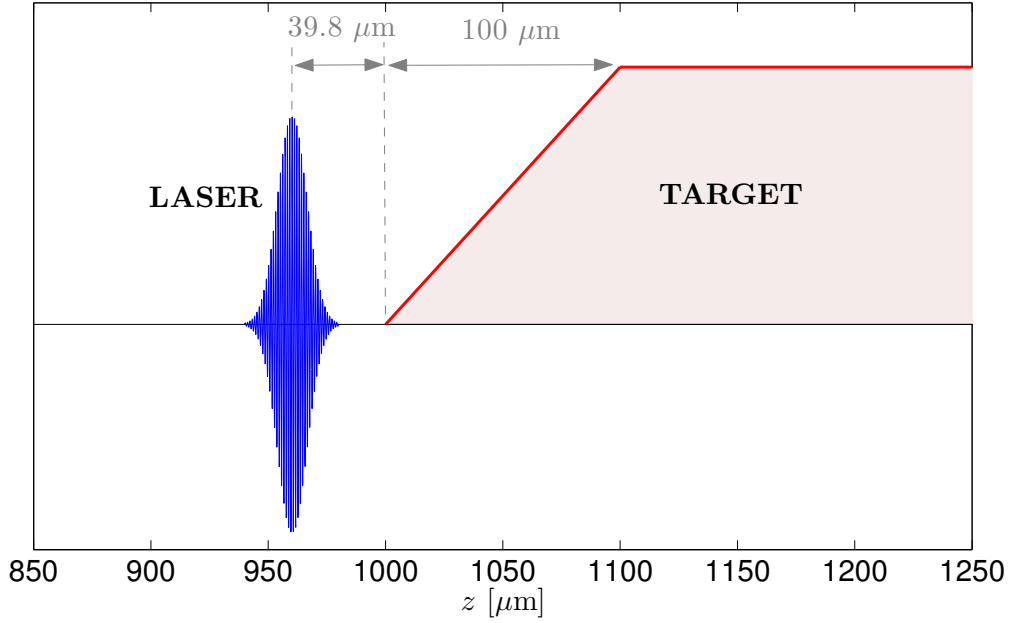


Figure 3.3.7: Geometry for the comparison MAXFLU 1D vs CALDER 1D. The laser pulse (blue curve) is located at 39.8 μm at the left of the interface. The initial density profile of neutrals (red curve) is shaped with a 100 - μm -long linear gradient.

CALDER 1D are expected to be observed.

Figure 3.3.9(a) superimposes the longitudinal linear momentum $p_z = m_e \gamma v_z$ distribution as a function of the longitudinal position z calculated by the code MAXFLU 1D (red curve) with the phase space calculated with the code CALDER 1D (colour bar), for argon ionized at 1.4×10^{18} W cm^{-2} . The agreement is very good in the first longitudinal cycles because the phase space, as expected, is monokinetic. This is not the case at 2.2×10^{19} W cm^{-2} , as illustrated in Fig. 3.3.9(b). The agreement between the two codes holds over the first cycle only; then the phase space broadens because the electrons resulting from the ionization of Ar^{9+} to Ar^{15+} are trapped. After that cycle, CALDER 1D reveals, as expected, that the frequency of the oscillating electrons increases due to the energy taken away from the longitudinal field through the trapping process. In contrast, the MAXFLU 1D code cannot cover similar broadening of the phase space; the plasma frequency does not change after the first cycle and its value keeps close to $\omega_p / \sqrt{\gamma}$. The differences between these two intensity levels are also seen when plotting the fields as a function of time. The agreement between the results of the two codes is very good in both longitudinal and transverse fields at 1.4×10^{18} W cm^{-2} [see Fig. 3.3.10 (a,b,c,d)]. However, at 2.2×10^{19} W cm^{-2} differences appear due to phase space broadening [see Fig. 3.3.10 (e,f)]. Only the first cycle of the longitudinal field is well described by MAXFLU 1D.

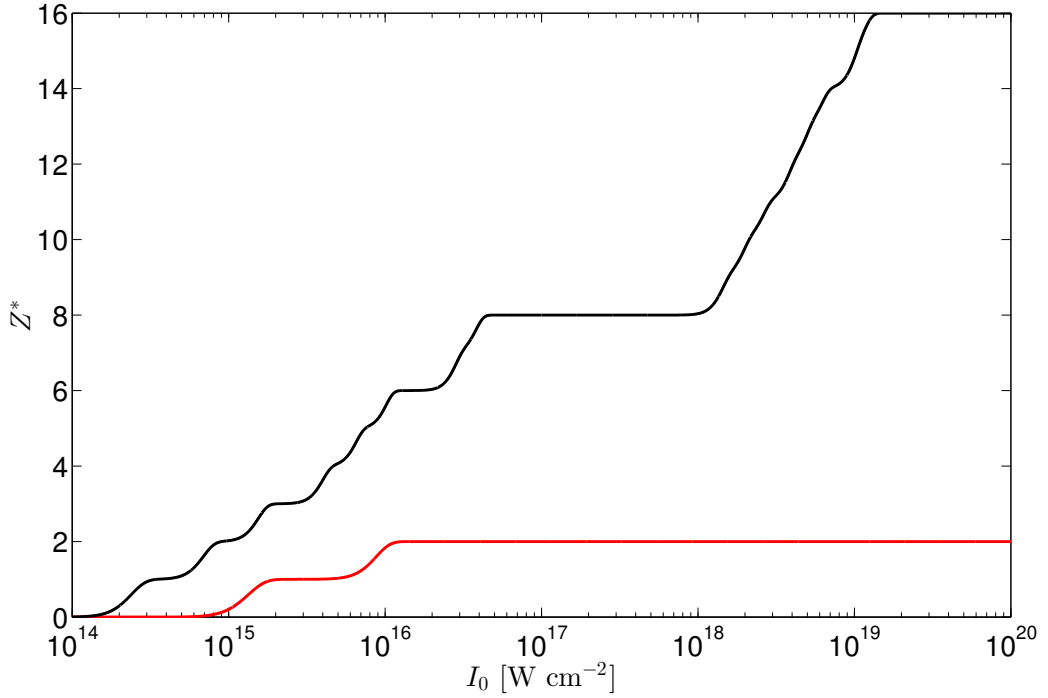


Figure 3.3.8: Degree of ionization, calculated with Eq. (2.2.41), for argon (black curves) and helium (red curves) by a single-colour laser pulse of $1\text{-}\mu\text{m}$ wavelength and FWHM duration of 35 fs. At $1.4 \times 10^{18} \text{ W cm}^{-2}$, argon is ionized ~ 8.6 times, whereas at $2.2 \times 10^{19} \text{ W cm}^{-2}$ it is fully ionized 16 times. Helium is fully ionized twice from $\sim 10^{16} \text{ W cm}^{-2}$.

Afterwards, as displayed by CALDER 1D, the amplitude and wavelength of these fields decrease. The head of the computed transverse terahertz pulse is well calculated by MAXFLU 1D because it is mostly due to photoionization; only differences between the results of MAXFLU 1D and CALDER 1D appear in its rear part.

For helium, instead, the phase space stays monokinetic due to the absence of further electron injection since only two electrons are available and immediately ionized (see Fig. 3.3.11) and, thus, both codes agree.

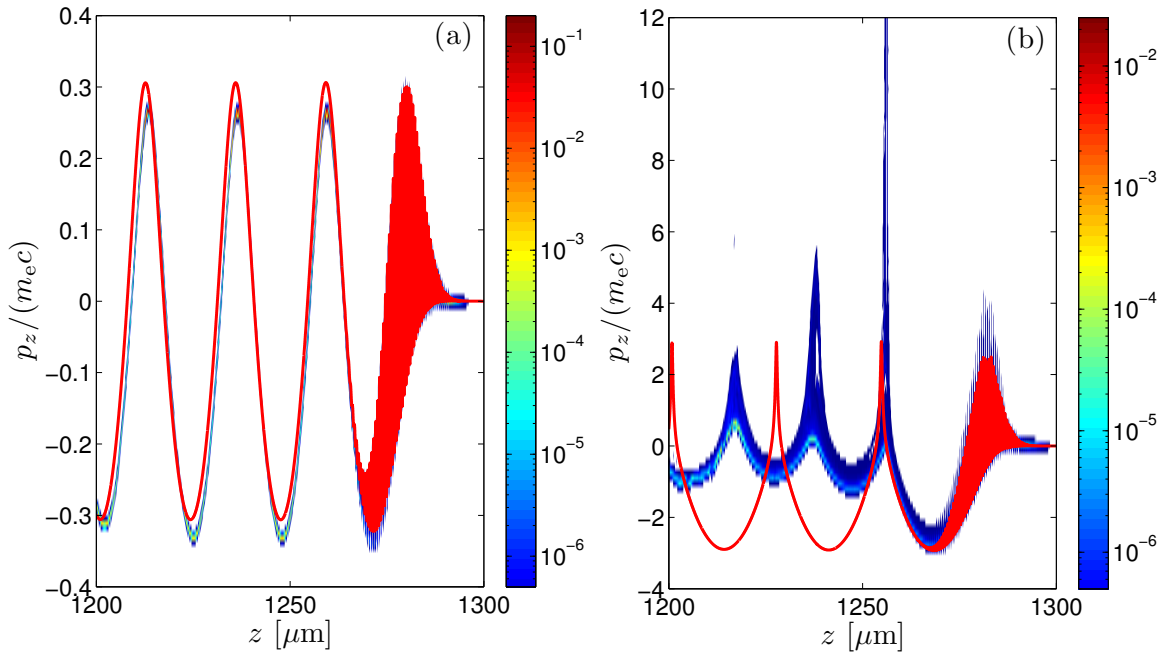


Figure 3.3.9: Linear momentum calculated by MAXFLU 1D (red curve) vs the phase space obtained from CALDER 1D (colour map), for argon, at $t = 1061$ fs, with a single-colour laser pulse. (a) At $1.4 \times 10^{18} \text{ W cm}^{-2}$. (b) At $2.2 \times 10^{19} \text{ W cm}^{-2}$. The resolution is $\Delta z = 7.6$ nm for MAXFLU 1D, and $\Delta z = 19.0$ nm and $\Delta p = 0.007 m_e c$ for CALDER 1D.

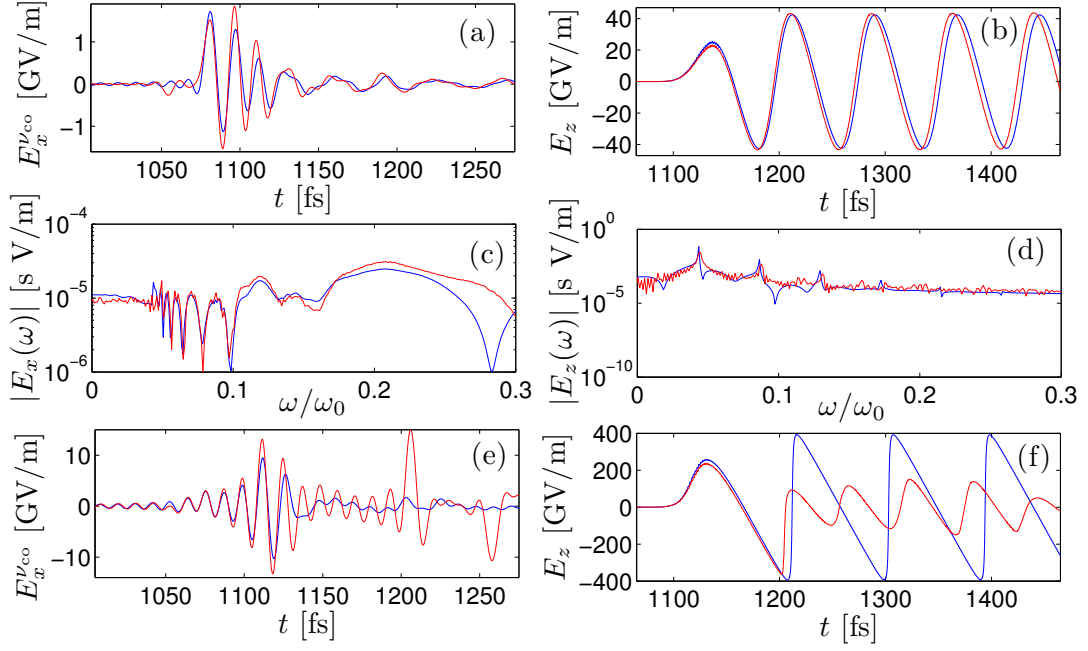


Figure 3.3.10: Transverse and longitudinal fields calculated by MAXFLU 1D (blue curves) and CALDER 1D (red curves), for argon, at $z = 300 \mu\text{m}$, with a single-colour laser pulse. (a) Transverse field (filtered at 90 THz) at $1.4 \times 10^{18} \text{ W cm}^{-2}$. (b) Longitudinal field at the same intensity. (c,d) Corresponding spectra. (e) Transverse field (filtered at 90 THz) at $2.2 \times 10^{19} \text{ W cm}^{-2}$. (f) Longitudinal field at the same intensity. The resolution is $\Delta t = 25.4$ as for (a,b,c,d), $\Delta t = 12.7$ as for (e,f) and $\Delta\nu = 0.26$ THz for MAXFLU 1D, and $\Delta t = 79.1$ as and $\Delta\nu = 0.47$ THz for CALDER 1D.

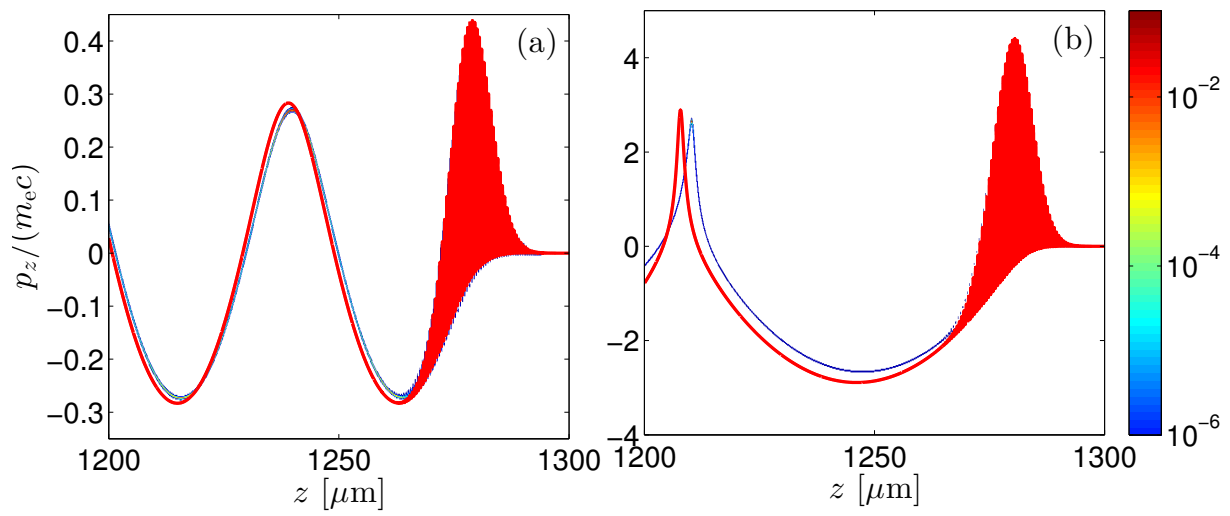


Figure 3.3.11: Longitudinal momentum as a function of the position z calculated by MAXFLU 1D (red curve) versus the phase space obtained from CALDER 1D (colour map), for helium, at $t = 1061$ fs, with a single-colour laser pulse. Intensities are (a) $1.4 \times 10^{18} \text{ W cm}^{-2}$, and (b) $2.2 \times 10^{19} \text{ W cm}^{-2}$.

3.4 Simplified 1/2D semi-analytical Maxwell-Fluid model

The one-dimensional version of the Maxwell-Fluid model [Eq. (3.2.6)] describes correctly the physics underlying laser-driven terahertz sources up to relativistic intensities. Thus, analytical solutions to these equations should improve the local current model (Section 2.4.2), and thereby supply quantitative evaluation of terahertz yields. That general solution is, however, not (still) achievable. Nevertheless, in this section a “1/2D” semi-analytical solution, obtained in a simplified context, is presented. The resulting equations include the local current model with the correct amplitude factor g and they are in good agreement with simulations of MAXFLU 1D. We call this model “1/2D” because the electric field evolves along the z -axis, but z is treated as a parameter.

Some hypothesis are here conjectured to simplify the starting Maxwell-Fluid model [Eq. (3.2.6)] into the “1/2D semi-analytical model”:

1. Laser intensities are limited to $\varepsilon_0\omega_0^2 m_e^2 c^3 e^{-2}/4 \sim 3.5 \times 10^{17} \text{ W cm}^{-2}$ for a wavelength of $1 \mu\text{m}$. This allows us to consider a constant Lorentz factor evaluated from the laser pulse only: $\gamma(t) = \gamma_L \simeq \sqrt{1 + 2I_0\varepsilon_0^{-1}\omega_0^{-2}m_e^{-2}c^{-3}e^2}$ (Sprangle *et al.* [152]).
2. The linear refractive index is $n_0 = 1$, i.e., the medium is non-dispersive and the laser pulse travels exactly at fixed group velocity equal to c .
3. The laser pulse, $E_L(t)$, which propagates forward, is assumed unperturbed upon propagation, which is a reasonable approximation for short distances of order of $100 \mu\text{m}$. The phaseshift between the different colours of the laser pulse can actually vary along the propagation axis, but this fact is omitted here.
4. Energy losses due to photoionization are neglected: $\mathbf{J}_{\text{loss}} = \mathbf{0}$.
5. The transverse electric field is expressed as the sum of the laser field and a perturbation caused by the propagation (i.e., the radiated field): $E_x = E_L + \tilde{E}_x$.
6. The transverse current is split accordingly: $J_x = J_L + \tilde{J}_x$. The laser-driven current is defined as $J_L = e^2 m^{-1} \gamma_L^{-1} (\partial_t + \nu_c)^{-1} N_{e,L} E_L$, where $N_{e,L} = \sum_s \sum_j q_{j,s} e^{-1} N_{j,s}$ is the electron density produced by photoionization.
7. No Kerr effect is considered on the longitudinal field. In the transverse field, the Kerr effect is assumed to be given only by the laser pulse: $J_{\text{KERR}} = J_{\text{NL,L}} = \partial_t(\chi^{(3)} E_L^3)$.
8. Since at subrelativistic intensities the electron velocities are small compared with the speed of light ($v_{x/z}^2 \ll c^2$), the convective terms of the currents, $\partial_z(\gamma v_z J_x) \sim v_x v_z$ and $\partial_z(\gamma v_z J_z) \sim v_z^2$, being of second order in \mathbf{v} , are neglected.

9. At leading order, it is reasonable to evaluate the source $\mathbf{\Pi}$ [Eq. (2.3.15)] from the laser fields ($J_x \simeq J_L$, $B_y \simeq B_L = E_L/c$ and $N_e \simeq N_{e,L}$).
10. Moreover, because E_L is assumed unperturbed, the *quasi-static hypothesis* is applied to longitudinal fields (Sprangle *et al.* [152]): $\partial_t + c\partial_z = 0$. This implies that the source for the longitudinal fields solely proceeds from the laser pulse and propagate at the speed of light together with the laser pulse.

Under these hypothesis, the one-dimensional Maxwell-Fluid model (3.2.6) reduces to two equation sets, one for the longitudinal fields [Eq. (3.4.1)] and one for the transverse fields [Eq. (3.4.2)]:

$$\begin{cases} \partial_t E_z = -\frac{1}{\varepsilon_0} J_z, & (3.4.1a) \\ \partial_t N_e + \partial_t \left(\frac{1}{ec} J_z \right) = \partial_t N_{e,L}, & (3.4.1b) \\ \gamma_L (\partial_t + \nu_c) J_z = \frac{e^2}{m} N_{e,L} E_z - \frac{e}{m} J_L B_L, & (3.4.1c) \end{cases}$$

$$\begin{cases} \partial_t B_y + \partial_z E_x = 0, & (3.4.2a) \\ \partial_t E_x + \partial_z (c^2 B_y) = -\frac{1}{\varepsilon_0} (J_x + J_{\text{KERR}}), & (3.4.2b) \\ \gamma_L (\partial_t + \nu_c) J_x = \frac{e^2}{m} N_e E_x + \frac{e}{m} J_z B_y. & (3.4.2c) \end{cases}$$

3.4.0.1 0D model for the longitudinal fields

The expressions for the longitudinal current and the electron density are directly given by Eqs. (3.4.1a) and (3.4.1b) as a function of E_z and the laser pulse:

$$J_z = -\varepsilon_0 \partial_t E_z, \quad (3.4.3)$$

$$N_e = N_{e,L} - \frac{J_z}{ec}. \quad (3.4.4)$$

By applying the operator $(\partial_t + \nu_c)$ to Eq. (3.4.3) and then combining it with Eq. (3.4.1c), the following equation for the longitudinal electric field is obtained:

$$\left(\partial_t^2 + \nu_c \partial_t + \tilde{\omega}_p^2 \right) E_z = \frac{e}{m_e \varepsilon_0 c \gamma_L} J_L E_L, \quad (3.4.5)$$

where the characteristic frequency of this system is:

$$\tilde{\omega}_p^2 = \frac{e^2 N_{e,L}}{m_e \varepsilon_0 \gamma_L}. \quad (3.4.6)$$

Eq. (3.4.5) simply means that all the longitudinal fields are initiated from the laser-driven ponderomotive force $\sim J_L E_L$ and then oscillate at the frequency $\tilde{\omega}_p = \omega_p / \sqrt{\gamma_L}$. By taking the Fourier transform of Eq. (3.4.5) and assuming that the plasma frequency is constant, the analytical spectrum can be obtained straightforwardly:

$$\hat{E}_z = -\frac{e}{m_e \varepsilon_0 c \gamma_L} \frac{\mathcal{F}[J_L E_L]}{(\omega^2 - i\nu_c \omega - \tilde{\omega}_p^2)}. \quad (3.4.7)$$

Similar expressions [Eqs. (2.4.33) and (2.4.41)] were earlier derived by Sprangle *et al.* [154] and D'Amico *et al.* [44] for a single wave in the non-relativistic limit $\gamma = 1$ by approximating the source term $\mathbf{\Pi}_z$ [Eq. (2.3.18)] with slowly-varying envelopes. Besides $\gamma \neq 1$, the three differences with these former works are the following:

1. In Eq. (3.4.5), the product of the rapid variations of $N_e(t)$ in $\tilde{\omega}_p^2$ through photoionization in the beam head [$\partial_t N_e(t) \sim \partial_t \sum_s \sum_j q_{j,s} e^{-1} N_{j,s}$] yields non-zero field contributions in the THz domain.
2. We account for wakefield plasma oscillations linked to a non-zero longitudinal field ($J_z \neq 0$) increasing from high enough laser intensities.
3. Our model equations apply to two-colour pulses and can easily be extended to more colours.

3.4.0.2 1D model for the transverse fields

By decomposing $J_x = J_L + \tilde{J}_x$ and $E_x = E_L + \tilde{E}_x$, Eq. (3.4.2c) gives:

$$\gamma_L (\partial_t + \nu_c) (J_L + \tilde{J}_x) = \frac{e^2}{m} N_e (E_L + \tilde{E}_x) + \frac{e}{m} J_z B_y, \quad (3.4.8)$$

which, by applying Eq. (3.4.4), (3.4.6) together with $J_L = e^2 m_e^{-1} \gamma_L^{-1} (\partial_t + \nu_c)^{-1} N_{e,L} E_L$, reduces to

$$(\partial_t + \nu_c) \tilde{J}_x = \varepsilon_0 \tilde{\omega}_p^2 \tilde{E}_x + \frac{e}{m_e \gamma_L} J_z \left(B_y - \frac{(E_L + \tilde{E}_x)}{c} \right). \quad (3.4.9)$$

In Eq. (3.4.9) one simplification is still performed: the transverse magnetic field is split as $B_y = B_L + \tilde{B}_y$, with $B_L = E_L/c$. Therefore, the second term of the right-hand side of Eq. (3.4.9) is proportional to $J_z (\tilde{B}_y - \tilde{E}_x/c)$. This term can be neglected for two reasons:

on the one hand, $\tilde{B}_y \simeq \tilde{E}_x/c$ holds and, on the other hand, $em_e^{-1}\gamma_L^{-1}c^{-1}J_z \ll \varepsilon_0\tilde{\omega}_p^2$ is reasonable at nonrelativistic intensities (oscillations of the electron density are small). Therefore, the equation for the radiated current density finally reads as:

$$\tilde{J}_x = (\partial_t + \nu_c)^{-1} \varepsilon_0 \tilde{\omega}_p^2 \tilde{E}_x. \quad (3.4.10)$$

Using Eqs. (3.4.2b) and (3.4.2a), the following wave equation is then easily obtained:

$$\left(\partial_t^2 - c^2\partial_z^2\right) E_x = -\frac{1}{\varepsilon_0}\partial_t(J_x + J_{\text{KERR}}). \quad (3.4.11)$$

By substituting $E_x = E_L + \tilde{E}_x$, knowing that the laser pulse verifies $(\partial_t^2 - c^2\partial_z^2)E_L = 0$, and $J_x = J_L + \tilde{J}_x$ with Eq. (3.4.10) into Eq. (3.4.11), the wave equation for the transverse radiated field follows:

$$\left(\partial_t^2 - c^2\partial_z^2 + \partial_t(\partial_t + \nu_c)^{-1}\tilde{\omega}_p^2\right) \tilde{E}_x = -\frac{1}{\varepsilon_0}\partial_t(J_L + J_{\text{KERR}}). \quad (3.4.12)$$

Remark 2. An equation similar to Eq. (3.4.12) was earlier proposed by Debayle *et al.* [45], where analytical solutions were obtained in the beam head and behind the laser pulse. Removing the propagation operator ∂_z^2 was proposed to obtain a non-propagating plasma-like model, equivalent to Eq. (3.4.5). That 0D model, however, is limited as it only provides a rough estimation of the first maximum oscillation in the transverse THz field.

The right-hand side of Eq. (3.4.12) depends, by hypothesis, exclusively on the laser field. It is therefore unperturbed during the propagation. Moreover, the plasma frequency $\tilde{\omega}_p$, given by Eq. (3.4.6), also depends exclusively on the same unperturbed laser field. Equation (3.4.12) is a wave equation and the only field that varies with the propagation distance z is \tilde{E}_x . This equation can thus be reduced in the laser comoving reference system by substituting the operator $\partial_t^2 - c^2\partial_z^2$ by $c^2(\partial_z + 2c^{-1}\partial_t)\partial_z$, where hereinafter z accounts for the propagated distance and t for the reduced time of the laser pulse (see González de Alaiza Martínez *et al.* [68])⁴:

$$\left[c^2\left(\partial_z + \frac{2}{c}\partial_t\right)\partial_z + \partial_t(\partial_t + \nu_c)^{-1}\tilde{\omega}_p^2\right] \tilde{E}_x = -\frac{1}{\varepsilon_0}\partial_t(J_L + J_{\text{KERR}}), \quad (3.4.13)$$

which contains the mechanisms yielding terahertz radiation along the laser polarization axis: the photocurrent mechanism (see Section 2.4.2), the Kerr effect (see Section 2.4.1) and the so-called plasma current oscillations related to the second term $\sim \tilde{\omega}_p^2\tilde{E}_x$ [45]. The

⁴With our change of variables $\tau = t - z/c$ and $\zeta = ct$ (and thus $\partial_t = \partial_\tau + \partial_\zeta$ and $\partial_z = -c^{-1}\partial_t$), we approximate the collisional term, assumed small, through the operator $(1 + \nu_c/(\partial_\tau + c\partial_\zeta))^{-1} \approx (1 + \nu_c/\partial_\tau)^{-1}$. For conciseness, we keep the name of the original variables (z, t) unchanged.

initial condition $\tilde{E}_x(t, z = 0) = 0$ is applied to deal with a well-posed problem.

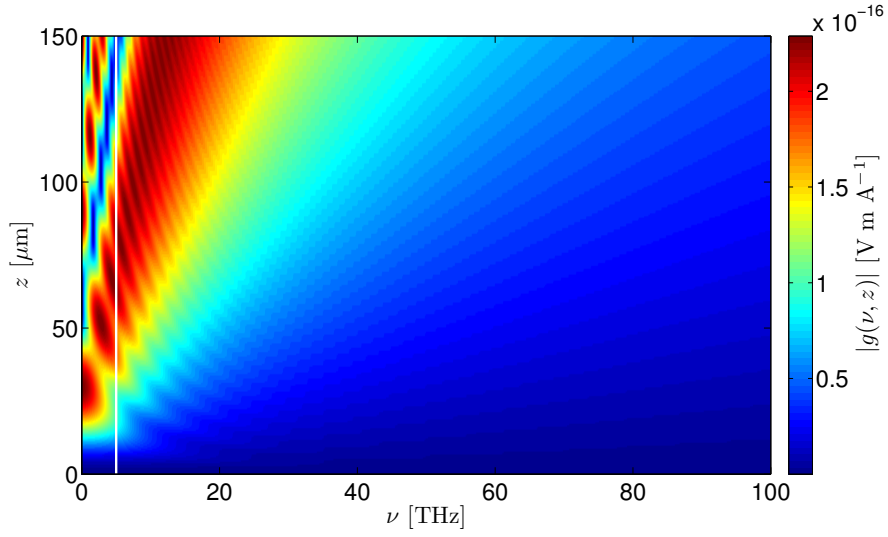


Figure 3.4.1: Prefactor of Eq. (3.4.16) as a function of the frequency and propagated distance for $\tilde{\nu}_p = 5$ THz ($\nu_c = 0$). The plasma frequency is indicated with a white line.

An analytical spectrum of Eq. (3.4.13) can be obtained assuming, for simplicity, that the plasma frequency, $\tilde{\omega}_p$, is constant. By Fourier transform, Eq. (3.4.13) reduces to an ordinary differential equation in z :

$$\left(c^2 \partial_z^2 + 2ci\omega \partial_z + \frac{\omega}{\omega - i\nu_c} \tilde{\omega}_p^2\right) \hat{E}_x = -\frac{1}{\varepsilon_0} \mathcal{F}[\partial_t (J_L + J_{\text{KERR}})], \quad (3.4.14)$$

whose solution, verifying $\hat{E}_x(\omega, z = 0) = 0$ and $\partial_z \hat{E}_x(\omega, z = 0) = 0$, is

$$\hat{E}_x = g(\omega, z) \mathcal{F}[\partial_t (J_L + J_{\text{KERR}})], \quad (3.4.15)$$

$$g(\omega, z) = -\frac{1}{\delta \tilde{\omega}_p^2 \varepsilon_0} \left[1 - \exp\left(-\frac{i\omega z}{c}\right) \left(\cos\left(\frac{z}{c} \Omega\right) + \frac{i\omega}{\Omega} \sin\left(\frac{z}{c} \Omega\right) \right) \right]. \quad (3.4.16)$$

$$\Omega = \sqrt{\omega^2 + \delta \tilde{\omega}_p^2}, \quad (3.4.17)$$

$$\delta = \frac{\omega}{\omega - i\nu_c}. \quad (3.4.18)$$

Equation (3.4.15) confirms the local current hypothesis done in Section 2.4.2, $\tilde{E}_x = g \partial_t J_L$, but with the correct factor g given by Eq. (3.4.16). This model predicts the following:

1. The photocurrent mechanism is the main mechanism of producing terahertz radiation, at least up to the relativistic limit, if ionization events contribute by constructive interference. This is confirmed in Sections 3.3.2, 5.1 and 5.2.
2. The Kerr effect has a direct contribution to the terahertz yield (see Section 4.1).
3. Terahertz emission increases with the propagated distance: a simple Taylor expansion can indeed reveal that $g(\omega, z) \sim z^2$ over short distances.
4. The prefactor $g(\omega, z)$ increases with the propagated distance in the neighbourhood of the plasma frequency $\tilde{\omega}_p$, as plotted in Fig. 3.4.1.
5. Plasma effects are accumulated along propagation, as also revealed by Fig. 3.4.1. Note that, however, Eq. (3.4.16) does not cover correctly the part of the spectrum $\omega < \tilde{\omega}_p$ due to the simplification of constant plasma frequency.

The simplified model given by Eqs. (3.4.5), (3.4.13) and (3.4.15) provides us with a useful tool for characterizing terahertz radiation: namely, photoionization and Kerr effect, in the laser beam, and plasma wakefield oscillations, beyond the laser head. The part involved with transverse currents unifies the Local Current theory with THz-driven four-wave mixing sources. Our model is, however, restricted to short distances for which the laser pulse remains unperturbed. In these conditions, the agreement with the code MAXFLU 1D, as displayed by Fig. 3.4.2, and with the on-axis results of CALDER 2D, as addressed in Section 5.2, is very good. The model does not include dispersion effects and it also discards the fact that terahertz generation is inherently nonlocal, so that the already produced terahertz can have a significant influence on the terahertz generation upon propagation (see Cabrera-Granado *et al.* [28]). Of course, our 1D model ignores multi-dimensional effects, which will be discussed in Section 5.2.

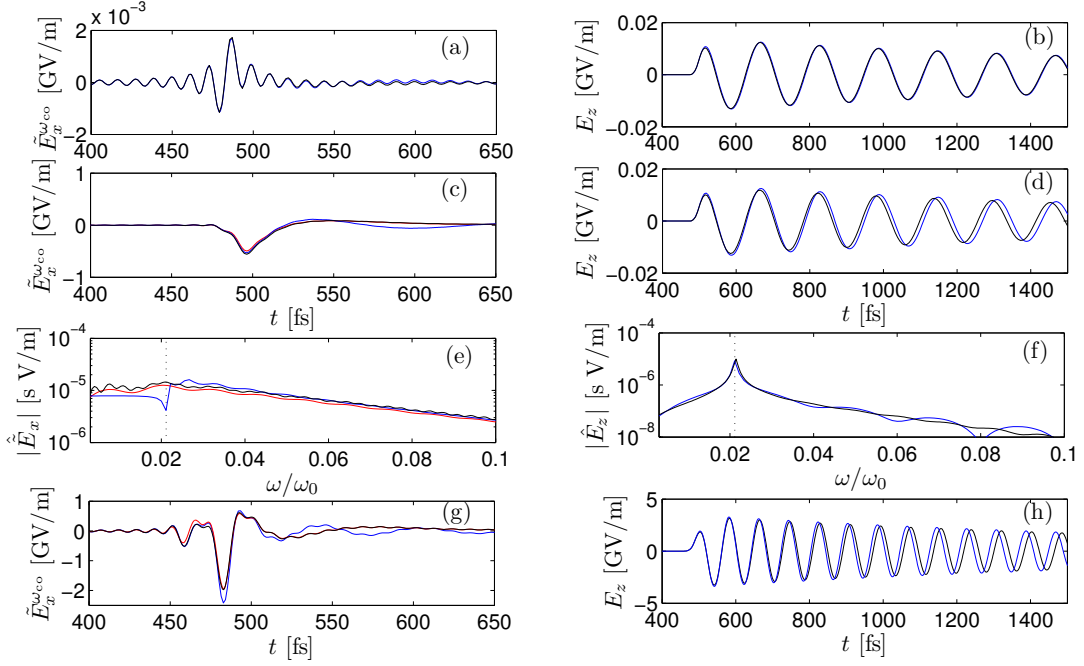


Figure 3.4.2: Comparison between the simplified Maxwell-Fluid model [black curves for Eqs. (3.4.5) and (3.4.13); red curves for Eq. (3.4.15)] and the code MAXFLU 1D (blue curves). The target (argon at 0.009 bar) starts at $z = 1000 \mu\text{m}$, and the peak of the envelope of the laser pulse is placed at $z = 850 \mu\text{m}$ at $t = 0$. Fields are calculated at $z = 1050 \mu\text{m}$. (a,b) Solutions for a single-colour 35-fs-FWHM $1\text{-}\mu\text{m}$ laser pulse at $10^{15} \text{ W cm}^{-2}$. (c,d) Solutions for a two-colour $1\text{-}\mu\text{m}$ laser pulse (35/17.5 fs-FWHM, $\pi/2$ phaseshift, 10% of intensity in the second harmonic) at the same intensity. (e,f) Corresponding spectra. The vertical dotted line corresponds to the plasma frequency $\tilde{\omega}_p \sim 0.021\omega_0$. (g,h) Solutions for the same two-colour laser pulse but at $10^{17} \text{ W cm}^{-2}$.

4 Terahertz generation at moderate intensities

Contents

3.1 Propagation and PIC codes	79
3.1.1 The UPPE code	79
3.1.2 The CALDER code	80
3.2 A new Maxwell-Fluid code: MAXFLU	83
3.2.1 Numerical strategy	86
3.3 Comparing MAXFLU with UPPE and CALDER	95
3.3.1 MAXFLU versus UPPE	95
3.3.2 MAXFLU versus CALDER: relativistic plasmas at 10^{18} - 10^{19} W cm $^{-2}$	98
3.4 Simplified ½D semi-analytical Maxwell-Fluid model	107

This section is devoted to laser-driven THz generation at moderate intensities ($\lesssim 10^{14}$ W cm $^{-2}$), which are typical of laser filamentation or loosely focused geometries, and for which the gas targets are weakly ionized ($Z^* \ll 1$). For more than two decades there has been an active experimental and theoretical research aiming to clarify the underlying physical mechanisms responsible for the THz emission from plasma gases. In 1993 Hamster *et al.* [72] reported the first experimental measurement of THz radiation emitted from an ionized gas by a single-colour laser pulse. The experimental setup is sketched in Fig. 4.0.1(a). The authors tightly focused a 50-mJ 800-nm laser pulse (peak power $\sim 10^{12}$ W) onto a helium gas cell at 1-bar pressure. The measured terahertz generation was attributed to the strong ponderomotive forces present at the focus, which generate a large density difference between ionic and electronic charges as the laser pulse length is short enough to inertially confine the ions. This charge separation results in a powerful subpicosecond electromagnetic transient delivery a THz pulse. A laser-to-THz conversion efficiency of less than 10^{-6} was measured in this experiment.

Some years later, the potential of two-colour setups started to be exploited in order to increase the laser-to-THz gain through a richer variety of nonlinear mechanisms. Two examples of these setups are represented in Fig. 4.0.1(b,c). The simplest setup [Fig. 4.0.1(b)]

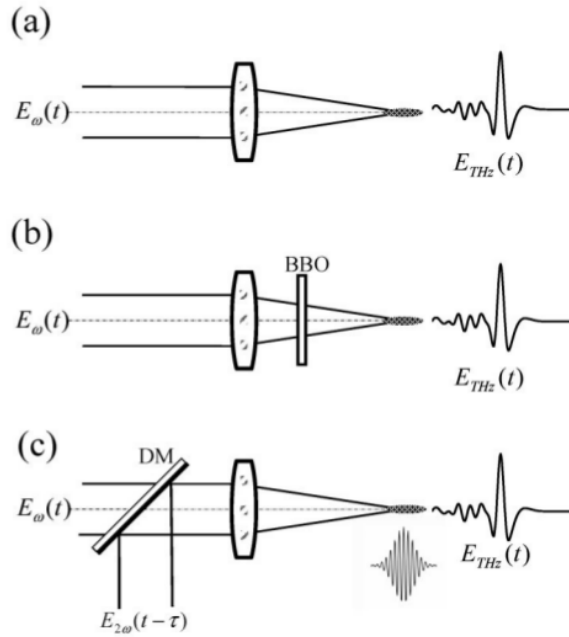


Figure 4.0.1: Three schematic illustrations of experimental setups. (a) A single optical beam excitation, in which the terahertz generation is assigned to the ponderomotive force to drive electrons and ions. (b) The common setup exploiting four-wave mixing from two colours that results from third-order nonlinear optical process. The 2ω -beam is generated from the fundamental colour passing through a type-I BBO crystal. (c) A dichroic mirror (DM) combines the second harmonic beam with the fundamental beam. Phase, amplitude, and polarization of both beams can be controlled individually. Source: Xie *et al.* [181].

uses a β -BBO (beta barium borate) crystal for second harmonic generation (SHG). The fundamental laser colour (ω), usually generated from a Ti:sapphire amplifier laser device, passes through the crystal after a linear focusing stage to generate the second-harmonic wave (2ω). Here, the second harmonic matches the phase of the fundamental. A more tunable step is presented in Fig. 4.0.1(c), which allows us to control individually the parameters of each laser colour: the phase, polarization, amplitude, and duration. The ω - and 2ω -colours are firstly separated by a dichroic mirror into different optical paths with individual polarizers, attenuators and a time-delay piezoelectric stage [not shown in Fig. 4.0.1(c)]. Then these beams are again recombined by another dichroic mirror and focused into the gas target. The latter setup allows to control the phaseshift between the two colours (ϕ) through the path difference between the two colours in the pulse propagation direction (Δl): $\phi = k_{2\omega}\Delta l = \omega_{2\omega}\tau$, where $k_{2\omega}$ and $\omega_{2\omega}$ are the wavenumber and frequency associated to the second harmonic and $\tau = \Delta l/c$ is the delay between the ω - 2ω beams.

Utilizing similar setups, Cook and Hochstrasser in 2000 improved the laser-to-THz gain to 10^{-5} - 10^{-4} by employing a two-colour 800+400-nm laser pulse focused in several gases (e.g., nitrogen, argon and air) at intensities $\sim 5 \times 10^{14}$ W cm $^{-2}$ [37]. They attributed the observed THz emission to the four-wave optical rectification in the gases [see Section 2.4.1]. They gave the following plane-wave expression for the radiated THz field, claiming that the THz radiation in the far field should be proportional to the second time derivative of the four-wave rectified component of the third-order polarization:

$$\tilde{E}_{\text{THz}}(t) \propto \chi^{(3)} E_{2\omega}(t) E_{\omega}^*(t) E_{\omega}^*(t) \cos \phi, \quad (4.0.1)$$

where

$$E_{\omega}(t) = \frac{a_{\omega}}{2} \exp [i\omega t] + \text{c.c.}, \quad (4.0.2)$$

$$E_{2\omega}(t) = \frac{a_{2\omega}}{2} \exp [i(2\omega t + \phi)] + \text{c.c.}, \quad (4.0.3)$$

and a_{ω} and $a_{2\omega}$ account for the amplitudes of the ω - and 2ω -pulses, respectively. In terms of the laser intensity, Eq. (4.0.1) is equivalent to:

$$\tilde{E}_{\text{THz}}(t) \propto \chi^{(3)} \sqrt{I_{2\omega} I_{\omega}} \cos \phi, \quad (4.0.4)$$

I_{ω} and $I_{2\omega}$ being the intensities of the ω - and 2ω -pulses, respectively, as earlier introduced in Eq. (2.4.4). The dependence of the THz radiation from four-wave mixing on the intensities and the phaseshifts ϕ was further studied by Xie *et al.* six years later [181]. These authors also applied to experimental measurements the model (4.0.4) in air plasma. They verified that, once the overall pulse energy exceeds the plasma ionization threshold, the measured THz energy was proportional to the energy of the ω -beam and the square root of the 2ω -beam energy, together with the coherent nature of the interference pattern with respect to $\cos \phi$. Moreover, they concluded that the optimal efficiency of the THz field generation is achieved when all the waves (ω , 2ω and the THz wave) possess the same polarization state in the four-wave mixing process, precisely as predicted by Cook and Hochstrasser. However, a surprising result is that this model predicts a THz field strength remaining four orders of magnitude lower than the measured THz field when the standard $\chi^{(3)}$ susceptibility of air is only considered. Since this phenomenological explanation based on the four-wave mixing mechanism could not match the conversion efficiency supplied by the third-order nonlinearity $\chi^{(3)}$, they already advanced that the laser-induced plasma should be a major nonlinearity in enhancing the THz generation.

One year later, Kim *et al.* [89, 90] performed several experiments using 800-nm one- and two-colour laser filaments in several gases (e.g., helium, dinitrogen, air, argon and

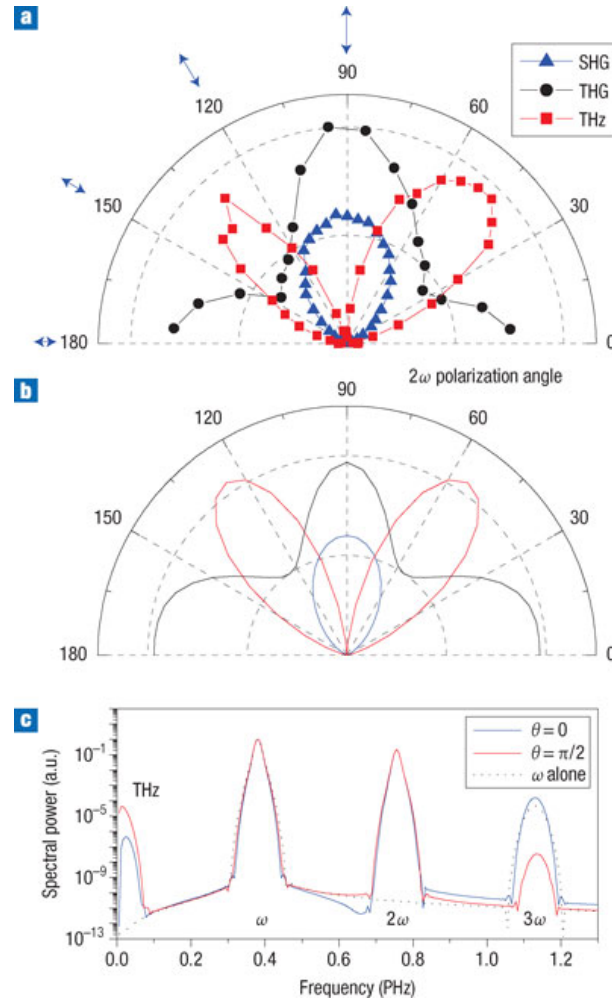


Figure 4.0.2: (a) experimental and (b) simulated harmonic generation (THz, second harmonic generation and third harmonic generation) with a two-colour setup where the polarization angle and intensity of the second laser harmonic vary. The simulations were performed for $I_\omega = 10^{14} \text{ W cm}^{-2}$ and $I_{2\omega} = 2 \times 10^{13} \text{ W cm}^{-2}$ with a relative phase $\phi = \pi/2$. (c) Anticorrelated THz and third harmonic spectral intensities for a phase of $\phi = 0$ and $\phi = \pi/2$. The relative phase is denoted as θ instead of ϕ . Source: Kim *et al.* [90].

krypton) at high intensities $\sim 10^{14} \text{ W cm}^{-2}$. They reported laser-to-THz energy conversion efficiencies $> 10^{-4}$ and broad THz spectra extending over 75 THz with two colours; the THz energy reported with a single colour was $< 1\%$ than the energy from the ω - 2ω setup. Microscopically, they associated the THz generation to the photoionization process, since the amount of far-field measured THz energy was consistent with the magnitudes of the tunnelling ionization rates of the gases. Indeed, they were the first to argue that when the laser field is asymmetric across individual optical cycles, a non-vanishing electron current surge can arise during optical field ionization, emitting the THz pulse

(see Section 2.4.2). For the laser pulse $E_L = E_\omega + E_{2\omega}$ [Eqs. (4.0.2) and (4.0.3)], they could explain the experimental measurements with the QST photoionization model and proposed a phase-matched condition depending on $\sin \phi$, under the assumption that the amplitudes are smaller than the atomic unit of electric field (i.e., $a_{2\omega} \ll a_\omega \ll E_{\text{au}}$):

$$\tilde{E}_{\text{THz}}(t) \propto \partial_t J \propto f(a_\omega) a_{2\omega} \sin \phi, \quad (4.0.5)$$

where

$$f(a_\omega) \approx \sqrt{\frac{E_{\text{au}}}{a_\omega}} \exp\left[-\frac{2}{3} \frac{E_{\text{au}}}{a_\omega}\right]. \quad (4.0.6)$$

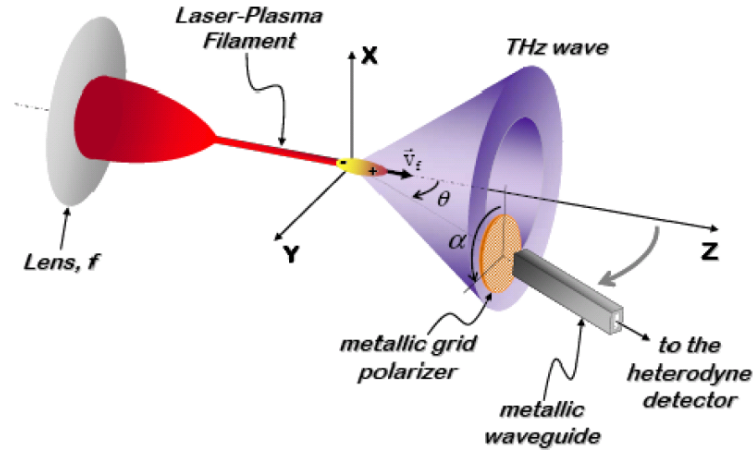


Figure 4.0.3: Experimental setup used for THz generation and measurement by D’Amico *et al.* [44]. The laser source is produced by a Ti:sapphire CPA amplifier. A single filament is produced when focusing the femtosecond laser pulse using a $f = 2$ m focal lens. Spectral components of the broadband THz radiation emitted by the plasma filament were detected with a heterodyne detector.

Equation (4.0.5) can be derived from the Local Current model [Section 2.4.2]. According to Eq. (2.4.24), the THz radiation is proportional to $v_f(t_n) \delta N_e^n$. By integrating in time the laser electric field, one easily has that $v_f(t_n) \propto a_{2\omega} \sin \phi$ provided that $a_{2\omega} \ll a_\omega$. On the other hand, for small degree of ionization, $\delta N_e^n \approx \sqrt{\pi} N_a \tau_n W[E_L(t_n)]$, given a limited Taylor expansion of Eq. (2.4.16). The ionization duration is given by $\tau_n \propto \sqrt{a_\omega / E_{\text{au}}}$ according to Eq. (2.4.10), where $|E(t_n)| \approx a_\omega$ and $|\ddot{E}(t_n)| \approx \omega^2 a_\omega$. The QST ionization rate for hydrogen [Eq. (2.2.28), with $2U_{i,H} U_{\text{au}}^{-1} = 1$] at ionization events is $W[E_L(t_n)] \approx W[E_\omega(t_n)] \propto (E_{\text{au}}/a_\omega) \exp[-(2/3)(E_{\text{au}}/a_\omega)]$. These values of $v_f(t_n)$, τ_n and $W(E_L(t_n))$ lead to Eq. (4.0.5). Figure 4.0.2 collects the experimental results by Kim *et al.* compared with their model of Eq. (4.0.5), evidencing the effect of the phase shift on the THz and high harmonic generation.

In the same years, several authors examine the directivity of the energy radiated by a laser-created plasma spot [9, 35, 117, 128, 130]. D'Amico *et al.* [44] also studied through experiments in air the off-axis THz emission from a femtosecond laser pulse propagating in a self-induced plasma channel (see Fig. 4.0.3). These authors supported their measurements by the transition-Cherenkov emission model, which simplifies the plasma channel as a L -long wire-antenna emitting from longitudinal plasma currents (see Section 2.4.4). In this context, THz emission by the plasma channel is usually evaluated through the flux of Poynting vector:

$$\mathbf{S} = \mathbf{E}_{\text{THz}} \times \mathbf{H}_{\text{THz}} = \frac{1}{\mu_0} \mathbf{E}_{\text{THz}} \times \mathbf{B}_{\text{THz}}. \quad (4.0.7)$$

One assumes that the THz electromagnetic fields verify $\mathbf{E}_{\text{THz}} = E_{\text{THz}} \hat{\mathbf{u}} = cB_{\text{THz}} \hat{\mathbf{v}}$ such that the direction vectors are perpendicular to each other and to the laser propagation direction $\hat{\mathbf{u}} \perp \hat{\mathbf{v}} \perp \mathbf{k}$. Thus, the flux of Poynting vector can be expressed in terms of the vector potential as:

$$\mathbf{S} = \frac{c}{\mu_0} B_{\text{THz}}^2 \hat{\mathbf{k}} = \frac{c}{\mu_0} |\nabla \times \mathbf{A}_{\text{THz}}|^2 \hat{\mathbf{n}}, \quad (4.0.8)$$

where $\hat{\mathbf{n}} = \mathbf{k}/k$. The vector potential radiated from the plasma channel, where the L -long distribution of longitudinal current $\mathbf{J}(\mathbf{r}, t)$ is considered independent of z , follows the well-known formula [79]:

$$\mathbf{A}(\mathbf{r}, t) = \frac{\mu_0}{4\pi} \iiint \frac{\mathbf{J}(\mathbf{r}', t')}{|\mathbf{r} - \mathbf{r}'|} d\mathbf{r}', \quad (4.0.9)$$

where $t' - t = |\mathbf{r}' - \mathbf{r}|/c$ is the time for the field to travel from the point of emission to the point of observation. By considering the far field limit, $r \gg r'$ and $r \gg k^{-1} = c/\omega$, Eq. (4.0.9) in Fourier domain simplifies to:

$$\hat{\mathbf{A}}(\mathbf{r}, \omega) = \frac{\mu_0}{4\pi} \frac{e^{ikr}}{r} \iiint \hat{\mathbf{J}}(\mathbf{r}', \omega) e^{-i\mathbf{k} \cdot \mathbf{r}'} d\mathbf{r}'. \quad (4.0.10)$$

The total THz energy is given by the integral of the Poynting vector:

$$U_{\text{THz}} = \int dt \int r^2 |\mathbf{S}| d\Omega, \quad (4.0.11)$$

where Ω accounts for the solid angle. Thanks to Parseval's theorem and by using Eq. (4.0.8), Eq. (4.0.11) is equivalent to:

$$U_{\text{THz}} = \frac{1}{\pi} \frac{c}{\mu_0} \int d\omega \int r^2 |\nabla \times \hat{\mathbf{A}}_{\text{THz}}|^2 d\Omega, \quad (4.0.12)$$

which, once differentiated and by utilizing Eq. (4.0.10), gives the following spectral THz energy density in the laser co-moving reference system (here $v_g = c$):

$$\frac{d^2 U_{\text{THz}}}{d\omega d\Omega} = \frac{1}{\pi} \frac{c}{\mu_0} r^2 |\nabla \times \hat{\mathbf{A}}_{\text{THz}}|^2 = \frac{c\mu_0}{16\pi^3} r^2 \left| \nabla \times \iiint \hat{\mathbf{J}}(\mathbf{r}', \omega) e^{i\omega z'/c - i\mathbf{k} \cdot \mathbf{r}'} d\mathbf{r}' \right|^2. \quad (4.0.13)$$

The integral of Eq. (4.0.13) is now calculated as

$$\begin{aligned} \iiint \hat{\mathbf{J}}(\mathbf{r}', \omega) e^{i\omega z'/c - i\mathbf{k} \cdot \mathbf{r}'} d\mathbf{r}' &= \int_0^L e^{i\omega z'/c - ik_z z'} \hat{\mathbf{J}}(\mathbf{k}_\perp, \omega) dz' = \\ \int_0^L e^{i\omega/c(1-\cos\theta)z'} \hat{\mathbf{J}}(\mathbf{k}_\perp, \omega) dz' &= -ic \frac{e^{i\omega/c(1-\cos\theta)L} - 1}{\omega(1-\cos\theta)} \hat{\mathbf{J}}(\mathbf{k}_\perp, \omega). \end{aligned} \quad (4.0.14)$$

After substituting Eq. (4.0.14) into Eq. (4.0.13) and applying Fraunhofer approximation $1/r^2 \ll k/r$, one finds:

$$\frac{d^2 U_{\text{THz}}}{d\omega d\Omega} = \frac{\omega^2 L^2}{16\varepsilon_0 \pi^3 c^3} \text{sinc}^2 \left[\frac{\omega L}{2c} (1 - \cos\theta) \right] |\hat{\mathbf{n}} \times \hat{\mathbf{J}}(\omega, \mathbf{k}_\perp)|^2. \quad (4.0.15)$$

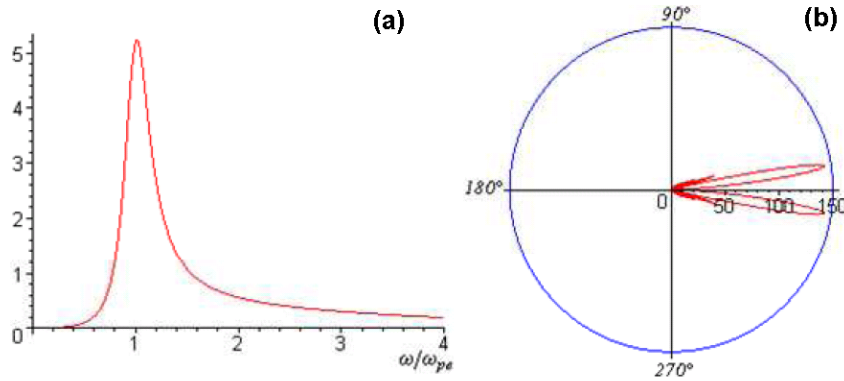


Figure 4.0.4: Examples of (a) spectrum and (b) angular distribution of a conical electromagnetic emission for a plasma length $L\omega/c = 200$ induced by longitudinal plasma waves according to the transition-Cherenkov radiation model. Source: D'Amico *et al.* [44].

Here, $\hat{\mathbf{J}}(\omega, \mathbf{k}_\perp)$ is the Fourier transform of the radiating current density expressed in the pulse retarded time $\tau \equiv t - z/c$ and in the (x, y) plane, ω is the pulse frequency, \mathbf{k}_\perp denotes its transverse wavevector, φ is the azimuthal angle while θ is the polar angle between $\hat{\mathbf{n}}$ and the laser field wavevector along the propagation axis [$k_z = (\omega/c) \cos\theta$]. Equation (4.0.15) holds for a current density \mathbf{J} assumed to be uniform over the propagation axis z and whenever the laser pulse components (colours) have walk-off and phase mismatch lengths much longer than the plasma length L . From Eq. (4.0.15) the directivity of a plasma-

induced THz emission is thus linked to that of the current density \mathbf{J} triggered by different source terms, such as photoionization or ponderomotive forces. This link is expected to provide crucial information on the nonlinearities prevailing in the far-field THz emissions, since the factor $|\hat{\mathbf{n}} \times \hat{\mathbf{J}}|^2 = \sum_j |\hat{J}_j|^2 f_j(\theta, \varphi)$ with $j = x, y, z$ has characteristic angular distributions $f_j(\theta, \varphi) = 1 - (\hat{\mathbf{n}} \cdot \hat{\mathbf{e}}_j)^2$, where $\hat{\mathbf{n}} = \sin \theta \cos \varphi \hat{\mathbf{e}}_x + \sin \theta \sin \varphi \hat{\mathbf{e}}_y + \cos \theta \hat{\mathbf{e}}_z$. In particular, if longitudinal forces are dominant ($f_z = \sin^2 \theta$), the angular distribution of the radiated power flow exhibits multiple (N) lobes at angular positions fixed by the relationship

$$\theta = 2 \arcsin \left(\sqrt{\frac{N\lambda}{4L}} \right), \quad (4.0.16)$$

$\lambda = 2\pi c/\omega$ being the emission wavelength. The angular pattern here consists of two off-axis symmetric lobes ($N = 1$) and the opening angle is inversely proportional to the plasma length [see Fig. 4.0.4(b)]. When transverse forces instead prevail, the geometrical factors f_x, f_y are close to unity for small angles $\theta \ll 1$ and the central lobe is filled, up to small conical deviations $\ll 10^\circ$ [186]. This feature holds except if \hat{J}_y vanishes on-axis ($k_\perp = 0$), which may be the case for instance for a ponderomotively driven current.

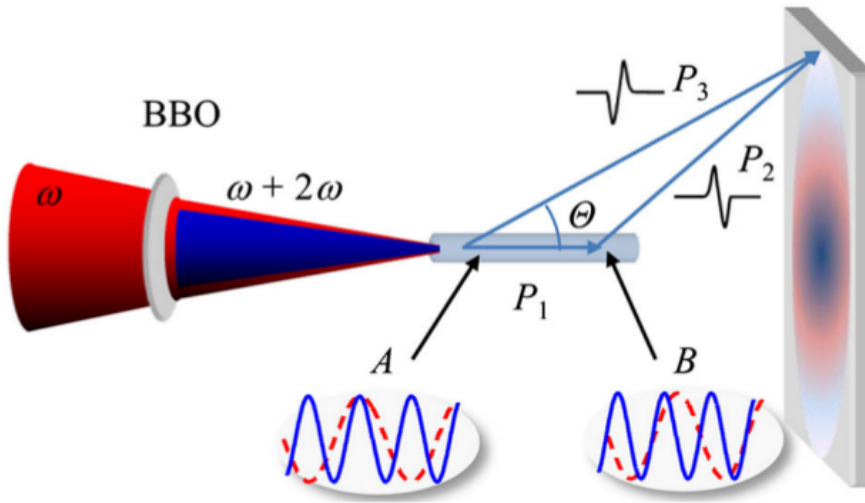


Figure 4.0.5: Schematic of THz emission from a long, two-colour laser-produced filament. The phase slippage between 800 nm (dashed red curves) and 400 nm (solid blue curves) pulses along the filament results in a periodic oscillation of microscopic current amplitude and polarity. The resulting far-field THz radiation is determined by interference between the waves emitted from the local sources along the filament. Source: You *et al.* [186].

When the laser-plasma filament is long (> 10 mm), the relative phase between the ω -

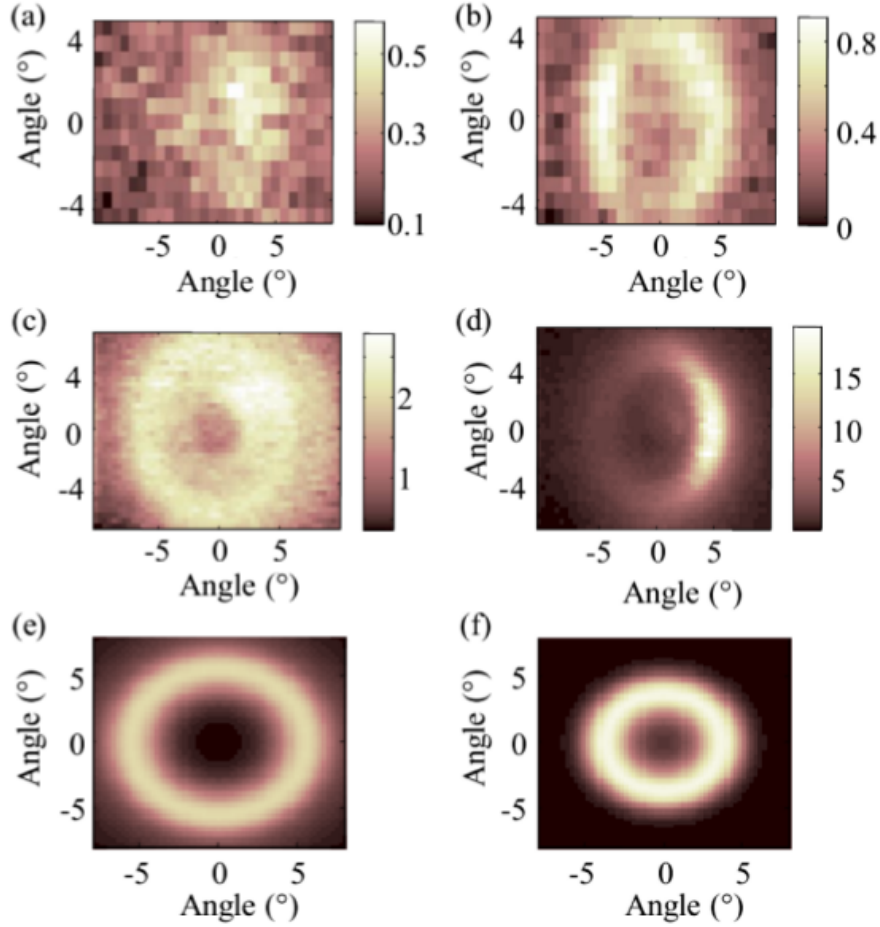


Figure 4.0.6: Measured far-field THz radiation profiles obtained with (a),(b) 10-mm-long and (c),(d) 40-mm-long filaments, all obtained by raster scanning of a pyroelectric detector with a silicon filter. For THz imaging, the pyroelectric detector is raster scanned over $5 \text{ cm} \times 3.5 \text{ cm}$, which provides a detection angle of $\sim 10^\circ$. Additional (a),(c) Teflon and (b), (d) germanium filters are used for low ($< 3 \text{ THz}$) and high ($< 10 \text{ THz}$) frequency band transmission. (e),(f) Simulated THz profiles (using phase matching conditions) for the long filament case. Source: You *et al.* [186].

and 2ω -beams is expected to vary along the distance as [17, 19, 69, 92, 127, 186]:

$$\phi = \frac{\omega L}{c} (n_\omega - n_{2\omega}) + \phi_0, \quad (4.0.17)$$

where n_ω and $n_{2\omega}$ are the refractive indices of the plasma channel at ω and 2ω frequencies, respectively, contributed from both air and plasma dispersion, i.e.,

$$n_{\text{filament},\omega} = n_{\text{air},\omega} + n_{\text{plasma},\omega}, \quad (4.0.18)$$

where $n_{\text{plasma},\omega} \approx \sqrt{1 - \omega_p^2/\omega^2}$, L is the plasma filament length and ϕ_0 is the relative phase at the starting point of the filament, determined by the frequency doubling process and air dispersion prior to filament formation. The dephasing length—the distance over which the resulting THz polarity remains the same—is given by

$$L_d = \frac{\lambda_{\text{THz}}}{2(n_\omega - n_{2\omega})}. \quad (4.0.19)$$

The fact that the phase between the two laser colours varies continuously along the filament distance causes an oscillatory THz output in the forward direction which is maximal when $L \approx L_d$. You *et al.* [186] claimed that such a phase matching occurs in the off-axis direction by a simple interference effect. As shown in Fig. 4.0.5, for channel length comparable or longer to L_d the THz waves produced along the filament have both positive and negative polarities. The waves produced at two points A and B, separated by a distance L_d and having a positive polarity in A and a negative one in B, interfere constructively if the path difference between the two THz emissions is:

$$\Delta l = (P_1 + P_2) - P_3 = \lambda_{\text{THz}} \left(m + \frac{1}{2} \right), \quad (4.0.20)$$

where $m = 0, 1, 2, \dots$ is an integer and λ_{THz} is the radiation wavelength. For $m = 0$, the law of cosines applied to Fig. 4.0.5 gives the following angle of constructive interference in the far field limit (i.e., $P_3 \gg L_d, \lambda_{\text{THz}}$):

$$\cos \theta = \frac{P_1^2 + P_3^2 - P_2^2}{2P_1P_3} \approx 1 - \frac{\lambda_{\text{THz}}}{2L_d}, \quad (4.0.21)$$

where $P_1 = L_d$ and P_2 is expressed as a function of P_3 thanks to Eq. (4.0.20).

This interference model explains the off-axis propagation of the THz radiation inside a cone, which produces a ring in the far-field. It has recently been validated through experiments with very good agreement [92, 127, 186]. In such experiments, a pyroelectric detector is employed to detect the THz radiation emitted from the filament, using for example a silicon filter to block unwanted infrared and optical light. You *et al.* [186] utilized additional filters to discriminate THz emission at different frequency bands: THz frequencies mostly at < 10 THz are detected by a germanium wafer, whereas a 3-mm-thick Teflon window is used as a low-pass filter to detect < 3 THz. In Fig. 4.0.6(a,b) the measured far-field THz profiles emitted from a short laser-plasma filament of ~ 10 mm are depicted (1.3-mJ-energy, 5-mm-beamwidth laser pulse focused with a lens of $f = 15$ cm). In Fig. 4.0.6(c,d), instead, the THz field radiated from a long laser-plasma filament of ~ 40 mm is captured (5-mJ-energy 10-mm-beamwidth laser pulse focused with lens of $f = 300$ cm). Here the dephasing length is $L_d \approx 22$ mm. When the length of the filament

is shorter than L_d , like in Fig. 4.0.6(a,b), all the THz waves have the same polarity and constructive interference occurs in the forward direction, producing THz radiation peaked on axis. In the opposite case, like in Fig. 4.0.6(c,d), interference acts destructively at centre and forms a ring profile (here the peak cone-emission angle is $\sim 5^\circ$), which, however, reaches stronger THz amplitudes.

Below we present two new results related to this field:

- On the one hand, comprehensive 3D numerical simulations supporting experimental measurements show the combined contribution of both bound and free electrons to the THz radiation generated by two-colour laser filaments in air. The THz signature of the bound electrons coming from the four-wave mixing mechanism is much weaker and higher in frequency than the distinctive plasma lower-frequency contribution of free electrons. The former is in forward direction while the latter is in a cone and reveals an abrupt downshift to the plasma frequency. This results have been published in Ref. [4].
- On the other hand, since early experiments already proved that photocurrents are the main mechanism responsible for THz emission when using two-colour laser setups, one wonders how to boost the THz generation by controlling the laser parameters, for instance by suitably distributing pulse energies and phaseshifts in multiple-frequency pumps. The LC model predicts that a sawtooth-like waveform is optimal for achieving this goal. Due to the impossibility of carrying out experiments on this latter topic during this thesis, comprehensive 3D simulations have been done, revealing 2% THz energy conversion efficiency when using four-colour sawtooth pulses in argon, a performance unequalled so far. This results have been published in Ref. [67].

4.1 Experimental study of the terahertz emission by laser-plasma filaments: action of bound electrons versus free electrons

Filament plasmas can promote continuous spectral bandwidths from 0.1 up to 100 THz depending on the pulse duration [17, 74, 86]. Importantly, coherent terahertz (THz) radiation can be delivered through the filamentation process to a desired remote position in the atmosphere, thereby avoiding its absorption by water vapour [15, 181]. As briefly recalled above, experiments on the spatial profile of THz radiation from laser-created plasmas demonstrated that this radiation propagates inside a cone and forms a ring in the far field [17, 19, 69, 92, 127, 186].

As introduced in Section 2.4, three major physical mechanisms can be triggered by a two-colour air filament for producing THz radiation, namely, the optical rectification by four-wave mixing [20, 37], which is the Kerr response related to bound electrons (see Section 2.4.1), plasma currents induced by tunneling ionization [8, 90, 108, 179] (see Section 2.4.2), as well as transverse and longitudinal plasma wave excitations [9, 45, 154, 44] (see Section 2.4.4). For this reason, a numerical approach accounting for both optical nonlinearities and plasma effects should be employed to explain the observed phenomena, which consists below in both neutrals and plasma contributions to the THz radiation.

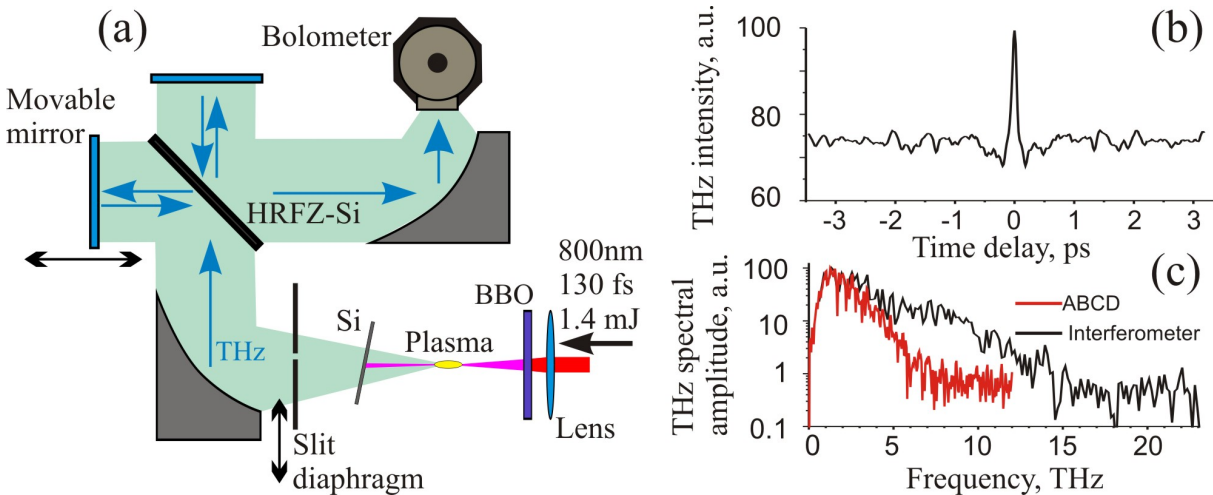


Figure 4.1.1: (a) Experimental setup. Note the slit moved across the THz transverse profile to scan the conical emission. (b) Typical interferogram and (c) THz spectrum (black curve), compared to that obtained with the ABCD technique (red curve).

First of all, the experimental setup is described¹. In the experiment a 800-nm beam supplied by a Ti:sapphire regenerative amplifier² is focused with a $f = 15$ cm plano-convex lens into ambient air [Fig. 4.1.1(a)]. A 0.1-mm-thick beta barium borate (β -BBO) crystal (I type) adjusted to reach the maximum THz yield is used for generating the second harmonic. A 1.5-cm laser spark formed near the geometrical focus locates the emitted THz radiation, which is collimated using an off-axis parabolic mirror (51.6 mm in diameter and 150-mm effective focal length). A 0.35-mm-thick silicon wafer filters the radiated field. To investigate the frequency-angular terahertz spectrum, a Michelson interferometer is coupled to a liquid helium-cooled silicon bolometer LN-6/C³, used as a detector of the THz radiation. A 3.5-mm-thick high-resistive silicon beam splitter⁴ with 50-mm aperture is employed for separation and recombination of the two arms of the interferometer ending with flat metallic mirrors, one of which is placed on a motorized translation stage. After recombination, the THz beam is refocused with an off-axis parabolic mirror into the aperture of the bolometer with filters transparent in the THz region (e.g., < 24 THz). Typical interferograms have 500-800 points with $2.5\text{-}\mu\text{m}$ increment ensuring spectral resolution up to 75 GHz. The reconstruction of the THz spectrum is done using the Fourier transform of the THz signal autocorrelation function. THz spectra recorded from 50 averaged interferograms have been obtained using 1.4-mJ, 130-fs two-colour pulses with $\sim 10\%$ fraction of second harmonic in amplitude. The resulting THz field is displayed in Fig. 4.1.1(b). Figure 4.1.1(c) details the spectrum plotted from the interferograms (black curve). The spectrum reaches noise level at 15 THz while the signal measured in similar conditions using the air-biased coherent detection (ABCD) method [19, 86] reaches noise level at 6-7 THz [see the black and red curves of Fig. 4.1.1(c)]. Thus, the autocorrelation experimental technique is adequate for the study of broadband THz spectra.

The measured spectra in the range 0-30 THz have been integrated over a 12-mm transverse aperture [Fig. 4.1.2(a), black dots]. The red curve plots numerical spectra computed from the UPPE equation [Eq. (2.1.81)] for comparable laser inputs. The experimentally measured THz spectrum is in good agreement with the simulated one. A maximum at around 0.5-1 THz in the experimentally obtained spectrum is due to the photocurrent induced by the plasma, whose signature is compatible with the peak around the electron plasma frequency, $\nu_p = \omega_p/(2\pi) = \sqrt{e^2 N_e m_e^{-1} \epsilon_0^{-1}} \approx 0.75$ THz, where $N_e \approx 7 \times 10^{15} \text{ cm}^{-3}$ is the typical free electron density for filaments. The spectral amplitudes at higher frequencies $\nu > 12.5$ THz are more attenuated in the experiment because of absorption by

¹Experiments were realized at the International Laser Center of M. V. Lomonosov Moscow State University (Moscow, Russia).

²The model is Spectra Physics Spitfire Pro, with characteristic values: 130 fs, < 1.5 mJ, 800 nm, 1 kHz.

³Infrared Laboratories.

⁴Tydex HRFZ-Si, with 54% transmittance.

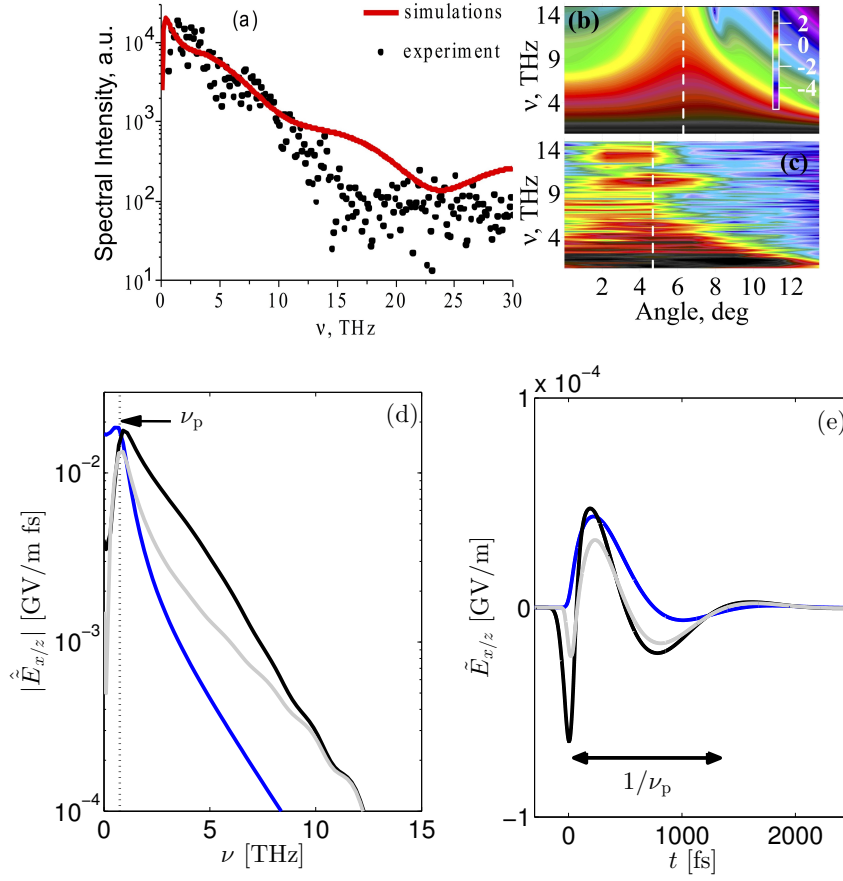


Figure 4.1.2: (a) Experimental (black dots) and simulated (red solid line) THz spectra from a two-colour pulse (800 nm: 1.4 mJ, 150 fs; 400 nm: 10 μ J, 220 fs) focused in air ($f = 15$ cm). (b),(c) Frequency-angular distributions: (b) simulation and (c) experiment in logarithmic color scale. Dashed vertical lines show the directions of maximum THz signals. (d) THz spectra peaked at $\nu = \nu_p$ (grey dashed line) and (e) 100-THz-filtered electromagnetic fields computed from the nonpropagating plasma fluid model Eq. (4.1.3). The black (grey) curves show the transverse field triggered by photoionization with (without) the Kerr nonlinearity; the blue curves refer to longitudinal plasma wakefields. Both fields are evaluated with the non-propagative model [Eq. (4.1.3)].

the HRFZ-Si beam splitter and filters used in the setup. In addition, measurements of frequency-angular spectra of the THz radiation were performed by moving a 1.5-mm slit across the diverging THz beam before collimation [Fig. 4.1.1(a)]. The angular distribution of THz radiation exhibits a maximum in the emission direction at 4-6° relative to the beam propagation axis [white dashed lines in Fig. 4.1.2(b,c)]. The off-axis maximum in the frequency-angular distribution corresponds to a ring in the far zone as already announced. In both the experiment and the simulations 15% of the THz energy in the

range 0.5-13 THz propagates forwardly (on axis) and 85% in the ring. The overall THz radiation energy in the range 0-30 THz is 9 nJ.

The numerical simulations by UPPE equation were carried out with laser and resolution in accordance with the experimental setup: broad beam size (3 mm), large non-paraxial radiation divergence (up to 45°) and frequency resolution of 0.05 THz. Axially symmetric propagation was assumed, pertinent to the single filament regime of the experiment. The input two-colour electric field, linearly polarized has been chosen as

$$E(r, \tau, z = 0) = \exp\left(-\frac{r^2}{w_0^2}\right) \left[a_1 \exp\left(-\frac{\tau^2}{t_{p,1}^2}\right) \cos(\omega_0\tau) + a_2 \exp\left(-\frac{\tau^2}{t_{p,2}^2}\right) \cos(2\omega_0\tau) \right], \quad (4.1.1)$$

where z is the longitudinal coordinate, $r = \sqrt{x^2 + y^2}$ is the transverse coordinate, τ is the time in the moving reference frame, $w_0 = 2.1$ mm is the initial beamwidth, $t_{p,1} = 106.1$ fs and $t_{p,2} = 155.6$ fs are the 1/e-duration of the laser beam components, and $\nu_0 = \omega_0/(2\pi) = 375$ THz is the fundamental frequency at a wavelength of 800 nm (the frequency of the second harmonic is thus 750 THz). The field amplitudes a_1 and a_2 are calculated in such a way that the energy of the fundamental and second harmonic are 1.4 mJ and 10 μ J, respectively. Geometrical focusing is described by multiplying Eq. (4.1.1) by the phase factor $\exp[(i\omega r^2)/(2cf)]$ in the frequency domain, where $f = 15$ cm is the focal length of the lens.

Air is modelled as a mixture of 80% of dinitrogen molecules (N_2) and 20% of dioxygen molecules (O_2), whose ionization is limited to a single electron. The binding energies of N_2 and O_2 are, respectively, 15.58 and 12.07 eV [124]. Following Talepbour *et al.* in Ref. [158], the effective charges of $Z_{\text{eff},O_2} = 0.53$ and $Z_{\text{eff},N_2} = 0.9$ are considered. The PPT ionization rate [Eq. (2.2.13)] is used with the instantaneous value of the electric field, even if originally this ionization model was derived for single-colour laser pulses, namely:

$$W_{\text{PPT}}(|E(t)|, \omega_0) = \frac{4\sqrt{2}}{\pi} \nu_{\text{au}} C A(|E(t)|, \omega_0) H_{\text{PPT}}(|E(t)|, \omega_0), \quad (4.1.2)$$

where the coefficient C is calculated via Eq. (2.2.14) and the terms A and H respectively through Eqs. (2.2.15) and (2.2.18). Note that this instantaneous PPT ionization rate does not follow the same evaluation of time-averaging over one optical cycle as done with ADK rate (see Section 2.2.2.2). However, Fig. 4.1.3 compares this ionization rate (black curve) with two other ionization models for the O_2 molecule: the standard ADK model [Eq. (2.2.27)] with the effective charge of Talepbour *et al.* (red curve) and the ADK molecular theory [125]. One can check that the discrepancies between Eq. (4.1.2) and the other two ADK rates remain only of order of unity for $|E(t)| < 30$ GV/m in the

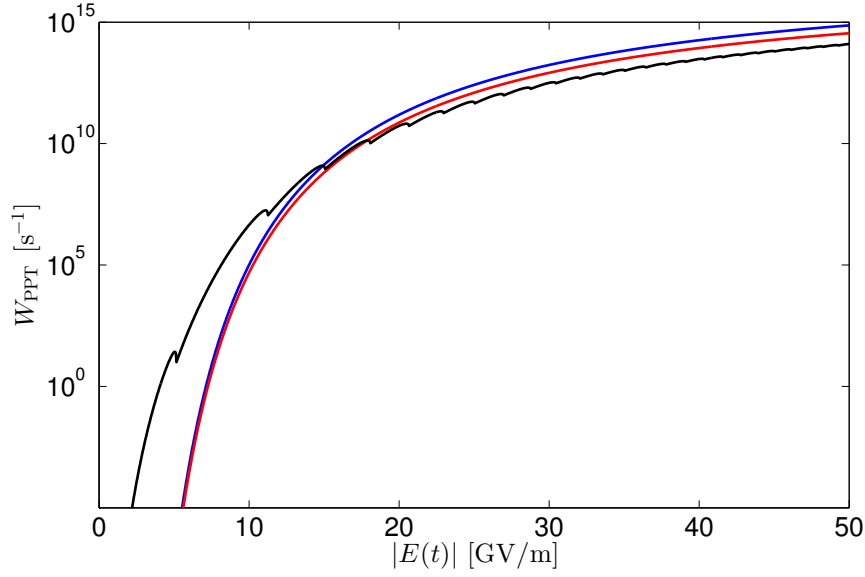


Figure 4.1.3: Comparison of different models for the ionization rate of O_2 molecule as a function of the instantaneous electric field: ADK molecular theory (blue curve), ADK ionization rate (red curve), instantaneous PPT ionization rate (black curve).

tunnelling regime. Unlike the latter two ionization rates, the former one also involves the multiphoton ionization up to $15 \text{ GV/m} \approx 3 \times 10^{13} \text{ W cm}^{-2}$. The nonlinear refractive index of air is taken equal to $10^{-19} \text{ cm}^2/\text{W}$ at 1-bar pressure [22, 188].

THz emissions of Fig. 4.1.2, which proceed from both four-wave mixing and plasma waves, can be explained inside the plasma by the simplified Maxwell-Fluid model of Section 3.4. Indeed, for this section, a non-propagative, non-relativistic version of that model is considered. Neglecting propagation (i.e., $\partial_z = 0$) and considering $\gamma = 1$, Eqs. (3.4.5) and (3.4.12) can be rewritten into a vectorial form as follows:

$$\left(\partial_t^2 + \nu_c \partial_t + \omega_p^2\right) \tilde{\mathbf{E}} = -\frac{1}{\varepsilon_0} (\mathbf{\Pi} + \partial_t \mathbf{J} + \partial_t \mathbf{J}_{\text{NL}}), \quad (4.1.3)$$

where $\tilde{\mathbf{E}}$ accounts for the low-frequency components of the radiated electric field, $\nu_c = 5 \text{ ps}^{-1}$ is the electron-neutral collision frequency [154], \mathbf{J} is the electron current density, $\mathbf{J}_{\text{NL}} = \partial_t \mathbf{P}_{\text{NL}}$ is the current density associated to the nonlinear polarization \mathbf{P}_{NL} (Kerr effect), and the source term $\mathbf{\Pi}$ comes from Eq. (2.3.15), which gathers the radiation pressure and ponderomotive effects:

$$\mathbf{\Pi} = -\nabla \cdot (\mathbf{v} \otimes \mathbf{J}) - \frac{e}{m_e} \mathbf{J} \times \mathbf{B}. \quad (4.1.4)$$

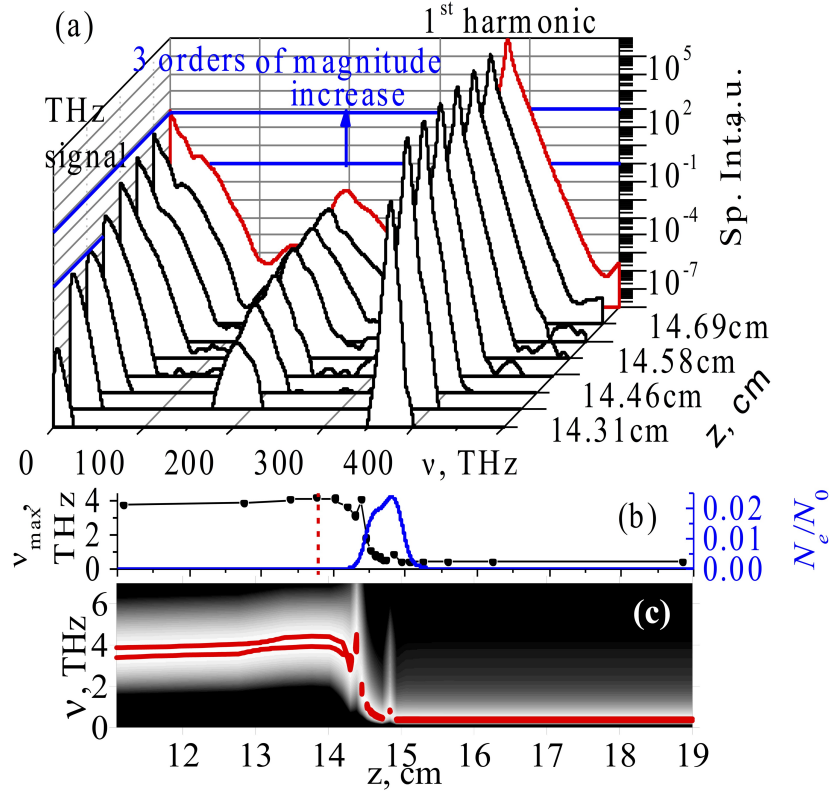


Figure 4.1.4: (a) Simulated frequency spectra along z in the two-colour filament. (b) Maximum of the THz spectrum (black circles joined by black line) and peak plasma density (blue line) as function of the propagation distance. Vertical dashed line indicates the position of the maximum THz signal emitted by neutrals. (c) Downshift of the THz spectral maximum from ~ 4 to ~ 0.5 THz as indicated by the red contour (99% of the maximum spectral intensity).

As highlighted by the LC model (Section 2.4.2), the radiated field polarized in the transverse plane of the 800-nm pulse polarization direction is due to photocurrents through the derivative $\partial_t \mathbf{J}$ [90]. Longitudinal low-frequency currents can also originate from the $\mathbf{\Pi}$ driving source term, as explained in Section 2.4.4. Figure 4.1.2(d,e) clearly confirms that, for the laser and material parameters used in the experiment, the transverse field component (black and grey curves) prevails over the longitudinal one (blue curve) at $\nu > 1$ THz. In addition, the transverse spectrum appears peaked at the same plasma frequency as that characterizing longitudinal plasma oscillations. Here, a plasma wave emerges over time scales longer than the laser pulse duration t_p , which explains the spectral peak reached at ν_p . Indeed, the photoionization emission range $1/t_p \approx 10$ THz is close to $\nu_p \approx 1$ THz and, thus, enhances plasma waves. It may be surprising that the longitudinal field, although smaller than its transverse counterpart, may not be negligible in our context. This follows probably from the small fraction of second harmonic that inhibits the efficiency of the

photocurrents, with only 1% of energy in the second harmonic. We will see in the next section that such longitudinal waves cannot go out of the plasma channel. Beyond the plasma frequency the spectrum rapidly falls down like $1/\nu^2$, faster than in the experiment [compare the grey curve of Fig. 4.1.2(d) and the black dots of Fig. 4.1.2(a)]. In fact, the Kerr contribution increases the spectral amplitude at frequencies $\nu > \nu_p$ [the black curve in Fig. 4.1.2(d), where $\mathbf{P}_{\text{NL}} \neq \mathbf{0}$]. This behaviour thus indicates that the spectral wing spreading up to 30 THz in Fig. 4.1.2(a) may be attributed to the nonlinearity of the bound electrons.

In the UPPE numerical simulations, the low-frequency part of the filament spectrum is integrated over the whole 12-mm transverse aperture as done in the experiments. The length of the plasma channel near focus with $f = 15$ cm is ~ 1.5 cm and the temporal walk-off between the fundamental and second harmonic is negligible within 20 cm of the optical path. As evidenced by Fig. 4.1.4(a), the simulations provide new insights into the filament-driven THz spectral dynamics. Close to the early self-focusing Kerr stage ($z \leq 14$ cm), where there are almost no free electrons, the nonlinear polarization of neutrals mainly contributes to the emitted THz spectrum. The THz signal from the neutrals reaches a maximum at $z \approx 13.8$ cm [vertical line in Fig. 4.1.4(b)] and at a comparatively high frequency of ~ 4 THz. This signature of the Kerr response agrees quantitatively with the simple four-wave mixing model [37, 20], which, following Eq. (2.4.2), supplies the parabolic signal $\mathcal{F}(\partial_t \mathbf{J}_{\text{NL}}) \sim -(3/4)\varepsilon_0 \chi^{(3)} a_1^2 a_2 \omega^2 \propto \omega^2$ for the laser parameters given by Eq. (4.1.1).

From there on, a first generation of plasma immediately overwhelms the higher-frequency THz signal from neutral air molecules. As plasma quickly builds up, the THz spectrum changes dramatically with an abrupt downshift around 0.5-1 THz corresponding to the plasma frequency [Fig. 4.1.4(b,c)]. Starting from $z \geq 15$ cm the downshifted spectrum corresponds to that typically observed in the experiment [Fig. 4.1.2(a)]. The intensity in this downshifted spectral maximum is about three orders of magnitude larger than in the initial Kerr-induced THz emission at $z < 14.5$ cm [see blue arrow in Fig. 4.1.4(a)].

The contribution from the four-wave mixing due to the Kerr nonlinearity can be seen clearly in the developed filament, since it is separated by a small dip at approximately 25 THz starting from $z \approx 14.58$ cm and further in Fig. 4.1.4(a). The spectral amplitude at $\nu \geq 25$ THz is almost three orders of magnitude less than the peak at $\nu \approx 0.75$ THz, rendering the Kerr contribution masked by the much stronger plasma contribution.

To clear up the physical mechanisms responsible for the on-axis and conical propagation of THz radiation⁵, now a purely Kerr medium is simulated, terminating the simulation as

⁵According to Eq. (4.0.16), the emission angle from longitudinal currents at a wavelength $\lambda_p = 300 \mu\text{m}$ ($\nu_p = 1$ THz) in a plasma channel of length $L = 1.5$ cm is $\theta \approx 8^\circ$ for the principal lobe $N = 1$.

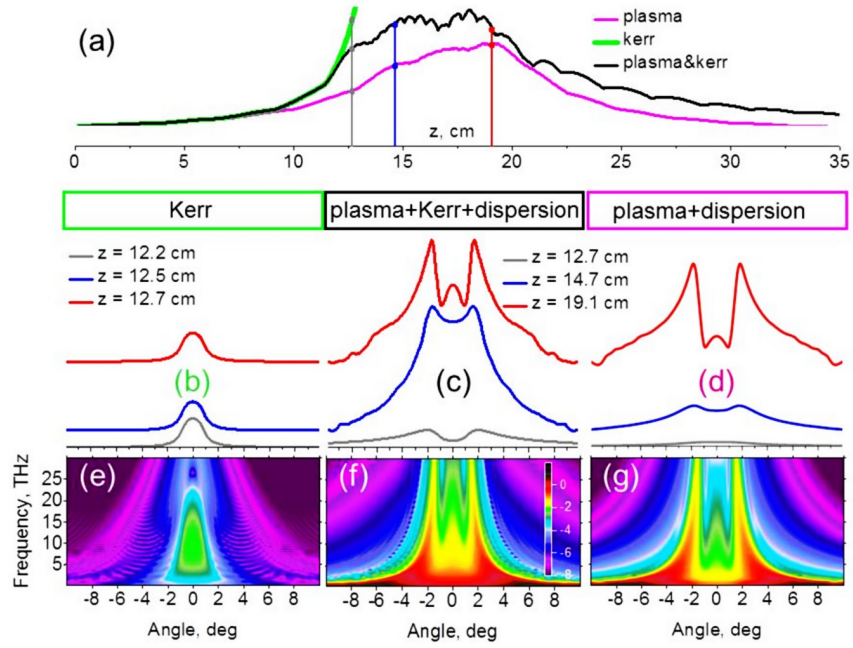


Figure 4.1.5: Simulated conical and on-axis THz emission from the two-color filament. The focal length is $f = 20$ cm, the pump pulse energy is 3.2 mJ and its duration is 54 fs. (a) Filament peak intensity. (b)-(d) THz angular distribution integrated over 0.05-30 THz at indicated distances and propagation media. (e)-(g) Frequency-angular spectra.

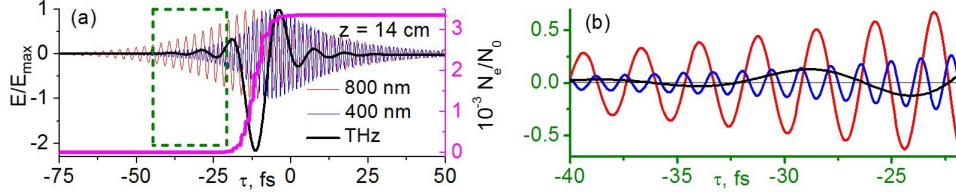


Figure 4.1.6: ω_0 (red) and $2\omega_0$ (blue) optical components, THz field (black), and plasma density (magenta curves) in the complete configuration [as in Fig. 4.1.5(c,f)]. The fields at ω_0 , $2\omega_0$, and THz frequency are normalized to their corresponding maximum values E_{\max} . (a) Overall pulse and the green frame detailing in (b) the $\omega - 2\omega$ phase matching in the front pulse region.

soon as the ionization threshold is reached [see green line interrupted at $z \approx 12.5$ cm in Fig. 4.1.5(a)]. The THz spectra remain confined in the forward direction [Fig. 4.1.5(e)]. Thus, starting from the onset of filamentation, the on-axis THz source is formed, which moves with the pulse front in the neutral medium and irradiates in the forward direction at each z point along the filament. In contrast, conical emission occurs as plasma defocusing does compete with the Kerr effect [Fig. 4.1.5(f)]. The spectral intensity in the ring (red curves) is two orders of magnitude larger than at the centre (green curves). When there is

no Kerr nonlinearity and the plasma only contributes to the spectrum, terahertz conical emission takes place very similarly to the complete configuration [Fig. 4.1.5(g)]. Hence, photocurrents produced by plasma generation are the major source of THz radiation [see Fig. 4.1.5(e,g)]. The influence of the Kerr response manifests by the enhancement of the forwardly directed THz radiation [“green” maximum in Fig. 4.1.5(f)], experimentally observed in Refs. [31, 32, 171]. The spatial distribution of THz radiation integrated over the range of 0.05-30 THz shows an increase in the on-axis THz yield when both free and bound electron responses are included [see Fig. 4.1.5(c,d)]. The ω_0 , $2\omega_0$, and THz radiation extracted by filtering the overall light field exhibit the characteristic phaseshift values 0 or π of Kerr-induced THz signals in the pulse front region $-32 < \tau < 20$ fs [37], as shown in Fig. 4.1.6(a,b). This confirms that THz radiation born in the front before the plasma rises (at $\tau \approx -20$ fs) is mainly due to four-wave mixing.

During the experimental campaign, the Kerr-induced broadband THz spectra could be identified by using an ABCD detection scheme [19, 86] for pump pulse energies of 30-60 μJ , which are below the photoionization threshold (100 μJ) in the particular focusing geometry of the experiment. In the experimental conditions, it is hard to separate the contributions from different parts of the pulse or the parts of the emitting zone. However, the THz emission due to the Kerr nonlinearity of neutral molecules has been isolated by decreasing the energy of the pump beam below the photoionization threshold. Measurements were performed using 120-fs-FWHM optical pulses focused by the lens with the focal distance $f = 20$ cm through a 100- μm -thick I-type BBO crystal with orientation and position allowing to achieve maximum THz output at high pump energy and ABCD detection. The spectra of THz pulses radiated for different pump energies are shown in Fig. 4.1.7(a). The broadband THz emission was collected from the beam waist even at lowest pump beam energies (30 and 60 μJ), where the photoionization does not occur yet. Indeed, plasma fluorescence starts at about 100 μJ for 120 fs pulse duration, as shown by Fig. 4.1.7(b). Thus, at low enough energies, plasma contribution to the signal is minimal compared to the Kerr contribution. The terahertz radiation is clearly observable and it is broadband. However, ABCD detection could not provide data for the correct shape of the THz spectrum at frequencies exceeding a few THz.

The results of our self-consistent simulations agree with the interference models [17, 69, 127, 186], which introduce $\omega - 2\omega$ phase mismatch and plasma dispersion phenomenologically as key mechanisms responsible for pushing the THz emission off axis and leading to ring formation in the far field.

In order to show the universality of the THz conical emission, the propagation of collimated beams is also simulated ($f = +\infty$), corresponding to a plasma channel length of ~ 50 cm. The overall frequency-angular spectra are plotted in Fig. 4.1.8. The conical

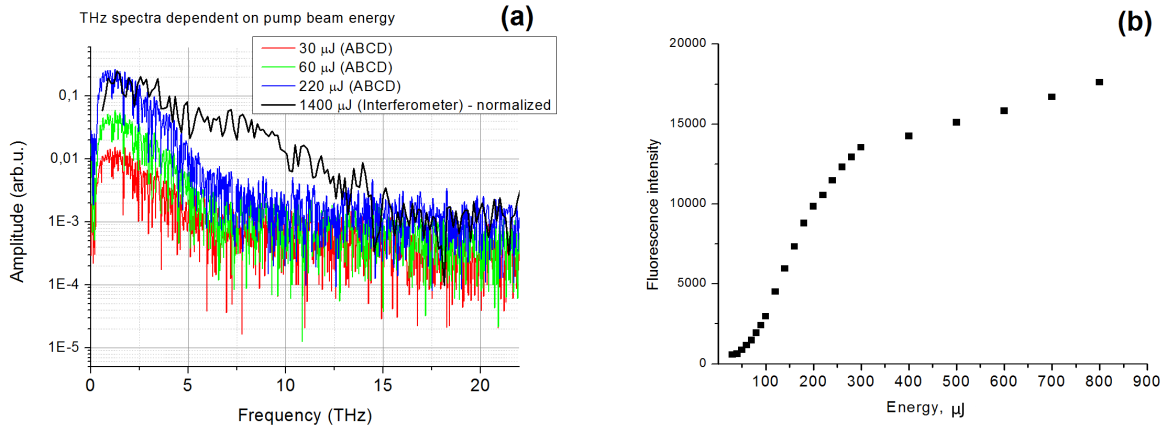


Figure 4.1.7: (a) THz spectra from ambient air for pump beam energies above and below the photoionization threshold. (b) Fluorescence measured from the beam waist at 391.4 nm, which is proportional to the plasma density dependent on the pump pulse energy [160].

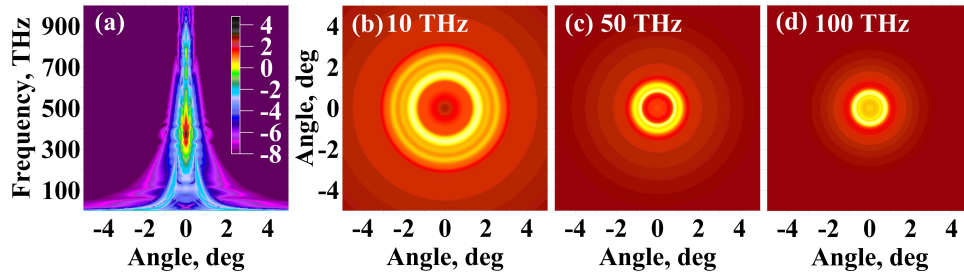


Figure 4.1.8: (a) Simulated frequency-angular spectra in the two-colour filament of collimated 800-nm and 400-nm beams with 54 fs pulse duration, 3.2 mJ and 10 μ J energies, respectively (spectral intensity is in logarithmic color scale). (b-d) Simulated angular distributions for the three selected frequencies of (a).

emission occupies all the low-frequency region, with an on-axis radiation being less than the conical emission propagating at $\sim 2^\circ$ from axis [see bottom of Fig. 4.1.8(a)]. Filtering the transverse distribution at 10, 50, and 100 THz shows the decrease in the field divergence with increasing frequency [see the ring radius in Fig. 4.1.8(b,d)], experimentally reported in Refs. [17, 92]. As already shown in Fig. 4.1.4(a), the higher frequencies of the THz and far infrared range are first produced by the Kerr nonlinearity of neutrals from the front pulse and they increase the overall forward THz emission. In addition, the natural diffraction is smaller for the higher frequencies. For a perfect Gaussian beam, the expected beamwidth $w(\nu)$ linearly decreases with the frequency: $w(\nu) \propto 1/\nu$ [33]. Therefore, at 10 THz there exists a ring with 1.8° half-cone angle, at 50 THz the half-cone angle decreases to 1° , and at 100 THz we observe on-axis propagation [Fig. 4.1.8(b,d)].

In conclusion, the numerical and experimental analysis of the mechanisms responsible for the THz generation in two-colour air filaments demonstrates that both neutrals and plasma contribute to the THz yield. The contribution of neutrals arises mainly from the front part of the self-focusing laser pulse, which always sees the neutral gas as it propagates. The polarizability of the bound electrons forms an on-axis THz source at the onset of filamentation, which is much weaker than the free electron photocurrent THz source. Terahertz radiation triggered by plasma photocurrents propagates inside a cone. Both experiments and simulations displayed evidence of an abrupt downshift of the spectral peak in the THz spectrum from higher-frequency Kerr contribution towards the electron plasma frequency accompanied by more than two orders of magnitude increase in the spectral intensity when photoionization takes place. The “plasma” peak in the THz spectrum appears close to the electron plasma frequency with electron densities fixed by the filamentation mechanism at moderate clamping intensities. Ring-shaped spatial distributions of the THz radiation are shown to be of universal nature and they occur in both collimated and focusing propagation geometries. Simulated THz conical distributions and THz spectra agree with the experimental data.

4.2 Boosting terahertz generation using a sawtooth-wave shape

The Local Current (LC) model presented in Section 2.4.2 predicts that the laser configurations fostering the interference of ionization events through the photocurrent component $J_B(t)$ are the most efficient to convert the energy of the pulse into THz radiation. Beyond the standard scenario of two-colour pulses, where the highest THz yields are attained when the phaseshift between the fundamental and second harmonics is $\pi/2$, one wonders what is the optimal pump waveform that promotes the greatest THz signals, as gathered through the expression:

$$\tilde{E}^{\omega_{co}}(t) = g[\partial_t J_A(t)]^{\omega_{co}} + g[\partial_t J_B(t)]^{\omega_{co}}. \quad (4.2.1)$$

To answer this question, among all the pump waveforms being suitable to fulfill certain requirements (for example, having a fixed intensity I_0 or producing a fixed degree of ionization Z^*N_a) the one that maximizes $g[\partial_t J_B(t)]^{\omega_{co}}$ and makes $g[\partial_t J_A(t)]^{\omega_{co}}$ vanish has to be found. Neglecting collisions for the sake of simplicity ($\nu_c = 0$), the inverse Fourier transform of Eq. (2.4.24) filtered at $\omega = \omega_{co}$ and Eqs. (2.4.29) and (2.4.31) give:

$$g[\partial_t J_B(t)]^{\omega_{co}} \approx -2\sqrt{2}\nu_{co} \frac{m_e}{e} \underbrace{\frac{1}{Z^*N_a} \sum_n \delta N_e^n v_f(t_n)}_{B_n} \text{sinc}(\omega_{co}(t - t_n)). \quad (4.2.2)$$

Maximizing Eq. (4.2.2) is equivalent to optimize the absolute value of B_n for a set $\{B_n\}$ being sign-definite. Each contribution B_n depends on the corresponding density jump, δN_e^n , and the velocity of free electrons at such ionization event, $v_f(t_n)$. The former, as claimed by Eq. (2.4.16), depends locally on the electric field, concretely on its values at ionization events, $\{E(t_n)\}$. The latter, instead, is influenced by the whole shape of the electric field, since $v_f(t)$ is the integral of the electric field according to Eq. (2.4.21). Thus, the waveform for which all $v_f(t_n)$ are local extrema and sign-definite would be the sought optimal solution, because moreover if $v_f(t_n)$ is an extremum then $r_f(t_n) \rightarrow 0^6$ and therefore $g[\partial_t J_A(t)]^{\omega_{co}} = 0$. Notwithstanding, no physical continuous waveshape⁷ of $E(t)$ verifies that both $E(t_n)$ and $v_f(t_n)$ are simultaneously local extrema because $\partial_t v_f(t) \sim E(t)$ and hence if $v_f(t_n)$ is a local extremum then necessarily $E(t_n) = 0$, which cannot be a local extremum. More generally, without requiring that $E(t)$ be differentiable, from

⁶Provided that the phase space (r_f, v_f) is symmetric with respect to the v_f -axis, which is the case when the interference via $J_B(t)$ is privileged (see Fig. 2.4.4). Free electrons then go across the equilibrium position $r_f(t_n) = 0$ at the highest velocities as a consequence of their oscillatory motion.

⁷Rigorously, we mean *differentiable* waveshape.

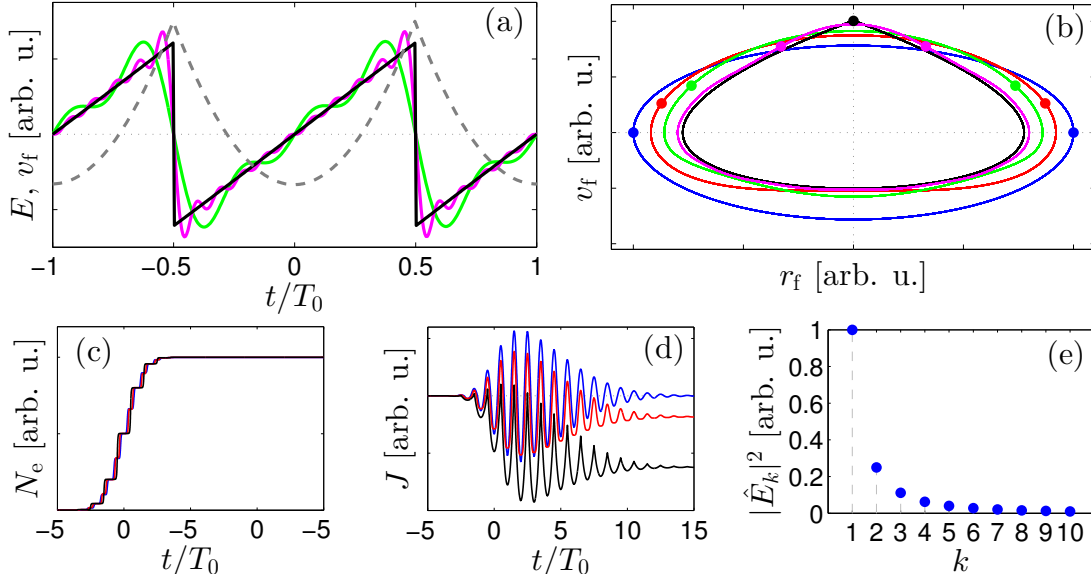


Figure 4.2.1: (a) Sawtooth waveform $E(t)$ given by Eq. (4.2.5) (black solid line) having the maxima of $|v_f(t)|$ (grey dashed line) at the same instants as the extrema of $E(t)$. Solid curves show the three-colour (green curve) and ten-colour (magenta curve) approximations to the ideal sawtooth shape. (b) Trajectories of free electrons in the phase space (r_f, v_f) for an increasing number of colours. Dots locate the maxima of $|E(t)|$. (c) Stepwise increase of the electron density $N_e(t)$ for a one-colour (blue curve), two-colour (red curve), and a sawtooth pulse with identical ionization yield in argon. (d) Corresponding current densities $J(t)$. The sawtooth pulse develops a larger low-frequency component in $J(t)$. (e) Spectrum of the sawtooth waveform containing all harmonics of ω_0 with intensities decreasing as $1/k$.

Eq. (2.4.21) $v_f(t_n)$ is an extremum if and only if $E(t)$ changes its sign at such instant [i.e., $E(t_n^-)E(t_n^+) \leq 0$, where $E(t_n^\pm) = \lim_{t \rightarrow t_n^\pm} E(t)$]. This fact is straightforwardly proven by computing

$$v_f(t_n) - v_f(t_n - \Delta t) = -\frac{e}{m_e} \int_{t_n - \Delta t}^{t_n} E(\tau) d\tau \approx -\frac{e}{m_e} E(t_n^-) \Delta t, \quad (4.2.3)$$

$$v_f(t_n) - v_f(t_n + \Delta t) = \frac{e}{m_e} \int_{t_n}^{t_n + \Delta t} E(\tau) d\tau \approx \frac{e}{m_e} E(t_n^+) \Delta t, \quad (4.2.4)$$

where $\Delta t > 0$ is small. If $v_f(t_n)$ is an extremum, then $[v_f(t_n) - v_f(t_n - \Delta t)][v_f(t_n) - v_f(t_n + \Delta t)] \geq 0$ and thus $-e^2 m_e^{-2} \Delta t^2 E(t_n^-) E(t_n^+) \geq 0$, which is true if $E(t_n^-) E(t_n^+) \leq 0$. Reciprocally, if $E(t_n^-) E(t_n^+) \leq 0$ one finds from Eqs. (4.2.3) and (4.2.4) that $v_f(t_n)$ is necessarily an extremum.

Consequently, the only way to achieve the maxima of both $|E(t)|$ and $|v_f(t)|$ at the same

instants is to have a discontinuous electric field and we advance here that the optimal solution is the sawtooth waveshape [67], given by:

$$E(t) = \mathcal{E}(t) \sqrt{\frac{3}{2}} a_0 \left(\frac{2t}{T_0} - 2 \left\lfloor \frac{1}{2} + \frac{t}{T_0} \right\rfloor \right), \quad (4.2.5)$$

where $0 \leq \mathcal{E}(t) \leq 1$ is the slowly-varying envelope, $a_0 = \sqrt{2\varepsilon_0^{-1}c^{-1}I_0}$ is the amplitude of the electric field with intensity I_0 , $T_0 = 2\pi\omega_0^{-1}$ is the fundamental period, and $\lfloor x \rfloor$ accounts for the ‘‘floor’’ function (the largest integer that is less or equal to x). In Fig. 4.2.1(a) this ideal waveform is plotted with $\mathcal{E}(t) = 1$ (black solid curve), together with its corresponding free electron velocity (grey dashed curve). The largest extrema of $|v_f(t_n)|$ are located at the instants when $E(t)$ is discontinuous, i.e., at the ionization events.

Nonetheless, such ideal sawtooth waveform cannot be created in laboratories. This should not represent a major problem because Eq. (4.2.5) can be decomposed into Fourier harmonics as

$$E(t) \approx E^N(t) = \sum_{k=1}^N E_k(t) = \sum_{k=1}^N \mathcal{E}(t) \frac{a_0}{k \sqrt{\sum_{j=1}^N j^{-2}}} \cos \left(k\omega_0 t + (-1)^k \frac{\pi}{2} \right), \quad (4.2.6)$$

where $E_k(t)$ is in fact the k -th Fourier harmonic of Eq. (4.2.5). The sawtooth profile is well approximated by its first harmonics ($N = 3$ or $N = 4$). In Fig. 4.2.1(a) the approximations $N = 3$ (green curve) and $N = 10$ (magenta curves) are compared with the ideal sawtooth shape, pointing out that already the three-colour electric field is close enough to the sawtooth profile. Indeed, as Fig. 4.2.1(e) displays, the intensity of harmonics falls like $\sim 1/k^2$, which reflects that first harmonics are the most efficient in the THz conversion process.

Neglecting the envelope [$\mathcal{E}(t) = 1$] and collisions ($\nu_c = 0$), the phase space given by the N -colour electric field of Eq. (4.2.6) is determined, by virtue of Eqs. (2.4.21) and (2.4.22), by

$$v_f^N(t) = -\frac{e}{m_e} \sum_{k=1}^N \frac{a_0}{k^2 \omega_0 \sqrt{\sum_{j=1}^N j^{-2}}} \sin \left(k\omega_0 t + (-1)^k \frac{\pi}{2} \right), \quad (4.2.7)$$

$$r_f^N(t) = \frac{e}{m_e} \sum_{k=1}^N \frac{a_0}{k^3 \omega_0^2 \sqrt{\sum_{j=1}^N j^{-2}}} \cos \left(k\omega_0 t + (-1)^k \frac{\pi}{2} \right). \quad (4.2.8)$$

The extrema of Eq. (4.2.6) are located at the ionization events given by

$$\{t_n\} = \left\{ \pm \frac{N}{N+1} \frac{T_0}{2} + nT_0 \right\}, \quad (4.2.9)$$

whereas the extrema of the free electron velocity [Eq. (4.2.7)] are always located at

$$\{\pm T_0/2 + nT_0\}, \quad (4.2.10)$$

for all N . The phase space, together with the pairs $(r_f^N(t_n), v_f^N(t_n))$, have been plotted in Fig. 4.2.1(b) for different values of N , in order to analyze qualitatively how ideal the sawtooth shape can be in terms of the THz conversion efficiency. For any number of harmonics the phase space is always symmetric with respect to the v_f -axis, which inhibits the interference due to $J_A(t)$ and enhances that due to $J_B(t)$ because the contributions $\{B_n\}$ are sign-definite. Increasing the number of harmonics converging towards the ideal sawtooth wave shape has two positive effects. On the one hand, the phase space gets more and more asymmetric with respect to the abscissa axis at increasing N , which increases the values of $|v_f^N(t_n)|$ and reduces the values of $|r_f^N(t_n)|$. On the other hand, the positions of the two ionization events, which are always symmetric with respect to the v_f -axis, get closer and closer when $N \rightarrow \infty$, which means that the two ionization events *fuse* together into one unique event for the ideal sawtooth of Eq. (4.2.5) and the extrema given by Eqs. (4.2.9) and (4.2.10) coincide. Therefore, from the phase space one concludes that the sawtooth waveform is ideal in the sense that it generates the THz energy exclusively through constructive interference from $J_B(t)$ and with the largest possible value of free electron velocity.

The optimal coupling of the laser harmonics following the intensity ratios and phase-shifts of Eq. (4.2.6) is proven numerically in Fig. 4.2.2(a,b,c). Here a generic N -colour laser pulse is considered:

$$E(t) = \sum_{k=1}^N E_k(t) = \sum_{k=1}^N \mathcal{E}(t) a_k \cos(k\omega_0 t + \phi_k), \quad (4.2.11)$$

where, in accordance with Eq. (4.2.6), a_k is the amplitude of the k -th harmonic and ϕ_k the corresponding phase. By definition, the colour amplitudes define the total intensity of the laser pulse, I_0 , as follows [Eq. (2.1.32)]:

$$I_0 = \frac{\varepsilon_0 c}{2} \sum_{k=1}^N a_k^2. \quad (4.2.12)$$

The pulse of Eq. (4.2.11) has $2N - 1$ degrees of freedom, N phases (ϕ_1, \dots, ϕ_N) and $N - 1$ amplitudes (a_1, \dots, a_{N-1}), because, for a given intensity I_0 , the amplitude of the highest harmonic, a_N , is calculated from Eq. (4.2.12). However, instead of fixing the pulse intensity, a more realistic assumption is to fix the ionization degree reckoned with I_0 . In Fig. 4.2.2(a) the THz pulse energy, filtered at 100 THz and yielded by a two-colour 40-fs-

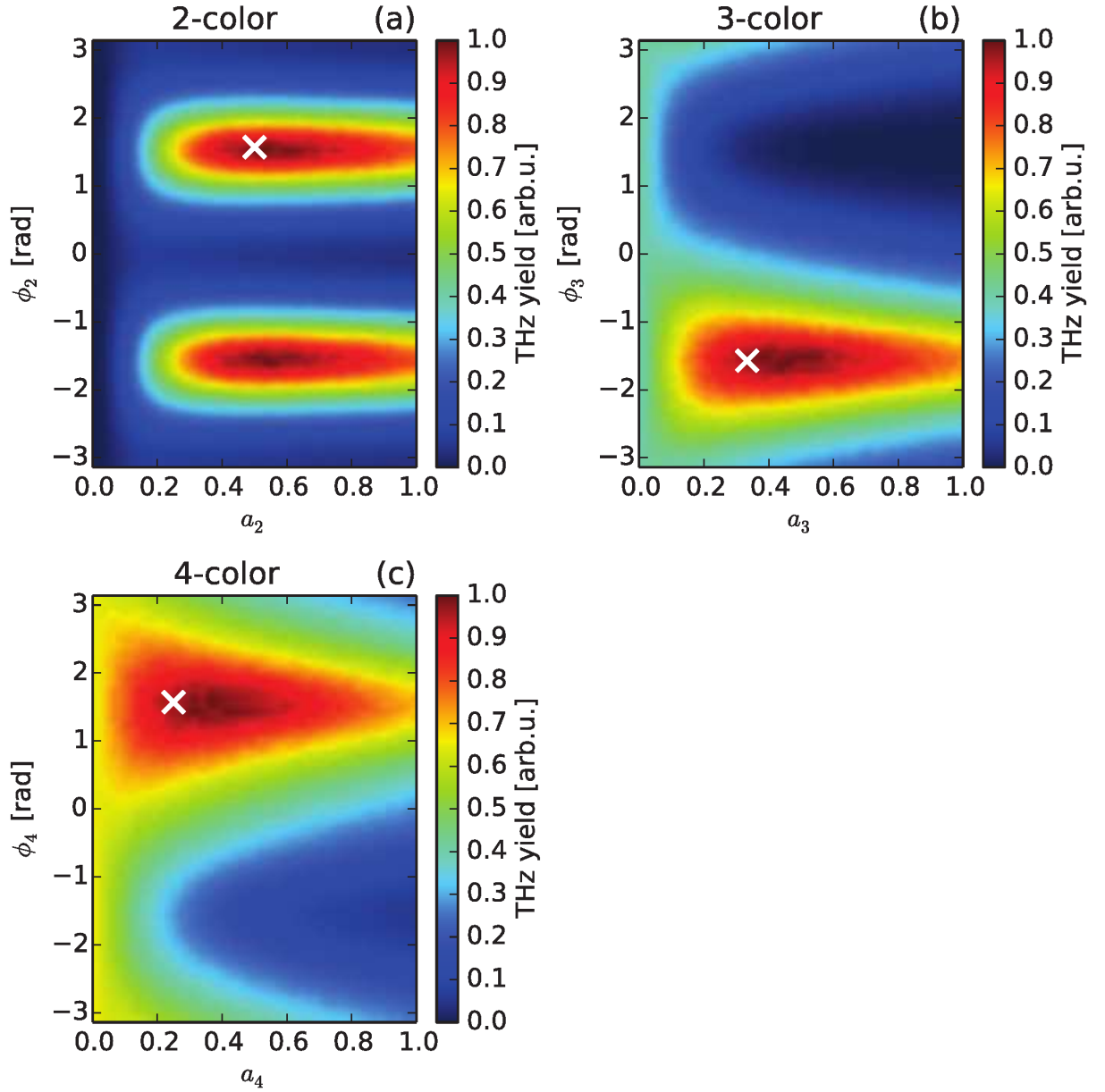


Figure 4.2.2: (a) Dependency of local THz yield on a_2 , ϕ_2 for a $N = 2$ colour field in Eq. (4.2.11). (b) Same for a_3 , ϕ_3 and $N = 3$. (c) Same for a_4 , ϕ_4 and $N = 4$. Relative amplitudes and phases of the lower harmonics in (a)-(c) are fixed according to the (optimum) sawtooth shape, i.e., $a_k = 1/k$, $\phi_k = (-1)^k \pi/2$. The total electric field amplitude a_0 is determined by the fixed ionization yield $Z^* N_a = 2.7 \times 10^{18} \text{ cm}^{-3}$. White crosses in (a)-(c) indicate the values of the sawtooth waveform.

FWHM laser pulse, is plotted as a function of a_2 and ϕ_2 , where we have set $\phi_1 = -\pi/2$ and $a_1 = 1$, computed for an argon gas ionized in the tunneling regime up to $Z^* = 0.1$ through the QST ionization rate [Eq. (2.2.28)] ($N_a = 2.7 \times 10^{19} \text{ cm}^{-3}$). Two optima are reached for $a_2 = 0.5$ and $\phi_2 = \pi/2$, and $a_2 = 0.5$ and $\phi_2 = -\pi/2$. That indicated by a

white cross is the second harmonic of Eq. (4.2.6). To this optimal configuration a third harmonic is added into Fig. 4.2.2(b). Again, the THz energy is represented as a function of $a_3/a_1 = 0.5$ and $\phi_3 = \pi/2$. The optimum for the third harmonic is $a_3/a_1 = 1/3$ and $\phi_2 = -\pi/2$, which, as expected, corresponds to the third harmonic of the sawtooth. Figure 4.2.2(c) concludes the same reasoning for four colours. By proceeding further, one would conclude that the optimal colour added to the pump is the corresponding harmonic of the sawtooth. This conclusion is universal and the same analysis has been done for different ionization degrees, e.g., $Z^* = 0.05$ and $Z^* = 0.5$. Figure 4.2.2(a,b,c) also reveal the robustness of this configuration against small variations in the laser parameters, which are expected in a realistic setup, since one can see in these figures that variations up to 10% in the relative amplitudes and/or phaseshifts do not decrease considerably the amount of THz radiation.

The optimal character of the sawtooth waveform can be also demonstrated for large N by maximizing $|v_f(t_n)|$ for the generic laser pulse given by Eq. (4.2.11). Neglecting again its slowly-varying envelope [$\mathcal{E}(t) = 1$] and assuming no collision ($\nu_c = 0$) for technical convenience, we define the unitary amplitudes $\tilde{a}_k = a_k/a_0 \geq 0$, so that $\sum_k \tilde{a}_k^2 = 1$. Equation (4.2.11) thus reads

$$E(t) = a_0 \sum_{k=1}^N \tilde{a}_k \cos(k\omega_0 t + \phi_k). \quad (4.2.13)$$

Without loss of generality, let $E(0)$ be an extremum. Then the derivative of Eq. (4.2.13) evaluated at $t_n = 0$ must be zero:

$$\partial_t E(0) = -a_0 \omega_0 \sum_{k=1}^N \tilde{a}_k k \sin \phi_k = 0. \quad (4.2.14)$$

From Eq. (2.4.21), the free electron velocity evaluated at $t_n = 0$ is thus

$$v_f(0) = -\frac{e}{m_e} \frac{a_0}{\omega_0} \sum_{k=1}^N \frac{\tilde{a}_k}{k} \sin \phi_k. \quad (4.2.15)$$

The optimization problem can thus be reexpressed as follows:

$$\left\{ \begin{array}{l} \text{Maximize: } |v_f(0)| = \frac{e}{m_e} \frac{a_0}{\omega_0} \left| \sum_{k=1}^N \frac{\tilde{a}_k}{k} \sin \phi_k \right|, \\ \text{subject to:} \\ \partial_t E(0) = -a_0 \omega_0 \sum_{k=1}^N \tilde{a}_k k \sin \phi_k = 0, \\ \sum_k \tilde{a}_k^2 - 1 = 0. \end{array} \right. \quad (4.2.16)$$

This problem is solved by the Lagrange multiplier technique. The optimum of Eq. (4.2.16) is necessarily a stationary point of the Lagrange function

$$\mathcal{L} = \frac{e}{m_e} \frac{a_0}{\omega_0} \left| \sum_{k=1}^N \frac{\tilde{a}_k}{k} \sin \phi_k \right| - \Lambda_0 a_0 \omega_0 \sum_{k=1}^N \tilde{a}_k k \sin \phi_k + \Lambda_1 \left(\sum_k \tilde{a}_k^2 - 1 \right), \quad (4.2.17)$$

where $\mathcal{L} = \mathcal{L}(\tilde{a}_k, \sin \phi_k, \Lambda_0, \Lambda_1)$ is a Lagrangian density and the variables Λ_0 and Λ_1 are Langrange multipliers. A stationary point of Eq. (4.2.17) satisfies simultaneously $\partial_{\tilde{a}_k} \mathcal{L} = \partial_{\sin \phi_k} \mathcal{L} = \partial_{\Lambda_0} \mathcal{L} = \partial_{\Lambda_1} \mathcal{L} = 0$. Taking into account that the problem (4.2.16) is equivalent to maximizing separately $v_f(0)$ and $-v_f(0)$ and then keeping the maximum between the optima, we can avoid dealing with absolute values when calculating the stationary points of Eq. (4.2.17). Therefore, the stationary points of maximizing $\pm v_f(0)$ satisfy simultaneously in both cases:

$$\partial_{\tilde{a}_k} \mathcal{L} = \pm \frac{e}{m_e} \frac{a_0}{\omega_0} \frac{\sin \phi_k}{k} - \Lambda_0 a_0 \omega_0 k \sin \phi_k + 2\Lambda_1 \tilde{a}_k = 0, \quad (4.2.18)$$

$$\partial_{\sin \phi_k} \mathcal{L} = \pm \frac{e}{m_e} \frac{a_0}{\omega_0} \frac{\tilde{a}_k}{k} - \Lambda_0 a_0 \omega_0 \tilde{a}_k k = 0, \quad (4.2.19)$$

$$\partial_{\Lambda_0} \mathcal{L} = -a_0 \omega_0 \sum_{k=1}^N \tilde{a}_k k \sin \phi_k = 0, \quad (4.2.20)$$

$$\partial_{\Lambda_1} \mathcal{L} = \left(\sum_k \tilde{a}_k^2 - 1 \right) = 0. \quad (4.2.21)$$

Equation (4.2.19) does not depend on the value of $\sin \phi_k$. This means that, for arbitrarily fixed values of $\{\tilde{a}_k\}$, Λ_0 and Λ_1 , the extrema of $\pm v_f(0)$ are retrieved for maximally or minimally possible values of $\sin \phi_k$, i.e., for $\sin \phi_k = \pm 1$. Since the terms $k\tilde{a}_k$ are non-negative, the only way to satisfy Eq. (4.2.20) in the limit $N \rightarrow +\infty$ is that $\sin \phi_k$

changes alternatively its sign, i.e. $\sin \phi_k = (-1)^k$ like in the sawtooth⁸. Knowing this, an equivalent problem to Eq. (4.2.16) is formulated in terms of vectors, again in terms of the absolute value $|v_f(0)|$:

$$\begin{cases} \text{Maximize: } |\mathbf{a} \cdot \mathbf{c}|, \\ \text{subject to:} \\ \mathbf{a} \cdot \mathbf{b} = 0, \\ \mathbf{a} \cdot \mathbf{a} = 1, \end{cases} \quad (4.2.22)$$

where the vector $\mathbf{a} = (\tilde{a}_1, \dots, \tilde{a}_k, \dots, \tilde{a}_N)$ contains unitary amplitudes, the vector $\mathbf{b} = (-1, \dots, (-1)^k k, \dots, (-1)^N N)$ denotes Eq. (4.2.14), and the vector $\mathbf{c} = (-1, \dots, (-1)^k k^{-1}, \dots, (-1)^N N^{-1})$ expresses Eq. (4.2.15). According to the above conditions, \mathbf{a} is a unitary vector orthogonal to \mathbf{b} . Denoting by \perp the components perpendicular to \mathbf{b} , the problem (4.2.22) is equivalent to maximize $|\mathbf{a}_\perp \cdot \mathbf{c}_\perp|$ since $\mathbf{a} = \mathbf{a}_\perp$. The optimum is trivial:

$$\mathbf{a} = \frac{\mathbf{c}_\perp}{\sqrt{\mathbf{c}_\perp \cdot \mathbf{c}_\perp}}, \quad (4.2.23)$$

where \mathbf{c}_\perp is calculated by projecting \mathbf{c} onto \mathbf{b} :

$$\mathbf{c}_\perp = \mathbf{c} - \mathbf{b} \frac{\mathbf{b} \cdot \mathbf{c}}{\mathbf{b} \cdot \mathbf{b}}, \quad (4.2.24)$$

where

$$\frac{\mathbf{b} \cdot \mathbf{c}}{\mathbf{b} \cdot \mathbf{b}} = \frac{6}{N(1+N)(1+2N)}. \quad (4.2.25)$$

This gives the following optimal amplitudes:

$$\tilde{a}_k \sqrt{\mathbf{c}_\perp \cdot \mathbf{c}_\perp} = \frac{1}{k} - (-1)^k k \frac{6}{N(1+N)(1+2N)}. \quad (4.2.26)$$

By taking the limit of Eq. (4.2.26) when $N \rightarrow \infty$, then $\mathbf{c}_\perp \rightarrow (-1, \dots, (-1)^k k^{-1}, \dots, (-1)^N N^{-1})$ with $\sqrt{\mathbf{c}_\perp \cdot \mathbf{c}_\perp} = \sqrt{\sum_{j=1}^N j^{-2}}$. Hence, the optimal unitary amplitudes are:

$$\tilde{a}_k = \frac{1}{k \sqrt{\sum_{j=1}^N j^{-2}}}, \quad (4.2.27)$$

which restore the sawtooth waveform amplitude [Eq. (4.2.6)]. Therefore, this demonstrates that the sawtooth shape provides the optimal high-frequency profile.

Once the *theoretical* optimality of Eq. (4.2.6) is proved, what matters *in practice* is to determine how much the THz conversion efficiency is actually improved when using N colours (for example, $N = 4$) with respect to the classical two-colour scenario. Obviously,

⁸The choice $\sin \phi_k = (-1)^{k+1}$ is also possible and gives an equivalent result.

the extra cost of using more laser harmonics must be justified by a substantial increase in THz energy. The growth in efficiency is studied numerically in an argon target with neutral density $N_a = 2.7 \times 10^{19} \text{ cm}^{-3}$. The fundamental wavelength of the laser pulse is set to $\lambda_0 = 1600 \text{ nm}$. This choice is clearly advantageous over the usual one, 800 nm, because more harmonics are accessible in practice. In particular, the first four harmonics are $\lambda_0/2 = 800 \text{ nm}$, $\lambda_0/3 = 533 \text{ nm}$ and $\lambda_0/4 = 400 \text{ nm}$. All these wavelengths can be produced from an 800-nm femtosecond laser source using, for instance, optical parametric amplification to obtain λ_0 and $\lambda_0/3$ and frequency doubling to obtain $\lambda_0/4$. In contrast, if the fundamental wavelength were 800 nm, then the fourth harmonic at 200 nm would lie already in the ultraviolet spectrum and would not be easy to produce. All the harmonics, including the pump, are endowed with 40-fs-FWHM Gaussian envelopes. The THz energy is studied in the frequency band of 0-100 THz.

The gains predicted by the LC model are analyzed for these physical parameters. In Fig. 4.2.3 the overall THz energy is plotted as a function of the number of harmonics in the sawtooth, normalized to the two-colour case. The behaviour is very similar in the two situations that are considered here. First, in Fig. 4.2.3(a) the laser intensity is adjusted, from 120 to 140 TW cm^{-2} , in order to preserve the ionization degree at $Z^* = 0.1$. Second, in Fig. 4.2.3(b) the intensity is fixed at $I_0 = 100 \text{ TW cm}^{-2}$. The horizontal dashed lines represent the THz energy that would be provided by the ideal sawtooth waveform in the limit $N \rightarrow +\infty$ [Eq. (4.2.5)], which is one order of magnitude greater than the energy supplied by the two-colour configuration. The energy increase is quasilinear for the first colours ($N \sim 5$), and then it starts to saturate as the N -colour approximation converges towards the ideal sawtooth profile. Looking at this figure, a four-colour configuration predicts a *fourfold gain* in the THz energy compared with the two-colour scenario.

The LC model allows to estimate analytically, for fixed ionization degree and assuming plane waves, the evolution of the THz energy gain as a function of N . According to Eq. (4.2.2) the THz energy is approximately $\sim (\sum_n B_n)^2 \sim (\sum_n \delta N_e^n v_f(t_n))^2$. A representative value of $v_f^N(t_n)$ can be obtained from Eqs. (4.2.7) and (4.2.9):

$$v_f^N(t_n) \propto a_0^N \frac{\chi(N)}{\sqrt{H_{N,2}}}, \quad (4.2.28)$$

where a_0^N is the amplitude of the N -colour laser pulse (adjusted to the desired ionization degree), $H_{N,2} = \sum_{j=1}^N j^{-2}$ (generalized harmonic number), and $\chi(N)$ is the series

$$\chi(N) = \sum_{k=1}^N \frac{(-1)^k}{k^2} \cos\left(\pi k \frac{N}{N+1}\right). \quad (4.2.29)$$

If $\delta N_e^{n,N}$ is the representative value of the density jumps, then the growth of the THz

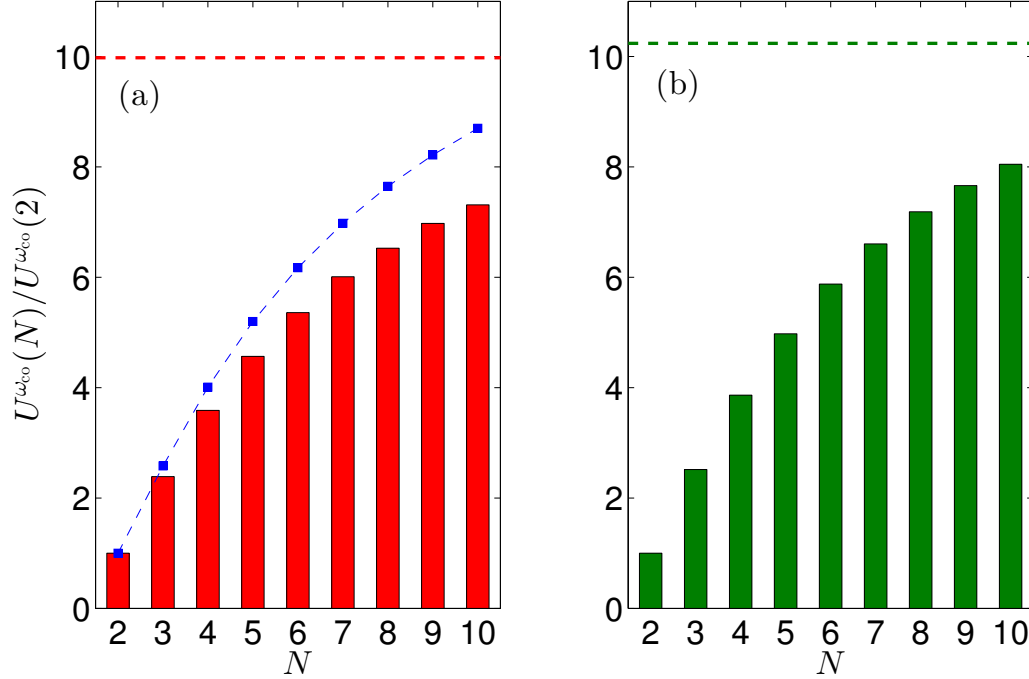


Figure 4.2.3: Terahertz energy ($\nu_{\text{co}} = 100 \text{ THz}$) in argon at ambient pressure calculated from the LC model [Eqs. (2.4.5) and (2.4.28)] with QST ionization rate for different N -colour approximations of the sawtooth waveform [Eq. (4.2.6)]. Energies are normalized to the corresponding two-colour case. The laser pulse has a fundamental wavelength of 1600 nm and a duration of 40 fs-FWHM (Gaussian envelope). (a) Growth of THz radiation for a fixed ionization degree $Z^* = 0.1$ (intensities vary between 120 and 140 TW cm^{-2}). (b) Growth of THz radiation for a fixed intensity of $I_0 = 100 \text{ TW cm}^{-2}$. The dashed lines indicate the energy yielded by an ideal sawtooth [Eq. (4.2.5)]. The dashed-square blue curve of (a) is the analytical plane-wave estimate of the gain given by Eq. (4.2.31).

energy with respect to the two-colour case is roughly given by:

$$\frac{U^{\omega_{\text{co}}}(N)}{U^{\omega_{\text{co}}}(2)} = \left(\frac{\delta N_e^{n,N}}{\delta N_e^{n,N=2}} \right)^2 \left(\frac{a_0^N}{a_0^{N=2}} \right)^2 \left(\frac{v_f^N(t_n)}{v_f^{N=2}(t_n)} \right)^2. \quad (4.2.30)$$

Assuming that $\delta N_e^{n,N} \approx \delta N_e^{n,N=2}$ and $a_0^N \approx a_0^{N=2}$, Eq. (4.2.30) simplifies as:

$$\frac{U^{\omega_{\text{co}}}(N)}{U^{\omega_{\text{co}}}(2)} = \frac{80}{9} \frac{\chi(N)^2}{H_{N,2}}, \quad (4.2.31)$$

which is plotted in Fig. 4.2.3(a) as the dashed-square blue curve. Even though this curve slightly overestimates the gain owing to the plane-wave approximation, it reflects correctly

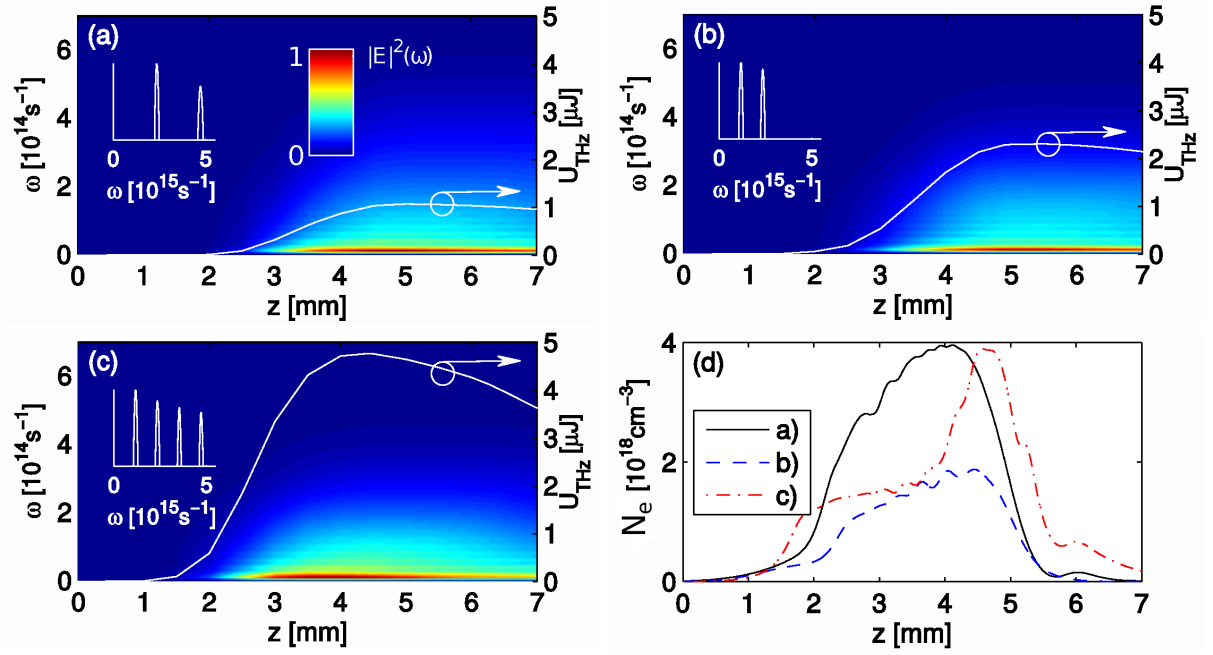


Figure 4.2.4: Low frequency spectra 0-100 THz (image plots) of (a) a 800-nm two-colour pulse whose second harmonic represents 6% of the laser energy, (b) a 1600-nm two-colour pulse whose second harmonic represents 40% of laser energy, and (c) a 1600-nm four-colour pulse following Eq. (4.2.6). The overall THz energy ($\nu_{\text{co}} = 100$ THz) contained in the numerical box (white curve) is shown as a function of the propagated distance on the right axis. (d) Evolution of the peak electron density for all these three pulses.

the behaviour of the gain with respect to N .

The advantage of using the four-colour approximation for the sawtooth field compared with the two-colour scenario is finally studied numerically employing the UPPE equation [Eq. (2.1.81)], which takes into account propagation effects in full space and time resolved geometry. The simulations have been performed using the UPPE 3D code [Section 3.1.1]. The fourfold increase in THz energy predicted by the LC model is expected to be reduced to some extent because of the 3D propagation effects, which affect the relative phases, local intensities and pulse durations.

For the 3D simulations, whose results are summarized in Fig. 4.2.4, the overall energy of the laser pump pulse is set to $300 \mu\text{J}$, its beam width to $100 \mu\text{m}$ and its FWHM duration to 40 fs (Gaussian envelope). The laser pulse is focused with a focal length of $f = 5$ mm into argon, whose linear refractive index is modelled following the dispersion relation by Dalgarno and Kingston [43]. Three situations are simulated:

- Figure 4.2.4(a): Two-colour laser configuration at the standard pump wavelength of $\lambda_0 = 800$ nm. The energy in the second harmonic represents 6% of the total pulse

energy, which is not the optimized energy ratio.

- Figure 4.2.4(b): Two-colour laser configuration at doubled pump wavelength, $\lambda_0 = 1600$ nm. The energy of the second harmonic is increased up to 40% of the overall laser energy to approach the first two harmonics of the sawtooth.
- Figure 4.2.4(c): Four-colour laser configuration ($\lambda_0 = 1600$ nm) and the energy repartition is given as in Eq. (4.2.6), adapted to a three-dimensional pulse geometry.

The spectra of the three laser configurations along the z -propagation axis exhibit analogous shapes. Their intensity is indicated by the colour bar and the frequency range on the left ω -axis extends from 0 to 100 THz. The THz pulse energy here appears confined mostly in the frequency band 0-30 THz due to tight focusing. The THz energy produced along the propagated distance is indicated by the white curve (see right-hand side axis). The first configuration yields $\sim 1 \mu\text{J}$ THz energy [Fig. 4.2.4(a)], whereas the second one generates $\sim 2 \mu\text{J}$ THz pulse energy [Fig. 4.2.4(b)]. Note that only a twofold increase of the THz energy when doubling the pump wavelength is achieved in the enhancement of the THz yield. The four-colour configuration [Fig. 4.2.4(c)] increases the THz energy until $\sim 5 \mu\text{J}$. Compared with the 1600-nm two-colour configuration, the gain is ~ 2.5 . A comparable fraction of $\approx 10\%$ of neutral atoms is ionized, as shown in Fig. 4.2.4(d). As expected, the gain ≈ 2.5 is smaller than the prediction ≈ 4 due to the 3D propagation effects which may affect the shape of the laser pulse over propagation. Nevertheless, these effects are not able to prevent the four-colour configuration from reaching a conversion efficiency of 2%, *which is unprecedented for THz generation in gases*.

In conclusion, the remarkable property of sawtooth waveforms has been confirmed numerically by these comprehensive 3D simulations, awaiting experimental proofs in future experiments. Surprisingly, somewhat similar wave shapes were found to increase the yield and electron recollision energy in the generation of high-order harmonics by up to two orders of magnitude [34, 71].

5 Terahertz generation in high-intensity regimes

Contents

4.1 Experimental study of the terahertz emission by laser-plasma filaments: action of bound electrons versus free electrons	126
4.2 Boosting terahertz generation using a sawtooth-wave shape	137

So far, our theoretical study of laser-driven terahertz sources in gases has been devoted to intensities below 10^{15} W cm⁻². Those regimes are reached in current experiments devoted to the filamentation or loosely focused propagation [9, 35, 117, 128, 130]. As explained in Section 4 and summarized in Fig. 5.0.1, in this scenario the terahertz radiation mainly originates from both the nonlinear Kerr effect (i.e., the response of bound electrons) at the lowest intensities, and the electron plasma (i.e., the response of free electrons). Plasma-induced THz fields are created mostly through photocurrents and also plasma wakefields. These are expected to be responsible for the Cherenkov-like conical radiation yielded by longitudinal plasma waves at higher intensities exceeding the gas ionization threshold. In this situation, gas targets (e.g., air or noble gases such as hydrogen, helium and argon) are only weakly ionized with an effective charge number less than unity. Thus, usually single-ionization models are applied in both MPI and tunnelling regimes that only solicit the outermost electronic shell of the gas atoms.

Since the last ten years, terahertz generation has emerged as a recurrent topic in the scope of relativistic laser-plasma interactions able to deliver strong radiated, i.e., secondary electromagnetic fields. For instance, several authors (Hamster *et al.* [72], Li *et al.* [106, 107], Li *et al.* [109], Sagisaka *et al.* [141]) have reported, experimentally and with Particle-In-Cell (PIC) simulations, impressive terahertz fields with energy > 400 μ J, amplitude > 0.1 GV/m and conversion efficiency > 1 ‰, when irradiating micrometre-width solid targets such as metal foils (copper, aluminium and titanium) or plastics (methylene) with ultrashort laser pulses at relativistic intensities above 10^{19} W cm⁻². In this configuration, terahertz radiation is explained by two main processes, namely, Transition Radiation Currents (TRC) and Target Normal Sheath Acceleration (TNSA) mechanisms. Both of

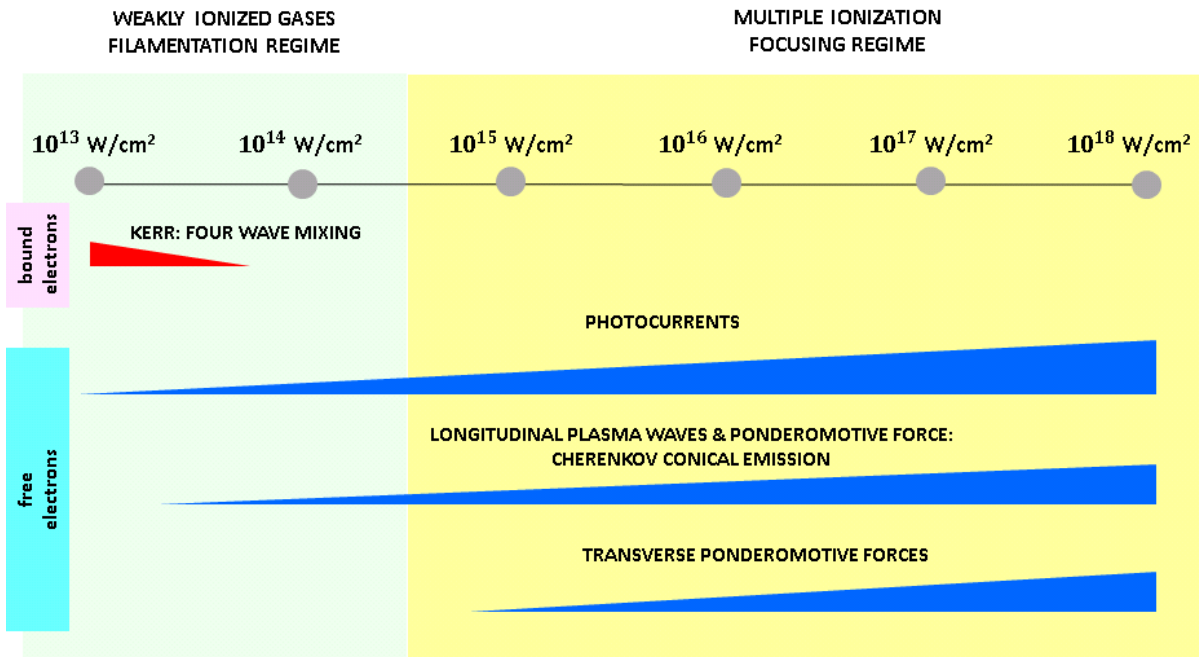


Figure 5.0.1: Schematic representation of the relevance of the different key players producing terahertz radiation as a function of the laser intensity. The Kerr effect and four-wave mixing play a role at low intensities before the onset of plasma generation. Free electrons convert part of the laser energy into terahertz radiation through photocurrents, longitudinal and transverse ponderomotive forces (plasma waves). The latter emitters grow in importance with the intensity, but the former (photocurrents) is very dependent on the laser configuration and the gas nature.

these involve acceleration of electrons and even ions by the strong ponderomotive forces driven inside the plasma. The former process states that the electron bunch ejected from the plasma into vacuum must radiate an electromagnetic pulse (part of which in the terahertz frequency domain) to satisfy the continuity of the electric field at the interface between the two media. This mechanism relies on the strong acceleration of electrons and ions (first ejected into vacuum in all directions and then confined into the plasma), which are caused by the rapid longitudinal and the slow transversal ion current densities driven by the optical field and which will irradiate also a part of the energy in their terahertz band.

Between the *classical* filamentation scenario and this *recent* scenario of strongly relativistic laser-plasma interactions, the broad range of intensities between 10^{15} W cm^{-2} and 10^{18} W cm^{-2} of laser-gas interactions has been little studied. However, it may be promising to produce intense terahertz sources reaching amplitudes of the order of GV/m and broad terahertz spectra up to 100 THz with an almost homogeneous spectral energy density distribution. Plasmas are expected to attain high ionization levels in the tunnelling

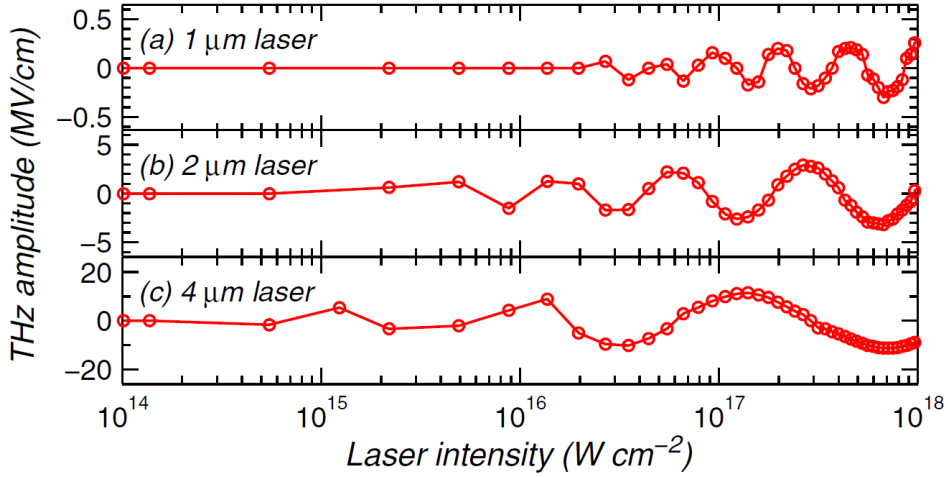


Figure 5.0.2: Maximum THz amplitude generated in hydrogen, as a function of a 50-fs-FWHM single-colour laser intensity for different wavelengths: (a) 1 μm , (b) 2 μm , (c) 4 μm . Source: Wang *et al.* [174].

regime ($Z^* \geq 1$). Furthermore, intense longitudinal and transverse plasma waves may occur in the wake of the laser pulse. A number of papers [26, 63, 154, 174] have addressed the terahertz wave generation in this intensity range by single-colour pulses, mostly in classical (non-relativistic) plasma regimes, i.e., taking only into account photoionization and emissions from longitudinal plasma waves. Terahertz field amplitudes of the order of 1 GV/m have been predicted. Moreover, Wang *et al.* [174], by means of 2D Particle-In-Cell simulations, observed in hydrogen that, instead of enhancing monotonically with the laser intensity, THz field strengths develop oscillations with a period increasing with a longer laser wavelength and a maximum amplitude growing as the laser intensity is enhanced (see Fig. 5.0.2). They reasoned in terms of the averaged velocity of the newly born electrons, with which the THz amplitude develops from the slow component of the current. This velocity scales linearly as

$$\langle v_{x,0} \rangle = -\frac{e}{m_e c N} \sum_{j=1}^N A_x(\xi_j), \quad (5.0.1)$$

where A_x is the vector potential, N being the total number of free electrons and $\xi_j = ct_j - z_j$ is determined by the birth position (z_j) and instant (t_j) of j -th electron. When the laser electric field is intense enough to ionize completely the gas (hydrogen) at its leading edge, the number distribution of newly born electrons versus the electron birth position ξ is asymmetric. This implies that $\langle v_{x,0} \rangle \neq 0$ and thus a THz pulse is emitted. Wang *et al.* [174] explained this oscillatory behaviour in the THz amplitude as a mismatch between the number distribution of newly born electrons and the laser cycles that ionize the gas.

From the viewpoint of wave coupling process, Singh and Sharma [149] besides examined the influence of external magnetic fields resulting in higher conversion efficiencies through the three-wave parametric decay mechanism. Much fewer researches, nonetheless, have been devoted to two-colour pulses in strongly ionized plasmas [9, 46, 173, 130, 181]. Some of these retrieved that the terahertz electric field can be proportional to the intensity of the fundamental and to the square root of the intensity of the second harmonic [like in Eq. (4.0.4)]. Let us recall here that Balakin *et al.* [9] justified that the terahertz emission originated from photocurrents scales as the sine of the phaseshift —this was shown in Section 2.4.2— and the THz emission induced by the radiation pressure force and the ponderomotive force (see Section 2.3.2) varies in proportion to the cosine of the phaseshift between the two laser colours. Contributions from ponderomotive and radiation pressure effects also vary according to the polarization state (orthogonal or parallel) of the second harmonic compared to that of the pump wave.

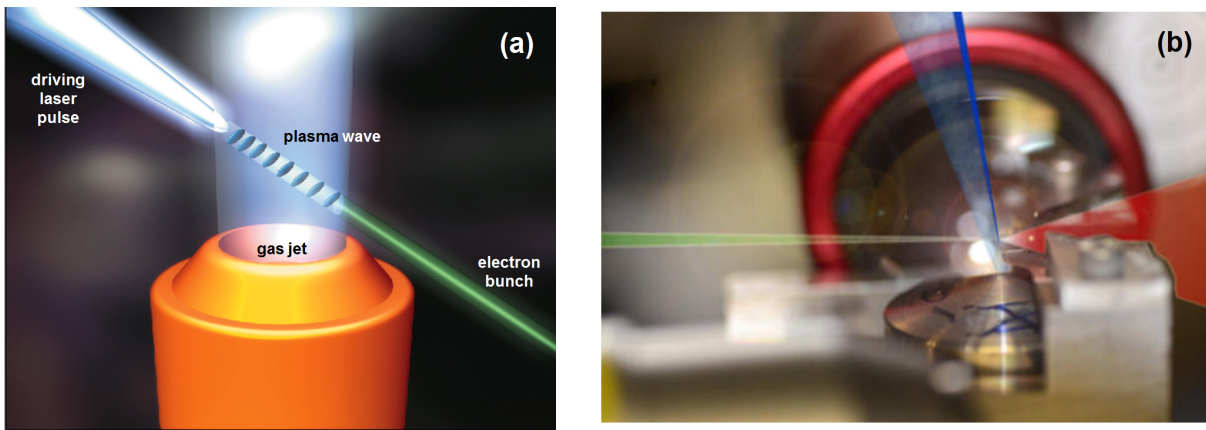


Figure 5.0.3: (a) Schematic representation of the laser-driven electron acceleration setup. Source: LOA/ENSTA Paris Tech/CNRS/École Polytechnique. (b) Details of a realistic setup: laser pulse (red), gas jet (blue) and electron bunch (green). Source: Max Planck Institute of Quantum Optics [121].

The goal of this section is to clarify, for the first time to our knowledge, which among the terahertz conversion mechanisms studied in Section 4 can be the most efficient when they play together in a gas target, for a general laser pump configuration (e.g., one or two colours) and at this high intensity range (from 10^{15} W cm⁻² to near-relativistic intensities $\sim 10^{18}$ W cm⁻²). We again assume a second harmonic pulse parallel to the fundamental polarization direction. The novelty of our research lies not only in modelling and analyzing numerically the terahertz generation inside the plasma taking into account all these processes, but also in studying numerically how a plasma volume with (realistic) finite extents transmits terahertz radiation out of the plasma zone into the vacuum, which is of practical interest in many situations. For the curious reader, Fig. 5.0.3 shows how

the gas volumes with density gradients at target-vacuum interfaces considered for our simulations at high intensities could be created practically. Basically, this appropriate volume could be produced in a vacuum chamber with gas flow streaming from a nozzle with supersonic velocity, in the same way as it is done in laser-driven electron acceleration setups [27].

The importance of the four potential THz emitters illustrated in Fig. 5.0.1 are here worth being shortly addressed for high laser intensities:

- The four-wave mixing mechanism (Kerr effect) becomes irrelevant in this context because it is mainly due to the response of the neutral atoms, whereas those are completely ionized in the very first cycles of the laser field at high intensities. Indeed, for a Z -charged atom, the third-order electric susceptibility $\chi^{(3)}$ at a certain position and instant can be approximated by linear weighting over all ions [from $j = 0$ (the neutrals) to $j = Z$]:

$$\chi^{(3)} = \frac{\sum_{j=0}^Z \chi_j^{(3)} N_j}{\sum_{j=0}^Z N_j}, \quad (5.0.2)$$

where N_j is the density of the j -th ion and $\chi_j^{(3)}$ the corresponding third-order electric susceptibility. The prevalence of neutrals (i.e., $\chi_{j \geq 1}^{(3)} \ll \chi_0^{(3)}$) usually implies that Eq. (5.0.2) reduces to $\chi^{(3)} = \chi_0^{(3)} N_0 / (\sum_{j=0}^Z N_j)$ [see Remark 1 in Section 2.1.1], which means that $\chi^{(3)}$ is virtually zero at high-ionization levels. Therefore, this process will be discarded in this intensity range.

- Equation (3.4.15) already advances that the on-axis radiated field along the laser polarization direction is proportional to the derivative of the transverse current. This signifies that the well-known and robust photocurrent mechanism, explained in Section 2.4.2, seems to be also a relevant mechanism above $10^{15} \text{ W cm}^{-2}$. Nonetheless, its efficiency above $10^{15} \text{ W cm}^{-2}$ is an open issue because at these intensities longitudinal plasma waves as well as transverse plasma waves appear as alternative key players which can take over in THz generation. Apart from its nonlinear dependence on the laser configuration (e.g., number of colours, phaseshifts and durations), a new nonlinearity comes into play: the successive ionization of all the electronic shells, namely, the evolution of the ionization degree as a function of the laser intensity [see Fig. 2.2.4]. Taking into account that laser-induced photoionization can be considered as a *sequential* process, the superposition principle holds over all shells and hence the contributions to the THz radiation by J_A [Eq. (2.4.30)] and

J_B [Eq. (2.4.31)] cumulated over the ionization events can now be expressed as

$$A_n = \sum_{j=0}^{Z-1} A_n^j = \sum_{j=0}^{Z-1} C \frac{\delta N_e^n}{Z^* N_a} \omega_{co} r_f(t_n), \quad (5.0.3)$$

$$B_n = \sum_{j=0}^{Z-1} B_n^j = \sum_{j=0}^{Z-1} \frac{\delta N_e^n}{Z^* N_a} v_f(t_n), \quad (5.0.4)$$

where j stands for the number of ion charge.

- Longitudinal plasma waves promoted by the longitudinal driving source $\mathbf{\Pi}_{\parallel}$ [Eq. (2.3.18)], emitting a conical terahertz radiation when the plasma channel is assumed to behave like a wire-antenna (see Section 4), depend principally on the laser pulse instantaneous intensity and on the plasma frequency (see Section 2.3.2). Therefore, the longitudinal electric field inside the plasma can be expected to grow with the laser intensity (with a similar behaviour if one or two colours are employed), even if ionization is saturated.
- Transverse plasma waves induced by the transverse driving source $\mathbf{\Pi}_{\perp}$ [Eq. (2.3.19)] should also increase with the intensity. Little information is, however, available on plasma geometries with finite transverse extents, as all the past literature proposed that only the plasma-gas boundaries should emit within the plasma skin depth¹.

In this section two new results are presented, which are of prime importance for the design of laser-driven terahertz sources in high-intensity laser-matter interaction:

- The nonmonotonic growth of terahertz generation with the intensity is clarified in Section 5.1. Here, the photoionization and plasma current oscillations are studied inside the plasma using our 1D model and numerical simulations. The sequential action of the successive electronic shells [Eqs. (5.0.3) and (5.0.4)] is the main responsible for the nonmonotonic growth of the terahertz radiation. This research helps to select specific intensity levels that best promote laser-to-THz energy production, according to the properties of the gas target. These results have been published in Ref. [46].
- How photoionization and wakefield effects compete in a multidimensional configuration is discussed in Section 5.2. The main result is that prevalence of the photocurrent mechanism is confirmed with a two-colour scheme and it is conditioned by the above nonmonotonic growth along the multiple ionization events [Section 5.1]. The

¹It is defined as the depth in a plasma which electromagnetic radiation can penetrate. From the plasma wave dispersion relation, $\omega^2 = \omega_p^2 + \omega_0^2$, one can easily express it as c/ω_p .

importance of transverse plasma wave oscillations is reported. This result opens the door to the design of laser-driven THz sources benefiting also from transverse ponderomotive emitters that could increase the amount of THz radiation. These results have been published in Ref. [68].

5.1 1D configuration: non-monotonic growth of the terahertz energy through multiple ionization

The purpose of this section is to understand how the THz pulse energy increases with the laser and target parameters. Unlike most of anterior studies which considered either hydrogen or singly ionized gas targets [37, 127, 170, 181], we shall here focus our attention on noble gases whose shell structures are not limited to one extractable electron. In this section the production of laser-driven THz radiation in common gases such as helium and argon is examined, allowing for multiple ionization events at laser intensities approaching $10^{17} \text{ W cm}^{-2}$.

For intensities beyond 10^{14} - $10^{15} \text{ W cm}^{-2}$, Debayle *et al.* recently showed for hydrogen, thanks to a one-dimensional non-relativistic Maxwell-Fluid model supported by Particle-In-Cell (PIC) simulations [45], that the forward-propagating transverse THz waves are initiated from both plasma current oscillations and photoionization. Here, single ionization was applied and the backward THz waves keep the trace of electron current oscillations at the plasma frequency. Transverse ponderomotive effects were discarded from this study because there were expected to be of secondary importance compared to photoionization in nonrelativistic interaction regimes ($< 10^{17} \text{ W cm}^{-2}$) [30, 148, 173, 178]. In this section we shall still stay in the context of one-dimensional geometry to address the impact of multiple ionization. The action of transverse wakefield effects will be treated in Section 5.2.

To start with, we describe both rapid laser oscillations and plasma wave excitations [45], extended to complex atoms [46]. The field propagating along the z -axis and the laser electric field being polarized along x -axis, this model is actually included in Eq. (3.4.12) derived in Section 3.4. Here we assume a non-relativistic plasma ($\gamma = 1$) and discard the Kerr effect ($J_{\text{KERR}} = 0$), so that:

$$\left(\partial_t^2 - c^2 \partial_z^2 + \partial_t (\partial_t + \nu_c)^{-1} \omega_p^2\right) \tilde{E}_x = -\frac{1}{\varepsilon_0} \partial_t J_L, \quad (5.1.1)$$

where the transverse electric field $E_x = E_L + \tilde{E}_x$ is decomposed into the laser pump E_L , which remains unperturbed over propagation by hypothesis, and the radiated field \tilde{E}_x . The plasma frequency is $\omega_p = \sqrt{m_e^{-1} \varepsilon_0^{-1} e^2 N_e}$, and ν_c accounts for the electron collision rate. The electron density is calculated in tunnel-based multiple ionization described by Eqs. (2.1.57) and (2.2.31) with the ADK ionization rate of Eq. (2.2.27). In the limit $\tilde{E}_x \ll E_L$, one can extract approximate solutions for both the reflected and transmitted secondary fields that self-consistently contain the THz field created by ionization [7] and plasma current oscillations [173]. We only address the forward emission.

In a first approach, a non-propagative model is employed from Eq. (5.1.1), which only provides a rough estimation of the first maximum oscillation in the transverse terahertz field. This “rapid” model, called 0D model, is enough to qualitatively evaluate the laser-to-THz energy conversion (see Remark 2 in Section 3.4.0.2). Removing the propagation effects ($\partial_z^2 = 0$) and assuming weak collisions ($2\pi\nu_c \ll \omega_p$), Eq. (5.1.1) indeed reduces to

$$\left(\partial_t^2 + \omega_p^2\right) \tilde{E}_x = -\omega_p^2 E_L, \quad (5.1.2)$$

where the transverse laser current $\partial_t J_L = e^2 m_e^{-1} N_e E_L$ is calculated in line with Eq. (2.1.56). In the comoving frame $\tau \equiv t - z/c$, the one- or two-colour laser electric field is given by

$$E_L(\tau) = \sqrt{\frac{2I_0}{c\varepsilon_0}} \left[\sqrt{1-r} \mathcal{E}_1(\tau) \cos(\omega_0\tau) + \sqrt{r} \mathcal{E}_2(\tau) \cos(2\omega_0\tau) \right], \quad (5.1.3)$$

$$\mathcal{E}_1(\tau) = \exp \left[-2 \ln 2 \left(\frac{\tau}{\tau_p} \right)^2 \right], \quad \mathcal{E}_2(\tau) = \exp \left[-8 \ln 2 \left(\frac{\tau}{\tau_p} \right)^2 \right], \quad (5.1.4)$$

where $\nu_0 = \omega_0/(2\pi)$ is the fundamental frequency, I_0 is the cycle-average intensity [as defined in Eq. (2.1.32)], $0 \leq r \leq 1$ is the intensity ratio between the second and the fundamental harmonics, τ_p is the FWHM duration of the fundamental pulse (the second harmonic has half duration). For simplicity, in Eq. (5.1.3) the two colours are in phase, i.e., their relative phase is zero.

In the laser comoving reference frame, the analytical solution to Eq. (5.1.2), with the initial condition $\tilde{E}_x(\tau \rightarrow -\infty) = 0$, reads as:

$$\begin{aligned} \tilde{E}_x(\tau) = & \cos(\omega_p\tau) \int_{-\infty}^{\tau} \omega_p E_L(\tau') \sin(\omega_p\tau') d\tau' - \\ & \sin(\omega_p\tau) \int_{-\infty}^{\tau} \omega_p E_L(\tau') \cos(\omega_p\tau') d\tau'. \end{aligned} \quad (5.1.5)$$

Figure 5.1.1 shows the numerical solution \tilde{E}_x to Eq. (5.1.2), in argon and helium with an initial density of neutrals $N_a = 1.2 \times 10^{18} \text{ cm}^{-3}$ for a 1- μm , single-colour laser pulse with $I_0 = 5 \times 10^{15} \text{ W cm}^{-2}$ and $\tau_p/(2\pi\omega_0^{-1}) = 10$ (black dotted line). The laser field ionizes both gases over times shorter than the pulse length. After the laser pulse has passed, the electrons retain a nonzero momentum $p_x = -e\partial_\tau E_x(\tau_n)/c$ proportional to the value of the derivative of the electric field at the ionization time $\tau = \tau_n$, yielding a low-frequency transverse current. This produces a radiated field \tilde{E}_x (cyan curve for helium) from which the THz emission is extracted using a low-pass filter with a cutoff frequency at 45 THz (dashed lines: red curve for helium and green curve for argon). The 0D model therefore

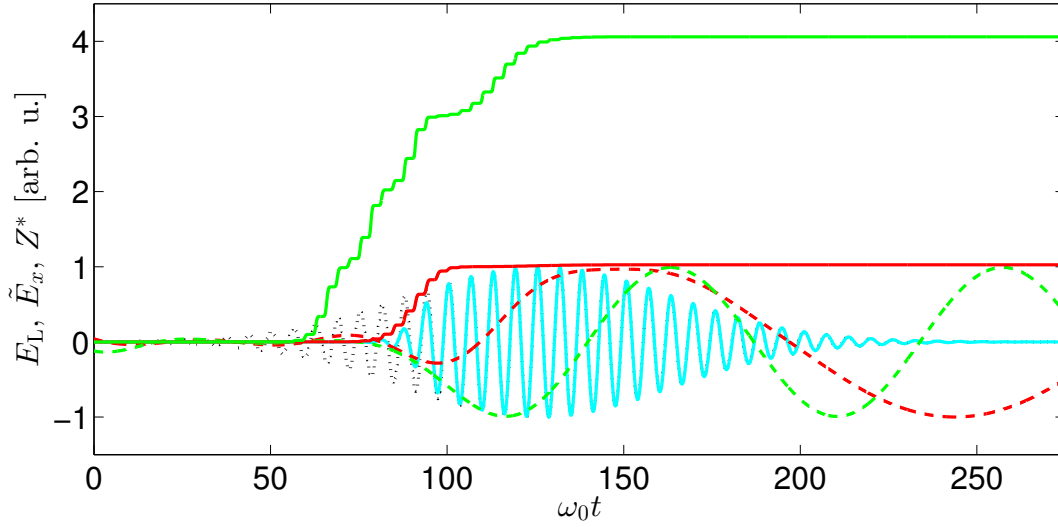


Figure 5.1.1: Solution of the 0D model given by Eq. (5.1.2), together with the electron density calculated in an ADK-based multiple ionization scheme by Eqs. (2.2.27), (2.1.57) and (2.2.31), in argon and helium (initial density of neutrals $N_a = 1.2 \times 10^{18} \text{ cm}^{-3}$) for a 1- μm , single-colour laser pulse with $I_0 = 5 \times 10^{15} \text{ W cm}^{-2}$ and $\tau_p/(2\pi\omega_0^{-1}) = 10$. Notation: laser field (dotted black curve), \tilde{E}_x in helium (cyan curve), filtered THz field in helium (dashed red curve), filtered THz field in argon (dashed green curve), ionization degree in helium (red curve), and ionization degree in argon (green curve). All the electric fields are normalized to their maximum value.

self-consistently incorporates plasma current oscillations in contrast to the LC model [8] (see Section 2.4.2), which relies on constructive interferences occurring *during* ionization only. The resulting THz field oscillates at the plasma frequency fixed by the ionization degree Z^* reached in the wake of the pulse ($Z^* = 1$ in He and $Z^* = 4$ in Ar). Because our model neglects propagation effects, the THz field oscillates with a constant amplitude.

This 0D model is an “easy means” to predict the main characteristics of the produced THz pulse with regard to the laser and gas parameters. These predictions will be afterwards validated by direct numerical simulations. Figure 5.1.2(a) displays the variations of the THz field maxima against the intensity of single-colour pulses as predicted by Eq. (5.1.2) to which the multiple ionization model [Eqs. (2.2.27), (2.1.57) and (2.2.31)] is coupled, for different pulse FWHM durations in argon and helium. Compared to the reference hydrogen case, THz amplitudes as high as 0.1 GV/m can be reached in argon at intensities of a few $10^{15} \text{ W cm}^{-2}$, provided the FWHM duration is short enough. The drop in the THz signal at long pulse durations stems from the increasing time symmetry in the ionization events (see Section 2.4.2). Indeed, if the laser duration is very short

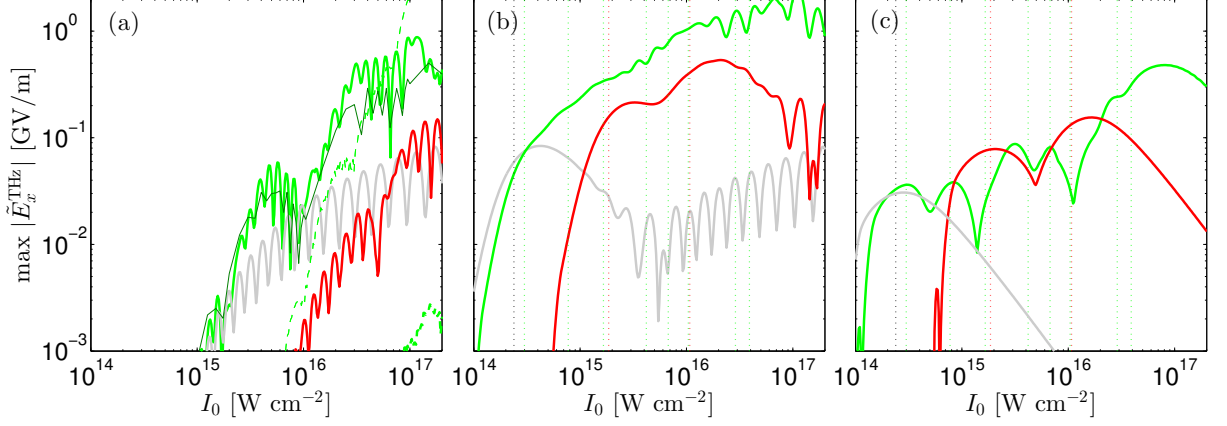


Figure 5.1.2: THz field strength versus pump intensity for argon (green curves), helium (red curves), and hydrogen (gray curves) predicted by Eq. (5.1.2) for $N_a = 1.2 \times 10^{18} \text{ cm}^{-3}$: (a) single-colour pulses with $\tau_p/(2\pi\omega_0^{-1}) = 10$ (solid curves) and $\tau_p/(2\pi\omega_0^{-1}) = 40$ (dashed curves); (b) two-colour pulses with $\tau_p/(2\pi\omega_0^{-1}) = 10$; (c) two-colour pulses with $\tau_p/(2\pi\omega_0^{-1}) = 40$. Dotted vertical lines visualize the ionization thresholds in each gas with same colour convention. In (a), the predictions of the LC model [Eqs. (2.4.5) and (2.4.28)] in argon are plotted as thin dark-green curves. THz emission is computed for the frequency window ≤ 45 THz.

compared with the plasma period, $\tau_p \ll 2\pi/\omega_p$, which implies that the unperturbed laser field $E_L(\tau)$ behaves with $\cos(\omega_p\tau) \approx 1$ and $\sin(\omega_p\tau) \approx 0$, the radiated field given by Eq. (5.1.5) reduces to

$$\tilde{E}_x(\tau) \approx -\frac{\omega_p}{N_e} \sin(\omega_p\tau)G(\tau), \quad (5.1.6)$$

where $G(\tau)$ is the source term of the ionization current, given by

$$G(\tau) = \int_{-\infty}^{\tau} N_e E_L(\tau') d\tau' = \frac{m_e}{e^2} J_L(\tau). \quad (5.1.7)$$

As the characteristic ionization time associated to the ionization event [see Eq. (2.4.10)] is much smaller than a laser cycle $2\pi/\omega_0$, the source term $G(\tau)$ can be approximated as

$$G(\tau) \approx \sum_{n=1}^{N_p} \delta N_e^n A_x(\tau_n), \quad (5.1.8)$$

where τ_n refers here to the ionization instants yielding the extrema of $E_L(\tau)$, N_p accounts for the number of ionization events, δN_e^n is the electron density jump induced by tunnel ionization at $\tau = \tau_n$, and $A_x(\tau) = \int_{-\infty}^{\tau} E_x(\tau') d\tau'$ is the laser potential vector.

For single-colour laser pulses, the ionization events are simply given by $\tau_n = n\pi/\omega_0$. In

this case, for perfectly monochromatic plane waves, the source term $G(\tau)$ vanishes. In the case of a time-varying laser envelope, the radiated field between two ionization events is conditioned by the variation of the vector potential [45]:

$$A_x(\tau_{n+1}) - A_x(\tau_n) \propto \sqrt{I_0} \frac{4\pi^2 \tau_p}{(\tau_p \omega_0)^2 - 16\pi^2} \sin\left(\frac{2\pi^2 n}{\tau_p \omega_0}\right), \quad (5.1.9)$$

which roughly scales as λ_0^2/τ_p if $\tau_p \omega_0 \gg 1$. During the laser pulse, successive alternating current bursts are excited, fostering destructive interferences when many laser cycles take place. The resulting dramatic drop of the THz signal, evidenced in argon in Fig. 5.1.2(a), is generic for all considered gases: the THz radiation induced in hydrogen and helium by single-colour pulses of FWHM duration $\tau_p/(2\pi\omega_0^{-1}) = 40$ barely reaches the kV/m level at $10^{17} \text{ W cm}^{-2}$ [it is not visible in Fig. 5.1.2(a)].

With two-colour pulses, the direct dependence of $A_x(\tau_n)$ upon the laser envelope breaks down due to the asymmetric field extrema. This leads to a slower decrease in the THz yield for increasing pulse duration, as one can see in Fig. 5.1.2(b,c).

In general, as shown in Fig. 5.1.2(a), the THz emission increases in high- Z gases due to the stronger laser fields required to ionize inner shells. The observed higher threshold intensity for THz emission in helium stems from its large first ionization energy, $U_{i,1} = 24.6 \text{ eV}$, compared to $U_{i,1} = 13.6 \text{ eV}$ and 15.76 eV in hydrogen and argon, respectively. As recalled in the introduction [45, 173], the THz signal in hydrogen presents an oscillatory dependence upon the laser intensity due to the varying number of the available ionizing optical cycles. For a given valence electron and pulse duration, the higher the laser intensity, the lesser the number of ionizing cycles, which, above a certain intensity value, may not be sufficient to constructively build the THz pulse. For instance, the THz field saturates in hydrogen around 0.1 GV/m at high intensities. This saturation can be partly overcome in argon and helium, where one to two orders of magnitude in the field strength can be gained for $I_0 = 10^{16}$ - $10^{17} \text{ W cm}^{-2}$. Figure 5.1.2(a) also plots with thin green curves the predictions of the LC model [8] in argon with the prefactor g calculated by Eq. (2.4.28) (see Section 2.4.2). Both non-propagative models agree reasonably well although they are built from different relationships between the radiated field and the current: the 0D model of Eq. (5.1.2) predicts $\tilde{E}_x(\tau) \propto J_L(\tau)$ according to Eqs. (5.1.6) and (5.1.7), whereas the LC model assumes $\tilde{E}_x(\tau) \propto \partial_\tau J_L(\tau)$.

Figure 5.1.2(b,c) show the results of Eq. (5.1.2) for two-colour pulses. As expected [90, 140], the THz yield is strongly increased, by at least two orders of magnitude with respect to the corresponding one-colour case shown in Fig. 5.1.2(a). THz fields above the GV/m level are thus obtained in argon with a laser pump of $\tau_p/(2\pi\omega_0^{-1}) = 10$ [Fig. 5.1.2(b)]. This enhancement is particularly pronounced for long pulses [see Fig. 5.1.2(c)], which have

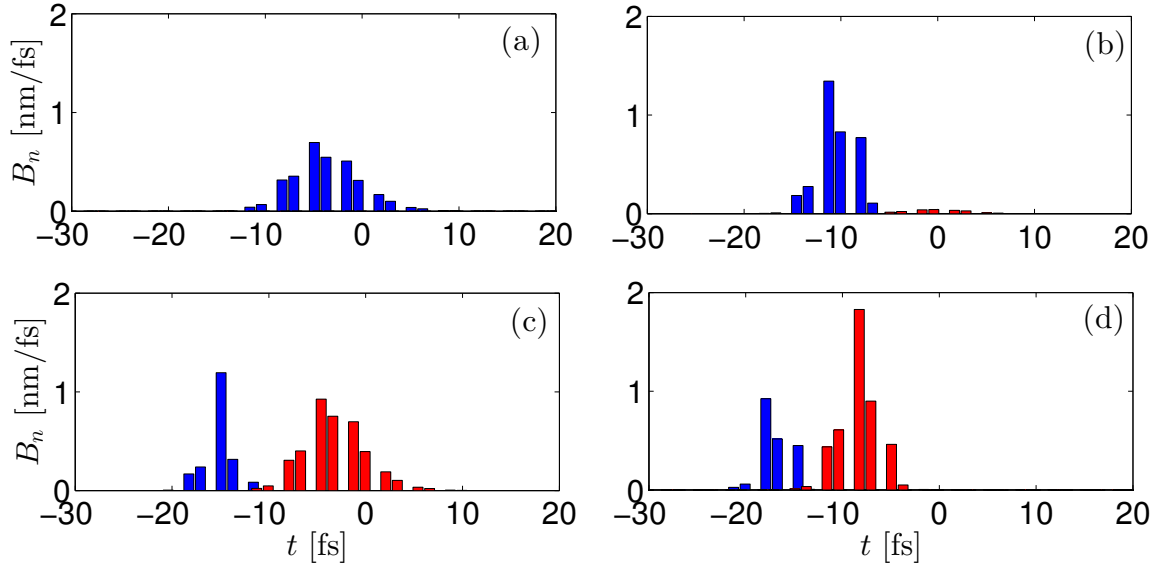


Figure 5.1.3: Oscillatory growth of the THz energy in helium predicted by the LC model (Section 2.4.2), for a two-colour 1- μm 20-fs-FWHM laser pump, whose second harmonic represents 10% of the total intensity and is shifted by $\pi/2$ with respect to the fundamental. The contributions of J_B , B_n given by Eq. (2.4.31), dominant in this case, are plotted for the two electrons (blue: first shell; red: second shell) and four intensities: (a) $2 \times 10^{15} \text{ W cm}^{-2}$, (b) $5 \times 10^{15} \text{ W cm}^{-2}$, (c) $1.2 \times 10^{16} \text{ W cm}^{-2}$, (d) $2 \times 10^{16} \text{ W cm}^{-2}$.

been associated with negligible THz emission in the single-colour case. Compared with hydrogen, the gain factor varies between 20 and 70 for short pulses ionizing helium and argon, respectively, and it can even exceed 100 for longer pulses at mean intensities close to $10^{16} \text{ W cm}^{-2}$. Another remarkable result is the persisting oscillations of the maximum THz field strength. Each THz maximum roughly corresponds to the ionization of a distinct electron shell. This effect is demonstrated by plotting the ionization thresholds in Fig. 5.1.2(b,c) (see vertical dotted lines). For the three gases considered, the local field maxima match the ionization thresholds. The number of oscillations qualitatively follows the averaged charge number. This behaviour is attributed to the THz source term $G(\tau)$, which is maximized each time a j -th shell of the ion population, with binding energy $U_{i,j+1}$ necessary to create the $(j+1)$ -th ion, becomes fully ionized around the pulse envelope maximum.

Equivalently, this oscillatory behaviour, coming from the successive ionization of electron shells, can also be predicted qualitatively by the LC model (see Section 2.4.2). Figure 5.1.3(a,b,c,d) show the contributions $B_n \sim \delta N_e^n v_f(\tau_n)/Z^*$ [Eq. (2.4.31)] for helium and

a two-colour 1- μm 20-fs-FWHM laser pump, whose second harmonic contains 10% of the total laser intensity and is shifted by $\pi/2$ with respect to the fundamental, at four intensities values: $2 \times 10^{15} \text{ W cm}^{-2}$, $5 \times 10^{15} \text{ W cm}^{-2}$, $1.2 \times 10^{16} \text{ W cm}^{-2}$, and $2 \times 10^{16} \text{ W cm}^{-2}$. In Fig. 5.1.3(a,b) only the ionization of the first shell is active. While many ionization events are developed with moderate amplitude, less but stronger events occur in the latter as the laser pump is strong enough to ionize the first shell in few cycles. The same happens to the second electronic shell in Fig. 5.1.3(c,d). There appear two relative maxima when summing up these contributions as a function of the intensity, each one being related to the ionization of each electronic shell. Oscillations in the produced THz field strength result from the balance between two opposite requirements for THz energy: achieving many ionization events and strong ionization strengths.

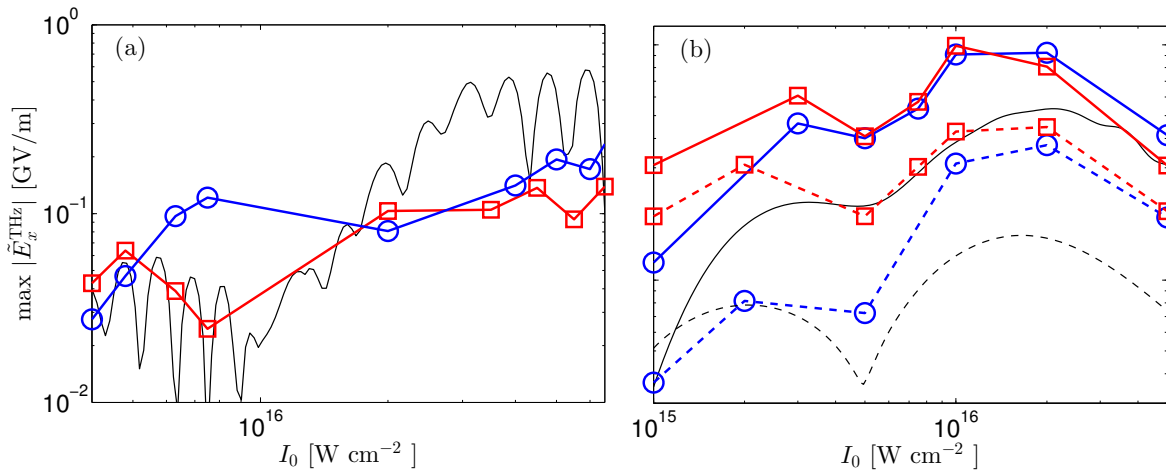


Figure 5.1.4: THz field strength versus pump intensity as predicted by Eq. (5.1.2) (black curve), CALDER 1D code (red curve linking squares), and UPPE 3D code (blue curve linking circles): (a) single-colour pulse with $\tau_p/(2\pi\omega_0^{-1}) = 10$ in argon; Two-colour pulses with (b) $\tau_p/(2\pi\omega_0^{-1}) = 10$ (solid curve) and $\tau_p/(2\pi\omega_0^{-1}) = 40$ (dashed curve) in helium.

To validate these predictions, 1D simulations using the electromagnetic Particle-In-Cell code CALDER have been carried out, which, as detailed in Section 3.1.2, resolves the full set of Vlasov-Maxwell equations that encompass multiple photoionization, kinetic, collective and plasma wakefield effects. Here the initial density profile of the gas (argon or helium) consists of a 90- μm -long plateau bordered by 5- μm -long linear ramps at each side. Additional simulations have been performed with the UPPE 3D code (see Section 3.1.1), rather used in the nonlinear optics community. While both codes employ the same multiple ionization scheme [Eq. (2.2.31)], UPPE 3D further models nonlinear Kerr and chromatic dispersion effects [15, 94]. The incident pulse profile is initialized according to Eq. (5.1.3). The maximum amplitude of the THz fields, measured after propagation

over $100 \mu\text{m}$ and filtered for frequencies below 45 THz, are presented in Fig. 5.1.4(a,b) for single- and two-colour pulses in the intensity range $10^{15} \leq I_0 \leq 6.5 \times 10^{16} \text{ W cm}^{-2}$. The oscillatory variations with the laser intensity predicted by the fluid model are reproduced by both codes to within one order of magnitude, apart from the rapid modulations in argon smoothed by the pump dispersion. Particularly good agreement between CALDER 1D and UPPE 3D results is obtained in all cases shown in Fig. 5.1.4 at high intensities $> 10^{16} \text{ W cm}^{-2}$. Although THz emission is dominated by photoionization and plasma currents rather than Kerr-induced four-wave mixing [20], discrepancies between CALDER 1D and UPPE 3D simulations are attributed to the action of Kerr self-focusing in the latter code, above all in argon at intensities $10^{16} \text{ W cm}^{-2}$ due to a higher Kerr index. In this configuration, as well as for helium, steady-state nonpropagating simulations of Eq. (5.1.2) (see black curves) tend to underestimate the THz fields, as these are expected to accumulate while they nonlinearly propagate [15, 148].

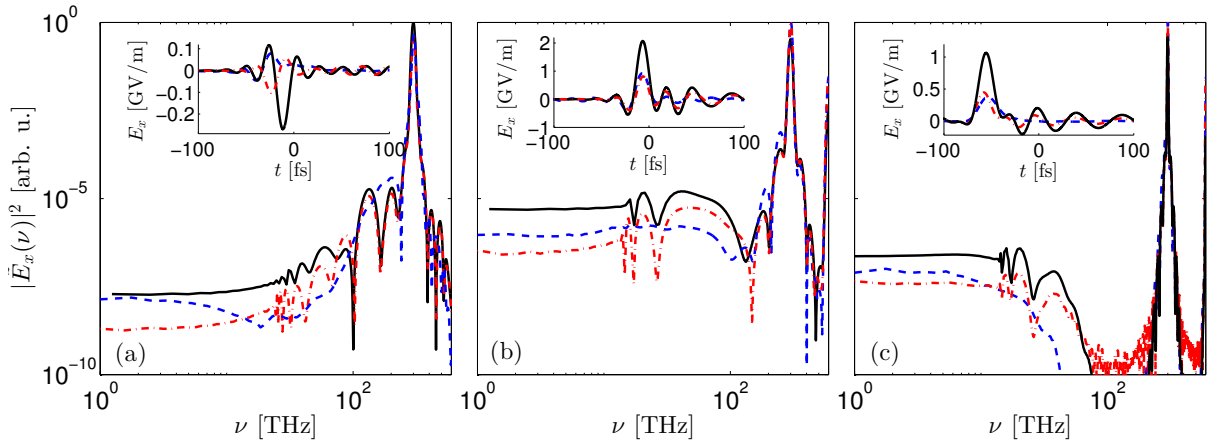


Figure 5.1.5: On-axis transmitted spectra with mean pulse intensity $I_0 = 2 \times 10^{16} \text{ W cm}^{-2}$ for (a) argon irradiated by a single-colour with $\tau_p/(2\pi\omega_0^{-1}) = 10$, (b) helium irradiated by a two-colour pulse with $\tau_p/(2\pi\omega_0^{-1}) = 10$, and (c) helium irradiated by a two-colour pulse with $\tau_p/(2\pi\omega_0^{-1}) = 40$. Red dash-dotted curves: CALDER 1D simulations ($\Delta\nu = 0.5 \text{ THz}$); blue dashed curves: UPPE 3D simulations ($\Delta\nu = 1 \text{ THz}$); black solid curves: 1D Maxwell-Fluid model of Eq. (5.1.1) ($\Delta\nu = 1 \text{ THz}$). Insets show the time-resolved THz field after propagation over $100 \mu\text{m}$.

In order to examine the spectra of the transmitted THz waves, the spatial derivative term ∂_z is retained in Eq. (5.1.1) and this wave equation is integrated numerically using a second-order explicit scheme. This numerical solution is similar to the output of MAXFLU 1D when the Lorentz factor is supposed equal to unity ($\gamma = 1$). The spectra thus predicted are compared with the results of CALDER 1D and UPPE 3D for a semi-

infinite gas² ($z > 0$) of neutral density $N_a = 1.2 \times 10^{18} \text{ cm}^{-3}$ and a mean pulse intensity $I_0 = 2 \times 10^{16} \text{ W cm}^{-2}$. The transmitted spectra are plotted in Fig. 5.1.5(a,b,c) for a set of laser and gas parameters. Good overall agreement between the results supplied by three numerical codes is observed. The plateau-like low-frequency spectra ($\omega \lesssim \omega_p$) are mainly generated by single-cycle current oscillations at the plasma frequency with quasi-DC components $\hat{E}_x(\omega \rightarrow 0) \neq 0$ [see insets of Fig. 5.1.5(a,b,c)].

By contrast, the THz components in the frequency range $\omega_p < \omega < \omega_0$ originate from the constructive interferences of attosecond current bursts emitted at each field maximum through tunnelling ionization (photocurrents) [45]. For sufficiently long plasmas of length L , the latter contribution becomes dominant as inferred from Eq. (5.1.1) in the laser region, $(c^2 \partial_z^2 - \partial_t^2) \tilde{E}_x \simeq \omega_p^2 E_L$, whose solution behaves as $2\omega_0 LG/c$ following Ref. [45]. In the three cases presented in Fig. 5.1.5, the plasma length is set to $L = 200\pi c\omega_0^{-1}$ and the spectrum due to photoionization indeed prevails. The cut-off frequency bounding the plateaulike spectrum scales as $\nu_{\text{co}} \sim \sqrt{Z^*} \nu_p^a$, where $\nu_p^a = \sqrt{e^2 m_e^{-1} \epsilon_0^{-1} N_a} / (2\pi)$ is the plasma frequency associated to the electron density reached when $Z^* = 1$. For $N_a = 1.2 \times 10^{18} \text{ cm}^{-3}$, $\nu_p^a \approx 9.9 \text{ THz}$; due to the higher ionization degree reached in argon ($Z^* = 6$ in argon versus $Z^* = 2$ in helium), ν_{co} increases from $\approx 17.2 \text{ THz}$ in helium to $\approx 30.8 \text{ THz}$ in argon. Filtered below 45 THz, the THz signal reaches $\sim 1 \text{ GV/m}$ with a two-colour pulse in helium [Fig. 5.1.5(b)] and ten times less with a single-colour pulse in argon [Fig. 5.1.5(a)]. The expected drop in conversion efficiency for longer pulses [45] is mitigated in a two-colour configuration: in agreement with Fig. 5.1.2(b,c), the THz amplitude only decreases by a factor of ~ 2 when increasing the two-colour pulse duration from $\tau_p / (2\pi\omega_0^{-1}) = 10$ to $\tau_p / (2\pi\omega_0^{-1}) = 40$ [compare insets of Fig. 5.1.5(b,c)].

As a conclusion, in this section we examined the THz emission produced by forward nonrelativistic femtosecond laser pulses in gases by taking into account the effects of multiple ionization. Our Maxwell-Fluid model supplies good agreement with the results of more sophisticated simulations carried out by CALDER 1D and UPPE 3D. A general result is that stronger THz fields can be achieved when allowing for multiple ionization in gases with high Z numbers. For a given medium, however, an oscillatory laser dependence of the THz emission is revealed, even though the overall THz signal tends to increase with the laser intensity. For two-colour pulses, an unprecedented rapid growth of the THz field against laser intensity is predicted due to the strong electron currents induced by ionization of the inner atomic shells. In this respect, a gain factor of about two orders of magnitude with two-colour pulses at pump intensities $\sim 10^{16} \text{ W cm}^{-2}$ when using argon

²As further shown in Section 5.2, the transmitted transverse field E_x keeps the amplitude produced inside the plasma. Therefore, we conjecture that we can compare the field computed by Eq. (5.1.1) in the plasma after a propagation of $100 \mu\text{m}$ with the transmitted fields computed by UPPE 3D and CALDER 1D codes.

or helium instead of hydrogen is reported. The THz modes below the plasma frequency originate from plasma current oscillations, while those above the plasma frequency are attributed to photocurrents during the ionization process. Our study suggests that the THz field strength may be monitored by changing the gas composition and exploiting multiple ionization effects. These results can thus be of prime importance for designing bright laser-driven THz sources using low-energy ultrashort laser pulses. However, this 1D study is incomplete because the impact of longitudinal and transverse wakefield effects on the THz generation, which may compete against the photocurrent mechanism, has not been addressed. This complete situation is treated below.

5.2 Multidimensional configuration: competition between photoionization and wakefield effects

This section is devoted to a complete physical scenario of laser-driven THz sources at high laser intensities approaching the relativistic threshold (from 10^{15} to $\sim 10^{18}$ W cm $^{-2}$). Thanks to comprehensive two-dimensional PIC simulations in argon and the Maxwell-Fluid model presented in Section 3.4, we offer, to the best of our knowledge, the first unified description of the main THz sources created in nearly-relativistic plasmas, i.e., the joint action of both tunnelling photoionization and longitudinal as well as transverse plasma wave excitations.

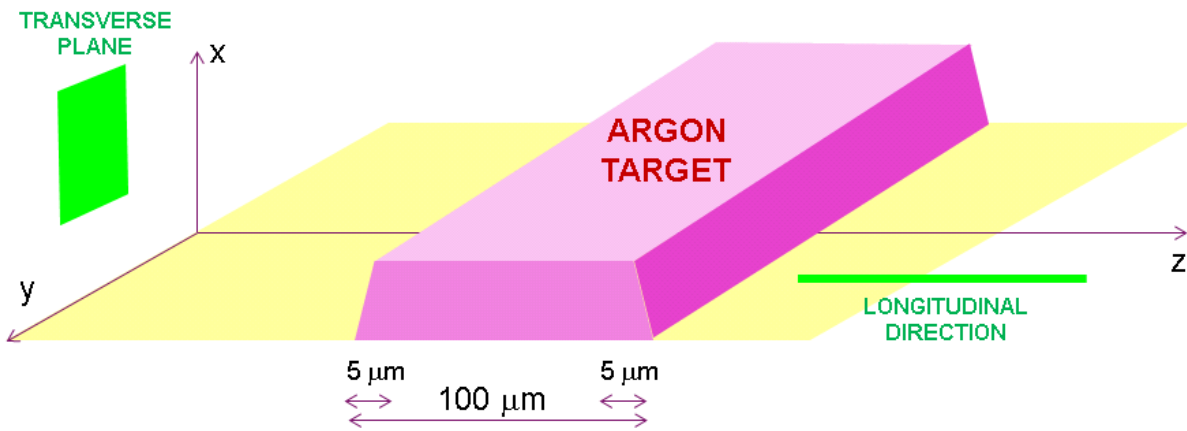


Figure 5.2.1: Geometry used in 2D Particle-In-Cell simulations. The propagation (longitudinal) direction is the z -axis and the transverse plane is (x, y) . The laser pulse is linearly polarized along x . The two-dimensional (y, z) argon target has a trapezoidal initial density profile, with a $90\text{-}\mu\text{m}$ -long plateau bordered by $5\text{-}\mu\text{m}$ -long linear ramps at each side.

To start with, we present the simulation parameters chosen for our multidimensional numerical analysis of THz emission at intensities $\geq 10^{15}$ W/cm 2 performed with the CALDER 2D code.

Figure 5.2.1 shows the geometry of our argon target. The laser pulse is linearly polarized along the x -axis and propagates along z through a $100\text{-}\mu\text{m}$ -long plasma of a 2D-geometrical (y, z) slab of argon. The initial density profile is trapezoidal along z , with a $90\text{-}\mu\text{m}$ -long plateau bordered by $5\text{-}\mu\text{m}$ -long linear ramps at each side, and constant along y . The initial ion temperature is 1 eV and the initial neutral density, $N_a = 2.4 \times 10^{17}$ cm $^{-3}$, guarantees an underdense plasma even at the highest intensities considered. As illustrated by Fig. 5.0.3, although these simulation parameters are chosen for an academic purpose, they can be approached using gas-jet tailoring techniques developed for laser-wakefield accelerators.

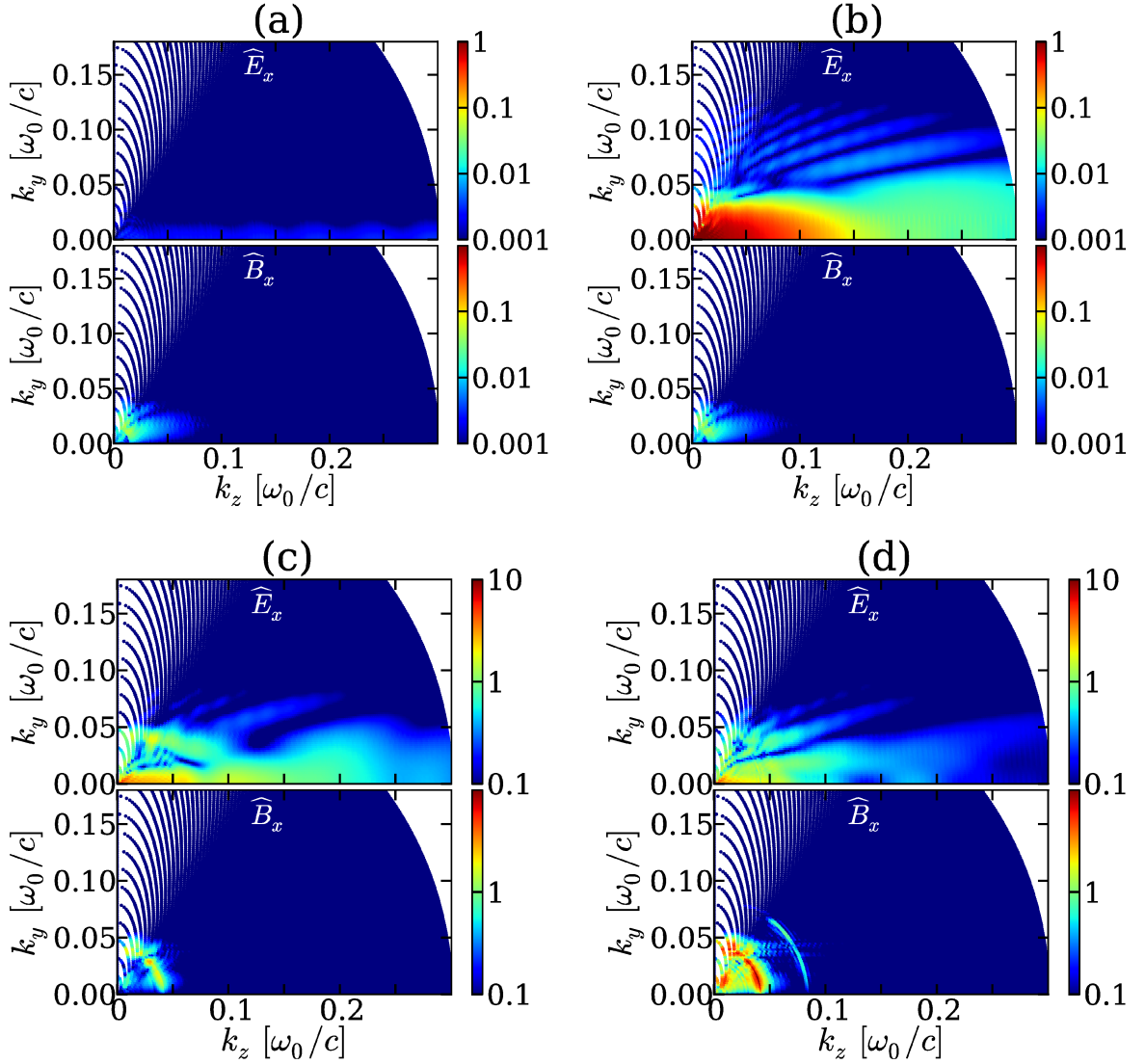


Figure 5.2.2: Spectral angular distribution of THz radiation (arb. units) in the (k_y, k_z) plane produced by E_x and B_x along the laser polarization axis in the following configurations: (a) Single-colour pulse and (b) two-colour pulse with mean intensity I_0 of 10^{15} W cm $^{-2}$; (c) two-colour pulse with 5×10^{16} W cm $^{-2}$ and (d) two-colour pulse with 3×10^{17} W cm $^{-2}$. The fields are recorded as a function of t and y at the given position $z = 175$ μ m (outside the plasma zone) and their spectra are discretized on a uniform, Cartesian mesh as a function of ω and k_y . Due to the quadratic dependence of $k_z^2 = \omega^2/c^2 - k_y^2$ on ω and k_y , the fields are plotted on a non-uniform mesh as a function of k_z and k_y . Each point in the (k_z, k_y) space is represented by a colour dot. The overlap of the dots creates the color map; this overlap cannot be achieved for the very low frequencies $k_z \ll k_y$.

In this scope sharp downward density transitions are created through shock fronts induced either by a knife edge or by nanosecond laser pulses into a supersonic gas target [82, 143]. A typical scheme could here employ 35-fs, 70-mJ pump pulses focused into a vacuum chamber by a $f/10$ off-axis mirror (numerical aperture ~ 0.02) and passing through a 0.1-mm-thin β -barium borate (BBO) crystal. At the centre of the vacuum chamber, the nozzle delivering a supersonic argon-gas jet would host a razor blade mounted laterally, allowing to switch a shock front transversally along the laser propagation axis and to monitor density gradients over $\sim 10 \mu\text{m}$ lengths. The forwardly emitted THz radiation would then be collected by a parabolic mirror and directed toward a pyroelectric detector equipped with a silicon filter.

In our numerical simulation the laser pulse is initialized at $z = 0$ via Gaussian profiles both in space and time:

$$E_L(t, y, z = 0) = \sqrt{\frac{2I_0}{c\varepsilon_0}} \mathcal{E}(y) \left[\sqrt{1-r} \mathcal{E}_1(t) \cos(\omega_0 t) + \sqrt{r} \mathcal{E}_2(t) \cos(2\omega_0 t + \phi) \right], \quad (5.2.1)$$

$$\mathcal{E}(y) = \exp \left[- \left(\frac{y}{w_0} \right)^2 \right], \quad (5.2.2)$$

$$\mathcal{E}_1(t) = \exp \left[-2 \ln 2 \left(\frac{t}{\tau_p} \right)^2 \right], \quad \mathcal{E}_2(t) = \exp \left[-8 \ln 2 \left(\frac{t}{\tau_p} \right)^2 \right], \quad (5.2.3)$$

where $\nu_0 = \omega_0/(2\pi)$ is the fundamental frequency, I_0 is the mean pump intensity, $0 \leq r \leq 1$ is the intensity ratio between the second and the fundamental harmonics, τ_p is the FWHM duration of the fundamental harmonic (the second harmonic has again half duration), and w_0 is the $1/e^2$ transverse width of the pulse. The relative phase ϕ between the fundamental and second harmonic is initially set to $\pi/2$. As explained in Section 2.4.2, this phase offset optimizes local photocurrents [8, 90, 108]. However, as the relative phase evolves along propagation, the gain factor achieved with another initial phase offset would remain of similar order of magnitude. The FWHM duration of the pump pulse centred at 1- μm wavelength is $\tau_p = 35$ fs and its $1/e^2$ transverse width along y is $w_0 = 20 \mu\text{m}$, allowing to form a rather thick plasma. We always consider an intensity ratio $r = 0.1$ between the fundamental pump and its second harmonic (0.5- μm wavelength) when two colours are employed ($r = 0$ for a single colour). Our intensity range, $I_0 \leq 3 \times 10^{17} \text{ W cm}^{-2}$, corresponds to the normalized laser vector potential $|a_L| = e|A_L|/m_e c^2 \leq 0.5$. The maximum values of ω_p , which initiate the THz spectra, are then comprised between $0.02 \omega_0$ and $0.04 \omega_0$ in argon, i.e., $\nu_p \equiv \omega_p/(2\pi) \approx 6\text{-}12$ THz.

The resolution in time and space is $\Delta t = 0.079$ fs, $\Delta y = 0.48 \mu\text{m}$, and $\Delta z = 0.024 \mu\text{m}$, for a spectral step of $\Delta\nu = 0.47$ THz. The CALDER code includes Ammosov-Delone-

Krainov (ADK)-based strong-field ionization modules [126] and Coulomb binary collisions [134]. Concerning the latter, we performed several tests on the impact of electron-electron and electron-ion collisions in the THz conversion efficiency and spectral patterns. A limited action of electron-electron collisions was found for intensities less than 10^{17} W cm⁻². Instead, electron-ion collisions dominate over long times and mainly condition the slow exponential damping of the longitudinal plasma waves. At larger, near-relativistic intensities, electron-electron collisions can, however, take over when the electrons acquire high drift velocities. For each simulation set, the collisional rate changes with the plasma characteristics and input laser parameters. The CALDER code does not describe electron-neutral collisions, which is a valid approximation for sufficiently ionized plasmas. With free electron densities about $\approx 10^{18}$ cm⁻³ levels, electron-ion collisions always persist with an effective rate ν_c , which varies with the input laser intensity and the achieved electron density as

$$\nu_c [\text{s}^{-1}] \sim 3 \times 10^{-6} (\ln \Lambda) Z^* \frac{N_e [\text{cm}^{-3}]}{(W_{\text{osc}}^2 [\text{eV}] + T_e^2 [\text{eV}])^{3/4}}, \quad (5.2.4)$$

where $W_{\text{osc}} \sim I_0$ is the electron oscillation energy in the laser field, T_e denotes the electron temperature, $\ln \Lambda \approx 10$ is the Coulomb logarithm, and Z^* is the ionization degree [47, 130]. Collisions thus decrease at increasing laser energy, up to the variations in the electron temperature that can reach ~ 0.1 keV in the intensity range considered in this section. 2D PIC simulations indicate an effective electron-ion collision time of ~ 200 fs at 10^{15} W cm⁻² intensity, being characteristic of weakly ionized gases [7], of about 1 ps at 5×10^{16} W cm⁻² intensity, and a collision time larger than 10 ps at 3×10^{17} W cm⁻² intensity. All these values satisfy $\nu_c^2/4 \ll \tilde{\omega}_p^2$, where the reduced plasma frequency $\tilde{\omega}_p$ is given by Eq. (3.4.6).

The different radiated field components ($\tilde{E}_x, \tilde{E}_y, \tilde{E}_z$) and their magnetic counterparts ($\tilde{B}_x, \tilde{B}_y, \tilde{B}_z$), indicated with tilde symbol, are extracted from the PIC simulations. Forward radiation is only regarded in the present study and the transverse field $E_x = E_L + \tilde{E}_x$ includes both the laser field E_L and the secondary (radiated) field \tilde{E}_x . Secondary fields are polarized along their respective current densities J_x, J_y and J_z , which should contain the spectral signature of the THz source terms at remote distances from the plasma channel [44] (see Section 4). In the chosen 2D (y, z) geometry, the Ampère's relationship $\mathbf{J} = -\varepsilon_0 \partial_t \mathbf{E} + \mu_0^{-1} \nabla \times \mathbf{B}$ invites us to map the THz spectrum yielded by J_x from E_x in order to capture photocurrents only, and use $\partial_t B_x = \partial_z E_y - \partial_y E_z$ to isolate contributions subject to the ponderomotive forces acting in the orthogonal plane.

Figure 5.2.2 shows the principal result of this section, which, to the best of our knowledge, consists of the first spectral mapping of laser-plasma-based THz generation accounting for both photocurrents and ponderomotive forces in multidimensional geometry. From

top to bottom are presented the spectra of the radiated field component \tilde{E}_x and of the transverse magnetic field \tilde{B}_x . As the two-colour laser field is linearly polarized on the x -axis, no propagation or plasma interaction effects will occur. Along this axis, the angular distribution in (k_y, k_z) of \tilde{E}_x thus reflects in Fourier space THz emission by photoionization, since $\partial_t \tilde{E}_x \propto J_x \propto \omega_p^2 A_L$ according to Eqs. (5.1.1) and (5.1.2). Here the electron plasma frequency $\omega_p = \sqrt{e^2 \varepsilon_0^{-1} m_e^{-1} N_e}$ increases with the free electron density $N_e(t)$ along fast ionization steps [8] and reaches its maximum value beyond the laser region. Along the same direction, the polar emission map of \tilde{B}_x displays THz radiation from \tilde{E}_y and \tilde{E}_z , which excludes photoionization but keeps the trace of plasma wakefield effects in the (y, z) plane.

For the main three intensity levels investigated here, $10^{15} \text{ W cm}^{-2}$, $5 \times 10^{16} \text{ W cm}^{-2}$ and $3 \times 10^{17} \text{ W cm}^{-2}$, THz emissions forwarded beyond the plasma zone ($z = 175 \mu\text{m}$) exhibit similar spectral signatures. Photocurrents induced by tunnelling ionization are known to play a major role in THz generation from gases irradiated by two-color laser pulses at filamentation intensities $\sim 10^{14} \text{ W/cm}^2$ [15]. As explained in Section 4.1, this property was recently confirmed by direct measurements supported by numerical simulations of two-colour filaments in air, the plasma response of which was shown to take over the Kerr nonlinearity in the conversion process, shifting the peak of the THz spectrum towards the electron plasma frequency [4]. For one order of magnitude larger intensities, photocurrents again persist as being the major mechanism in driving THz emissions, whereas single-colour pulses mostly initiate THz radiation from plasma wakefields [compare Fig. 5.2.2(a) and Fig. 5.2.2(b)]. One or two-colour schemes do not change the wakefield contributions to the THz yield. The E_x -field spectra, peaked on-axis ($\theta = 0$), decay at larger θ angles according to the sinc function of Eq. (4.0.15). At laser intensities high enough to promote large ion charge numbers $Z^* = N_e/N_a \rightarrow 8$, photoionization still competes with wakefield effects for emitting THz electromagnetic fields, despite the important strength of the driving sources $\mathbf{\Pi}$ [see Fig. 5.2.2(c)]. Close to the relativistic limit, $I_0 = 3 \times 10^{17} \text{ W cm}^{-2}$, the conversion efficiency due to photocurrents, however, somewhat saturates due to the particularly stable electronic configuration of Ar^{8+} , but goes on delivering intense THz pulses [Fig. 5.2.2(d)]. In summary, along x , photocurrents increase the THz yield as the pump intensity is augmented till saturation at near-relativistic intensity. THz components due to wakefield emitters along the orthogonal directions, by contrast, monotonically increase.

Understanding the results of Fig. 5.2.2 requires to scan the field dynamics initiated inside the plasma channel. Working with high laser intensities and strong plasma excitations, a minor role from bound electrons is assumed and all optical effects are discarded here, such as Kerr self-focusing and chromatic dispersion (i.e., $n_0 = 1$ and $\chi^{(3)} = 0$). By

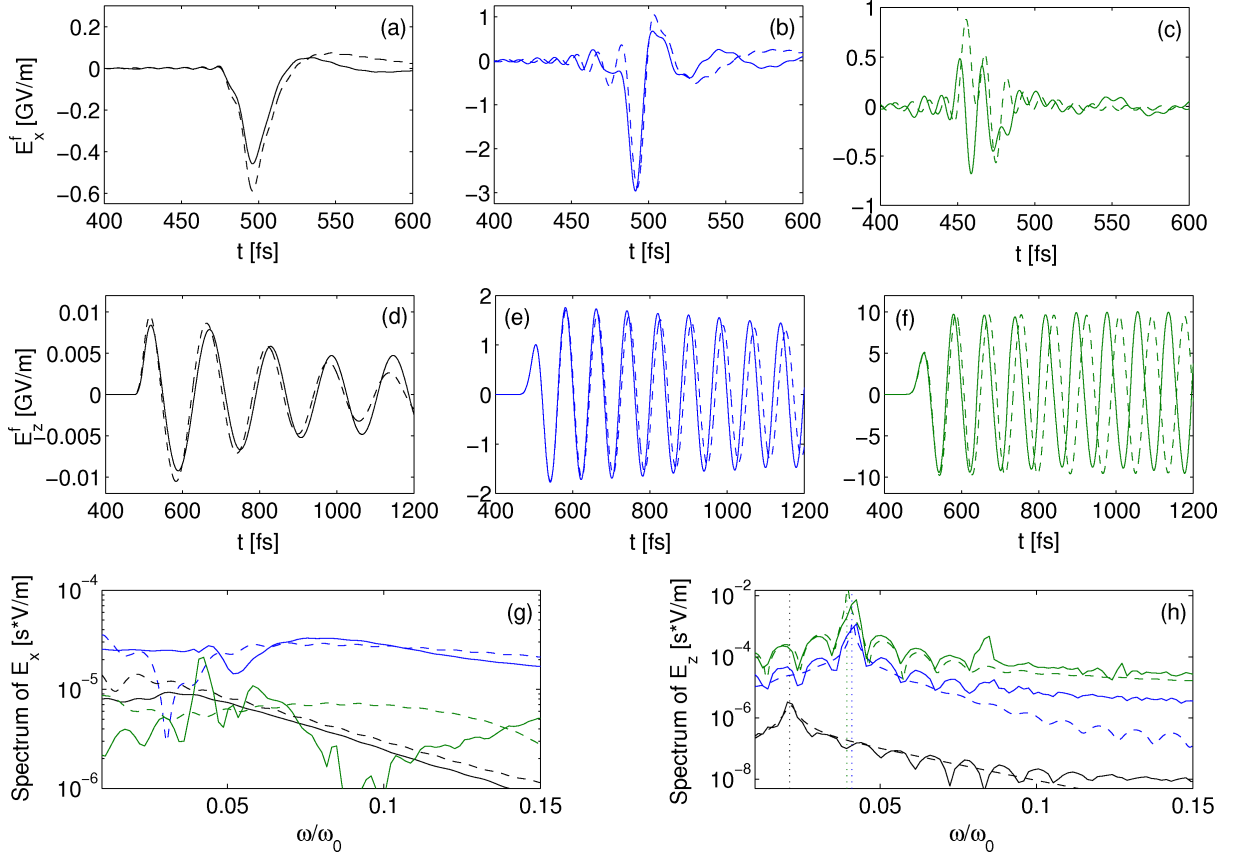


Figure 5.2.3: Comparison between 2D Particle-In-Cell results (solid curves) and semi-analytical solutions of the 1D model of Eqs. (3.4.5) and (3.4.13) (dashed curves) for the on-axis electric fields (top row) \tilde{E}_x and (middle row) \tilde{E}_z emitted by two-colour pulses inside the plasma channel at $z = 50 \mu\text{m}$ for the mean pump intensity (a,d) $I_0 = 10^{15} \text{ W cm}^{-2}$ (black curves), (b,e) $I_0 = 5 \times 10^{16} \text{ W cm}^{-2}$ (blue curves), and (c,f) $I_0 = 3 \times 10^{17} \text{ W cm}^{-2}$ (green curves). (Bottom row) On-axis spectra of the radiated fields (g) \tilde{E}_x and (h) \tilde{E}_z with same colour plotstyles. The vertical dotted lines indicate values of the plasma frequency.

combining the Faraday and Ampère laws [Eqs. (2.1.3) and (2.1.4)] with the cold-plasma fluid equations [Eqs. (2.1.49) and (2.3.10)], omitting the loss current \mathbf{J}_{loss} due to plasma absorption supposed small in underdense plasmas, the propagation equation for the electric field \mathbf{E} is directly retrieved:

$$\left(\partial_t^2 + c^2 \nabla \times \nabla \times + \frac{\omega_p^2}{\gamma} \right) \mathbf{E} + (\partial_t \ln \gamma + \nu_c) \left(\partial_t \mathbf{E} + c^2 \nabla \times \nabla \times \mathbf{A} \right) = -\frac{\mathbf{\Pi}}{\varepsilon_0 \gamma}, \quad (5.2.5)$$

where $\mathbf{A}(t) = \int_{-\infty}^t \mathbf{E}(t') dt'$ is the vector potential. The electron density $N_e = m_e \varepsilon_0 e^{-2} \omega_p^2$ is calculated in an ADK-based multiple ionization context by Eqs. (2.2.27), (2.1.57) and (2.2.31). The electric field being the solution to Eq. (5.2.5) contains both the laser electric

field polarized along the x -axis and the field components radiated from photocurrents and the driving source term $\mathbf{\Pi}$ [Eq. (2.3.15)].

For simplicity, we shall use a reduced model discriminating THz emitters only promoted by the x - and z -polarized fields, since photocurrents generate THz pulses along the laser polarization axis and propagation aspects mainly concern the longitudinal axis. Neglecting the diffraction operators ($\partial_x = 0$ and $\partial_y = 0$), Eq. (5.2.5) reduces to the one-dimensional Maxwell-Fluid model presented in Section 3.2 and numerically solved by the MAXFLU 1D code. We will use the results given by the Simplified Maxwell-Fluid model [Eqs. (3.4.5) and (3.4.13)] derived in Section 3.4 in order to interpret the numerical simulations carried out with CALDER 2D.

Figures 5.2.3(a-f) proceed with a direct comparison between the on-axis transverse (x) and axial (z) components of the electromagnetic field emitted in a 90-THz-wide frequency window ($\omega < 0.3\omega_0$) at the middle of the plasma channel, i.e., at $z = 50 \mu\text{m}$. Black, blue and green curves in solid lines refer to CALDER 2D computations for increasing intensities; dashed curves plot the corresponding solutions to Eqs. (3.4.5) and (3.4.13) with the same colour plotstyle. The dominant part of the solution to Eq. (3.4.13) is a single-cycle pulse due to photoionization, as plasma current oscillations only form a residual tail modulated at plasma frequency [Fig. 5.2.3(a-c)]. The axial field is connected with plasma wave oscillations, where the plasma frequency increases like $\sqrt{N_e}$, i.e., with the ionization state Z^* when the laser intensity is increased [Fig. 5.2.3(d-f)]. For each intensity value, Fig. 5.2.3 displays evidence of a very good agreement between 2D PIC computations and the 1D simplified Maxwell-Fluid model of Section 3.4. Small discrepancies occur in the THz pulse profiles at near-relativistic intensity. These are linked to two-dimensional effects (e.g., transverse diffraction), small deviations from the assumption of constant γ , and the non-negligible influence of electron-electron collisions—discarded in our one-dimensional model—compared to electron-ion collisions at near relativistic intensities. They, however, preserve an accurate estimate of the THz field strength. Maximum achievable field strengths are 3 GV/m for the transverse field produced at $5 \times 10^{16} \text{ W cm}^{-2}$ and 10 GV/m for the longitudinal field emitted at $3 \times 10^{17} \text{ W/cm}^{-2}$ inside the plasma. These are record values reported in this context.

Figures 5.2.3(g,h) detail the spectral dynamics corresponding to the emitted fields at $z = 50 \mu\text{m}$ calculated in Fig. 5.2.3(a-c) and Fig. 5.2.3(d-f), respectively. The dotted vertical lines locate the plasma frequency $\tilde{\omega}_p$ achieved in the wake of the laser field and expressed in ω_0 units. In Fig. 5.2.3(h) the spectrum of the longitudinal field remains highly peaked around the plasma frequency, as justified by its direct dependency on $I_0(\omega^2 + i\nu_c\omega - \tilde{\omega}_p^2)^{-1}$ [see Eq. (3.4.7)]. By contrast, the spectrum of the transverse field, given by Eq. (3.4.15), increases in amplitude and towards *long* wavelengths with the laser

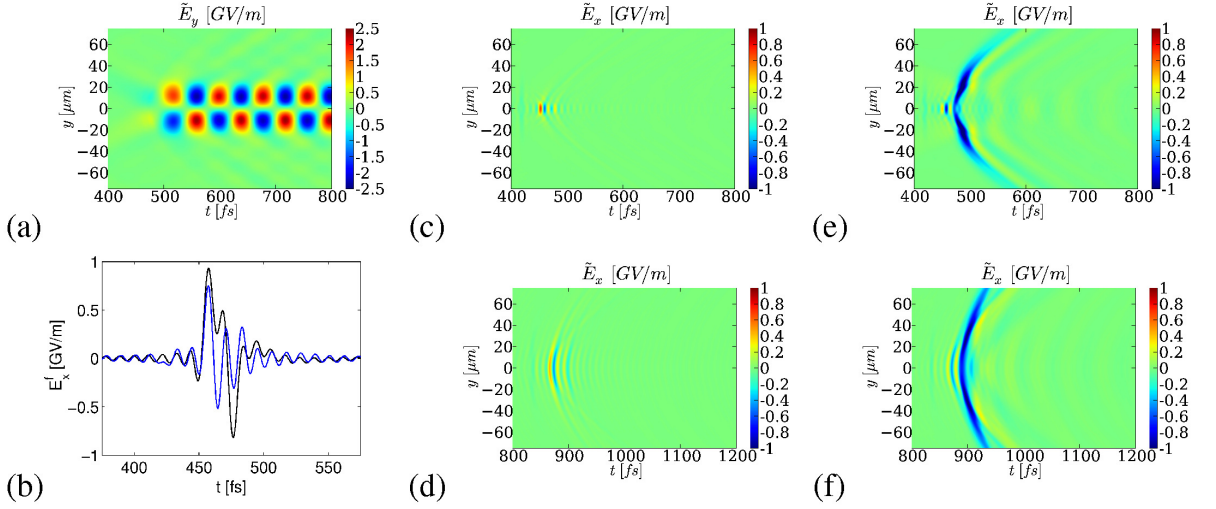


Figure 5.2.4: (a) 2D Particle-In-Cell spatio-temporal map of \tilde{E}_y triggered by two-colour pulses for $I_0 = 3 \times 10^{17} \text{ W cm}^{-2}$. (b) 2D Particle-In-Cell simulation (blue curve) and 1D semi-analytical solution given by Eq. (3.4.13) (black curve) of the on-axis x -polarized radiated field at $z = 50 \mu\text{m}$ for a single colour with the same intensity. Spatio-temporal maps $\tilde{E}_x(y, t)$ for (c) a single-colour pulse and (e) a two-colour pulse at the same distance and intensity. (d, f) Same patterns at remote distance $z = 175 \mu\text{m}$ outside the plasma channel. The colour bars of (c-f) are cut at $\pm 1 \text{ GV/m}$ for better visibility of the emitted waves. Note the change of scale in time.

intensity, before saturating at $3 \times 10^{17} \text{ W cm}^{-2}$ due to the stability of Ar^{8+} [Fig. 5.2.3(g)]. Initiated around the plasma frequency ($0.02 < \omega_p/\omega_0 \leq 0.04$), the transverse THz spectrum develops a broad extent comparable with the patterns of Fig. 5.2.2. The overall agreement between PIC simulations and our 1D Maxwell-Fluid model is good, except in the very low-frequency limit.

Figure 5.2.4(a) confirms that, at the highest intensity $I_0 = 3 \times 10^{17} \text{ W cm}^{-2}$, the y -polarized fields induced by transverse ponderomotive forces generate in-situ off-axis THz components ($\Pi_y \propto \partial_y E_L^2$) being weaker than their longitudinal counterpart [compare with Fig. 5.2.3(f)]. This justifies a posteriori our 1D semi-analytical Maxwell-Fluid model. At the same intensity level and for one colour, the on-axis CALDER \tilde{E}_x field and its semi-analytical evaluation are shown in Fig. 5.2.4(b), evidencing that the semi-analytical model again provides reliable approximations at near-relativistic intensities for a single-colour pulse, apart from the aforementioned discrepancies. By comparison of this subplot with Fig. 5.2.3(c), one can observe that both the single- and two-colour pulse schemes supply analogous on-axis x -field strengths ($\sim \text{GV/m}$). The maximum THz field amplitudes delivered by tunnel ionization being located on-axis, one infers a clear saturation in the

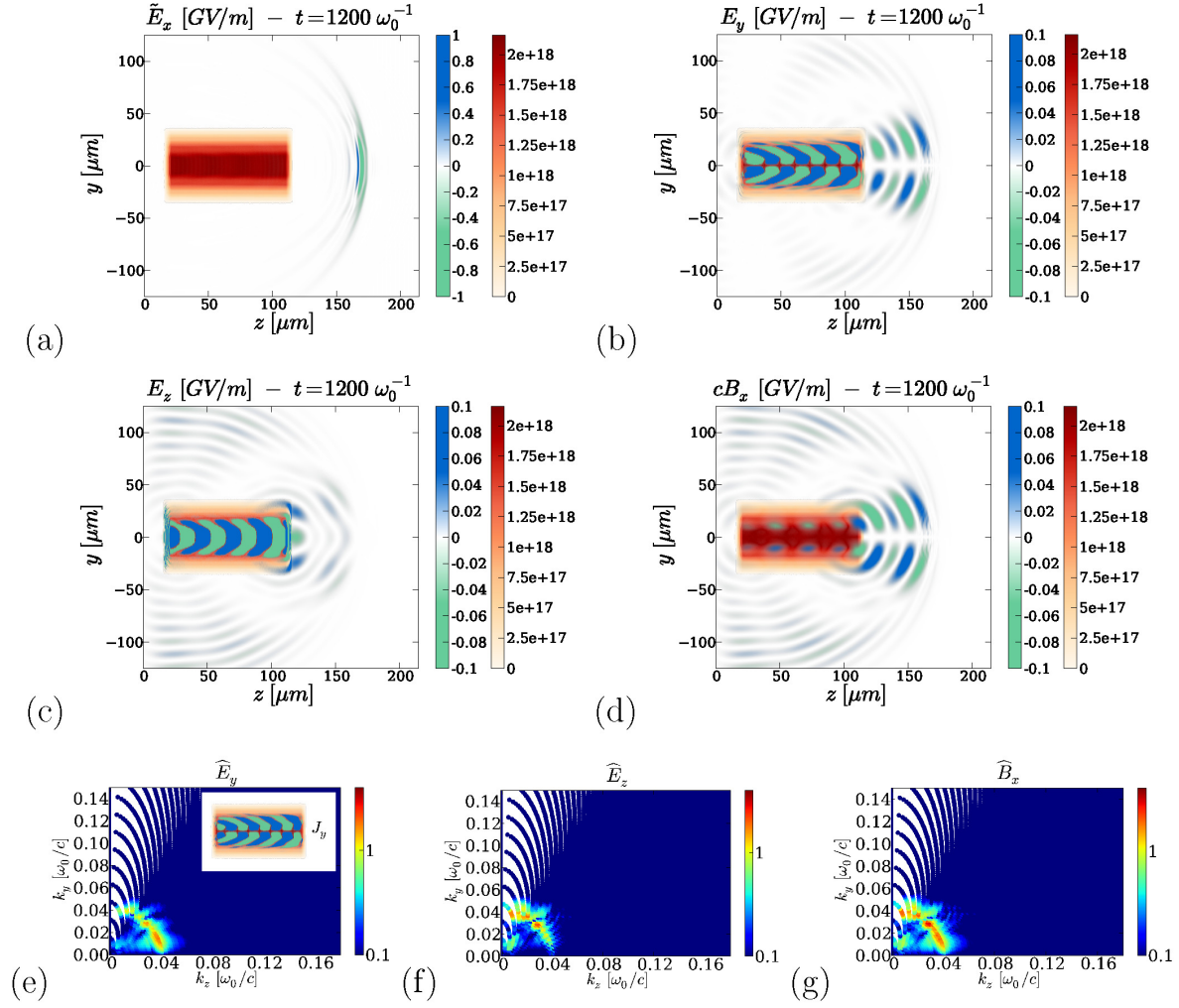


Figure 5.2.5: Two-colour pulses for $I_0 = 5 \times 10^{16} \text{ W cm}^{-2}$. Top: (y, z) mapping of the fields emitted inside and outside the plasma channel at time $t = 1200 \omega_0^{-1}$. The left-hand side blue/green colour bar indicates the field strength value in GV/m; the right-hand side red colour bar indicates the electron density in cm^{-3} . (a) \hat{E}_x (the laser field is filtered out), (b) E_y , (c) E_z and (d) cB_x . Bottom: Angular spectral distribution (arb. units) of (e) \hat{E}_y , (f) \hat{E}_z , and (g) \hat{B}_x at $z = 175 \mu\text{m}$. In (e) the inset represents the y -component of the current density generated inside the plasma.

conversion efficiency of the two-colour scheme near the relativistic intensity threshold. The reason of this saturation is that, at intensities close to $10^{18} \text{ W cm}^{-2}$, argon atoms have their outermost electron shell empty ($Z^* = 8$); so the remaining Ar^{8+} ion is shaped into a stable neon-like atom configuration. This property manifests itself by a long plateau in the curve Z^* versus I_0 [46] (see Fig. 2.2.4), signalling the hardness to further ionize the ion. Approaching $Z^* = 9$ with $1.4 \times 10^{18} \text{ W cm}^{-2}$ intensities re-activates the two-colour

pulse efficiency by the delivery of 7.6 GV/m THz transverse fields (not shown here), which, however, remains comparable with the present performances. This explains why the ionization process loses efficiency near relativistic intensities. The same saturation phenomenon can be expected in other gases, for instance helium, once the available two electrons have been ionized at similar intensities. It is worth noticing that although photocurrents cannot produce stronger THz fields, they can supply more energetic THz pulses as the volume of the secondary radiation is broader along the y -axis for two colours [compare Figs. 5.2.4(c,e)]. Figure 5.2.4(d,f) show that the field values ~ 1 GV/m achieved inside the plasma are preserved at remote distances.

While the secondary transverse and longitudinal fields contain the THz signature of their respective nonlinear sources, it is not guaranteed that outside the plasma channel all these components preserve their field strength —thus the transmitted THz power— all the way to the detector. Figure 5.2.5 answers this point by detailing the (y, z) maps of the electric field and x -magnetic components inside the plasma zone and transmitted in vacuum, once the pulse has propagated along the whole gas length ($t = 1200\omega_0^{-1}$). The free electron density (red colour bar) and the field amplitude level (blue/green colour bar) are specified. It is clearly seen that the THz field \tilde{E}_x created through photoionization keeps an amplitude \sim GV/m comparable with the one produced inside the plasma tube, as already reported above. By contrast, \tilde{E}_y decreases by a factor ~ 2.5 and \tilde{E}_z vanishes rapidly. Along y , transverse ponderomotive forces generate obliquely-propagating THz pulses. This behaviour can be understood from the ponderomotive source term $(\mathbf{J} \cdot \nabla)(\gamma\mathbf{J}/eN_e) \propto \partial_y E_L^2$ [Eq. (2.3.15)] computed on the laser field of Eq. (5.2.1), which is zero at $y = 0$ and maximum near $y = 10 \mu\text{m}$. For comparison, the longitudinal field is maximum at centre ($y = 0$), but its amplitude rapidly falls down outside the plasma channel. Amongst these two players, the transverse ponderomotive force hence conveys the highest THz field contribution, unlike the longitudinal field that becomes unable to transmit the THz pulse. As shown by Fig. 5.2.5(d), the peaks of the magnetic field \tilde{B}_x outside the plasma are mainly those of the \tilde{E}_y component. Inside the plasma region, \tilde{B}_x arises from the current components in the transverse gradients of the plasma profile. Spectrally, \tilde{B}_x keeps the signature of the transverse and longitudinal fields created inside the plasma channel, in such a way that it consists in the direct sum of \tilde{E}_y and \tilde{E}_z conical emissions. In this respect, Fig. 5.2.5(e,f,g) indeed display evidence that the longitudinal field spectrum \tilde{E}_z is non-zero at an angle larger than that of \tilde{E}_y , so that \tilde{B}_x simply superimposes both contributions. In connection with Eq. (4.0.15), the inset of Fig. 5.2.5(e) reveals that J_y is an odd function of y and has no on-axis spectral component [$\hat{J}_y(k_y = 0) = 0$]. The transverse ponderomotive currents, therefore, emit oblique THz waves, which was never reported before.

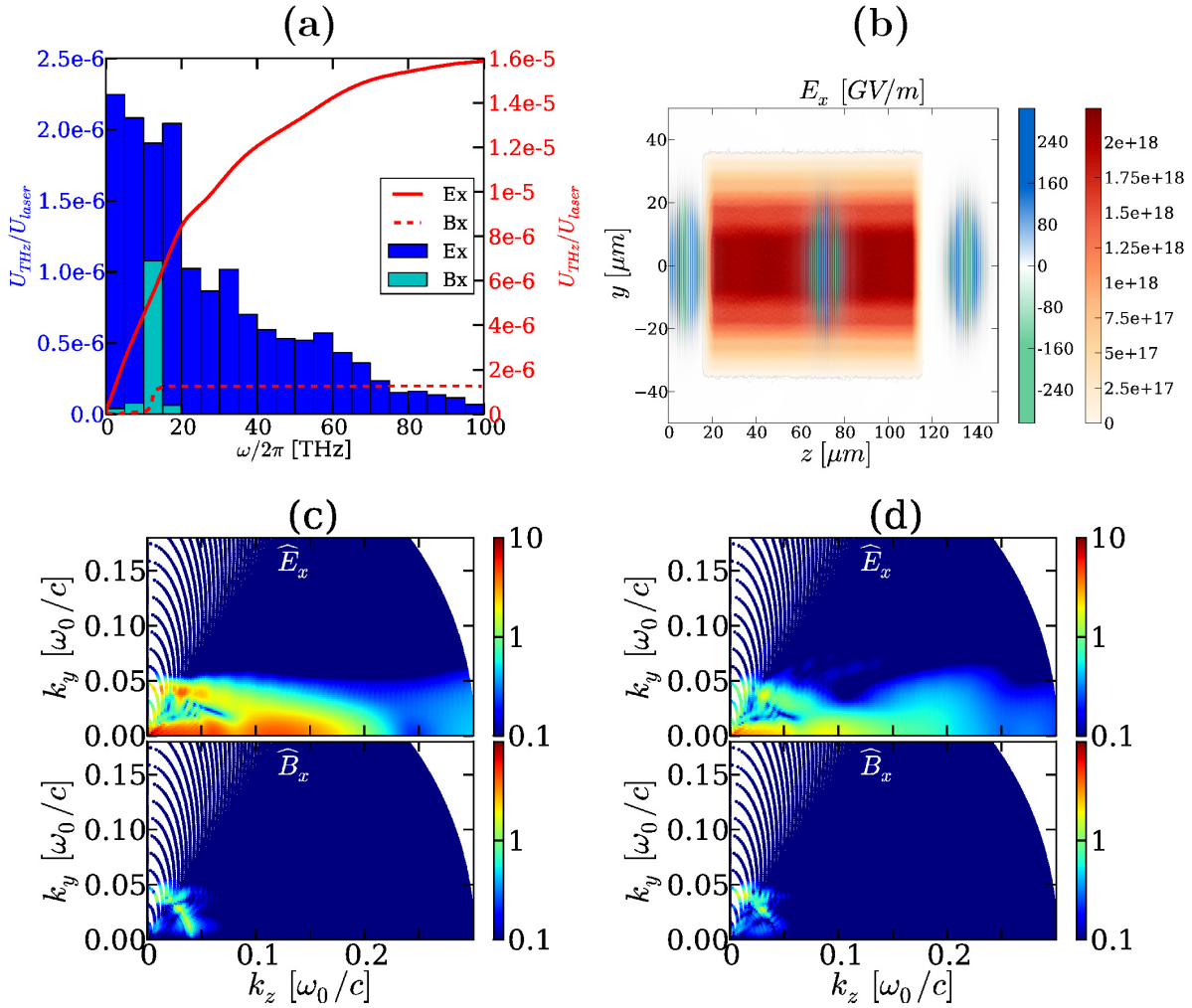


Figure 5.2.6: (a) THz energy distribution U_{THz} normalized to laser energy versus the electromagnetic frequency $\nu \equiv \omega/2\pi$ at $z = 175 \mu\text{m}$ in the two-colour case with $I_0 = 5 \times 10^{16} \text{ W/cm}^2$ from the ponderomotive forces (B_x) and photocurrents (E_x). The solid line represents the cumulative distribution function in frequency that integrates the THz energy yields over the antecedent frequency domains. (b) Spatial map of the laser field E_x at three different propagation distances along and outside the plasma channel (electron density is plotted in red). (c,d) Influence on the angular far-field spectra (arb. units) of the laser pulse duration and longitudinal plasma profile for the same intensity and (c) a pump FWHM of 17.5 fs (second harmonic length remains unchanged) and a higher initial ion density level $N_a \approx 5 \times 10^{17} \text{ cm}^{-3}$ at $z = 175 \mu\text{m}$ ($\phi = 0$); (d) a longer plasma gradient [50 μm instead of 5 μm in the rear part of the plasma profile, which still extends over 100 μm]; the laser parameters are unchanged compared with Fig. 5.2.2(c)]. The x -field spectrum radiated by photocurrents built from fewer optical cycles is broader and more intense.

To end with, in Fig. 5.2.6(a) the energy converted to the THz and infrared domains over the 100- μm long plasma channel for the same laser characteristics as those of Fig. 5.2.5 is presented. One can see that the energy radiated outside the plasma region ($z = 175 \mu\text{m}$) is located around the plasma frequency ($\sim 10 \text{ THz}$) due to wakefield and plasma wave emitters (B_x). Yet most of this energy results from photoionization (E_x) and accumulates over a broader frequency range. This property is reflected by the solid red line, plotting the cumulative distribution function in frequency. Note that the value of conversion efficiency is weak, i.e., the plasma-to-THz conversion scheme is not optimal, but it is achieved over 100 μm of an underdense plasma only. For completeness, Fig. 5.2.6(b) details the evolution of the spatial structure of the laser field along the propagation range exceeding the plasma zone. This map clearly shows that over short propagation ranges the laser pulse profile remains preserved, which is consistent with the small energy losses.

The previous behaviours, of course, depend on the number of optical cycles contributing to THz pulse generation, on the initial gas atomic density and on the laser and plasma geometry. However, they should be generic. Figure 5.2.6(c,d) confirm this expectation by showing 2D PIC simulations of a two-colour pulse whose fundamental has 17.5-fs-FWHM duration and interacts with a twice higher initial density of atoms [Fig. 5.2.6(a)] or with a plasma profile having a longer gradient length [Fig. 5.2.6(b)]. The spectral pattern delivered by \tilde{E}_x exhibits a broader extent and higher amplitude, as fewer optical cycles render the pump profile more asymmetric [45], and there is a decrease in the ponderomotive spectral signal of \tilde{B}_x with longer density gradients in agreement with the recent reference [110]. Apart from these modifications, the THz spectra present generic features and we can anticipate that in a three-dimensional geometry the field distributions should remain close to the present ones, including solely an additional ponderomotive component along the x -axis.

To conclude, in this section we have reported PIC simulation results on the interaction of two-colour laser Gaussian beams with an underdense plasma generating THz pulses. Our objective was to discriminate THz emissions promoted by photocurrents along the laser polarization axis from those produced by plasma wave oscillations that develop at high intensities. These results have been corroborated by our semi-analytical 1D Maxwell-Fluid model. This model can be faithfully used for a broad range of laser intensities to predict THz fields occurring *inside plasmas* through photoionization and longitudinal wakefields in various experimental setups. We showed that, in the range of laser intensities between $10^{15} \text{ W cm}^{-2}$ and $3 \times 10^{17} \text{ W cm}^{-2}$ covering the domain of classical laser-plasma physics, THz pulse generation proceeds from both photoionization and ponderomotive forces. While the photocurrent mechanism prevails at intensities of $5 \times 10^{16} \text{ W cm}^{-2}$ in argon, the resulting THz field strength saturates when the relativistic limit $I_0 \rightarrow 10^{18} \text{ W}$

cm^{-2} is approached. This saturation stems from the fact that all outermost electrons of the valence shell have been ionized, leaving the ion in a relatively stable atomic state, unless resorting to much higher relativistic intensities. Finally, we demonstrated that the longitudinal fields alone rapidly decay away from the plasma and cannot transmit significant THz power remotely. It turns out that in multidimensional configurations the fields produced by transverse ponderomotive forces prevail outside the plasma zone over their longitudinal counterparts. Therefore, the radiated THz magnetic field along the laser polarization axis conveys the most relevant information on the plasma ponderomotive emitters.

Conclusions and perspectives

Today the terahertz region of the electromagnetic spectrum, which until a recent past was barely accessible in practice, has raised a huge interest in many scientific domains because of its rich potential applications in, e.g., medical imaging and the remote identification of drugs and explosives. These applications require strong terahertz fields, transmitting amplitudes up to the GV/m and broadband, tunable spectra from 0.1 to 100 THz. Current terahertz generation technologies based on solid emitters, like quantum cascade lasers and rectification in asymmetric crystals, are limited by damage thresholds or narrowness of the emitted spectra. An alternative technique recently happened with the potential for yielding very intense terahertz pulses compared with most of the existing technologies, namely, terahertz emissions driven by multicoloured femtosecond laser pulses. Demonstrated experimentally for the first time in 1993 by Hamster *et al.* [72], this technique consists of ionizing a gas (e.g., air or noble gases) by focusing a femtosecond infrared two-colour laser pulse (fundamental plus second harmonic) and creating a plasma spot that acts as a nonlinear frequency converter turning a small part of the laser energy into the THz spectral domain. Since plasma is a state of matter supporting very high powers without undergoing material damage, laser-driven terahertz sources can supply strong and broadband terahertz fields with record energy conversion efficiencies ($\gg 10^{-4}$).

This thesis proposed to understand better the main physical mechanisms responsible for producing terahertz radiation from ultrashort laser pulses, build the numerical tools for this goal and explore novel interaction regimes at near relativistic laser intensities. Our objective was to reveal the best laser and gas configurations to maximize the laser-to-terahertz energy conversion efficiency and enhance the quality of the yielded terahertz radiation while controlling its amplitude and the spectral bandwidth up to ~ 100 THz. During these three years of PhD an ample study has been realized, whose main effort has focused on analytical modelling and high-performance numerical computations, some of them being confronted to new experimental data.

The different physical models as well as the corresponding numerical codes have been described in Sections 2 and 3, respectively. The ultimate physical equations that govern the laser-matter interaction in this context are the Maxwell equations coupled to a kinetic description of the plasma (Vlasov equation). Unlike past theoretical studies, the gas

target is here ionized in a complete multiple ionization context, including laser-induced photoionization and electron-impact ionization. Three different mathematical models have been exploited, namely, Maxwell-Vlasov model, Maxwell-Fluid model, and Unidirectional Pulse Propagation Equation (UPPE) model, all derived from Maxwell-Vlasov equations. At the beginning of this PhD, two fully-parallel high-performance codes were already available at CEA-DAM-DIF, namely, the Particle-In-Cell code CALDER, which discretizes Maxwell-Vlasov equations and describes the evolution of macroparticles and their related fields, and the spectral code UPPE, which computes the forward propagating solution of the Maxwell wave equation. This latter approach treats the rich nonlinear optics but discards several plasma effects, such as the ponderomotive forces. In between these two models, the Maxwell-Fluid approach, the macroscopic average of the Vlasov equation coupled to Maxwell equations, has been derived and coded during this thesis. This approach has been very fruitful. On the one hand, the one-dimensional version of the new finite-volume code MAXFLU has been successfully programmed and its results agree with those of both CALDER and UPPE under their respective validity limits. In the future, the numerical strategy conceived for the MAXFLU 1D code should be extended to a three-dimensional geometry thanks to a dimensional splitting distributed over the x , y and z dimensions. On the other hand, we have managed to obtain a semi-analytical solution of these equations for the on-axis transverse and longitudinal secondary radiation. The resulting simplified Maxwell-Fluid equations extends the Local Current model based on photocurrents to high intensities and it integrates contributions from the longitudinal plasma waves and plasma ponderomotive oscillations.

In Section 4 we have tackled terahertz generation at moderate intensities ($\lesssim 10^{14} \text{ W cm}^{-2}$), typical of laser filamentation for which gas targets are weakly ionized ($Z^* \ll 1$). The novelty of our study lies in the fact that we have examined within the same framework the characteristics of the radiated field from the three main mechanisms yielding terahertz pulses and acting together, i.e., photoionization and Kerr optical rectification emitting close to axis, and longitudinal plasma oscillations emitting out of axis.

First, thanks to experimental measurements interpreted by comprehensive numerical UPPE simulations and the simplified Maxwell-Fluid model, we have demonstrated the combined contribution of both bound and free electrons to the THz radiation in two-colour laser filaments in air [4]. At the onset of filamentation the polarizability of the bound electrons forms a forward-propagating on-axis THz source by four-wave rectification, which is much weaker and higher in frequency than the distinctive free-electron photocurrent THz source. Terahertz radiation from the photocurrents then occurs to balance Kerr self-focusing and propagates inside a cone, with small emission angle $< 10^\circ$.

The associated ring-shaped spatial distribution is of universal nature in both collimated and focusing propagation geometries. We displayed evidence of an abrupt downshift of the spectral peak in the THz spectrum from higher-frequency Kerr contribution towards frequencies close to the electron plasma frequency and accompanied by more than two orders of magnitude increase in the spectral intensity when photoionization takes place.

Second, since early experiments already proved that in two-colour setups photocurrents provide the main mechanism yielding THz radiation, we wondered whether THz emissions could be boosted beyond a classical two-colour setup. To answer this question, we identified the optimal coupling parameters of laser configurations employing more than two spectral components and determined their best duration, energy and mutual phaseshifts. We predicted from the Local Current model that ideally a sawtooth waveform is optimal [67]. Since such a wave shape is not feasible in practice, we also demonstrated that only coupling a few (e.g., three or four) laser colours following the harmonics of a sawtooth field profile could remarkably increase the THz yield. Comprehensive 3D simulations revealed a THz energy conversion efficiency of 2% when using a four-colour pulse in argon, which is a performance unequalled so far. We hope that future experiments will confirm this finding.

At this point, since the progress on laser technology makes it possible to deliver ultra-short laser pulses with intensities higher than $10^{15} \text{ W cm}^{-2}$, we have examined in Section 5 terahertz generation in the rarely-explored intensity range between $10^{15} \text{ W cm}^{-2}$ and $10^{18} \text{ W cm}^{-2}$ (relativistic threshold), taking into account, for the first time to our knowledge, all the physical mechanisms that play a role at such intensities (not only photoionization, but also longitudinal and transverse ponderomotive forces), for single-colour and two-colour laser configurations.

We analyzed, inside the plasma, the effect of photocurrents and longitudinal plasma current oscillations on terahertz emissions in a one-dimensional geometry. Through the Maxwell-Fluid model and numerical simulations performed with the CALDER and UPPE codes, we reported that the growth of the terahertz yield with the intensity is nonmonotonic for one- and two-colour laser pulses [46]. We reported an oscillatory increase in the THz field strength which we related to the successive ionization of each electronic shell of a given gas atom. Our research, thereby, should permit to adjust the best pump intensity level to maximize THz production from a given gas.

Next, we revealed how terahertz radiation is generated from photocurrents, longitudinal and transverse ponderomotive forces in a two-dimensional plasma volume with finite extents at nearly relativistic intensities, and which radiated fields are transmitted outside the plasma volume [68]. Thanks to comprehensive two-dimensional Particle-In-Cell simulations, we have concluded that the photoionization is still the main mechanisms up to

the relativistic limit ($10^{18} \text{ W cm}^{-2}$), which propagates forwards close to axis. Longitudinal plasma oscillations triggered by ponderomotive motions do not emit outside the plasma, whereas their transverse counterparts are able to transmit off-axis components still keeping THz field amplitudes of the order of GV/m outside the plasma at high laser intensities. Both mechanisms, photocurrents and plasma wakefield effects, usually compete in this intensity range. From the Maxwell-Fluid model, we succeeded in inferring analytically the on-axis fields created inside the plasma in a simplified one-dimensional geometry showing good agreement with PIC simulations. This method allowed us to understand that the influence of both photoionization and plasma oscillations increase at growing intensities but the former process is limited according to the solicited electronic shell. This explains why the efficiency of the two-colour configuration saturates in argon at intensities $\sim 10^{18} \text{ W cm}^{-2}$, due to the stability of Ar^{8+} electronic configuration.

Our results pave the way to design laser-driven THz sources benefiting also from the strong off-axis terahertz fields radiated by transverse ponderomotive forces in order to increase the overall amount of THz radiation. We believe that they will find further links with recent research on the impressive THz emissions recently reported from solid targets irradiated by laser pulses operating at ultra-high intensities ($> 10^{19} \text{ W cm}^{-2}$). In this context, other key mechanisms, such as Transtion Radiation Currents and Target Normal Sheath Acceleration mechanisms [72, 106, 107, 109, 141], should moreover strongly enhance the terahertz signal.

Appendices

A Atomic units

The atomic system of units (a.u.) fixes m_e , e , \hbar , K_C and k_B as unity. Let a physical magnitude be of dimension $[m]^\alpha [s]^\beta [kg]^\gamma [A]^\delta [K]^\epsilon$ in S.I. units, where α is the dimension of length (m), β of time (s), γ of mass (kg), δ of electric current (A) and ϵ of temperature (K). This magnitude will be of dimension

$$[m_e]^{\alpha'} [e]^{\beta'} [\hbar]^{\gamma'} [K_C]^{\delta'} [k_B]^{\epsilon'} \quad (\text{A.1})$$

in the atomic system of units, where α' , β' , γ' , δ' and ϵ' are calculated by solving the following change-of-basis system:

$$\begin{pmatrix} 0 & 0 & 2 & 3 & 2 \\ 0 & 1 & -1 & -4 & -2 \\ 1 & 0 & 1 & 1 & 1 \\ 0 & 1 & 0 & -2 & 0 \\ 0 & 0 & 0 & 0 & 1 \end{pmatrix} \begin{pmatrix} \alpha' \\ \beta' \\ \gamma' \\ \delta' \\ \epsilon' \end{pmatrix} = \begin{pmatrix} \alpha \\ \beta \\ \gamma \\ \delta \\ \epsilon \end{pmatrix}. \quad (\text{A.2})$$

In Eq. (A.2), the rows of the matrix refer to the S.I. dimensions (m, s, kg, A, K) and the columns to the basis of atomic units (m_e , e , \hbar , K_C , k_B) expressed in terms of those dimensions.

The atomic units for the principal magnitudes used in this dissertation are:

Symbol	Atomic unit of ...	Value (a.u. basis)	Value (S.I.)
t_{au}	time	$m_e^{-1} e^{-4} \hbar^3 K_C^{-2}$	2.4189×10^{-17} s
ν_{au}	frequency	$m_e e^4 \hbar^{-3} K_C^2$	4.1341×10^{16} Hz
E_{au}	electric field	$m_e^2 e^5 \hbar^{-4} K_C^3$	5.1422×10^{11} V m ⁻¹
U_{au}	energy	$m_e e^4 \hbar^{-2} K_C^2$	4.3597×10^{-18} J

The atomic unit of energy, U_{au} , also called Hartree energy, is approximately equal to the double of the ionization energy of hydrogen atom (H) in its ground state.

B Gaussian and squared-cosine slowly-varying envelopes

The slowly-varying envelopes chosen for the laser electric field, $\mathcal{E}(t)$, are unitary (i.e., $0 \leq \mathcal{E}(t) \leq 1$) and defined by a pulse duration. Two measurements for this duration are widely used:

- The full width at half maximum (FWHM), τ_p , is the difference between the two instants for which the envelope of intensity $\sim \mathcal{E}(t)^2$ takes the value $1/2$.
- The $1/e$ -duration, t_p , is the half of the difference between the two instants for which the envelope $\mathcal{E}(t)$ values $1/e$ or, equivalently, for which $\mathcal{E}(t)^2$ values $1/e^2$.

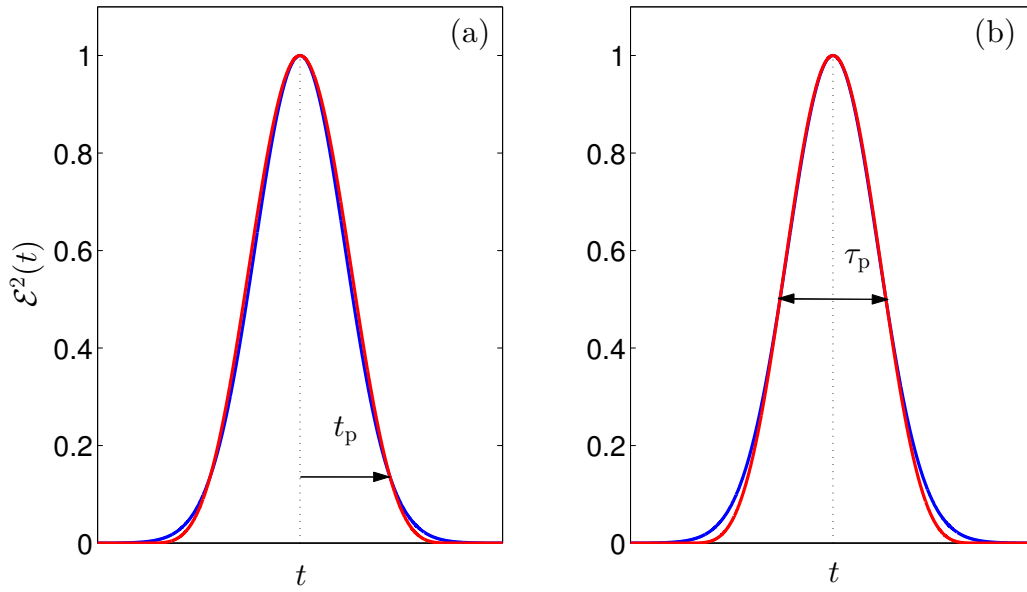


Figure B.1: Comparison between a Gaussian (blue curve) and squared-cosine (red curve) envelopes, plotted in intensity, i.e., $\mathcal{E}^2(t)$. (a) Both envelopes have the same duration t_p . (b) Both envelopes have the same duration τ_p .

There are two widely used pulse profiles, namely, Gaussian envelopes and squared-cosine envelopes, respectively defined by

$$\mathcal{E}(t) = \exp \left[- \left(\frac{t}{t_p} \right)^2 \right], \quad (\text{B.1})$$

$$\mathcal{E}(t) = \begin{cases} \cos^2 \left(\frac{c_p t}{t_p} \right), & \text{if } |t| \leq \frac{\pi t_p}{2c_p} \approx 1.7090 t_p, \\ 0, & \text{otherwise,} \end{cases} \quad (\text{B.2})$$

where the coefficient c_p is

$$c_p = \arccos\left(e^{-\frac{1}{2}}\right) \approx 0.9191. \quad (\text{B.3})$$

The squared-cosine envelope [Eq. (B.2)] is of compact support from which the number of cycles can be controlled.

The two durations, τ_p and t_p , are related to one another as

$$\text{Gaussian: } t_p = \frac{\tau_p}{\sqrt{2 \ln 2}} \approx 0.8493 \tau_p, \quad (\text{B.4})$$

$$\text{Squared-cosine: } t_p = \frac{c_p \tau_p}{2 \arccos\left(\frac{1}{\sqrt[4]{2}}\right)} \approx 0.8036 \tau_p. \quad (\text{B.5})$$

The envelopes (B.1) and (B.2) are compared in Fig. B.1.

C Moments of Vlasov equation for electrons

Zeroth-order moment

The zeroth-order moment of the Vlasov equation [Eq. (2.1.42)] is given by the identity

$$\iiint_{\mathbb{R}^3} \left(\frac{\partial f}{\partial t} + \frac{\mathbf{p}}{m_e \gamma} \cdot \frac{\partial f}{\partial \mathbf{r}} - e \left(\mathbf{E} + \frac{\mathbf{p}}{m_e \gamma} \times \mathbf{B} \right) \cdot \frac{\partial f}{\partial \mathbf{p}} - S(\mathbf{E}, \mathbf{p}) \delta(\mathbf{p}) \right) d\mathbf{p} = 0. \quad (\text{C.1})$$

The four parts of Eq. (C.1) are calculated separately. The first integral term is calculated straightforwardly by inverting the order of operators ∂_t and $\iiint_{\mathbf{p}}$ and applying Eq. (2.1.36):

$$\iiint_{\mathbb{R}^3} \frac{\partial f}{\partial t} d\mathbf{p} = \frac{\partial}{\partial t} \iiint_{\mathbb{R}^3} f d\mathbf{p} = \frac{\partial}{\partial t} \langle N_e \rangle. \quad (\text{C.2})$$

Since \mathbf{r} and \mathbf{p} are independent variables, the second integral term is calculated by inverting the order of operators $\partial_{\mathbf{r}} \cdot \equiv \nabla \cdot$ and $\iiint_{\mathbf{p}}$, and by applying Eq. (2.1.38):

$$\iiint_{\mathbb{R}^3} \left(\frac{\mathbf{p}}{m_e \gamma} \cdot \frac{\partial f}{\partial \mathbf{r}} \right) d\mathbf{p} = \iiint_{\mathbb{R}^3} \frac{\partial}{\partial \mathbf{r}} \cdot \left(f \frac{\mathbf{p}}{m_e \gamma} \right) d\mathbf{p} = \frac{\partial}{\partial \mathbf{r}} \cdot \iiint_{\mathbb{R}^3} f \frac{\mathbf{p}}{m_e \gamma} d\mathbf{p} = \nabla \cdot \langle N_e \mathbf{v} \rangle. \quad (\text{C.3})$$

The third integral term is split into the part integrating \mathbf{E} and that integrating $\mathbf{v} \times \mathbf{B}$. As the electric and magnetic fields do not depend on \mathbf{p} , the first part is directly zero by applying Eq. (2.1.35):

$$\iiint_{\mathbb{R}^3} \left(-e \mathbf{E} \cdot \frac{\partial f}{\partial \mathbf{p}} \right) d\mathbf{p} = -e \mathbf{E} \cdot \iiint_{\mathbb{R}^3} \frac{\partial f}{\partial \mathbf{p}} d\mathbf{p} = 0, \quad (\text{C.4})$$

and the second part is treated as

$$\begin{aligned} \iiint_{\mathbb{R}^3} \left(-e \left(\frac{\mathbf{p}}{m_e \gamma} \times \mathbf{B} \right) \cdot \frac{\partial f}{\partial \mathbf{p}} \right) d\mathbf{p} &= \iiint_{\mathbb{R}^3} \left(-e \left(\frac{\partial f}{\partial \mathbf{p}} \times \frac{\mathbf{p}}{m_e \gamma} \right) \cdot \mathbf{B} \right) d\mathbf{p} = \\ &= -e \mathbf{B} \cdot \iiint_{\mathbb{R}^3} \left(\frac{\partial f}{\partial \mathbf{p}} \times \frac{\mathbf{p}}{m_e \gamma} \right) d\mathbf{p}. \end{aligned} \quad (\text{C.5})$$

The vectorial product inside the integral is transformed thanks to the identity (0.0.3) and $\gamma = \sqrt{1 + p^2 m_e^{-2} c^{-2}}$:

$$\frac{\partial f}{\partial \mathbf{p}} \times \frac{\mathbf{p}}{m_e \gamma} = \frac{\partial}{\partial \mathbf{p}} \times \left(f \frac{\mathbf{p}}{\sqrt{m_e^2 + \frac{p^2}{c^2}}} \right) - f \frac{\partial}{\partial \mathbf{p}} \times \left(\frac{\mathbf{p}}{\sqrt{m_e^2 + \frac{p^2}{c^2}}} \right) = \frac{\partial}{\partial \mathbf{p}} \times \left(f \frac{\mathbf{p}}{\sqrt{m_e^2 + \frac{p^2}{c^2}}} \right), \quad (\text{C.6})$$

where $\partial_{\mathbf{p}} \times [\mathbf{p}(m_e^2 + p^2 c^{-2})^{-1/2}] = \mathbf{0}$ after easy calculations. By substituting Eq. (C.6) into Eq. (C.5) and using Eq. (2.1.35), the second part of the third integral term becomes:

$$-e\mathbf{B} \cdot \iiint_{\mathbb{R}^3} \left(\frac{\partial f}{\partial \mathbf{p}} \times \frac{\mathbf{p}}{m_e \gamma} \right) d\mathbf{p} = -e\mathbf{B} \cdot \iiint_{\mathbb{R}^3} \left(\frac{\partial}{\partial \mathbf{p}} \times \left(f \frac{\mathbf{p}}{\sqrt{m_e^2 + \frac{p^2}{c^2}}} \right) \right) d\mathbf{p} = 0. \quad (\text{C.7})$$

The fourth integral term represents ionization for which electrons are born with zero linear moment:

$$\iiint_{\mathbb{R}^3} (-S(\mathbf{E}, \mathbf{p}) \delta(\mathbf{p})) d\mathbf{p} = -S(\mathbf{E}, \mathbf{p} = \mathbf{0}). \quad (\text{C.8})$$

Therefore, by combining Eqs. (C.2), (C.3), (C.4), (C.7) and (C.8) the zeroth-order moment of Vlasov equation restores the conservation relation

$$\frac{d}{dt} \langle N_e \rangle + \nabla \cdot \langle N_e \mathbf{v} \rangle = S(\mathbf{E}, \mathbf{p} = \mathbf{0}), \quad (\text{C.9})$$

which is the continuity equation for the electron density.

First-order moment

The first-order moment is provided by

$$\iiint_{\mathbb{R}^3} \mathbf{p} \left(\frac{\partial f}{\partial t} + \frac{\mathbf{p}}{m_e \gamma} \cdot \frac{\partial f}{\partial \mathbf{r}} - e \left(\mathbf{E} + \frac{\mathbf{p}}{m_e \gamma} \times \mathbf{B} \right) \cdot \frac{\partial f}{\partial \mathbf{p}} - S(\mathbf{E}, \mathbf{p}) \delta(\mathbf{p}) \right) d\mathbf{p} = 0. \quad (\text{C.10})$$

Again, the four parts of Eq. (C.10) are calculated separately. The first integral term is directly calculated as

$$\iiint_{\mathbb{R}^3} \mathbf{p} \frac{\partial f}{\partial t} d\mathbf{p} = \iiint_{\mathbb{R}^3} \frac{\partial}{\partial t} (f \mathbf{p}) d\mathbf{p} = \frac{\partial}{\partial t} \iiint_{\mathbb{R}^3} f \mathbf{p} d\mathbf{p} = \frac{\partial}{\partial t} \langle N_e \mathbf{p} \rangle. \quad (\text{C.11})$$

First, the identity (0.0.2) is applied to the second integral term:

$$\begin{aligned} \iiint_{\mathbb{R}^3} \mathbf{p} \left(\frac{\mathbf{p}}{m_e \gamma} \cdot \frac{\partial f}{\partial \mathbf{r}} \right) d\mathbf{p} &= \iiint_{\mathbb{R}^3} \mathbf{p} \left[\frac{\partial}{\partial \mathbf{r}} \cdot \left(f \frac{\mathbf{p}}{m_e \gamma} \right) - f \frac{\partial}{\partial \mathbf{r}} \cdot \left(\frac{\mathbf{p}}{m_e \gamma} \right) \right] d\mathbf{p} = \\ &= \iiint_{\mathbb{R}^3} \mathbf{p} \frac{\partial}{\partial \mathbf{r}} \cdot \left(f \frac{\mathbf{p}}{m_e \gamma} \right) d\mathbf{p}, \end{aligned} \quad (\text{C.12})$$

which we combine with the identity (C.12) to get

$$\begin{aligned} \iiint_{\mathbb{R}^3} \mathbf{p} \frac{\partial}{\partial \mathbf{r}} \cdot \left(f \frac{\mathbf{p}}{m_e \gamma} \right) d\mathbf{p} &= \iiint_{\mathbb{R}^3} \left[\frac{\partial}{\partial \mathbf{r}} \cdot \left(\mathbf{p} \otimes f \frac{\mathbf{p}}{m_e \gamma} \right) - \cancel{\frac{\partial \mathbf{p}}{\partial \mathbf{r}} \cdot \left(f \frac{\mathbf{p}}{m_e \gamma} \right)} \right] d\mathbf{p} = \\ &= \iiint_{\mathbb{R}^3} \frac{\partial}{\partial \mathbf{r}} \cdot \left(\mathbf{p} \otimes f \frac{\mathbf{p}}{m_e \gamma} \right) d\mathbf{p}, \end{aligned} \quad (\text{C.13})$$

where

$$\begin{aligned} \iiint_{\mathbb{R}^3} \frac{\partial}{\partial \mathbf{r}} \cdot \left(\mathbf{p} \otimes f \frac{\mathbf{p}}{m_e \gamma} \right) d\mathbf{p} &= \frac{\partial}{\partial \mathbf{r}} \cdot \iiint_{\mathbb{R}^3} \left(\mathbf{p} \otimes f \frac{\mathbf{p}}{m_e \gamma} \right) d\mathbf{p} = \\ &= \frac{\partial}{\partial \mathbf{r}} \cdot \langle \mathbf{p} \otimes N_e \frac{\mathbf{p}}{m_e \gamma} \rangle = \nabla \cdot \langle \mathbf{p} \otimes N_e \mathbf{v} \rangle. \end{aligned} \quad (\text{C.14})$$

The third integral term is separated into the part including \mathbf{E} and that containing $\mathbf{v} \times \mathbf{B}$. To the former, the identity (0.0.2) gives

$$\begin{aligned} \iiint_{\mathbb{R}^3} \mathbf{p} \left(-e \mathbf{E} \cdot \frac{\partial f}{\partial \mathbf{p}} \right) d\mathbf{p} &= \iiint_{\mathbb{R}^3} \mathbf{p} \left[\frac{\partial}{\partial \mathbf{p}} \cdot (-e \mathbf{E} f) - \cancel{f \frac{\partial}{\partial \mathbf{p}} \cdot (-e \mathbf{E})} \right] d\mathbf{p} = \\ &= - \iiint_{\mathbb{R}^3} \mathbf{p} \left[\frac{\partial}{\partial \mathbf{p}} \cdot (e \mathbf{E} f) \right] d\mathbf{p}, \end{aligned} \quad (\text{C.15})$$

and using the identity (0.0.5) one has:

$$\begin{aligned} - \iiint_{\mathbb{R}^3} \mathbf{p} \left[\frac{\partial}{\partial \mathbf{p}} \cdot (e \mathbf{E} f) \right] d\mathbf{p} &= - \iiint_{\mathbb{R}^3} \left[\cancel{\frac{\partial}{\partial \mathbf{p}} \cdot (\mathbf{p} \otimes e \mathbf{E} f)} - e \mathbf{E} f \right] d\mathbf{p} = \\ &= \iiint_{\mathbb{R}^3} e \mathbf{E} f d\mathbf{p} = e \mathbf{E} \iiint_{\mathbb{R}^3} f d\mathbf{p} = e \mathbf{E} \langle N_e \rangle. \end{aligned} \quad (\text{C.16})$$

To the second part of the third integral, the invariance of the scalar triple product under a circular shift and Eq. (C.6) yield

$$\begin{aligned} \iiint_{\mathbb{R}^3} \mathbf{p} \left[-e \left(\frac{\mathbf{p}}{m_e \gamma} \times \mathbf{B} \right) \cdot \frac{\partial f}{\partial \mathbf{p}} \right] d\mathbf{p} &= \iiint_{\mathbb{R}^3} \mathbf{p} \left[-e \mathbf{B} \cdot \left(\frac{\partial f}{\partial \mathbf{p}} \times \frac{\mathbf{p}}{m_e \gamma} \right) \right] d\mathbf{p} = \\ &= \iiint_{\mathbb{R}^3} \mathbf{p} \left(-e \mathbf{B} \cdot \left[\frac{\partial}{\partial \mathbf{p}} \times \left(f \frac{\mathbf{p}}{m_e \gamma} \right) \right] \right) d\mathbf{p}, \end{aligned} \quad (\text{C.17})$$

to which the identities (0.0.4) and (0.0.5) are applied, resulting in:

$$\begin{aligned} \iiint_{\mathbb{R}^3} \mathbf{p} \left(-e \mathbf{B} \cdot \left[\frac{\partial}{\partial \mathbf{p}} \times \left(f \frac{\mathbf{p}}{m_e \gamma} \right) \right] \right) d\mathbf{p} &= \iiint_{\mathbb{R}^3} \mathbf{p} \left[\frac{\partial}{\partial \mathbf{p}} \cdot \left(-e f \frac{\mathbf{p}}{m_e \gamma} \times \mathbf{B} \right) \right] d\mathbf{p} = \\ &= e \left[\iiint_{\mathbb{R}^3} \left(f \frac{\mathbf{p}}{m_e \gamma} \right) d\mathbf{p} \right] \times \mathbf{B} = e \langle N_e \mathbf{v} \rangle \times \mathbf{B}. \end{aligned} \quad (\text{C.18})$$

The fourth integral term is straightforward:

$$- \iiint_{\mathbb{R}^3} \mathbf{p} S(\mathbf{E}, \mathbf{p}) \delta(\mathbf{p}) d\mathbf{p} = \mathbf{0}. \quad (\text{C.19})$$

Hence, by combining Eqs. (C.11), (C.14), (C.16), (C.18) and (C.19) the first-order momentum of Vlasov equation produces the conservation of the averaged electron linear momentum:

$$\frac{\partial}{\partial t} \langle N_e \mathbf{p} \rangle + \nabla \cdot \langle N_e \mathbf{v} \otimes \mathbf{p} \rangle = -e \langle N_e \rangle (\mathbf{E} + \langle \mathbf{v} \rangle \times \mathbf{B}). \quad (\text{C.20})$$

Equation (C.20) is usually expressed in terms of the kinetic pressure tensor, defined as

$$\bar{\bar{\Psi}} = \iiint_{\mathbb{R}^3} f (\mathbf{p} - \langle \mathbf{p} \rangle) \otimes (\mathbf{v} - \langle \mathbf{v} \rangle) d\mathbf{p}. \quad (\text{C.21})$$

By making use of the distributivity property and Eqs. (2.1.36), (2.1.37) and (2.1.38) to Eq. (C.21), the kinetic pressure tensor is applied to macroscopic averaged fields:

$$\begin{aligned} \bar{\bar{\Psi}} &= \iiint_{\mathbb{R}^3} f \mathbf{p} \otimes \mathbf{v} d\mathbf{p} - \langle \mathbf{v} \rangle \iiint_{\mathbb{R}^3} f \mathbf{p} d\mathbf{p} - \langle \mathbf{p} \rangle \iiint_{\mathbb{R}^3} f \mathbf{v} d\mathbf{p} + \langle \mathbf{p} \rangle \otimes \langle \mathbf{v} \rangle \iiint_{\mathbb{R}^3} f d\mathbf{p} = \\ &\langle N_e \mathbf{v} \otimes \mathbf{p} \rangle - \langle \mathbf{v} \rangle \otimes \langle N_e \mathbf{p} \rangle = \langle N_e \mathbf{v} \otimes \mathbf{p} \rangle - \langle N_e \rangle \langle \mathbf{v} \rangle \otimes \langle \mathbf{p} \rangle. \end{aligned} \quad (\text{C.22})$$

By substituting Eq. (C.22) into Eq. (C.20), the conservation of the averaged electron linear moment finally expresses as

$$\frac{\partial}{\partial t} \langle N_e \mathbf{p} \rangle + \nabla \cdot \bar{\bar{\Psi}} + \nabla \cdot [\langle N_e \rangle \langle \mathbf{v} \rangle \otimes \langle \mathbf{p} \rangle] = -e \langle N_e \rangle (\mathbf{E} + \langle \mathbf{v} \rangle \times \mathbf{B}). \quad (\text{C.23})$$

D An algorithm to calculate the matrix of ionization probabilities

The algorithm to compute Eq. (2.2.37) is presented here. Let us denote by A , V and P the matrix of ionization rates, the matrix containing by columns the eigenvalues of A and the matrix of ionization probabilities, respectively. These matrices are of size $n \times n$.

1. The matrices are initialized to zero:

```

for  $i$  going from 1 to  $n$  do
  for  $j$  going from 1 to  $n$  do
     $P_{i,j} = 0$ 
     $V_{i,j} = 0$ 
  end for
end for

```

2. The eigenvalues of A are calculated and saved in the lower triangular part of V :

```

 $V_{n,n} = 1$ 
for  $i$  going from  $n - 1$  to 1 (decreasing) do
   $V_{i,i} = 1$ 
  if  $|A_{i,i}| > 0$  then
    for  $j$  going from  $i + 1$  to  $n$  do
       $V_{j,i} = -\frac{1}{A_{j,j} - A_{i,i}} \text{DOT\_PRODUCT}(V_{i:j-1,i}, A_{j,i:j-1})$ 
    end for
  end if
end for

```

3. The inverse of eigenvalues of A are calculated and saved in the upper triangular part of V :

```

 $V_{1,2:n} = -V_{2:n,1}$ 
for  $i$  going from 2 to  $n$  do
   $V_{i,i+1:n} = -V_{i+1:n,i}$ 
  for  $j$  going from  $i + 1$  to  $n$  do
     $V_{1:i-1,j} = V_{1:i-1,j} + V_{i,j} V_{1:i-1,i}$ 
  end for
end for

```

4. The probability matrix is finally calculated:

```

for  $i$  going from 1 to  $n$  do

```

```

$$P_{i,i} = \text{EXP}(\Delta t A_{i,i})$$

$$V_{i:n,i} = P_{i,i} V_{i:n,i}$$
for  $j$  going from 1 to  $i - 1$  do  
     $P_{i,j} = V_{i,j} + P_{i,i} V_{j,i} + \text{DOT\_PRODUCT}(V_{i,j+1:i-1}, V_{j,j+1:i-1})$   
end for  
end for
```

E ADK-based degree of ionization for single-colour lasers

We start by considering a hydrogen-like atom subject to the QST ionization rate [Eq. (2.2.28)]:

$$W_{\text{QST}}[E(t)] = \frac{\alpha}{|E(t)|} e^{-\frac{\beta}{|E(t)|}}, \quad (\text{E.1})$$

where $\alpha = \nu_{\text{au}} E_{\text{au}} 4(2U_i U_{\text{au}}^{-1})^{5/2}$ and $\beta = (2/3) E_{\text{au}} (2U_i U_{\text{au}}^{-1})^{3/2}$. Following the local photocurrent theory of Babushkin *et al.* [8] (see Section 2.4.2), ionization events occur in the neighbourhood of the electric field extrema and the density can be approximated as $N_e(t) \approx \sum_n \delta N_e^n H_n(t - t_n)$ according to Eq. (2.4.15), where t_n are the instants of ionization events, $H_n(t) = [1 + \text{erf}(t/\tau_n)]/2$ are steplike functions [Eq. (2.4.13)], τ_n defines the duration of the n -th ionization event [Eq. (2.4.10)] and δN_e^n is the associated density jump [Eqs. (2.4.16) and (2.4.17)]. The sum of such density jumps over all the ionization events determines the degree of ionization. For single ionization, we get:

$$N_e(t) = N_a \left[1 - \exp \left(- \int_{-\infty}^t W_{\text{QST}}(\tau) d\tau \right) \right], \quad (\text{E.2})$$

with

$$\int_{-\infty}^t W_{\text{QST}}(\tau) d\tau \approx \sum_n \sqrt{\pi} \tau_n W_{\text{QST}}(t_n) H_n(t - t_n). \quad (\text{E.3})$$

To evaluate the exponential of this sum, step functions $H_n(t)$ are approximated by standard Heaviside functions [Eq. (2.4.14)], so that we can establish the direct recurrence:

$$\delta N_e^1 = N_a \left(1 - e^{-\sqrt{\pi} \tau_1 W_{\text{QST}}(t_1)} \right), \quad (\text{E.4})$$

$$\delta N_e^2 = N_a e^{-\sqrt{\pi} \tau_1 W_{\text{QST}}(t_1)} \left(1 - e^{-\sqrt{\pi} \tau_2 W_{\text{QST}}(t_2)} \right), \quad (\text{E.5})$$

...

$$\delta N_e^n = N_a e^{-\sum_{m=1}^{n-1} \sqrt{\pi} \tau_m W_{\text{QST}}(t_m)} \left(1 - e^{-\sqrt{\pi} \tau_n W_{\text{QST}}(t_n)} \right), \quad n > 1. \quad (\text{E.6})$$

By summing up all ionization events, we obtain

$$Z^* = \frac{N_e(t \rightarrow \infty)}{N_a} \approx 1 - e^{-\sum_n \sqrt{\pi} \tau_n W_{\text{QST}}[E(t_n)]}. \quad (\text{E.7})$$

The exponential argument can be estimated as

$$\sqrt{\pi} \tau_n W_{\text{QST}}[E(t_n)] \approx \sqrt{2\pi} \frac{\alpha}{\beta \omega_0} \phi \left(\frac{\beta}{a_0 \mathcal{E}(t_n)} \right), \quad (\text{E.8})$$

where $\phi(x) = \sqrt{x} e^{-x}$. This approximation is acceptable when the FWHM duration is

greater than $1.5(2\pi\omega_0^{-1})$. With the Gaussian envelope $\mathcal{E}(t)$, we apply the approximation of compact support:

$$\phi\left(\frac{\beta}{a_0}e^{2\ln 2(t/\tau_p)^2}\right) \approx \begin{cases} \phi\left(\frac{\beta}{a_0}\right) \cos^2\left(\frac{\pi}{4}\sqrt{\frac{2\beta}{a_0}}\frac{t}{\tau_p}\right), & \text{if } |t| \leq \sqrt{\frac{2a_0}{\beta}}\tau_p, \\ 0, & \text{otherwise,} \end{cases} \quad (\text{E.9})$$

which holds for $a_0 \leq 2\beta$, i.e., if $I_0 \leq 62.4 \times 10^{15} \text{ W cm}^{-2}$. Higher intensities closer to $10^{17} \text{ W cm}^{-2}$ are discarded.

The time separation between two ionization events being π/ω_0 , we obtain an approximation of the number N of ionization events:

$$N \approx \frac{2}{\pi} \sqrt{\frac{2a_0}{\beta}} \omega_0 \tau_p, \quad (\text{E.10})$$

which, without loss of generality, is supposed to be an even integer. This gives the following arithmetic progression for the instants of ionization:

$$t_n \approx \sqrt{\frac{2a_0}{\beta}} \tau_p \left(\frac{2n}{N} - 1\right), \quad (\text{E.11})$$

where $0 \leq n \leq N$. As

$$\sum_{n=0}^N \cos^2\left(\frac{\pi}{4}\sqrt{\frac{2\beta}{a_0}}\frac{t_n}{\tau_p}\right) = \frac{N}{2} = \frac{1}{\pi} \sqrt{\frac{2a_0}{\beta}} \omega_0 \tau_p, \quad (\text{E.12})$$

we can sum up the terms of Eq. (E.8) and substitute the result into Eq. (E.7) to obtain finally

$$Z^* \simeq 1 - \exp\left(-\frac{2}{\sqrt{\pi}} \frac{\alpha}{\beta} \tau_p e^{-\frac{\beta}{a_0}}\right). \quad (\text{E.13})$$

For complex atoms such as argon and helium, the same reasoning must be extended to the complete multiple ionization scheme [Eqs. (2.2.24) and (2.2.31)]. After cumbersome calculations, we can obtain the formula [Eq. (2.2.41)]

$$Z^*(I_0, \tau_p) = Z - \sum_{j=0}^{Z-1} \exp\left[-\Phi_j \frac{\tau_p}{t_{\text{ref}}}\left(\frac{\bar{I}_{0,j}}{I_{\text{ref}}}\right)^{1-n_j^*} \exp\left(-\Psi_j \sqrt{\frac{I_{\text{ref}}}{\bar{I}_{0,j}}}\right)\right], \quad (\text{E.14})$$

where

$$\Phi_j = (2l_j + 1) \frac{(j+1)^{6n_j^*-4} (n_j^*)^{3-6n_j^*}}{\Gamma(2n_j^*)}, \quad (\text{E.15})$$

$$\Psi_j = \frac{1}{6} \left(\frac{j+1}{n_j^*}\right)^3, \quad (\text{E.16})$$

$$t_{\text{ref}} = \frac{\sqrt{\pi}}{12} t_{\text{au}} \simeq 3.57 \times 10^{-3} \text{ fs}, \quad (\text{E.17})$$

$$I_{\text{ref}} = 8c\varepsilon_0 E_{\text{au}}^2 \simeq 5.62 \times 10^{17} \text{ W cm}^{-2}, \quad (\text{E.18})$$

$$\bar{I}_{0,j} = \begin{cases} I_0, & \text{if } n_j^* \leq 1, \\ \min \left\{ I_0, \frac{(j+1)^6}{144(n_j^{*8} - 2n_j^{*7} + n_j^{*6})} I_{\text{ref}} \right\}, & \text{otherwise.} \end{cases} \quad (\text{E.19})$$

$\bar{I}_{0,j}$ of Eq. (E.19) is an artificial saturation of Eq. (E.14) originating from the validity limit of Eq. (E.9). This guarantees that a fully ionized shell will remain untouched at higher intensities. Equation (E.14) is valid for any gas ionized in the tunnelling regime by a laser pulse whose FWHM duration is at least $1.5(2\pi\omega_0^{-1})$.

F Anti-dispersive correction conserving the monotonicity

The resolution of the advective part [Eq. (3.0.3) in Section 3] is the numerical challenge that the MAXFLU 1D has to face. An explicit three-point finite volume method solving Eq. (3.0.3) has the following structure:

$$\mathbf{U}_i^{n+1} = \mathcal{H}(\mathbf{U}_{i-1}^n, \mathbf{U}_i^n, \mathbf{U}_{i+1}^n) = \mathbf{U}_i^n - \frac{\Delta t}{\Delta z} \left(\Phi_{i+\frac{1}{2}}^{n+\frac{1}{2}} - \Phi_{i-\frac{1}{2}}^{n+\frac{1}{2}} \right), \quad (\text{F.1})$$

where $\Phi_{i+\frac{1}{2}}^{n+\frac{1}{2}}$ is the numerical flux at the intercell position $z_{i+\frac{1}{2}}$ (see the discretization in Fig. 3.0.2). The numerical fluxes for the FORCE scheme [Eq. (3.2.30)] and the Lax-Wendroff scheme [Eq. (3.2.31)] are, respectively (see Chen and Toro [29])

$$\Phi_{i+\frac{1}{2}}^{\text{FORCE}, n+\frac{1}{2}} = \frac{1}{4} \left[\mathbf{F}_{i+1}^n + \mathbf{F}_i^n + 2\mathbf{F}_i^{n+\frac{1}{2}} - \frac{\Delta z}{\Delta t} (\mathbf{U}_{i+1}^n - \mathbf{U}_i^n) \right], \quad (\text{F.2})$$

$$\Phi_{i+\frac{1}{2}}^{\text{LW}, n+\frac{1}{2}} = \mathbf{F}_i^{n+\frac{1}{2}}. \quad (\text{F.3})$$

The finite volume scheme of Eq. (F.1) is said *monotonic* if it does not change the monotonicity of the field, i.e., $\|\mathbf{U}_i^n\| \leq \|\mathbf{U}_{i+1}^n\| \Leftrightarrow \|\mathbf{U}_i^{n+1}\| \leq \|\mathbf{U}_{i+1}^{n+1}\|$. This is equivalent to the fact that all the eigenvalues of all the Jacobian matrices $\partial_{\mathbf{U}_{i-1}^n} \mathcal{H}(\mathbf{U}_{i-1}^n, \mathbf{U}_i^n, \mathbf{U}_{i+1}^n)$, $\partial_{\mathbf{U}_i^n} \mathcal{H}(\mathbf{U}_{i-1}^n, \mathbf{U}_i^n, \mathbf{U}_{i+1}^n)$ and $\partial_{\mathbf{U}_{i+1}^n} \mathcal{H}(\mathbf{U}_{i-1}^n, \mathbf{U}_i^n, \mathbf{U}_{i+1}^n)$ are non-negative (see Jennings [81]). This class of schemes does not produce any spurious oscillation by definition. However, monotonicity is a very restrictive condition and only holds for certain first-order accurate schemes such as the FORCE method. The main disadvantage of these methods is that they suffer from strong numerical diffusion, i.e., at every iteration, the amplitudes of the relative maxima and the relative minima can noticeable decrease.

The total variation of \mathbf{U}^n at instant t_n is defined by $\text{TV}(\mathbf{U}^n) = \sum_i \|\mathbf{U}_{i+1}^n - \mathbf{U}_i^n\|$. The finite volume scheme of Eq. (F.1) is said *total variation diminishing* (TVD) if $\text{TV}(\mathbf{U}^{n+1}) \leq \text{TV}(\mathbf{U}^n)$. This criterion is less restrictive than monotonicity (a monotonic scheme is TVD, but a TVD scheme is not necessarily monotonic) and high-order resolution can be achieved [104, 163]. These schemes limit the numerical fluxes so that the variations of the slopes $\mathbf{U}_{i+1}^n - \mathbf{U}_i^n$ stay controlled (i.e., *small*) by the TVD criterion.

As built in Section 3.2.1, the advective part of the Maxwell-Fluid model is decoupled into two independent advections: the advection of the Maxwell electromagnetic fields [Eq. (3.2.26)] and the advection of the Fluid (plasma) fields [Eq. (3.2.27)]. Each part is treated separately by the code MAXFLU 1D.

Since the Maxwell part [Eq. (3.2.26)] is a hyperbolic system and the Kerr nonlinear refractive index—the only source of nonlinearities in this advective part—is expected to

be small in front of the linear index, the code MAXFLU 1D uses directly the Lax-Wendroff scheme [Eq. (3.2.31)], yielding accurate results.

The numerical problem lies in the weakly hyperbolic Fluid part [Eq. (3.2.27)]. Here the spurious oscillations must be avoided because they destabilize the simulation. To overcome this problem, an *antidispersive correction* hybridizing the FORCE and Lax-Wendroff schemes has been conceived, inspired by the flux-corrected transport (FCT) algorithm (see Boris and Book [18], and Zalesak [189]):

$$\left\{ \begin{array}{l} \mathbf{U}_i^{\text{D}, n+1} = \mathbf{U}_i^n - \frac{\Delta t}{\Delta z} \left(\Phi_{i+\frac{1}{2}}^{\text{LW}, n+\frac{1}{2}} - \Phi_{i-\frac{1}{2}}^{\text{LW}, n+\frac{1}{2}} \right), \\ \mathbf{A}_{i+\frac{1}{2}}^{n+\frac{1}{2}} = \Phi_{i+\frac{1}{2}}^{\text{FORCE}, n+\frac{1}{2}} - \Phi_{i+\frac{1}{2}}^{\text{LW}, n+\frac{1}{2}}, \\ \mathbf{U}_i^{n+1} = \mathbf{U}_i^{\text{D}, n+1} - \frac{\Delta t}{\Delta z} \left(\psi_{i+\frac{1}{2}}^{n+\frac{1}{2}} \mathbf{A}_{i+\frac{1}{2}}^{n+\frac{1}{2}} - \psi_{i-\frac{1}{2}}^{n+\frac{1}{2}} \mathbf{A}_{i-\frac{1}{2}}^{n+\frac{1}{2}} \right), \end{array} \right. \quad (\text{F.4})$$

where $\mathbf{U}_i^{\text{D}, n+1}$ is the *dispersive* solution at t_{n+1} calculated by the Lax-Wendroff method, $\mathbf{A}_{i+\frac{1}{2}}^{n+\frac{1}{2}}$ is the antidispersive numerical flux that corrects $\mathbf{U}_i^{\text{D}, n+1}$ and $0 \leq \psi_{i+\frac{1}{2}}^{n+\frac{1}{2}} \leq 1$ is a flux limiter acting on $\mathbf{A}_{i+\frac{1}{2}}^{n+\frac{1}{2}}$. If $\psi_{i+\frac{1}{2}}^{n+\frac{1}{2}} = 0$, Eq. (F.4) is identical to the Lax-Wendroff scheme; if $\psi_{i+\frac{1}{2}}^{n+\frac{1}{2}} = 1$, then it is identical to the FORCE method. The key issue lies in choosing an appropriate flux limiter. In the bibliography many TVD flux limiters are found [18, 104, 163]. However, they are based on numerical fluxes that give the *smallest* slopes ($\mathbf{U}_{i+1}^n - \mathbf{U}_i^n$, $\mathbf{U}_{i+2}^n - \mathbf{U}_{i+1}^n$ and so on). Therefore, they act indiscriminately on both physical and numerical oscillations. Taking into account that the terahertz yield is related to the low-frequency components of $N_e E_x$ (see Section 2.4.2), modifying the physical oscillations of the fluid part is not acceptable. At a first glance, using a monotonic scheme would not be a priori acceptable because of its strong numerical diffusion. However, it is acceptable if one physical constraint is applied: the wave propagation speed of the fluid fields, v_z , is smaller than c (i.e., $|v_z| \ll c$). This means that the fluid part must be solved using a time step $\Delta t = c^{-1} \Delta z$ (fixed by the Maxwell part) which is smaller than the maximum time step of the CFL condition for the Fluid part: $|v_z|^{-1} \Delta z$.

For the linear advection given by Eq. (3.0.1), the flux limiter assuring that the scheme of Eq. (F.4) is monotonic for any ratio $\Delta t / \Delta t_{\text{CFL}}$, with $\Delta t_{\text{CFL}} = |\lambda|^{-1} \Delta z$, is

$$\psi = \frac{2 \frac{\Delta t}{|\lambda|^{-1} \Delta z}}{1 + \frac{\Delta t}{|\lambda|^{-1} \Delta z}}. \quad (\text{F.5})$$

To prove Eq. (F.5), let us consider the linear advection equation [Eq. (3.0.1)]:

$$\partial_t u(z, t) + \lambda \partial_z u(z, t) = 0, \quad (\text{F.6})$$

where λ is the constant propagation velocity. For Eq. (F.6), the Lax-Wendroff and FORCE fluxes at the intercells [Eqs. (F.2) and (F.3)] are

$$\Phi_{i+\frac{1}{2}}^{\text{LW}, n+\frac{1}{2}} = \frac{1}{2} \lambda (u_i^n + u_{i+1}^n) - \frac{\Delta t}{2 \Delta z} \lambda^2 (u_{i+1}^n - u_i^n). \quad (\text{F.7})$$

$$\Phi_{i+\frac{1}{2}}^{\text{FORCE}, n+\frac{1}{2}} = \frac{1}{2} \lambda (u_i^n + u_{i+1}^n) - \frac{\Delta t}{4 \Delta z} \lambda^2 (u_{i+1}^n - u_i^n) - \frac{\Delta z}{4 \Delta t} (u_{i+1}^n - u_i^n), \quad (\text{F.8})$$

According to Eq. (F.4), the *dispersive* solution is calculated from the Lax-Wendroff scheme:

$$u_i^{\text{LW}, n+1} = u_i^n - \frac{\Delta t}{\Delta z} \left(\Phi_{i+\frac{1}{2}}^{\text{LW}, n+\frac{1}{2}} - \Phi_{i-\frac{1}{2}}^{\text{LW}, n+\frac{1}{2}} \right), \quad (\text{F.9})$$

which is corrected by the antidispersive flux limiter as

$$u_i^{n+1} = u_i^{\text{LW}, n+1} - \frac{\Delta t}{\Delta z} \left(\psi_{i+\frac{1}{2}}^{n+\frac{1}{2}} A_{i+\frac{1}{2}}^{n+\frac{1}{2}} - \psi_{i-\frac{1}{2}}^{n+\frac{1}{2}} A_{i-\frac{1}{2}}^{n+\frac{1}{2}} \right), \quad (\text{F.10})$$

where

$$A_{i+\frac{1}{2}}^{n+\frac{1}{2}} = \Phi_{i+\frac{1}{2}}^{\text{FORCE}, n+\frac{1}{2}} - \Phi_{i+\frac{1}{2}}^{\text{LW}, n+\frac{1}{2}} = \frac{\Delta t}{4 \Delta z} \lambda^2 (u_{i+1}^n - u_i^n) - \frac{\Delta z}{4 \Delta t} (u_{i+1}^n - u_i^n). \quad (\text{F.11})$$

Let us now define the following derivatives

$$\alpha_j^k = \partial_{u_k^n} u_j^{\text{LW}, n+1}, \quad (\text{F.12})$$

$$\beta_j^k = \frac{\Delta t}{\Delta z} \partial_{u_k^n} A_{j+\frac{1}{2}}^{n+\frac{1}{2}}. \quad (\text{F.13})$$

As explained in Section F, the scheme (F.10) is monotonic if and only if $\psi_{i+\frac{1}{2}}^{n+\frac{1}{2}}$ verifies simultaneously the following four conditions:

$$\alpha_i^i - \psi_{i+\frac{1}{2}}^{n+\frac{1}{2}} \beta_i^i \geq 0, \quad (\text{F.14})$$

$$\alpha_i^{i+1} - \psi_{i+\frac{1}{2}}^{n+\frac{1}{2}} \beta_i^{i+1} \geq 0, \quad (\text{F.15})$$

$$\alpha_{i+1}^i + \psi_{i+\frac{1}{2}}^{n+\frac{1}{2}} \beta_i^i \geq 0, \quad (\text{F.16})$$

$$\alpha_{i+1}^{i+1} + \psi_{i+\frac{1}{2}}^{n+\frac{1}{2}} \beta_i^{i+1} \geq 0. \quad (\text{F.17})$$

The monotonicity-preserving flux limiter (F.5) results from Eqs. (F.14), (F.15), (F.16) and (F.17).

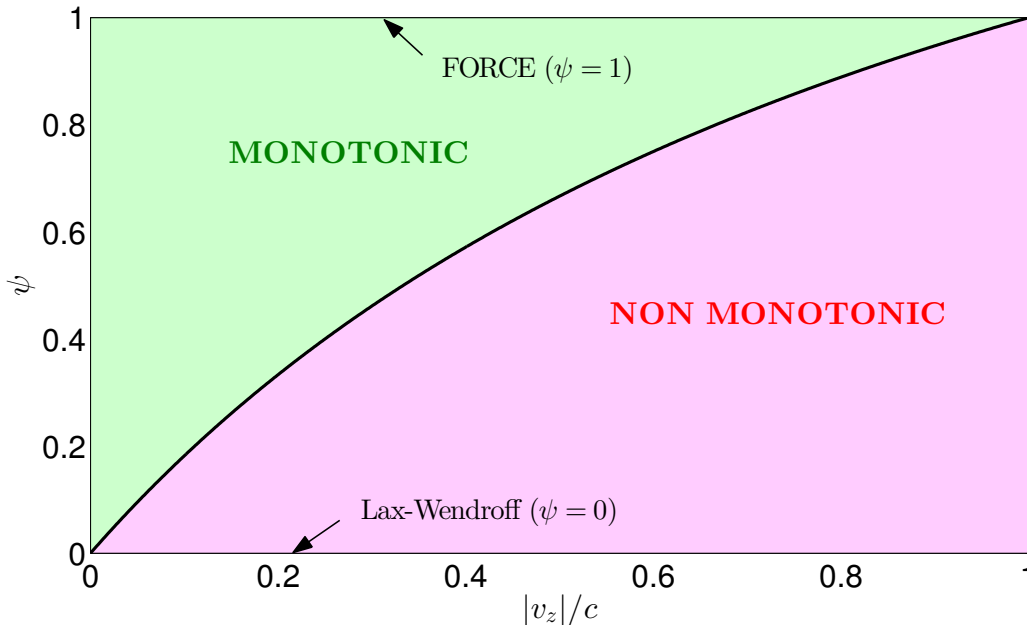


Figure F.1: Antidispersive flux limiter for the Fluid part [Eq. (F.18)] as a function of $|v_z|/c$ (black curve). The monotonic zone (light green area) lies above the undesirable non-monotonic zone (light red area).

For the Fluid part [Eq. (3.2.27)], calculating the optimal flux limiter preserving the monotonicity must take into account the ratio between Δt and $|v_z|^{-1} \Delta z$. This ratio is very cumbersome to evaluate. In practice, the MAXFLU 1D code *heuristically* extrapolates the limiter of Eq. (F.5) to the Fluid part in this way:

$$\psi_{i+\frac{1}{2}}^{n+\frac{1}{2}} = \frac{2|v_z(\mathbf{U}_i^{\text{D}, n+\frac{1}{2}})|}{c + |v_z(\mathbf{U}_i^{\text{D}, n+\frac{1}{2}})|}, \quad (\text{F.18})$$

where $v_z(\mathbf{U}_i^{\text{D}, n+\frac{1}{2}})$ is calculated with Eq. (3.2.21) and the values of the first stage of the Lax-Wendroff scheme [Eq. (3.2.31a)]. This flux limiter for the Fluid part, plotted in Fig. F.1, is very easy to compute. In fact, most of the standard TVD flux limiters are computed with five points, from $\mathbf{U}_{i-2}^{\text{D}, n+1}$ to $\mathbf{U}_{i+2}^{\text{D}, n+1}$, which would imply extra communications between processors. No spurious oscillations have been noticed, even at high intensities, when using this limiter. Therefore, this limiter is suitable for the scheme (F.4)

applied to the Fluid part of the Maxwell-Fluid model. Note that, since $\psi > 0$ if $|v_z| > 0$, the scheme is first-order accurate and thus numerically diffusive. Nevertheless, as almost always $|v_z| \ll c$ holds, the limiter will be close to zero so that diffusion remains negligible.

Complete list of publications and communications

Publications

First author publications

- González de Alaiza Martínez, P., Davoine, X., Debayle, A., Gremillet, L., & Bergé, L. (2016). Terahertz radiation driven by two-color laser pulses at near-relativistic intensities: Competition between photoionization and wakefield effects. *Scientific Reports* **6**, p. 26743.
- González de Alaiza Martínez, P., Babushkin, I., Bergé, L., Skupin, S., Cabrera-Granado, E., Köhler, C., Morgner, U., Husakou, A., & Herrmann, J. (2015). Boosting terahertz generation in laser-field ionized gases using a sawtooth wave shape. *Phys. Rev. Lett.* **114**, p. 183901.
- González de Alaiza Martínez, P., Compant La Fontaine, A., Köhler, C., & Bergé, L. (2015). Effect of multiple ionization in atomic gases irradiated by one- and two-color ultrashort pulses. *J. Phys. B: At. Mol. Opt. Phys.* **48**, p. 094010.
- González de Alaiza Martínez, P., & Bergé, L. (2014). Influence of multiple ionization in laser filamentation. *J. Phys. B: At. Mol. Opt. Phys.* **47**, p. 204017.

Co-author publications

- Andreeva, V. A., Kosareva, O. G., Panov, N. A., Shipilo, D. E., Solyankin, P. M., Esaulkov, M. N., González de Alaiza Martínez, P., Shkurinov, A. P., Makarov, V. A., Bergé, L., & Chin, S. L. (2016). Ultrabroad terahertz spectrum generation from an air-based filament plasma. *Phys. Rev. Lett.* **116**, p. 063902.
- Debayle, A., González de Alaiza Martínez, P., Gremillet, L., & Bergé, L. (2015). Nonmonotonic increase in laser-driven THz emissions through multiple ionization events. *Phys. Rev. A Rapid Communication* **91**, p. 41801.

- Nuter, R., Grech, M., González de Alaiza Martínez, P., Bonnaud, G., & d’Humières, E. (2014). Maxwell solvers for the simulations of the laser-matter interaction. *Eur. Phys. J. D* **68**, p. 177.

Internal reports

- González de Alaiza Martínez, P., Bergé, L., Babushkin, I., Morgner, U., Skupin, S., Cabrera-Granado, E., Köhler, C., Husakou, A., & Herrmann, J. (2016). Rayonnement térahertz généré par des lasers en dents de scie. *Bilan 2015 des publications scientifiques et techniques de la Direction des Applications Militaires*, pp. 4-5.

Conferences, workshops and seminars

Invited talks

- *Mathematical models for terahertz emissions by laser-gas interaction* (28/09/2015-02/10/2015). WORKSHOP ON QUASILINEAR AND NONLOCAL NONLINEAR SCHRÖDINGER EQUATIONS, Vienna (Austria).
- *Models for laser-driven generation of THz radiation* (11-14/08/2014). SIAM CONFERENCE ON NONLINEAR WAVES AND COHERENT STRUCTURES, Cambridge (UK).

Oral presentations

- *Génération de sources térahertz intenses par des impulsions laser ultrabrèves* (08/06/2016). JOURNÉE DES THÈSE, DES DOCTORANTS ET DES POST-DOCS DE LA DIF, Bruyères-le-Châtel (France).
- *Photoionization versus plasma wakefield effects in laser-induced terahertz emissions at near-relativistic intensities* (20-22/03/2016). HIGH-INTENSITY LASERS AND HIGH-FIELD PHENOMENA (HILAS), Long Beach, California (USA).
- *Multiple ionization of noble gases by intense femtosecond laser pulses enhances THz generation* (21-25/06/2015). CLEO/Europe-EQEC 2015, Munich (Germany).
- *Increasing laser-driven THz emission with sawtooth pulse profiles* (21-25/06/2015). CLEO/Europe-EQEC 2015, Munich (Germany).

- *Sujets Phares CEA 2013: Optique ultra-rapide et génération de sources térahertz intenses* (16/04/2015). Entretien à mi-thèse avec Monsieur le Haut-Commissaire à l'énergie atomique, Saclay (France).
- *Optique ultra-rapide et génération de sources térahertz intenses* (18-19/02/2015). Journées scientifiques de l'École Doctorale Ondes et Matière, Orsay (France).

Seminars

- *Génération de sources térahertz intenses par des impulsions laser ultrabrèves* (03/10/2016). CEA/DAM/DIF, Bruyères-le-Châtel (France).
- *Generation of intense terahertz sources by ultrashort laser pulses* (16/09/2016). Centre Lasers Intenses et Applications (CELIA), Université de Bordeaux, Talence (France).

Poster presentations

- *Maxwell-Fluid code for simulating the terahertz generation in high-intensity laser-plasma interaction* (10-12/05/2016). PRACE days 2016: PRACE Scientific and Industrial Conference, Prague (Czech Republic).
- *Generation of Intense THz sources by ultrafast laser pulses* (10/11/2015). Réunion de rentrée de l'École Doctorale Ondes et Matière, Palaiseau (France).
- *Generation of Intense THz sources by ultrafast laser pulses* (03/06/2015). Journées des thèses, des doctorants et des post-docs de la DIF, Bruyères-le-Châtel (France).

Bibliography

- [1] Agrawal, G. P. (2001). *Nonlinear Fiber Optics* (3rd ed.). San Diego, United States of America: Academic Press (Elsevier Science).
- [2] Ammosov, M. V., Delone, N. B., & Krařnov, V. P. (1986). Tunnel ionization of complex atoms and of atomic ions in an alternating electromagnetic field. *Sov. Phys. JETP* **64**, pp. 1191-1194.
- [3] Ammosov, M. V., Golovinsky, P. A., Kiyan, I. Y., Krařnov, V. P., & Ristic, V. M. (1992). Tunneling ionization of atoms and atomic ions in an intense laser field with a nonhomogeneous space-time distribution. *J. Opt. Soc. Am. B* **9**, pp. 1225-1230.
- [4] Andreeva, V. A., Kosareva, O. G., Panov, N. A., Shipilo, D. E., Solyankin, P. M., Esaulkov, M. N., González de Alaiza Martínez, P., Shkurinov, A. P., Makarov, V. A., Bergé, L., & Chin, S. L. (2016). Ultrabroad terahertz spectrum generation from an air-based filament plasma. *Phys. Rev. Lett.* **116**, p. 063902.
- [5] Augst, S., Talebpour, A., Chin, S. L., Beaudoin, Y., & Chaker, M. (1995). Nonsequential triple ionization of argon atoms in a high-intensity laser field. *Phys. Rev. A: Rapid Communications* **52**, pp. 917-919.
- [6] Auston, D. H., & Smith, P. R. (1983). Generation and detection of millimeter waves by picosecond photoconductivity. *Appl. Phys. Lett.* **43**, pp. 631-633.
- [7] Babushkin, I., Kuehn, W., Köhler, C., Skupin, S., Bergé, L., Reimann, K., Woerner, M., Herrmann, J., & Elsaesser, T. (2010). Ultrafast spatiotemporal dynamics of terahertz generation by ionizing two-color femtosecond pulses in gases. *Phys. Rev. Lett.* **105**, p. 053903.
- [8] Babushkin, I., Skupin, S., Husakou, A., Köhler, C., Cabrera-Granado, E., Bergé, L., Herrmann, J. (2011). Tailoring THz radiation by controlling tunnel photoionization events in gases. *New J. Phys.* **13**, p. 123029.
- [9] Balakin, A. V., Borodin, A. V., Kotelnikov, I. A., & Shkurinov, A. P. (2010). Terahertz emission from a femtosecond laser focus in a two-color scheme. *J. Opt. Soc. Am. B* **27**, pp. 16-26.

- [10] Bannister, M. E. (1996). Absolute cross sections for electron-impact single ionization of Ne^{q+} ($q = 2, 4 - 6$) ions. *Phys. Rev. A* **54**, pp. 1435-1444.
- [11] Becker, A., & Faisal, F. H. M. (1996). Mechanism of laser-induced double ionization of helium. *J. Phys. B: At. Mol. Opt. Phys.* **29**, pp. L197-L202.
- [12] Belic, D. S., Lecointre, J., & DeFrance, P. (2010). Electron impact multiple ionization of argon ions. *J. Phys. B: At. Mol. Opt. Phys.* **43**, p. 185203.
- [13] Berenzhiani, V. I., Garuchava, D. P., Mikeladze, S. V., Sigua, K. I., Tsintsadze, N. L., Mahajan, S. M., Kishimoto, Y., & Nishikawa, K. (2005). Fluid-Maxwell simulation of laser pulse dynamics in overdense plasmas. *Physics of Plasmas* **12**, p. 062308.
- [14] Bergé, L., Skupin, S., Nuter, R., Kasparian, J., & Wolf, J. P. (2007). Ultrashort filaments of light in weakly ionized, optically transparent media. *Rep. Prog. Phys.* **70**, pp. 1633-1713.
- [15] Bergé, L., Skupin, S., Köhler, C., Babushkin, I., & Herrmann, J. (2013). 3D numerical simulations of THz generation by two-color laser filaments. *Phys. Rev. Lett.* **110**, p. 073901.
- [16] Bideau-Mehu, A., Guern, Y., Abjean, R., & Johannin-Gilles, A. (1981). Measurement of refractive indices of neon, argon, krypton and xenon in the 253.7-140.4 nm wavelength range. Dispersion relations and estimated oscillator strengths of the resonance lines. *J. Quant. Spectrosc. Radiat. Transfer* **25**, pp. 395-402.
- [17] Blank, V., Thomson, M. D., & Roskos, H. G. (2013). Spatio-spectral characteristics of ultra-broadband THz emission from two-colour photoexcited gas plasmas and their impact for nonlinear spectroscopy. *New J. Phys.* **15**, p. 075023.
- [18] Boris, J. P., & Book, D. L. (1973). Flux-corrected transport. I. SHASTA, a fluid transport algorithm that works. *J. Comp. Phys.* **11**, pp. 38-69.
- [19] Borodin, A. V., Esaulkov, M. N., Kuritsyn, I. I., Kotelnikov, I. A., & Shkurinov, A. P. (2012). On the role of photoionization in generation of terahertz radiation in the plasma of optical breakdown. *J. Opt. Soc. Am. B* **29**, pp. 1911-1919.
- [20] Borodin, A. V., Panov, N. A., Kosareva, O. G., Andreeva, V. A., Esaulkov, M. N., Makarov, V. A., Shkurinov, A. P., Chin, S. L., & Zhang, X.-C. (2013). Transformation of terahertz spectra emitted from dual-frequency femtosecond pulse interaction in gases. *Opt. Lett.* **38**, pp. 1906-1908.

-
- [21] Börzsönyi, A., Heiner, Z., Kalashnikov, M. P., Kovács, A. P., & Osvay, K. (2008). Dispersion measurement of inert gases and gas mixtures at 800 nm. *Applied Optics* **47**, pp. 4856-4863.
- [22] Börzsönyi, A., Heiner, Z., Kovács, A. P., Kalashnikov, M. P., & Osvay, K. (2010). Measurements of the pressure dependent nonlinear refractive index of inert gases. *Optics Express* **18**, p. 25848.
- [23] Boyd, R. W. (1992). *Nonlinear optics* (1st ed.). San Diego, United States of America: Academic Press (Elsevier Science).
- [24] Brabec, T., & Krausz, F. (1997). Nonlinear optical pulse propagation in the single-cycle regime. *Phys. Rev. Lett.* **78**, pp. 3282-3285.
- [25] Brunel, F. (1990). Harmonic generation due to plasma effects in a gas undergoing multiphoton ionization in the high-intensity limit. *J. Opt. Soc. Am. B* **7**, pp. 521-526.
- [26] Buccheri, F., & Zhang, X.-Ch. (2015). Terahertz emission from laser-induced microplasma in ambient air. *Optica* **2**, pp. 366-369.
- [27] Buck, A., Wenz, J., Xu, J., Khrennikov, K., Schmid, K., Heigoldt, M., Mikhailova, J. M., Geissler, M., Shen, B., Krausz, F., Karsch, S., & Veisz, L. (2013). Shock-Front Injector for High-Quality Laser-Plasma Acceleration. *Phys. Rev. Lett.* **110**, p. 185006.
- [28] Cabrera-Granado, E., Chen, Y., Babushkin, I., Bergé, L., & Skupin, S. (2015). Spectral self-action of THz emission from ionizing two-color laser pulses in gases. *New J. Phys.* **17**, p. 023060.
- [29] Chen, G.-Q., & Toro, E. F. (2004). Centred schemes for nonlinear hyperbolic equations. *J. Hyper. Differential Equations* **1**, p. 531-566.
- [30] Chen, M., Pukhov, A., Peng, X.-Y., & Willi, O. (2008). Theoretical analysis and simulations of strong terahertz radiation from the interaction of ultrashort laser pulses with gases. *Phys. Rev. E* **78**, p. 046406.
- [31] Chen, Y.-P., Marceau, C., Liu, W.-W., Sun, Z.-D., Zhang, Y.-Z., Théberge, F., Châteauneuf, M., Dubois, J., & Chin, S. L. (2008). Elliptically polarized terahertz emission in the forward direction of a femtosecond laser filament in air. *Appl. Phys. Lett.* **93**, p. 231116.

- [32] Chen, Y.-P., Marceau, C., Géniera, S., Théberge, F., Châteauneuf, M., Dubois, J., & Chin, S. L. (2009). Elliptically polarized Terahertz emission through four-wave mixing in a two-color filament in air. *Optics Communications* **282**, pp. 4283-4287.
- [33] Chiao, R. Y., Garmire, E., & Townes, C. H. (1964). Self-trapping of optical beams. *Phys. Rev. Lett.* **13**, pp. 479-482.
- [34] Chipperfield, L. E., Robinson, J. S., Tisch, J. W. G., & Marangos, J. P. (2009). Ideal waveform to generate the maximum possible electron recollision energy for any given oscillation period. *Phys. Rev. Lett.* **102**, p. 063003.
- [35] Clerici, M., Peccianti, M., Schmidt, B. E., Caspani, L., Shalaby, M., Giguère, M., Lotti, A., Couairon, A., Légaré, F., Ozaki, T., Faccio, D., & Morandotti, R. (2013). Wavelength scaling of terahertz generation by gas ionization. *Phys. Rev. Lett.* **110**, p. 253901.
- [36] Clough, B., Dai, J.-M., & Zhang, X.-Ch. (2012). Laser air photonics: beyond the terahertz gap. *Materials Today* **15**, pp. 50-58.
- [37] Cook, D. J., & Hochstrasser, R. M. (2000). Intense terahertz pulses by four-wave rectification in air. *Opt. Lett.* **25**, pp. 1210-1212.
- [38] Corkum, P. B., Burnett, N. H., & Brunel, F. (1989). Above-threshold ionization in the long-wavelength limit. *Phys. Rev. Lett.* **62**, pp. 1259-1262.
- [39] Corkum, P. B. (1993). Plasma perspective on strong field multiphoton ionization. *Phys. Rev. Lett.* **71**, p. 1994-1997.
- [40] Crandall, D. H., Phaneuf, R. A., & Gregory, D. C. (1979). *Electron impact ionization of multicharged ions*. ORNL/TM-7020, Oak Ridge National Laboratory (Tennessee, Unites States of America).
- [41] Dai, J.-M., Xie, X., & Zhang, X.-C. (2006). Detection of broadband terahertz waves with a laser-induced plasma in gases. *Phys. Rev. Lett.* **97**, p. 103903.
- [42] Daigle, J.-F., Théberge, F., Henriksson, M., Wang, T.-J., Yuan, S., Châteauneuf, M., Dubois, J., Piché, M., & Chin, S. L. (2012). Remote THz generation from two-color filamentation: long distance dependence. *Optics Express* **20**, pp. 6825-6834.
- [43] Dalgarno, A., & Kingston, A. E. (1960). The refractive indices and Verdet constants of the inert gases. *Proc. R. Soc. Lond. A* **259**, pp. 424-429.

-
- [44] D'Amico, C., Houard, A., Akturk, S., Liu, Y., Le Bloas, J., Franco, M., Prade, B., Couairon, A., Tikhonchuk, V. T., & Mysyrowicz, A. (2008). Forward THz radiation emission by femtosecond filamentation in gases: theory and experiment. *New J. Phys.* **10**, p. 013015.
- [45] Debayle, A., Gremillet, L., Bergé, L., & Köhler, C. (2014). Analytical model for THz emissions induced by laser-gas interaction. *Optics Express* **22**, pp. 13691-13709.
- [46] Debayle, A., González de Alaiza Martínez, P., Gremillet, L., & Bergé, L. (2015). Nonmonotonic increase in laser-driven THz emissions through multiple ionization events. *Phys. Rev. A* **91**, p. 041801.
- [47] Decoster, A., Markowich, P. A., & Perthame, B. (1998). *Modelling of Collisions*. Raviart, P. A. (Editor). *Series in Applied Mathematics*. France: Gauthier-Villars.
- [48] Defrance, P., Chantrenne, S., Rachafi, S., Belic, D. S., Jureta, J., Gregory, D., & Brouillard, F. (1990). Absolute cross-section measurements for electron impact ionisation of Li-like N^{4+} , O^{5+} and Ne^{7+} ions. *J. Phys. B: At. Mol. Opt. Phys.* **23**, pp. 2333-2342.
- [49] DeMartini, F., Townes, C. H., Gustafson, T. K., & Kelley, P. L. (1967). Self-steepening of light pulses. *Phys. Rev.* **164**, pp. 312-323.
- [50] Desforges, F. G., Paradkar, B. S., Hansson, M., Ju, J., Senje, L., Audet, T. L., Persson, A., Dobosz-Dufrénoy, S., Lundh, O., Maynard, G., Monot, P., Vay, J.-L., Wahlström, C.-G., & Cros, B. (2014). Dynamics of ionization-induced electron injection in the high density regime of laser wakefield acceleration. *Physics of Plasmas* **21**, p. 120703.
- [51] Diserens, M. J., Harrison, M. F. A., & Smith, A. C. H. (1984). A measurement of the cross section of electron impact ionisation of Ne^+ . *J. Phys. B: At. Mol. Phys.* **17**, pp. 621-624.
- [52] Dolder, K. T., Harrison, M. F. A., & Thonemann, P. C. (1961). A Measurement of the ionization cross-section of helium ions by electron impact. *Proc. R. Soc. Lond. A* **264**, pp. 367-378.
- [53] Dolder, K. T., Harrison, M. F. A., & Thonemann, P. C. (1963). A measurement of the ionization cross-section of Ne^+ to Ne^{2+} by electron impact. *Proc. R. Soc. Lond. A* **274**, pp. 546-551.

- [54] Duponchelle, M., Khouilid, M., Oualim, E. M., Zhang, H., & Defrance, P. (1997). Electron-impact ionization of neon ions ($q = 4 - 8$). *J. Phys. B: At. Mol. Opt. Phys.* **30**, pp. 729-747.
- [55] Dushek, O., & Kuzmin, S. V. (2004). The fields of a moving point charge: a new derivation from Jefimenko's equations. *Eur. J. Phys.* **25**, pp. 343-350.
- [56] Esarey, E., Schroeder, C. B., & Leemans, W. P. (2009). Physics of laser-driven plasma-based electron accelerators. *Reviews of Modern Physics* **81**, pp. 1229-1285.
- [57] Esirkepov, T. Z. (2001). Exact charge conservation scheme for Particle-in-Cell simulation with an arbitrary form-factor. *Computer Physics Communications* **135**, pp. 144-153.
- [58] Fibich, G., Ilan, B., & Tsynkov, S. (2002). Computation of nonlinear backscattering using a high-order numerical method. *Journal of Scientific Computing* **17**, pp. 351-364.
- [59] Fittinghoff, D. N., Bolton, P. R., Chang, B., & Kulander, K. C. (1992). Observation of nonsequential double ionization of helium with optical tunneling. *Phys. Rev. Lett.* **69**, pp. 2642-2645.
- [60] Flesch, R. G., Pushkarev, A., & Moloney, J. V. (1996). Carrier wave shocking of femtosecond optical pulses. *Phys. Rev. Lett.* **76**, pp. 2488-2491.
- [61] Geissler, M., Tempea, G., Scrinzi, A., Schnürer, M., Krausz, F., & Brabec, T. (1999). Light propagation in field-ionizing media: extreme nonlinear optics. *Phys. Rev. Lett.* **83**, pp. 2930-2933.
- [62] Gente, R., & Koch, M. (2015). Monitoring leaf water content with THz and sub-THz waves. *Plant Methods* **11**, p. 15.
- [63] Gildenburg, V. B., & Vvedenskii, N. V. (2007). Optical-to-THz wave conversion via excitation of plasma oscillations in the tunneling-ionization process. *Phys. Rev. Lett.* **98**, p. 245002.
- [64] Glassey, R. T. (1977). On the blowing up of solutions to the Cauchy problem for nonlinear Schrödinger equations. *Journal of Mathematical Physics* **18**, pp. 1794-1797.
- [65] González de Alaiza Martínez, P., & Vázquez-Cendón, M. E. (2014). *Operator-Splitting on Hyperbolic Balance Laws*, pp. 279-287. Casas, F., & Martínez, V. (Editors). *Advances in Differential Equations and Applications. SEMA SIMAI Springer Series Vol. 4*. Springer International Publishing Switzerland.

-
- [66] González de Alaiza Martínez, P., & Bergé, L. (2014). Influence of multiple ionization in laser filamentation. *J. Phys. B: At. Mol. Opt. Phys.* **47**, p. 204017.
- [67] González de Alaiza Martínez, P., Babushkin, I., Bergé, L., Skupin, S., Cabrera-Granado, E., Köhler, C., Morgner, U., Husakou, A., & Herrmann, J. (2015). Boosting terahertz generation in laser-field ionized gases using a sawtooth wave shape. *Phys. Rev. Lett.* **114**, p. 183901.
- [68] González de Alaiza Martínez, P., Davoine, X., Debayle, A., Gremillet, L., & Bergé, L. (2016). Terahertz radiation driven by two-color laser pulses at near-relativistic intensities: Competition between photoionization and wakefield effects. *Scientific Reports* **6**, p. 26743.
- [69] Gorodetsky, A., Koulouklidis, A. D., Massaouti, M., & Tzortzakis, S. (2014). Physics of the conical broadband terahertz emission from two-color laser-induced plasma filaments. *Phys. Rev. A* **89**, p. 033838.
- [70] Gregory, D. C., Dittner, P. F., & Crandall, D. H. (1983). Absolute cross-section measurements for electron-impact ionization of triply charged inert-gas ions: Ne^{3+} , Ar^{3+} , Kr^{3+} , and Xe^{3+} . *Phys. Rev. A* **27**, pp. 724-736.
- [71] Haessler, S., Balčiunas, T., Fan, G., Andriukaitis, G., Pugžlys, A., Baltuška, A., Witting, T., Squibb, R., Zair, A., Tisch, J. W. G., Marangos, J. P., & Chipperfield, L. E. (2014). Optimization of quantum trajectories driven by strong-field waveforms. *Phys. Rev. X* **4**, p. 021028.
- [72] Hamster, H., Sullivan, A., Gordon, S., White, W., & Falcone, R. W. (1993). Sub-picosecond, electromagnetic pulses from intense laser-plasma interaction. *Phys. Rev. Lett.* **71**, pp. 2725-2728.
- [73] Hauri, C. P., Lopez-Martens, R. B., Blaga, C. I., Schultz, K. D., Cryan, J., Chirila, R., Colosimo, P., Doumy, G., March, A. M., Roedig, C., Sistrunk, E., Tate, J., Wheeler, J., DiMauro, L. F., & Power, E. P. (2007). Intense self-compressed, self-phase-stabilized few-cycle pulses at $2\ \mu\text{m}$ from an optical filament. *Optics Letters* Vol. **32**, pp. 868-870.
- [74] Houard, A., Liu, Y., Prade, B., Tikhonchuk, V. T., & Mysyrowicz A. (2008). Strong enhancement of terahertz radiation from laser filaments in air by a static electric field. *Phys. Rev. Lett.* **100**, p. 255006.
- [75] Hu, B.-B., & Nuss, M. C. (1995). Imaging with terahertz waves. *Optics Letters* **20**, pp. 1716-1718.

- [76] Husakou, A. V., & Herrmann, J. (2001). Supercontinuum generation of higher-order solitons by fission in photonic crystal fibers. *Phys. Rev. Lett.* **87**, p. 203901.
- [77] Ilkov, F. A., Decker, J. E., & Chin S. L. (1992). Ionization of atoms in the tunnelling regime with experimental evidence using Hg atoms. *J. Phys. B: At. Mol. Opt. Phys.* **25**, pp. 4005-4020.
- [78] Ishigaki, K., Shiraishi, M., Suzuki, S., Asada, M., Nishiyama, N., & Arai, S. (2012). Direct intensity modulation and wireless data transmission characteristics of terahertz-oscillating resonant tunnelling diodes. *Electronics Letters* **48**, pp. 582-583.
- [79] Jackson, J. D. (1965). *Classical Electrodynamics* (3rd ed.). New York, United States of America: Wiley.
- [80] Jefimenko, O. D. (1994). Direct calculation of the electric and magnetic fields of an electric point charge moving with constant velocity. *Am. J. Phys.* **62**, pp. 79-85.
- [81] Jennings, G. (1974). Discrete shocks. *Communications on Pure and Applied Mathematics* **27**, pp. 25-37.
- [82] Kaganovich, D., Gordon, D. F., Helle, M. H., & Ting, A. (2014). Shaping gas jet plasma density profile by laser generated shock waves. *J. Appl. Phys.* **116**, p. 013304.
- [83] Kampfrath, T., Tanaka, K., & Nelson, K. A. (2013). Resonant and nonresonant control over matter and light by intense terahertz transients. *Nature Photonics* **7**, pp. 680-690.
- [84] Kandidov, V. P., Kosareva, O. G., Golubtsov, I. S., Liu, W., Becker, A., Akozbek, N., Bowden, C. M., & Chin, S. L. (2003). Self-transformation of a powerful femtosecond laser pulse into a white-light laser pulse in bulk optical media (or supercontinuum generation). *Applied Physics B* **77**, pp. 149-165.
- [85] Karpowicz, N., Dai, J.-M., Lu, X.-F., Chen, Y.-Q., Yamaguchi, M., Zhao, H.-W., Zhang, X.-C., Zhang, L.-L., Zhang, C.-L., Price-Gallagher, M., Fletcher, C., Mamer, O., Lesimple, A., & Johnson, K. (2008). Coherent heterodyne time-domain spectrometry covering the entire “terahertz gap”. *Appl. Phys. Lett.* **92**, p. 011131.
- [86] Karpowicz, N., Lu, X.-F., & Zhang, X.-C. (2009). Terahertz gas photonics. *Journal of Modern Optics* **56**, pp. 1137-1150.
- [87] Keldysh, L. V. (1965). Ionization in the Field of a Strong Electromagnetic Wave. *Sov. Phys. JETP* **20**, pp. 1307-1314.

-
- [88] Kennedy, P. K. (1995). A first-order model for computation of laser-induced breakdown thresholds in ocular and aqueous media: Part I-Theory. *IEEE Journal of Quantum Electronics* **31**, pp. 2241-2249.
- [89] Kim, K.-Y., Glowina, J. H., Taylor, A. J., & Rodriguez, G. (2007). Terahertz emission from ultrafast ionizing air in symmetry-broken laser fields. *Optics Express* **15**, 4577-4584.
- [90] Kim, K.-Y., Glowina, J. H., Taylor, A. J., & Rodriguez, G. (2008). Coherent control of terahertz supercontinuum generation in ultrafast laser-gas interactions. *Nature Photonics* **2**, pp. 605-609.
- [91] Kim, Y.-K., & Rudd, M. E. (1994). Binary-encounter-dipole model for electron-impact ionization. *Phys. Rev. A* **50**, pp. 3954-3967.
- [92] Klarskov, P., Strikwerda, A. C., Iwaszczuk, K., & Jepsen, P. U. (2013). Experimental three-dimensional beam profiling and modeling of a terahertz beam generated from a two-color air plasma. *New J. Phys.* **15**, p. 075012.
- [93] Kolesik, M., Moloney, J. V., & Mlejnek, M. (2002). Unidirectional optical pulse propagation equation. *Phys. Rev. Lett.* **89**, p. 283902.
- [94] Kolesik, M., & Moloney, J. V. (2004). Nonlinear optical pulse propagation simulation: from Maxwell's to unidirectional equations. *Phys. Rev. E* **70**, p. 036604.
- [95] Kreß, M., Löffler, T., Thomson, M. D., Dörner, R., Gimpel, H., Zrost, K., Ergler, T., Moshhammer, R., Morgner, U., Ullrich, J., & Roskos, H. G. (2006). Determination of the carrier-envelope phase of few-cycle laser pulses with terahertz-emission spectroscopy. *Nature Physics* **2**, pp. 327-331.
- [96] Kuznetsov, E. A. (1996). Wave collapse in plasmas and fluids. *Chaos: An Interdisciplinary Journal of Nonlinear Science* **6**, pp. 381-390.
- [97] Landau, L. M., & Lifschitz, E. M. (1965). *Quantum Mechanics* (2nd ed.). New York, United States of America: Pergamon.
- [98] Larochelle, S., Talepbour, A., & Chin, S. L. (1998). Non-sequential multiple ionization of rare gas atoms in a Ti: Sapphire laser field. *J. Phys. B: At. Mol. Opt. Phys.* **31**, pp. 1201-1214.
- [99] Larochelle, S. F. J., Talepbour, A., & Chin, S. L. (1998). Coulomb effect in multiphoton ionization of rare-gas atoms. *J. Phys. B: At. Mol. Opt. Phys.* **31**, pp. 1215-1224.

- [100] Lax, P., & Wendroff, B. (1960). Systems of conservation laws. *Communications on Pure and Applied Mathematics* **13**, pp. 217-237.
- [101] Lecointre, J., Jureta, J. J., & Defrance, P. (2008). Electron-impact ionization of singly-charged neon ions. *J. Phys. B: At. Mol. Opt. Phys.* **41**, p. 095204.
- [102] Lefebvre, E., Cochet, N., Fritzler, S., Malka, V., Aléonard, M.-M., Chemin, J.-F., Darbon, S., Disdier, L., Faure, J., Fedotoff, A., Landoas, O., Malka, G., Méot, V., Morel, P., Rabec Le Gloahec, M., Rouyer, A., Rubbelynck, C., Tikhonchuk, V., Wrobel, R., Audebert, P., & Rousseaux, C. (2003). Electron and photon production from relativistic laser-plasma interactions. *Nuclear Fusion* **43**, pp. 629-633.
- [103] Leonard, P. J. (1974). Refractive indices, Verdet constants, and polarizabilities of the inert gases. *Atomic Data and Nuclear Data Tables* **14**, pp. 21-37.
- [104] LeVeque, R. J. (2002). *Finite volume methods for hyperbolic problems* (1st ed.). New York, United States of America: Cambridge University Press.
- [105] L'Huillier, A., Lompré, L. A., Mainfray, G., & Manus, C. (1983). Multiply charged ions induced by multiphoton absorption. *J. Phys. B: At. Mol. Phys.* **16**, pp. 1363-1381.
- [106] Li, Ch., Zhou, M.-L., Ding, W.-J., Du, F., Liu, F., Li, Y.-T., Wang, W.-M., Sheng, Zh.-M., Ma, J.-L., Chen, L.-M., Lu, X., Dong, Q.-L., Wang, Zh.-H., Lou, Zh., Shi, Sh.-C., Wei, Zh.-Y., & Zhang, J. (2011). Effects of laser-plasma interactions on terahertz radiation from solid targets irradiated by ultrashort intense laser pulses. *Phys. Rev. E* **84**, p. 036405.
- [107] Li, Ch., Cui, Y.-Q., Zhou, M.-L., Du, F., Li, Y.-T., Wang, W.-M., Chen, L.-M., Sheng, Zh.-M., Ma, J.-L., Lu, X., & Zhang, J. (2014). Role of resonance absorption in terahertz radiation generation from solid targets. *Optics Express* **22**, pp. 11797-11803.
- [108] Li, M., Li, W.-X., Shi, Y., Lu, P.-F., Pan, H.-F., & Zeng, H.-P. (2012). Verification of the physical mechanism of THz generation by dual-color ultrashort laser pulses. *Appl. Phys. Lett.* **101**, p. 161104.
- [109] Li, Y.-T., Li, C., Zhou, M.-L., Wang, W.-M., Du, F., Ding, W.-J., Lin, X.-X., Liu, F., Sheng, Z.-M., Peng, X.-Y., Chen, L.-M., Ma, J.-L., Lu, X., Wang, Z.-H., Wei, Z.-Y., & Zhang, J. (2012). Strong terahertz radiation from relativistic laser interaction with solid density plasmas. *Appl. Phys. Lett.* **100**, p. 254101.

-
- [110] Liao, G.-Q., Li, Y.-T., Li, C., Su, L.-N., Zheng, Y., Liu, M., Wang, W.-M., Hu, Z.-D., Yan, W.-C., Dunn, J., Nilsen, J., Hunter, J., Liu, Y., Wang, X., Chen, L.-M., Ma, J.-L., Lu, X., Jin, Z., Kodama, R., Sheng, Z.-M., & Zhang, J. (2015). Bursts of terahertz radiation from large-scale plasmas irradiated by relativistic picosecond laser pulses. *Phys. Rev. Lett.* **114**, p. 255001.
- [111] Liu, J.-L., Dai, J.-M., Chin, S.-L., & Zhang, X.-C. (2010). Broadband terahertz wave remote sensing using coherent manipulation of fluorescence from asymmetrically ionized gases. *Nature Photonics* **4**, pp. 627-631.
- [112] Liu, J.-L., & Zhang, X.-Ch. (2014). Terahertz radiation-enhanced-emission-of-fluorescence. *Front. Optoelectron.* **7**, pp. 156-198.
- [113] Löffler, T., Jacob, F., & Roskos, H. G. (2000). Generation of terahertz pulses by photoionization of electrically biased air. *Appl. Phys. Lett.* **77**, pp. 453-455.
- [114] Löffler, T., & Roskos, H. G. (2000). Gas-pressure dependence of terahertz-pulse generation in a laser-generated nitrogen plasma. *J. Appl. Phys.* **91**, pp. 2611-2614.
- [115] Lotz, W. (1967). An empirical formula for the electron-impact ionization cross-section. *Zeitschrift für Physik* **206**, pp. 205-211.
- [116] MacCormack, R. (2003). The Effect of Viscosity in Hypervelocity Impact Cratering. *Journal of Spacecraft and Rockets* **40**, pp. 757-763.
- [117] Magesh Kumar, K. K., Kumar, M., Yuan, T., Sheng, Z.-M., & Chen, M. (2015). Terahertz radiation from plasma filament generated by two-color laser gas plasma interaction. *Laser and Particle Beams* **33**, pp. 473-479.
- [118] Man, K. F., Smith, A. C. H., & Harrison, M. F. A. (1987). A measurement of the cross section for electron impact ionisation of Ne^+ , Ar^+ , Kr^+ and Xe^+ . *J. Phys. B: At. Mol. Phys.* **20**, pp. 5865-5880.
- [119] Mansfield, C. R. (1969). Dispersion of helium. *J. Opt. Soc. Am.* **59**, pp. 199-204.
- [120] Matsumoto, A., Danjo, A., Ohtani, S., Suzuki, H., Tawara, H., Takanayagi, T., Wakiya, K., Yamada, I., Yoshino, M., & Hirayama, T. (1990). Measurements of absolute cross sections for electron-impact ionization of doubly charged rare gas ions: Ne^{2+} , Ar^{2+} , Kr^{2+} and Xe^{2+} . *Journal of the Physical Society of Japan* **59**, pp. 902-917.
- [121] Max Planck Institute of Quantum Optics (2013). Cool electron acceleration: Electron pulses from laser accelerator. *ScienceDaily*: www.sciencedaily.com/releases/2013/06/130603113348.htm.

- [122] Montague, R. G., Harrison, M. F. A., & Smith, A. C. H. (1984). A measurement of the cross section for ionisation of helium by electron impact using a fast crossed beam technique. *J. Phys. B: At. Mol. Phys.* **17**, pp. 3295-3310.
- [123] Muller, A., Tinschert, K., Achenbach, C., Becker R., & Salzborn, E. (1985). Electron impact double ionisation of Ar^+ and Ar^{4+} ions. *J. Phys. B: At. Mol. Phys.* **18**, pp. 3011-3016.
- [124] NIST Atomic Spectra Database: <http://www.nist.gov/pml/data/asd.cfm>.
- [125] Nuter, R., & Bergé, L. (2006). Pulse chirping and ionization of O_2 molecules for the filamentation of femtosecond laser pulses in air. *J. Opt. Soc. Am. B* **23**, pp. 874-884.
- [126] Nuter, R., Gremillet, L., Lefebvre, E., Lévy, A., Ceccotti, T., & Martin, P. (2011). Field ionization model implemented in Particle in Cell code and applied to laser-accelerated carbon ions. *Physics of Plasmas* **18**, p. 033107.
- [127] Oh, T. I., You, Y.-S., Jhajj, N., Rosenthal, E. W., Milchberg, H. M., & Kim, K.-Y. (2013). Intense terahertz generation in two-color laser filamentation: energy scaling with terawatt laser systems. *New J. Phys.* **15**, p. 075002.
- [128] Panov, N., Andreeva, V., Kosareva, O., Shkurinov, A., Makarov, V. A., Bergé, L., & Chin, S. L. (2014). Directionality of terahertz radiation emitted from an array of femtosecond filaments in gases. *Laser Physics Letters* **11**, p. 125401.
- [129] Peart, B., Walton, D. S., & Dolder, K. T. (1969). The ranges of validity of the Born and Bethe approximations for the single ionization of He^+ and Li^+ ions by electron impact. *J. Phys. B: Atom. Molec. Phys.* **2**, pp. 1347-1352.
- [130] Peñano, J., Sprangle, P., Hafizi, B., Gordon, D., & Serafim, P. (2010). Terahertz generation in plasmas using two-color laser pulses. *Phys. Rev. E* **81**, p. 026407.
- [131] Perelomov, A. M., Popov, V. S., & Terent'ev, M. V. (1966). Ionization of atoms in an alternating electric field. *Sov. Phys. JETP* **23**, pp. 924-934.
- [132] Perelomov, A. M., Popov, V. S., & Terent'ev, M. V. (1967). Ionization of atoms in an alternating electric field: II. *Sov. Phys. JETP* **24**, pp. 207-217.
- [133] Perelomov, A. M., & Popov, V. S. (1967). Ionization of atoms in an alternating electric field: III. *Sov. Phys. JETP* **25**, pp. 336-343.
- [134] Pérez, F., Gremillet, L., Decoster, A., Drouin, M., & Lefebvre, E. (2012). Improved modeling of relativistic collisions and collisional ionization in particle-in-cell codes. *Physics of Plasmas* **19**, p. 083104.

-
- [135] Pindzola, M. S., Griffin, D. C., Bottcher, C., Crandall, D. H., Phaneuf, R. A., & Gregory, D. C. (1984). Electron-impact double ionization of rare-gas ions. *Phys. Rev. A* **29**, pp. 1749-1756.
- [136] Rachafi, S., Belic, D. S., Duponchelle, M., Jureta, J., Zambra, M., Zhang, H., & De-france, P. (1991). Absolute cross section measurements for electron impact ionization of Ar^{7+} . *J. Phys. B: At. Mol. Opt. Phys.* **24**, pp. 1037-1047.
- [137] Rae, S. C., & Burnett, K. (1992). Detailed simulations of plasma-induced spectral blueshifting. *Phys. Rev. A* **46**, pp. 1084-1090.
- [138] Rejoub, R., Lindsay, B. G., & Stebbings, R. F. (2002). Determination of the absolute partial and total cross sections for electron-impact ionization of the rare gases. *Phys. Rev. A* **65**, p. 042713.
- [139] Richtmyer, R. D. (1962). A survey of difference methods for non-steady fluid dynamics. *NCAR Technical Notes* **63-2**.
- [140] Roskos, H. G., Thomson, M. D., Kreß, M., & Löffler, T. (2007). Broadband THz emission from gas plasmas induced by femtosecond optical pulses: From fundamentals to applications. *Laser & Photon. Rev.* **1**, pp. 349-368.
- [141] Sagisaka, A., Daido, H., Nashima, S., Orimo, S., Ogura, K., Mori, M., Yogo, A., Ma, J., Daito, I., Pirozhkov, A. S., Bulanov, S. V., Esirkepov, T. Zh., Shimizu, K., & Hosoda, M. (2008). Simultaneous generation of a proton beam and terahertz radiation in high-intensity laser and thin-foil interaction. *Applied Physics B* **90**, pp. 373-377.
- [142] Schiesser, W. E. (1991). *The numerical method of lines: Integration of partial differential equations* (1st ed.). San Diego, United States of America: Academic Press.
- [143] Schmid, K., Buck, A., Sears, C. M. S., Mikhailova, J. M., Tautz, R., Herrmann, D., Geissler, M., Krausz, F., & Veisz, L. (2010). Density-transition based electron injector for laser driven wakefield accelerators. *Phys. Rev. ST Accel. Beams* **13**, p. 091301.
- [144] Schram, B. L., Boerbomm, A. J. H., & Kistemaker, J. (1966). Partial ionization cross sections of noble gases for electrons with energy 0.5-16 keV. *Physica* **32**, pp. 185-196.
- [145] Sellmeier, W. (1871). Zur Erklärung der abnormen Farbenfolge im Spectrum einiger Substanzen. *Annalen der Physik und Chemie* **219**, pp. 272-282.

- [146] Shadwick, B. A., Schroeder, C. B., & Esarey, E. (2009). Nonlinear laser energy depletion in laser-plasma accelerators. *Physics of Plasmas* **16**, p. 056704.
- [147] Shah, M. B., Elliott, D. S., & Gilbody, H. B. (1987). Pulsed crossed-beam study of the ionisation of atomic hydrogen by electron impact. *J. Phys. B: At. Mol. Phys.* **20**, 3501-3514.
- [148] Shin, J.-H., Zhidkov, A., Jin, Z., Hosokai, T., & Kodama, R. (2012). Non-linear plasma effects on laser-induced terahertz emission from the atmosphere. *Physics of Plasmas* **19**, p. 023117.
- [149] Singh, M., & Sharma, R. P. (2013). Generation of THz radiation by laser plasma interaction. *Contributions to Plasma Physics* **53**, pp. 540-548.
- [150] Sirtori, C. (2002). Bridge for the terahertz gap. *Nature* **417**, pp. 132-133.
- [151] Slocum, D. M., Slingerland, E. J., Giles, R. H., & Goyette T. M. (2013). Atmospheric absorption of terahertz radiation and water vapor continuum effects. *Journal of Quantitative Spectroscopy and Radiative Transfer* **127**, pp. 49-63.
- [152] Sprangle, P., Esarey, E., & Ting, A. (1990). Nonlinear interaction of intense laser pulses in plasmas. *Phys. Rev. A* **41**, pp. 4463-4469.
- [153] Sprangle, P., Peñano, J. R., & Hafizi, B. (2002). Propagation of intense short laser pulses in the atmosphere. *Phys. Rev. E* **66**, p. 046418.
- [154] Sprangle, P., Peñano, J. R., Hafizi, B., & Kapetanakos, C. A. (2004). Ultrashort laser pulses and electromagnetic pulse generation in air and on dielectric surfaces. *Phys. Rev. E* **69**, p. 066415.
- [155] Stephan, K., Helm, H., & Maerk, T. D. (1980). Mass spectrometric determination of partial electron impact ionization cross sections of He, Ne, Ar and Kr from threshold up to 180 eV. *The Journal of Chemical Physics* **73**, pp. 3763-3778.
- [156] Strang, G. (1968). On the construction and comparison of difference schemes. *SIAM J. Numer. Anal.* **5**, pp. 506-517.
- [157] Straub, H. C. (1996). *Absolute partial cross sections for electron-impact ionization of argon, hydrogen, nitrogen, oxygen, and carbon dioxide from threshold to 1000 eV*. Doctoral Thesis, Rice University (Houston, Texas, United States of America).
- [158] Talebpour, A., Yang, J., & Chin, S. L. (1999). Semi-empirical model for the rate of tunnel ionization of N₂ and O₂ molecule in an intense Ti:sapphire laser pulse. *Optics Communications* **163**, pp. 29-32.

-
- [159] Tawara, H., & Kato, T. (1987). Total and partial ionization cross sections of atoms and ions by electron impact. *Atomic Data and Nuclear Data Tables* **36**, pp. 167-353.
- [160] Théberge, F., Liu, W.-W., Simard, P. T., Becker, A., & Chin, S. L. (2006). Plasma density inside a femtosecond laser filament in air: Strong dependence on external focusing. *Phys. Rev. E* **74**, p. 036406.
- [161] Tinschert, K., Muller, A., Phaneuf, R. A., Hofmann, G., & Salzborn, E. (1989). Electron impact double ionisation of Ar^{q+} ions ($q = 1, 2, \dots, 7$): two-electron processes compared with inner-shell contributions. *J. Phys. B: At. Mol. Opt. Phys.* **22**, pp. 1241-1248.
- [162] Tonouchi, M. (2007). Cutting-edge terahertz technology. *Nature Photonics* **1**, pp. 97-105.
- [163] Toro, E. F. (2009). *Riemann solvers and numerical methods for fluid dynamics: A practical introduction* (3rd ed.). Berlin & Heidelberg, Germany: Springer-Verlag.
- [164] Tushentsov, M., Kim, A., Cattani, F., Anderson, D., & Lisak, M. (2001). Electromagnetic energy penetration in the self-induced transparency regime of relativistic laser-plasma interactions. *Phys. Rev. Lett.* **87**, p. 275002.
- [165] Tzortzakis, S., Prade, B., Franco, M., & Mysyrowicz, A. (2000). Time-evolution of the plasma channel at the trail of a self-guided IR femtosecond laser pulse in air. *Optics Communications* **181**, pp. 123-127.
- [166] van der Weide, D. W., Murakowski, J., & Keilmann, F. (2000). Gas-Absorption Spectroscopy with Electronic Terahertz Techniques. *IEEE Transactions on Microwave Theory and Techniques* **48**, pp. 740-743.
- [167] Vicario, C., Monozslai, B., & Hauri, C. P. (2014). GV/m single-cycle terahertz fields from a laser-driven large-size partitioned organic crystal. *Phys. Rev. Lett.* **112**, p. 213901.
- [168] Vlasov, S. N., Petrishchev, V. A., & Talanov, V. I. (1971). Averaged description of wave beams in linear and nonlinear media (the method of moments). *Izvestiya Vysshikh Uchebnykh Zavedenii Radiofizika* **14**, pp. 1353-1363.
- [169] Walker, B., Sheehy, B., DiMauro, L. F., Agostini, P., Schafer, K. J., & Kulander, K. C. (1994). Precision measurement of strong field double ionization of helium. *Phys. Rev. Lett.* **73**, pp. 1227-1230.

- [170] Wang, T.-J., Chen, Y.-P., Marceau, C., Théberge, F., Châteauneuf, M., Dubois, J., & Chin, S. L. (2009). High energy terahertz emission from two-color laser-induced filamentation in air with pump pulse duration control. *Appl. Phys. Lett.* **95**, p. 131108.
- [171] Wang, T.-J., Marceau, C., Chen, Y.-P., Yuan, S., Théberge, F., Châteauneuf, M., Dubois, J., & Chin, S. L. (2010). Terahertz emission from a dc-biased two-color femtosecond laser-induced filament in air. *Appl. Phys. Lett.* **96**, p. 211113.
- [172] Wang, T.-J., Yuan, S., Chen, Y.-P., Daigle, J.-F., Marceau, C., Théberge, F., Châteauneuf, M., Dubois, J., & Chin, S. L. (2010). Toward remote high energy terahertz generation. *Appl. Phys. Lett.* **97**, p. 111108.
- [173] Wang, W.-M., Sheng, Z.-M., Wu, H.-C., Chen, M., Li, C., Zhang, J., & Mima, K. (2008). Strong terahertz pulse generation by chirped laser pulses in tenuous gases. *Optics Express* **16**, pp. 16999-17006.
- [174] Wang, W.-M., Kawata, S., Sheng, Zh.-M., Li, Y.-T., Chen, L.-M., Qian, L.-J., & Zhang, J. (2011). Efficient terahertz emission by mid-infrared laser pulses from gas targets. *Opt. Lett.* **36**, pp. 2608-2610.
- [175] Williams, B. S. (2007). Terahertz quantum-cascade lasers. *Nature Photonics* **1**, pp. 517-525.
- [176] Woodfruff, P. R., Hublet, M.-C., & Harrison, M. F. A. (1978). A measurement of the cross section for electron impact of Ar^+ , *J. Phys. B: At. Mol. Phys.* **11**, pp. 305-308.
- [177] Wu, D., Zheng, C.-Y., Yan, X.-Q., Yu, M.-Y., & He, X.-T. (2013). Breather-like penetration of ultrashort linearly polarized laser into over-dense plasmas. *Physics of Plasmas* **20**, p. 033101.
- [178] Wu, H.-Ch., Meyer-ter-Vehn, J., & Sheng, Zh.-M. (2008). Phase-sensitive terahertz emission from gas targets irradiated by few-cycle laser pulses. *New J. Phys.* **10**, p. 043001.
- [179] Wu, J., Tong, Y.-Q., Li, M., Pan, H.-F., & Zeng, H.-P. (2010). THz generation by a two-color pulse in prealigned molecules. *Phys. Rev. A* **82**, p. 053416.
- [180] Wu, M.-Y., Wang, Y.-L., Liu, X.-J., Li, W.-D., Hao, X.-L., & Chen, J. (2013). Coulomb-potential effects in nonsequential double ionization under elliptical polarization. *Phys. Rev. A* **87**, p. 013431.

- [181] Xie, X., Dai, J.-M., & Zhang, X.-C. (2006). Coherent control of THz wave generation in ambient air. *Phys. Rev. Lett.* **96**, p. 075005.
- [182] Yablonovitch, E., & Bloembergen, N. (1972). Avalanche ionization and the limiting diameter of filaments induced by light pulses in transparent media. *Phys. Rev. Lett.* **29**, pp. 907-910.
- [183] Yamamoto, K., Yamaguchi, M., Miyamaru, F., Tani, M., Hangyo, M., Ikeda, T., Matsushita, A., Koide, K., Tatsuno, M., & Minami, Y. (2004). Noninvasive Inspection of C-4 Explosive in Mails by Terahertz Time-Domain Spectroscopy. *Japanese Journal of Applied Physics* **43**, pp. L414-L417.
- [184] Yee, K. S. (1966). Numerical solution of initial boundary value problems involving Maxwell's Equations in isotropic media. *IEEE Transactions on Antennas and Propagation* **14**, pp. 302-307.
- [185] Yeh, K.-L., Hoffmann, M. C., Hebling, J., & Nelson, K. A. (2007). Generation of 10 μ J ultrashort terahertz pulses by optical rectification. *Appl. Phys. Lett.* **90**, p. 171121.
- [186] You, Y.-S., Oh, T. I., & Kim, K.-Y. (2012). Off-axis phase-matched terahertz emission from two-color laser-induced plasma filaments. *Phys. Rev. Lett.* **109**, p. 183902.
- [187] Yu, C., Fan, Sh.-T., Sun, Y.-W., & Pickwell-MacPherson, E. (2012). The potential of terahertz imaging for cancer diagnosis: A review of investigations to date. *Quant. Imaging Med. Surg.* **2**, pp. 33-45.
- [188] Zahedpour, S., Wahlstrand, J. K., & Milchberg, H. M. (2015). Measurement of the nonlinear refractive index of air constituents at mid-infrared wavelengths. *Opt. Lett.* **40**, pp. 5794-5797.
- [189] Zalesak, S. T. (2012). *The design of flux-corrected transport (FCT) algorithms for structured grids*, pp. 29-78. Kuzmin, D., Löhner, R., & Turek, S. (Editors). *Flux-corrected transport: Principles, algorithms, and applications*. Berlin & Heidelberg, Germany: Springer-Verlag.
- [190] Zambra, M., Belic, D., Defrance, P., & Yu, D.-J. (1994). Electron impact double ionization of singly charged ions C^+ , N^+ , O^+ and Ne^+ . *J. Phys. B: At. Mol. Opt. Phys.* **27**, pp. 2383-2397.
- [191] Zhang, H., Cherkani-Hassani, S., Belenger, C., Duponchelle, M., Khouilid, M., Oualim, E. M., & Defrance, P. (2002). Electron impact ionization of argon ions ($q = 4 - 11$). *J. Phys. B: At. Mol. Opt. Phys.* **35**, pp. 3829-3845.

- [192] Zhang, X.-C. (2002). Terahertz wave imaging: horizons and hurdles. *Phys. Med. Biol.* **47**, pp. 3667-3677.

Titre : Génération de sources térahertz intenses par des impulsions laser ultrabrèves

Mots clés : Sources térahertz intenses, Interaction laser-matière, Optique non-linéaire, Oscillations plasma, Photoionisation

Résumé : Les ondes térahertz (THz) appartiennent à une bande étroite du spectre électromagnétique, comprise entre les micro-ondes et les ondes optiques. Le rayonnement THz intense est très prometteur pour la spectroscopie résolue en temps et l'identification des explosifs à distance. Le but de cette thèse est précisément d'étudier la génération d'un tel rayonnement THz par couplage de deux impulsions laser ultracourtes capables d'ioniser un gaz. Le plasma créé par photoionisation joue le rôle de convertisseur nonlinéaire de fréquence, transformant une partie de l'énergie du champ laser dans la bande THz via une gamme riche de mécanismes physiques. À des intensités laser modérées (10^{12} - 10^{14} W/cm²) nous identifions, à l'aide d'une expérience faite dans l'air, la signature de l'effet Kerr dans le spectre THz émis, qui, plus faible, se révèle complémentaire de celle du plasma. De plus, nous démontrons que,

au-delà de la configuration laser « classique » à deux couleurs, coupler plusieurs fréquences laser suivant les harmoniques d'une forme d'onde en dents de scie maximise l'émission THz. Nos simulations prédisent une efficacité de conversion d'énergie THz de 2% avec quatre couleurs, une valeur record inégalée à ce jour. À des intensités laser élevées (10^{15} - 10^{18} W/cm²), nous démontrons que le rayonnement THz émis croît de manière non-monotone parce qu'il existe une valeur d'intensité maximisant l'énergie THz produite par chaque couche électronique. Finalement, nous avons étudié l'effet combiné de la photoionisation et des forces pondéromotrices à des intensités proches de 10^{18} W/cm². Ces dernières forces augmentent avec l'intensité laser et ouvrent des perspectives intéressantes pour la génération de champs térahertz très intenses dans le régime relativiste de l'interaction laser-matière.

Title : Generation of intense terahertz sources by ultrashort laser pulses

Keywords : Intense terahertz sources, Laser-matter interaction, Nonlinear optics, Plasma oscillations, Photoionization

Abstract : Terahertz (THz) waves belong to a narrow frequency band of the electromagnetic spectrum, wedged between microwaves and optical waves. Intense THz radiations are highly promising for time-resolved spectroscopy and remote identification of explosives. The goal of this thesis is precisely to study the production of intense THz waves by coupling two ultrashort laser pulses able to ionize a gas target. The plasma created by photoionization acts as a nonlinear frequency converter, transforming part of the laser energy into the THz band via a wide range of physical mechanisms. At moderate laser intensities (10^{12} - 10^{14} W/cm²) we identify, with an experiment done in air, the optical Kerr signature in the emitted THz spectrum, which, even weaker, looks complementary to the plasma signature. Moreover, we demonstrate that, be-

yond the "classical" two-colour setup, coupling several laser frequencies following the harmonics of a sawtooth waveform is optimal to enhance THz emission. Simulations predict a laser-to-THz energy conversion efficiency of 2% with four colours, a record value unequalled so far. At high laser intensities (10^{15} - 10^{18} W/cm²), we prove that the emitted THz radiation grows nonmonotonically, because there exists an optimal intensity value that maximizes the THz energy produced by each electronic shell of the irradiated atom. Finally, we have studied the combined effect of photoionization and ponderomotive forces at intensities close to 10^{18} W/cm². The latter increase with the laser intensity and thus open interesting perspectives for the generation of very intense terahertz fields in the relativistic regime of laser-matter interaction.

